
THE UNIVERSITY *of* EDINBURGH

# The Production and Optimisation of Molten Salt Compatible Micro- and Nanoelectrodes for Enhanced Electroanalysis in LiCl-KCl Eutectic


THE UNIVERSITY
*of* EDINBURGH

Hannah Jo Levene

2019

# Abstract

The unique properties of molten salts have made their utilisation in a variety of industrial processes indispensable. Many of these benefits make them an attractive option for the reprocessing of spent nuclear fuel. In the UK, electrochemical pyroprocessing is being developed using a molten salt of LiCl-KCl eutectic. Fully understanding the electrochemical processes which would occur and developing a robust sensing system for on-line monitoring is essential to advance understanding and maintain both control and safety over the process. Performing measurements within a molten salt is challenging due to the inherently high temperatures (usually around 450°C) and corrosive species that can be present in the molten salt.

For the purpose of electrochemical sensing, microelectrodes and nanoelectrodes have been shown to have enhanced properties, including lower detection limits and insensitivity to convection, because of the increased efficiency of their mass transport and the more rapid establishment of their steady-state diffusion profile. These properties make them ideal for both studying the fundamental electrochemical processes and for on-line monitoring of a pyroprocessing system. Traditional methods of manufacture of these miniaturised devices do not allow precise control over size, which limits reproducibility and requires extensive calibration of the exact dimensions. Microfabrication enables reliable production of both single microelectrodes and microelectrode arrays of exact dimension and offers a route to nanoelectrodes for quantitation in aqueous systems. However, attempts to use such microelectrodes in molten salt have also been hampered by materials degradation particularly at the seals between different materials. Whilst the traditional methods often use materials that are not compatible with molten salts, microfabrication has another advantage of being able to choose certain materials and tune their properties.

This work aimed to bring the greatly needed, enhanced sensing properties of micro and ring nanoelectrodes to the field of molten salts, and hence pyroprocessing, by leveraging the greater

control over device manufacture offered by microfabrication techniques. It presents the systematic development, production, characterisation and iterative optimisation of the single micro- and nano-electrode designs which can withstand the harsh environment of the molten salt. For nanoelectrodes there was evidence of contribution to the measured signal from the conductive adhesion layer. Eliminating this requirement of an adhesion layer enabled the fabrication of molten-salt-compatible nanoelectrodes for the first time.

These optimised micro- and nanoelectrodes were then used to gain insight into charge transfer kinetics and mass transfer processes during molten salt electrochemistry. This work demonstrates the fundamentals of utilising a single nanoelectrode for measurement, avoiding the array overlap which can complicate the electroanalysis. Europium was studied within this work due to its nuclear relevance and soluble-soluble one electron transfer process. Quantitative analysis has enabled the relative contributions of mass transport, alongside charge transfer kinetics and thermodynamics, when using these micro- and nanoelectrode systems to be obtained, compared and contrasted. Together this demonstrates the potential for these electrodes to be utilised to study other nuclear relevant species and to perform on-line monitoring in molten salt systems.

# Lay Summary

At the same time as the world's energy demands are increasing it is also desirable to limit the affect of climate change. Whilst renewables are under development, nuclear fission is capable of providing a reliable energy output with very low emissions of carbon dioxide and is thus likely to play an important role in the mid to long term energy mix. To reduce the amount of nuclear waste requiring long term geological storage, maximise the efficiency of the process and minimise the amount of uranium mined (thus further reducing the carbon dioxide emissions) it is important to recycle the waste fuel and reuse parts of it. One method of reprocessing the waste fuel is electrochemical pyroprocessing, in which the spent fuel is dissolved into a molten salt which is at a high temperature (usually around 450°C). The elements which can be reused are then extracted using electrochemistry (applying a voltage) which causes the elements to be deposited onto an electrode. It is important to understand the processes occuring to maximise the efficiency of the process. Sensors also need to be developed for a monitoring system which will eventually allow control over the industrial process. The harsh conditions in the molten salt are very challenging for the development of sensors, particularly the high temperatures and the presence of impurities which can cause deterioration of the materials.

Micro- and nanoelectrodes have several benefits for analytical measurements in comparison to larger macroelectrodes. This is mainly due to the very efficient diffusion which can bring reagents to the electrode surface. Semiconductor manufacturing techniques have been utilised to consistently produce small electrodes, with a well defined size. Adjustments to the materials used to make these devices have been guided by analysis of the causes of electrode failure when they have been used in the molten salt environment. This has led to the optimisation of nanoelectrodes which can provide reliable measurements within the molten salt. These have been used to investigate a reaction of europium, which is an element which would be present in nuclear waste. Comparison

is made between the different sizes of electrode used to study this reaction, demonstrating the benefits gained by using miniaturised electrodes enabling the fundamental steps in the reaction to be understood.

# Declaration

I hereby declare that the work presented in this thesis is my own unless otherwise credited and the instances here. Figures 1.6, 2.1, 2.3, 2.4 and 2.5 were created by Dr. Justin Elliott. Figure 1.9 was created by Dr. Ewen Blair.

This thesis has not entirely or in part been submitted for any other degree or professional qualification.

Hannah Levene

# Acknowledgements

The PhD journey has been just as fun and challenging as everyone told me it would be. It has at times felt like a long road, and I am very grateful for the help and support of so many people along the way.

Thank you to all of my family who have continually supported me and believed in me - even if they still don't fully understand what I actually do. Especially to my mum - Debbie Penhale and brother Sam Levene I could never have got through it without you. Don't worry you still don't have to read it all!

Thank you Bede Pratt for listening so many times I think you can repeat many parts of this verbatim.

Thank you to my supervisors Professor Andy Mount, Professor Anthony Walton and Dr. Jon Terry for the opportunity to work on this project and guidance along the way.

Thank you to Dr. Justin Elliott and Dr. Simon Reeves who I've worked very closely to discuss molten salt reseach and set-up our national lab. Thanks to Dr Damion Corrigan for the initial guidance and continued encouragements.

Thank you to everyone at the Scottish Microelectronics Centre: Prof Ian Underwood, Dr. Peter Lomax, Cami Dunare, Ewan MacDonald, Richard Blair and Stewart Ramsay for helping me with all the microfab guidance and help. You made me so welcome I'm still here.

Thank you to the past and present members of the Mount and Campbell groups' for all the camraderie and a great group of friends: Kate, Richard, Charlotte, Justin, Simon, Ewen, Ilka, Andrew, Ugne, Katie and Ahmet. Thanks to Jessica Dean, Callum Stone, Mary Jones, Ashleigh Bairstow and Richard Cave - it takes a great group of friends, and you all are.

# Contents

# Nomenclature

| | |
|---|---|
| $A$ | Area of electrode |
| $\alpha$ | Transfer coefficient |
| $B$ | Geometrical constant for electrodes |
| $C$ | Capacitance |
| $c$ | Concentration |
| $C_{dl}$ | Double layer capacitance |
| $d$ | Double layer thickness/ Diameter of electrode |
| $E$ | Potential |
| $E'$ | Formal potential |
| $E_{ac}$ | AC potential |
| $E_{dc}$ | DC potential |
| $E_f$ | Fermi level |
| $\varepsilon_0$ | Permittivity of free space |
| $\eta$ | Dynamic viscosity |
| $E^\theta$ | Standard potential |
| $F$ | Faraday's constant |
| $\gamma$ | Spread parameter |
| $i$ | Current |
| $i_p$ | Peak current |
| $i_c$ | Charging current |
| $i_l$ | Limiting current of micro- or nanoelectrode |
| $J$ | Flux |
| $j$ | Imaginary unit |
| $k$ | Rate of electron transfer |
| $k_B$ | Boltzmann's constant |

| | |
|---|---|
| $k^{\theta}$ | Standard heterogeneous rate constant |
| $\Lambda$ | Reversibility parameter |
| $n$ | Number of electrons |
| $\omega$ | Radial frequency |
| $ox$ | Oxidised species |
| $\phi$ | Phase shift |
| $R$ | Gas constant/ Apparent resistance |
| $r$ | Radius |
| $R_{ct}$ | Charge transfer resistance |
| $red$ | Reduced species |
| $R_{nl}$ | Non-linear resistance |
| $R_s$ | Solution resistance |
| $\sigma$ | Warburg coefficient |
| $T$ | Temperature |
| $t$ | Time |
| $\tau$ | Charging constant |
| $v$ | Scan rate |
| $\xi$ | Spread of the Gaussian distribution |
| $Y_0$ | Warburg admittance |
| $Z$ | Impedance |
| CE | Counter electrode |
| CV | Cyclic voltammetry/ cyclic voltammogram |
| EDX | Energy dispersive x-ray spectroscopy |
| EIS | Electrochemical impedance spectroscopy |
| FFC | Ferri/ferrocyanide solution |
| HOMO | Highest occupied molecular orbital |
| ICP- MS | Inductively coupled plasma mass spectrometry Molar |
| LiCl-KCl | Lithium chloride - potassium chloride eutectic |
| MNEE | Microsquare nanoband edge electrode |
| OCP | Open circuit potential |
| PUREX | Plutonium Uranium Reduction EXtraction |
| RDE | Rotating disc electrode |

| | |
|---|---|
| RE | Reference electrode |
| STTM | Super thin track microelectrode |
| TBP | Tributyl phosphate |
| TTM | Thin track microelectrode |
| WE | Working electrode |

# Chapter 1

# Introduction

## 1.1 Is nuclear power necessary?

As the world's energy demands continue to increase, due to both an increase in population and the technological development of countries, it is putting an increasing burden on energy resources.[1] Low carbon sources are becoming increasingly desired, as the results of global climate change become more apparent, and many countries have signed up to $CO_2$ emissions limits, including the UK which has targeted reducing emissions by at least 80% from 1990 levels by 2050.[2]

It is highly likely that multiple sources of energy will be required to meet this huge challenge as any one source or type of energy is unlikely to be able to meet all of the requirements for the low carbon energy needed. In order to meet these targets, the UK government predicts, there will be large changes with electricity being decarbonised through reliance on renewable and nuclear

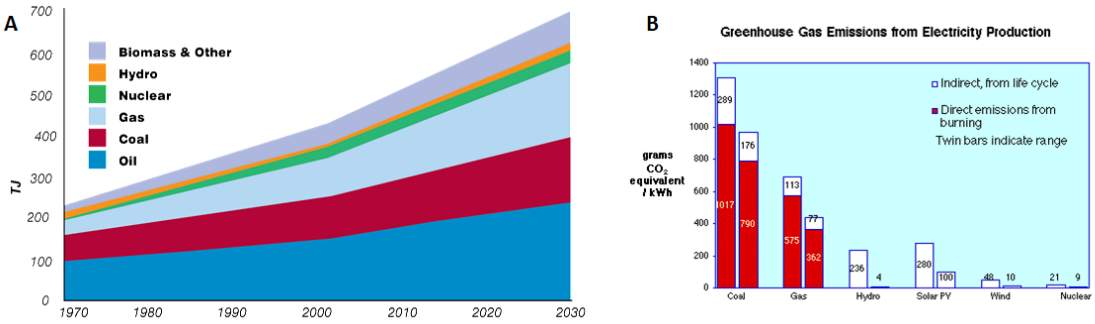


**Figure 1.1:** The breakdown of global energy needs and predictions by source (A). Carbon dioxide emissions from electricity production (B). Taken from [3]

power.[4] Renewable energy sources, such as solar and wind, are attractive but in the short term will struggle to meet the global demand, particularly due to the diffuse nature of the energy source and intermittent availability. Nuclear power thus presents, and is likely to continue to present, an important source of low carbon energy,[5] as it is capable of providing base-load power with low greenhouse-gas emissions. The main $CO_2$ emissions are indirect, for example from power plant construction, decomissioning, mining and fuel transport.[6] Considering the long lifetime of the plant and the high energy density of nuclear energy, this means that, as an energy source, it has very low $CO_2$ emissions per unit energy produced, as can be seen in Figure 1.1.[3, 6] The major drawback of nuclear fission is the generation of radioactive waste, which requires long term storage and potentially cooling (which would add an energy cost).[7, 8] There is also a challenge in overcoming negative connotations in the public perception, after accidents such as Fukushima and Chernobyl.[9, 10] Using historical production data, it has been calculated that nuclear power has actually prevented an average of 76,000 deaths per year from 2000-2009 that would have resulted from fossil fuel burning.[10] The negative impacts on health from other energy sources, such as air pollution from fossil fuels, are often less immediately apparent, but are still long term concerns. There is therefore a desire to overcome the current drawbacks of nuclear fission, with new reactor designs, fuel sources and recycling of used fuel currently being investigated.

## 1.2 Nuclear power production

Nuclear energy is produced by induced fission; destabilising an atom so the nucleus divides into various products and releases energy. This is usually achieved using the uranium isotope 235 ($^{235}$U). The $^{235}$U can absorb a neutron, which briefly creates an unstable uranium 236 nucleus; this 'mother' atom then undergoes a radioactive decay into several lighter 'daughter' atoms. The total mass of the daughter atoms is less than the mass of the target atom, with the mass difference being converted into new neutrons and energy according to Einstein's relationship, $E = mc^2$. The neutrons released from the fission event can then collide with other heavy atoms and cause subsequent fissions, creating a chain reaction; this is shown in Figure 1.2. Nuclear fission energy production aims to control this process by sustaining a controlled chain reaction. This is achieved by ensuring an adequate amount of fissile material (material which can undergo fission and sustain a chain reaction), the use of moderators to slow neutrons and maintain the chain reaction alongside

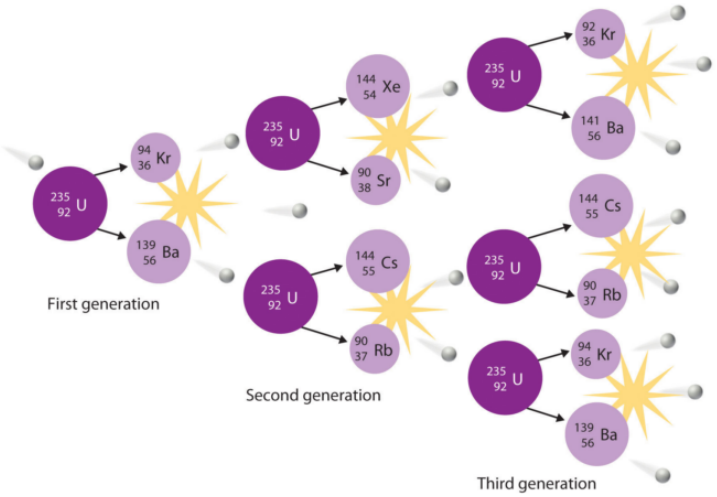


**Figure 1.2:** Illustration of a chain reaction caused by the fission of a $^{235}$U atom which has collided with a thermal neutron (grey circle) producing two lighter daughter atoms, energy and three neutrons which can then cause subsequent fissions. [11]

control rods which can be used to absorb neutrons and prevent a run-away reaction. The energy is used to produce electricity; this is traditionally done in the same way as other fuel sources, by heating water to produce steam which causes turbines to rotate. The lighter elements created in the process are called fission products, many of these are unstable and will themselves decay to other species over time.

Uranium ore naturally contains $^{238}$U which is not a fissile isotope, at 99.3% abundance. Although it can be made to undergo nuclear fission, it does not produce enough neutrons to sustain a chain reaction. In order to produce $^{235}$U, which can sustain a chain reaction, the uranium oxide ore is converted into gaseous $UF_6$. The proportion of $^{235}$U can then be enriched to 5% by separating molecules based on differences in mass, either by filtration or more commonly by gas centrifugation.[12] The uranium is then converted into ceramic form ($UO_2$), either by precipitation from aqueous solutions or by decomposition and reduction with steam and hydrogen.[13] Subsequently it is heated and pressed into fuel pellets, which are loaded into fuel pins then assemblies. Controlling the composition of the fuel is important so that it can sustain a chain reaction. It is also vital to control the process to ensure that supercriticality (where the rate of fission will increase exponentially) will not occur. Over time the fuel rods must be replaced, as the proportion of $^{235}$U to $^{238}$U decreases and there is a build up of fission products which absorb neutrons, stopping the reaction, to maintain efficiency and ensure the chain reaction can be sustained.

## 1.3 Nuclear waste processing

Gradually the fuel efficiency is lowered as the proportion of $^{238}$U increases and as the build-up of fission products 'poison' the fuel rod (as these are efficient neutron capturers and thus inhibit the chain reaction). This means that after about four years, when the fuel rods are no longer viable and require replacement, they still contain a significant amount of $^{235}$U. During fission the uranium nucleus splits approximately in half; however, there are numerous ways that this can happen resulting in a probabilistic distribution in the range of product elements formed. As many of these can also undergo fission, the waste fuel can contain a wide variety of elements. For thermal neutron reactors, which are in widespread use, the typical relative proportions of the waste fuel are shown in Figure 1.3.

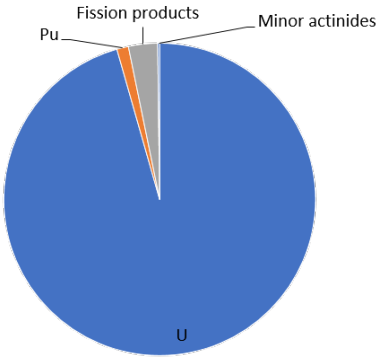


**Figure 1.3:** Illustration of the typical composition of spent nuclear fuel from a thermal reactor.

The minor actinides are transuranic elements (higher atomic numbers than uranium) which are formed by neutron capture succeeded by beta decay. Although only constituting a very small part of the waste fuel, transuranic elements are the main source of radioactivity within the waste, due to the high energy radiation they emit and their long half lives.[14]

After use, the waste fuel may either be stored in a geological repository or be reprocessed and reused, as shown in Figure 1.4. In an open or once-through cycle, the spent fuel is put into interim storage to allow it to cool and reduce the levels of ionising radiation it emits before it is placed into a long term storage repository, which is intended to contain and isolate radiotoxic spent fuel. Geological disposal has many issues, including local acceptance, long term safety and uncertain costs.[7, 8] Another major disadvantage of the once-through cycle is the inefficient use of resources. The uranium component of the spent fuel contains enough $^{235}$U to make recycling

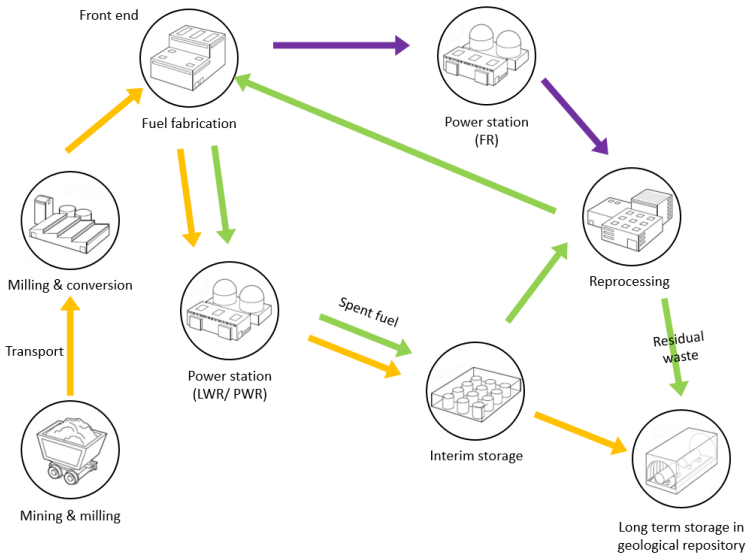


**Figure 1.4:** Illustration of the nuclear fuel cycle. Yellow arrows indicate the open fuel cycle where uranium is mined, enriched, used for fission and is then disposed of in a geological repository. The green arrows show a closed cycle where uranium is recycled and re-enters the front-end of the process. Additionally uranium, plutonium and the minor actinides can be extracted and used as fuel or undergo transmutation in an advanced fast reactor system shown by the purple arrows. Light water reactors (LWR) and pressurised water reactors (PWR) represent current generation II and III reactors which rely on thermal neutrons for the chain reaction, fast reactors (FR) represent generation IV reactors which use fast neutrons and are capable of transmuting minor actinides.

worthwhile, enhancing both energy and resource efficiency. Furthermore Generation IV reactors use fast neutrons which will make $^{238}$U a viable fuel. There are reprocessing methods to reclaim it for future fission by separating it from the minor actinides and lanthanides. This can then be fed back into the front-end of the cycle. Alternatively it can be combined with plutonium and other fission products to create mixed oxide fuel which can be used in certain advanced reactors. Reprocessing and separating out the fission products significantly reduces the volume of high level waste for geological disposal.

The Generation IV International Forum has identified goals for research into the next generation of nuclear systems which include the minimal production of nuclear waste and a further reduction of the risk of materials proliferation, as plutonium is built up in the spent fuel.[15] The closure of the fuel cycle is highly desirable as most of the spent fuel is still fissionable and contains large energy reserves. The main advantage of reprocessing is the preservation of materials, particularly as there is only a finite supply of mine-able uranium in the world. It would also be of benefit

environmentally, as mining uranium accounts for 32% of nuclear greenhouse gas emissions whereas reprocessing accounts for only 7%.[16]

## 1.4 History of spent nuclear fuel reprocessing and the current UK position

There are two candidate methods of reprocessing spent fuel: hydroprocessing and pyroprocessing, which are explained in Sections 1.5 and 1.6 respectively. Reprocessing of spent nuclear fuel originated in the USA in the 1940s by hydroprocessing, when weapons-grade plutonium was extracted by solvent extraction following precipitation, in a process known as PUREX (Plutonium Uranium Redox EXtraction).[17] In the 1960s the UK and France utilised and adapted the PUREX process in reprocesing for second generation plants. This left fission products in the high-level waste disposal stream. In the 80s the process was further improved to reduce the discharge of radioactive waste and produce mixed oxide fuel for the third generation plants.[18] The UK has been closing reprocessing facilities recently, with an end goal of 2020, and is moving towards an open fuel cycle.[19, 20] Alongside this, the UK government is supporting the build of new nuclear reactors up to 16 GW capacity. Combined with the current waste fuel this will amount to 31,200 tonnes of spent fuel, which will require storage prior to disposal in a geological repository - with a predicted date of commencement around 2075.[19, 20] While a suitable site has still to be identified, in 2015 the UK government allocated £250 million to be invested in the nuclear industry over five years, to address deficits in the nuclear industry.[21] This is mainly focused on re-skilling the workforce and performing research aimed at developing the next generation of reactors. This should allow the UK to progress on developing a low carbon future energy supply capable of producing the base-load required.

There are currently two nuclear pyroprocessing systems, both of which use chloride salts as the electrolyte. In the USA there is one at Argonne National Laboratory which uses LiCl-KCl eutectic to reprocess metallic fuel for the Integral Fast Reactor.[22] The other is in Russia at the Research Institute for Atomic Reactors which uses NaCl-KCl eutectic to reprocess oxide fuel for the Fast Breeder Reactor.[23] Advancements have also been made in nuclear pyroprocessing on small scales in Europe and Japan.[6, 24] There is a global desire to limit proliferation, the spread of fissile

material rich in Pu suitable for weapons, within a reprocessing system, so pyroprocessing is highly desirable as plutonium intrinsically should not be recovered in pure form.[25–27]

## 1.5 Hydroprocessing - the PUREX process

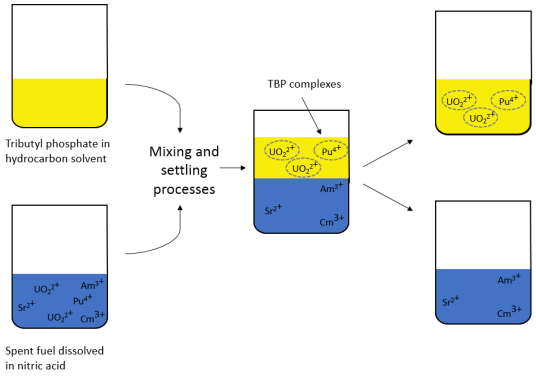


**Figure 1.5:** Illustration of the generalised PUREX process showing the selective separation of uranium and plutonium from other elements by forming TBP complexes which make them soluble in the organic phase leaving the fission products such as americium in the aqueous phase.

Recycling spent fuel from thermal reactors is currently performed by an aqueous-based process, the PUREX (Plutonium Uranium Redox EXtraction) process. Aqueous reprocessing is performed at low temperatures, under 100°C, to ensure the water remains liquid, so the spent fuel must be cooled as it will generate its own heat prior to reprocessing.[28] A scheme of the process is shown in Figure 1.5. The oxide fuel is dissolved into highly concentrated nitric acid. Uranium and plutonium, present as $UO_2^{2+}$ and $Pu^{4+}$, are then extracted selectively as complexes, at the phase boundary, formed with tributyl phosphate (TBP) in a two phase system. TBP is typically added at 30% vol% in an organic solvent such as kerosene.[29,30] The uranium and plutonium may be precipitated and converted into oxides, by thermal decomposition or by the sol-gel process, to make them suitable for fabrication into reactor elements. [28] The organic compounds used in this system break down due to the radiation produced by the nuclear waste. As such, the system needs to be monitored, and degraded compounds must be extracted and replaced. It is also possible to extract pure plutonium using this method, from the organic phase, with dilute nitric acid, after reducing the valence of the plutonium from +4 to +3,[28] which presents a proliferation risk. Multiple cycles are often

needed to ensure sufficient separation is achieved, and it is difficult to separate fission products from transuranics which adds to the other disadvantage of creating large volumes of radioactive and corrosive liquid waste. There have been multiple adaptions to the process to ameliorate some of these drawbacks. The UREX process which adds acetohydroxamic acid to the extraction and scrubbing processes reduces the extractability of neptunium and plutonium to reduce the risk of proliferation.[25,31] Numerous other extraction agents have been developed to create processes such as TRUEX (transuranic extraction) and SANEX (selective actinide extraction) to enable extraction of various transuranic species in the raffinate.[32–36]

## 1.6 Pyroprocessing

Pyroprocessing is currently being developed as an alternative fuel reprocessing approach. The process, which is shown in Figure 1.6, recycles the spent fuel from a molten salt by electrochemically reducing the uranium and also the actinides, and is capable of producing a high-fissile content fuel. The main advantages of this process are the inherent high irradiation resistance of the molten salt system (due to the inorganic components), applicability to different fuel types and compact nature of the plant required. This means it can be situated beside a reactor, removing the need for off-site transportation and interim storage of the waste. As the process is performed at high temperature and is radiation-resistant, it also removes the need for long cooling periods for the spent fuel prior to reprocessing. It is suitable for metal fuels and reprocessing fuel suitable for advanced generation IV systems due to the high resistance of the solvents against criticality.[15, 23]

Pyroprocessing of oxide fuels begins by the chopped spent fuel being anodically dissolved into the molten salt system. Uranium has multiple stable oxidation states (III, IV, V and VI) within a LiCl-KCl melt. X-ray spectroscopic studies have indicated good agreement for classical six coordinate uranium species ($[U(III)Cl_6]^{3-}$, $[U(IV)Cl6]^{2-}$, $[U(V)O_2Cl_4]^{3-}$ and $[U(VI)O_2Cl_4]^{2-}$).[37] The speciation depends on the reducing potential of the melt and quantity of oxygen present. Normally U(III) and U(IV) are the most stable oxidation states.[6, 38, 39] In molten salts typically electrochemical studies have demonstrated the one electron reduction $U^{4+} + e^- \rightleftharpoons U^{3+}$ and the subsequent three electrode reduction to metallic uranium: $U^{3+} + 3e^- \rightleftharpoons U$.[40–43] The uranium, which is the main constituent of the spent fuel, is usually extracted by electroreduction onto a solid steel cathode. Other actinides such as Pu and Np also show similar electrochemical reactions at

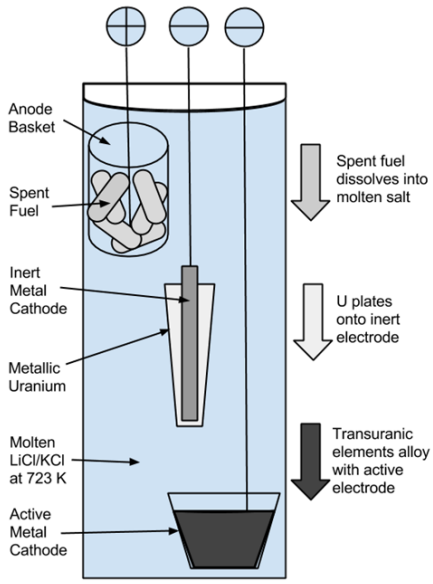


**Figure 1.6:** Illustration of the pyroprocessing method

more negative potentials. There are numerous other species in the waste fuel, so other reactions will also occur. There can be a large variety in the composition of spent fuel; various reactors utilise different fuels and also the length of cooling affects the composition due to ongoing radioactive decay.[37, 42, 44, 45] Both Pu, remaining U along with the actinides, which can also be used for fuel in fast reactors and are present in much lower concentrations, are recovered using an active electrode. These active electrodes are usually either cadmium or bismuth liquid electrodes.[46–48] Alternatively, a solid aluminium electrode can be used.[49–51] The actinides form alloys with these metals, as these are more stable than the pure metallic form less energy is required. Another benefit is that the reduction potentials become more similar for different species. This means that plutonium cannot be extracted in a pure form which is a great benefit, as it ensures inherent nuclear non-proliferation. One issue is the difficulty of achieving 100% separation of lanthanides and actinides due to their chemical similarity.[23, 52] Lanthanides act as neutron poisons, they absorb neutrons but do not undergo fission; if they are present in the recycled fuel it will greatly reduce the efficiency of the fuel.

Most plants have focused on cadmium as a reactive electrode metal due to its high vapour pressure, which helps facilitate the product recovery of the extracted material by distillation of the liquid cadmium.[52, 53] This trait can also pose a risk of loss, which creates a heavy financial burden for replacement. Bismuth is another suitable candidate for an active electrode material as it has a lower

vapour pressure than cadmium and is non-toxic. One possible issue is that neutron irradiation of bismuth produces polonium 210 which is highly toxic, although has a half life of only 138 days.[54,55] Both these liquid electrode materials are also sufficiently dense that the liquid electrode material will remain in the crucible. Aluminium should offer the best separation efficiency of actinides from lanthanides; however, the rate of extraction is expected to be slower, as diffusion is through the solid medium.[49] Pyroprocessing could also become more important with the advanced reactors, such as the generation IV fast nuclear reactors, which use unmoderated fast neutrons rather than slower moderated thermal neutrons to induce fission, producing hotter and more radioactive waste, to which molten salts should be resilient and not suffer degradation. It is unclear as to what fuel will be used for these advanced reactors (for example metal, oxide and carbide) as this is still under investigation. Pyroprocessing could be advantageous for this, as it is capable of reprocessing different fuel types, whilst hydro is unable to tolerate metal fuels.[27]

Significant complications exist with the process, particularly the technological barriers of utilising molten salts, which have hampered the transition of pyroprocessing from theory to industrial applications. The high working temperature of molten salts and the corrosive properties, when reactive species are present in them, create a very challenging environment in which to work.[56,57] Additionally the fundamental properties of molten salts are still not fully understood. There is an active literature focusing on molten salts themselves and development of *in-situ* monitoring methods in molten salt.

### 1.6.1 Molten Salts

Molten salts (MS) are a type of ionic liquid that are typically inorganic salts which melt at high temperatures. Molten salts have a variety of uses due to the beneficial properties they exhibit. Typically they have high ionic conductivity, good thermal stability and the ability to dissolve inorganic compounds.[58–63] There are many different salts and combinations of these, leading to a wide compositional and thermal stability range. This enables molten salts systems to be tailored to the function required. Molten salts are used in a range of industries, including molten salt batteries, the production of chemicals and metals (for example aluminium which uses cryolite), and molten salt reactors.[64–68] The wide electrochemical window of molten salts, the voltage range which can be applied without oxidising or reducing the salt itself, is utilised for stabilising and extracting

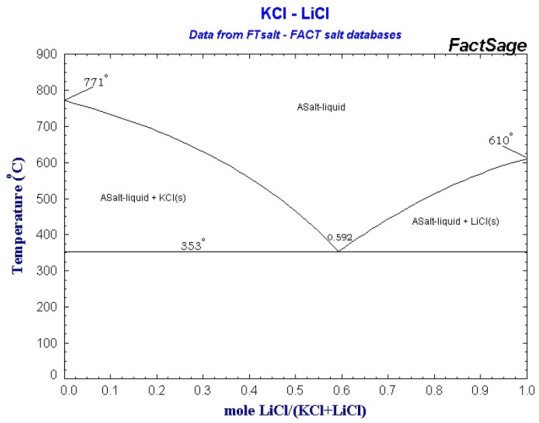


**Figure 1.7:** Phase diagram for the LiCl-KCl binary system.[70]

elements that are unstable in aqueous solution. An example of this is the extraction of rare earth elements,[69] and it is key to pyrochemical reprocessing.

There are several varieties of chloride and fluoride salts which are candidates for pyroprocessing. Each of these have different electrochemical windows. The composition of the salt will also impact the speciation of the dissolved species from the fuel and thus the thermodynamic behaviour of it. There are, however, several challenges in using molten salts. The main complication is the harsh environment presented by the high operating temperatures and corrosion, particularly due to dissolved reactive species such as oxygen.[56, 71–73] One of the disadvantages of using a molten salt solvent is the high temperature and implicit energy costs required to maintain it as a liquid. The heat emitted from some of the very radioactive materials present may also mitigate this energy penalty. Using a mixture of salts can lower the melting point thereby reduce the operating temperature and limit the energy cost. The high energy cost of maintaining a salt phase in liquid form can be reduced by utilising a mixture of salts. The reduction in melting point is due to the increase in entropy upon melting. The eutectic is known as the composition when the melting point of the system is at its lowest, as can be seen in the phase diagram for LiCl-KCl systems in Figure 1.7. The relatively low melting temperature of LiCl-KCl (353°C) and the low cost of these salts make it both practical to work with at lab level and reduce the costs industrially. This is the salt used by the National Nuclear Laboratory, the UK government owned and operated nuclear services technology provider, and is the molten salt used in this study to enhance the UK nuclear relevance and applicability of the work.

### 1.6.2 On-line monitoring of reprocessing in molten salts

It is essential to maintain tight control over any reprocessing system, both in order to safeguard the nuclear processes, ensuring supercriticality may not occur, and also to maximise the efficiency. For these reprocessing methods it is therefore extremely important to develop on-line monitoring. This would be in or near real-time measurement of the system, thus decreasing the delay between identification and resolution of issues. This is complicated by the harsh environments of both systems, but particularly for the molten salts used in pyroprocessing, making only a limited number of techniques for monitoring possible. This has been predominantly accomplished for measurements in fused salts either by spectroscopic or electrochemical techniques. Various spectroscopic techniques have been used to investigate molten salt parameters including; ultraviolet-visible,[74, 75] nuclear magnetic resonance[76] and X-ray.[61, 77] The optical spectroscopic techniques have been shown as promising candidates, as absorption peaks have been found to follow the Beer-Lambert law, which simplifies the conversion of the absorbance measured to the concentration of the species.[44, 74, 75, 78, 79] However, in a real system with many species present, there is the likelihood of overlap from different species in the absorbance spectrum. However, these techniques all require windows which are transparent to the electromagnetic radiation in use, and due to the harsh conditions, these can be quickly corroded. Many of these lab-scale measurements have relied on the authors adapting set-ups due to the paucity of suitable commercially available equipment.[74, 76]

Electrochemical methods have also been utilised to measure chemical parameters in molten salts. As the nuclear pyrochemical reprocessing uses electrochemistry, both to dissolve spent fuel into the melt and also for the extraction of species, this is a promising approach. It is important to understand the parameters involved and so there is a large amount of literature devoted to electrochemical measurements in molten salts.[49, 80–82] For *in-situ* measurements the set up is significantly less complicated for electrochemical measurement, compared to spectroscopic methods; however, the analysis can be more complicated. Voltammetric techniques have been shown to deviate from expected behaviour, either due to uncompensated resistance, convection or at high concentrations (above 1.7 wt%).[83, 84] As concentrations could be as much as 8 %, this presents limitations. An improvement to electrochemical data recorded would be to use miniaturised electrodes, as they offer many benefits over conventional macroelectrodes, such as a higher signal to noise ratio, and they are less affected by convection which would likely to be high at elevated temperatures or within a flowing reprocessing system. The advantages of microelectrodes and nanoelectrodes will be more

thoroughly covered in Chapter 2. Miniaturised electrodes enable the reproducible, sensitive and quantifiable characterisation of redox systems in solution, but the fabrication of suitable sensors for use in such extreme conditions presents a major materials challenge.

## 1.7 Methods of miniaturised electrode manufacture

### 1.7.1 Microelectrode production

A common method of microelectrode manufacture is sealing a thin wire in glass. This can then either be cut perpendicular to the length and polished, to expose a flat disc electrode, or it can be heated and pulled to thin and create a microcone (this may then be polished back to form a disc electrode, if required). These traditional methods are very simple and relatively cheap to manufacture; however, they suffer from disadvantages due to the manual fabrication which causes the area and geometry of the electrode to vary significantly between electrodes.[85,86] To a degree this has been improved, with automated pulley systems available. The electroactive area of the microelectrode must then be determined using microscopy or measurement of a known electrochemical system, such as, the hydrogen evolution reaction on platinum, although this would be difficult to do in molten salt. When these sort of devices have been tested in molten salt, the quartz has been observed to suffer material damage and rapid signal degradation was previously observed, as can be seen for Corrigan's use in LiCl-KCl shown in Figure 1.8.[87]

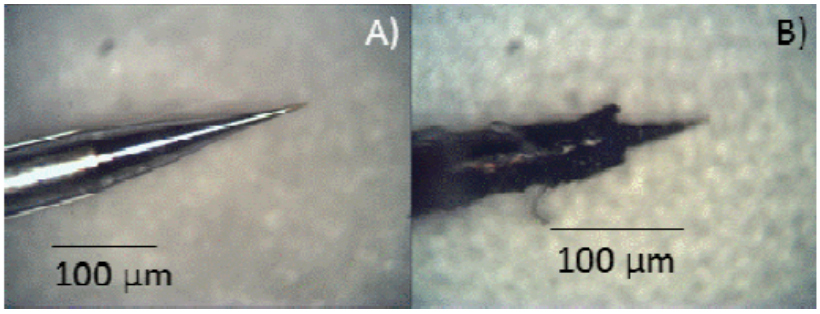


**Figure 1.8:** Optical image of a commercially obtained glass pulled microelectrode and the damage after use in a molten salt. [87]

Photolithography offers an alternative way to manufacture microelectrodes and reliably gives well defined areas.[88–90] This technique can be used to create microelectrodes by either patterning a metal film and then insulating the connections or patterning a film of insulator over metal to

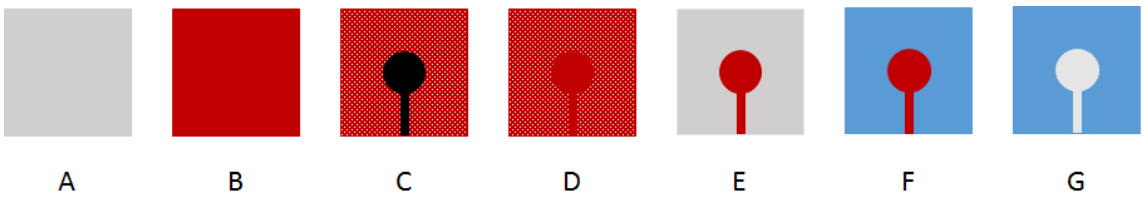


**Figure 1.9:** Illustration of photolithographical patterning (using positive resist) of a thin metal layer shown in grey (A) coating with a layer of photoresist shown in red (B). The photoresist is exposed to UV light while blocking certain areas using a mask shown here in black (C). The exposed area is then soluble to developer solutions indicated by patterned red areas (D) this is removed (E) and the metal can then be etched (F) with resist protecting the desired area. After etching, the remaining resist is removed by dissolution leaving the patterned metal (G).

create a window to the metal of micro-scale dimension. The process, which is depicted in Figure 1.9, involves coating the surface to be patterned with a thin film of a light-sensitive polymer which is known as photoresist. This is then patterned by exposing the resist to ultraviolet (UV) light through a photomask, which masks desired areas from being exposed to the light. For a positive resist, as shown in Figure 1.9, the UV light breaks the cross-linked photoresist causing the exposed area to become soluble in a developer solution. The selectively exposed area can then be etched using various methods such as wet or plasma etching. The remaining resist is then removed, leaving a patterned film. The drawbacks to this method are the high set-up costs and complex development of the processes involved, although this is then mitigated by the numerous microelectrode devices that can be fabricated in one throughput, which brings the cost per device down.

Screen printing is an alternative method of producing microelectrodes reproducibly, but at a cheaper cost than photolithography. However, the resolution is far more limited than for photolithography.[91–93] More recently this has been combined with laser ablation to improve the achievable resolution.[94] Predominantly screen printing has been used to manufacture microelectrodes where cost is a major concern, and the techniques is limited in the materials used as the electrode, because paste is required for the process, and these are unsuitable for use within a molten salt.[91]

### 1.7.2 Nanoelectrode manufacture

Nanoelectrodes, where one electrode dimension must be on the nanoscale, present a bigger challenge to produce as precise control is required in manufacturing methods. Nanobands were the first type

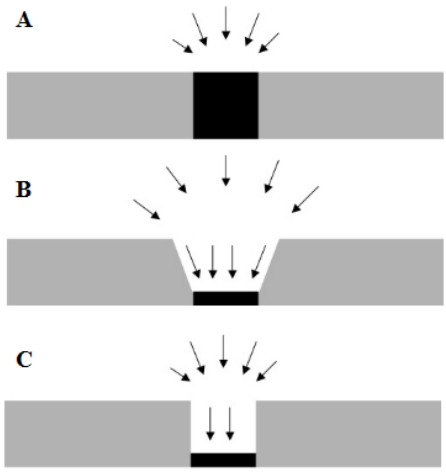


**Figure 1.10:** Suggested diffusion profiles to an inlaid electrode(A), one which is recessed with vertical walls (C) and the intermediate case with angled sidewalls (B) which was found to occur for nanoelectrodes created by FIB milling by Lanyon.[100]

of nanoelectrodes to be fabricated, as these are easier to produce.[95] These can be simply based on a thin film of metal which can be deposited either by sputtering or evaporation, the edge of this layer is then exposed rather than the planar surface. The vertical dimension is then the dimension that is on the nanoscale, and this is more easily controlled within the deposition, rather than patterning the planar surface. White and co-workers first produced these by sputtering platinum, encapsulating it in an epoxy cylinder and grinding flat to produce a nanoband electrode which was nominally between 2-50 nm wide and 1 cm long.[96,97] Ring-shaped nanoband electrodes have also been fabricated in this manner, by depositing a thin film of metal around a glass rod which is then covered with an insulator before the edge is exposed to create a ring electrode as the active surface.[98,99] Focused ion-beam milling (FIB), following standard microfabrication processes, has been used to create recessed nanoband and nanodisc electrodes. This technique was also used to create a well ordered array of nanoelectrodes.[100] The ion beam milling process does not etch the walls isotropically and the sidewalls were found to have an angle of about 19°, due to redeposition of etched material. This was also found to be an issue as some of the surface of the recessed disc electrodes was thought to have been blocked. The diffusion profile to these recessed discs was thought to be intermediate between an inlaid disc and a recessed disc at the base of a cylinder, and that the mass transport control was to the pore opening, as shown in Figure 1.10, due to the non-vertical sidewalls. Photolithography has also been used to produce nanoband electrodes.[101–103]

Electrochemical etching of a wire and encapsulation within an insulator is the most popular method that has been employed to create single nanoelectrodes.[100] This has been utilised when hemispherical or disc electrode geometries have been desired.[104,105] Electrophoretic paint and polymer have been used as insulation, which shrinks when subjected to elevated temperatures, exposing the tip of the thinned metal wire.[106] Glass pulled nanoelectrodes have also been fabricated.[107] Again these suffer from the disadvantages of manual fabrication, as they are made individually, so it is a time consuming process and variability within the process leads to a lack of control over the size of the nanoelectrode produced. Consequently, the nanoelectrodes still require characterisation to determine the exact electroactive area. The seal between the metal and the insulation is another possible source of failure and again would be of greater concern in the harsh environment investigated within this work.

A different approach is depositing metallic layers through a polymeric membrane which creates an ensemble of nanoelectrodes.[108, 109] An advantage of ensembles of multiple nanoelectrodes is the increased current measured. However, these approaches have often led to diffusional overlap, due to the large numbers of electrodes and poor control over positioning. None of the techniques discussed have been established for use within molten salt, and considering the challenges encountered with the seal between the active metal and insulator, a very controlled process and careful choice of materials is likely required.

### 1.7.3 Miniaturised electrodes in molten salts

#### 1.7.3.1 Microelectrodes

The majority of research into microelectrode use within a high temperature molten salt was performed in the 1960s and 1970s, when the potential of molten salt nuclear reactors were under investigation. Polarography was first pursued, where a drop of liquid metal is immersed in a solution, the potential is then swept and the current produced from reactions at the surface of the drop is monitored. This necessitates scans to be performed quickly to ensure that the surface of the drop does not change. In aqueous systems typically mercury is used as the liquid metal due to its low melting point. In high temperature molten salts, dropping mercury electrodes cannot be used because of the high vapour pressure of mercury.[110] Various metals have instead been employed as a dropping electrode in molten salts; the majority of the studies use bismuth and cadmium.[110]

The metals are limited to the requirement of a moderate melting point and relatively noble to have a reasonable potential window that can be investigated.[111] Laitinen highlights some of the limitations of polarography in molten salts, such as the poorly understood wetting properties between the melt and the metal and the fragility of the capillaries used, which are usually broken upon the liquid metal solidifying.[110–112] Other limitations noted are creepage between the metal and insulator which has been observed and corrosion, which was particularly noted for the silver and gold dropping electrodes which Stehle investigated.[113] In an imitation of the behaviour of a dropping electrode, Lyalikov and Karmazin used a solid platinum electrode sheathed in an insulating tube which had an inert gas flushed through it, causing the electrode to periodically have contact with the molten salt. They demonstrated that this was suitable up to temperatures of 1000°C in molten silicates. [112,114]

Attempts have also been made to use other solid microelectrodes in molten salt measurements. Most of these are based upon the pulled wire design and many are at diameters larger than can truly be considered a microelectrode, for instance Laitinen describes the fabrication of a microelectrode at 26 gauge, equivalent to around 400 μm diameter.[115] Carlin and Osteryoung used a 25 μm diameter tungsten wire sealed in pyrex as the insulator to investigate lithium, and separately bismuth plating in LiCl-KCl melt.[116] Although the scan rates used for cyclic voltammetry were very high, and thus the typical microelectrode response was not observed, chronamperometry and pulsed voltammetry allowed more quantitative analysis, particularly for the study of bismuth. They noted corrosion of the insulator after extended use or during deposition and stripping of lithium, which resulted in larger measured currents. Others have used oscillating or rotating electrodes with Pint and Flengas using an oscillating platinum disc with a diameter of 500 μm in nitrate salts at 330°C and NaCl-KCl at 700°C.[117] Brass bellows were used to oscillate the electrode and gave rise to steady-state currents, but these were at slow scan rates of around 3.3 mV/s. Black and deVries used platinum wires of between 250 and 400 μm diameter sealed in lead glass and a typical rotation rate of 264 r.p.m., they found a linear relation between wave height and mole fraction for dilute solutions of cadmium chloride, cobalt chloride, nickel chloride, lead chloride, zinc chloride, and potassium chromate in LiCl-KCl.[118] This was at even slower scan rates of 1.24 mV/s. The use of oscillation or rotation also adds further complication to an already complex high temperature set-up. All of these works have commented on the challenges of sealing the wires into an insulator, as this either interfered with the measurement, due to species such as lead present in the glass, or failed

to maintain a tight seal with the metal.[115] It was also usually noticed after measurements that the the insulator was etched by the molten salt.[115, 116, 118] The complications with production of these microelectrodes and poor control for manufacturing the pulled-wire electrodes are evident in these studies. Black and deVries, in particular, comment on the difficulties encountered for duplicating the behaviour of an electrode and could not draw comparisons between the different sizes investigated.[118] Using photolithography to reliably define the active microelectrode areas has been shown capable of overcoming these difficulties in aqueous conditions.[119] This has been transferred to the molten salt system by Brady who demonstrated qualitative evidence of silver plating and stripping in LiCl-KCl, but this was not quantifiable and the microelectrodes were badly damaged by the harsh conditions.[120, 121] Blair optimised these devices to enhance the lifetime of the devices and produce quantifiable measurements of various species in LiCl-KCl, which is more thoroughly discussed in Chapter 5.[57, 122, 123] This work seeks to further improve these devices to enhance the electroanalysis of nuclear relevant species and progress this to even smaller sized devices.

#### 1.7.3.2 Nanoelectrodes

The difficulties encountered with developing microelectrodes for use in high temperature molten salts have to date largely precluded the production of nanoelectrodes for use in molten salt. As discussed, the complications of ensuring a very small active electrode using insulating materials require the need for a very good seal, which is challenging with the corrosion damage observed in a molten salt, and the possibility of creepage between two materials.[111, 115, 118] To the author's knowledge, the only previously published attempt to employ a nanoelectrode device in a high temperature molten salt was Blair's use of a platinum nanoband electrode with an edge length of 100 μm.[123] This was converted from a microelectrode sensor, by etching through to expose a band electrode as described in Section 1.7.2, to expose a 50 nm band (as the critical dimension) around the edge of the square aperture, in similarity of band nanoelectrodes used for aqueous measurements.[101, 124, 125] A typical response for a nanoelectrode was observed; however, the limiting current recorded was 60.5% larger than the theoretical prediction. Cracks and delamination were observed after use.[123] This represents a proof-of-concept nanoelectrode use in molten salt, and represents the start of this current work for further optimisation of microelectrodes and the

development of nanoelectrodes for use within a high temperature molten salt, for the investigation of nuclear-relevant processes.

## 1.8 Objectives

There is a clear need to develop robust electrochemical sensors suitable for use in high temperature molten salt systems, moving towards the development of sensors suitable for on-line monitoring and also to gain insight into the electrochemical processes occurring during extraction. In this context this thesis aims to:

1. Characterise europium in LiCl-KCl eutectic, a benchmark redox couple present in spent fuel, using macroelectrodes.
2. Develop enhancements to microelectrode production which improves the yield and lifetime of microelectrodes, to enable the reliable characterisation of redox species.
3. Investigate the europium couple using these enhanced microelectrodes
4. Develop reliable nanoelectrodes for use in molten salts and repeat the characterisation of europium using these devices, to gain fundamental insight into the nature of electron transfer reactions in molten salt.

# Chapter 2

# Theory

## 2.1 Electrochemistry

Electrochemistry describes the field of study of the inter-conversion of electrical energy and chemical energy. A reaction will generally occur by the process of electron exchange at the interface between a conducting electrode and an ionic solution, the electrolyte.[126] The exchange of electrons across the interface is called an electron transfer reaction. A typical reaction usually involves mass transfer of the reagent to the electrode followed by electron transfer.

### 2.1.1 Electron transfer

Typically electrodes are metals, the electronic structure of which can be described by Band Theory. This is due to the large number of atoms that are present which have many overlapping atomic orbitals and give rise to a set of electron orbitals of near continuous energy distribution (a band). Metals have overlapping valence and conduction bands meaning that valence electrons are able to move through the material. The Fermi level, $E_f$, is defined as the energy level which would have 50% probability of being occupied by an electron at any given time at equilibrium. The thermodynamics of electron transfer between the metal electrode and the redox species will be governed by the relative energy of the Fermi level of the metal relative to either the highest occupied molecular orbital (HOMO) for oxidation or lowest unoccupied molecular orbital (LUMO) energy

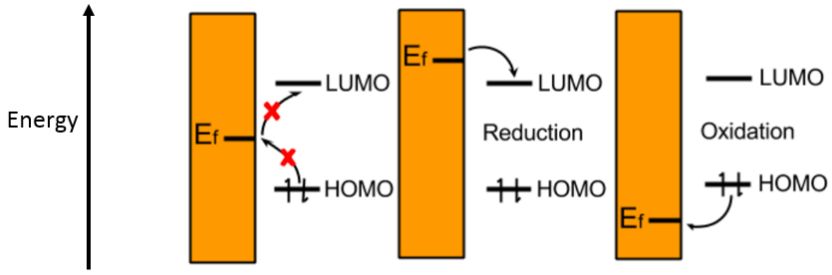


**Figure 2.1:** Illustrative representation of how the potential on the electrode and hence the position of the Fermi level of electrode effects the transfer of electrons between the electrode and the redox species. When $E_f$ is above the LUMO electrons can thermodynamically be transferred to the redox species and reduction will be favoured. If $E_f$ is between the HOMO and LUMO no net reaction will occur. If $E_f$ is below the HOMO then the redox species will be oxidised.

level for reduction of the electronic structure of the redox species. This is shown schematically in Figure 2.1.

The general expression for a reversible one electron transfer is:

$$ox + e^- \rightleftharpoons red$$

where $ox$ represents the oxidised species and $red$ the reduced species. The energy difference between $E_f$ and the energy level of the redox species orbital acts as a driving force for electron transfer. The reaction will also depend on the thermal energy of the system. Applying a potential to the electrode will change the Fermi level, and thus this can be used to control the driving force and hence the rate of the electron transfer occurring. Utilising this enables the study of the oxidation or the reduction of a redox species. The rate of the electron transfer, $k$ , is described by the Butler-Volmer equation:

$$k_s = k^\theta \exp^{[\pm\alpha_s nF(E-E^\theta)/RT]} \tag{2.1}$$

where $s$ represents either $ox$ or $red$ respective of the direction the process occurring, $n$ is the number of electrons transferred, $F$ is Faraday's constant (96485 $\text{Cmol}^{-1}$), $R$ is the gas constant (8.314 $\text{JK}^{-1}\text{mol}^{-1}$), $T$ is the temperature, $\alpha$ is the transfer coefficient, $E$ is the applied potential, $E^\theta$ is the standard electrode potential and $k^\theta$ is the standard heterogeneous rate constant.

Marcus theory is a useful consideration for electron transfer relating activation and rate constant to the thermodynamics of the system. It replaces Eyring's transition state theory for the event where

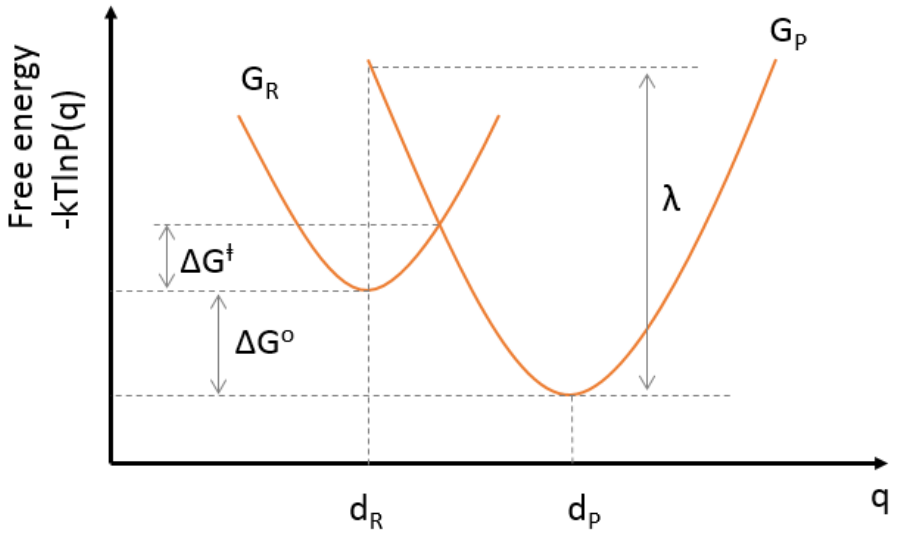


**Figure 2.2:** Diagram to represent the variation of free energy with reaction co-ordinate for electron transfer events from Marcus theory. The free energy of the transfer and therefore rate can thereby be related to the free energy difference between the electron donor and acceptor pair before and after electron transfer and the reorganisation energy ($\lambda$).

an electron moves from a chemical species (electron donor) to another (electron acceptor). A similar diagram represents the event relating free energy to the reaction co-ordinate ($q$), as shown in Figure 2.2. Rather than forming a structurally defined transition complex the species involved are only weakly coupled and remain independent. On the timescale of electronic transitions nuclear moments and positions do not significantly alter (Frank-Condon principle) only the electron jumps so instead it is the reorganisation of the surrounding solvent which creates the geometrically favoured transfer. The theory was initially developed for outer-sphere reactions where the solvent molecules are loosely bound such as charge transfer between aromatic hydrocarbons and $[Ru(NH_3)_6]^{3+} + e^- \rightleftharpoons [Ru(NH_3)_6]^{2+}$.[126–128]

Considering the parabolic shape of the diagram in Figure 2.2for both the reagents (represented by R, which are the donor and acceptor pair before transfer) and products (represented by P, which are the donor and acceptor pair after transfer) leads to the relationship between the energy barrier for the electron transfer, $\Delta G^{\dagger}$, to the standard free energy of the transfer, $\Delta G^o$, and the reorganisation energy, $\lambda$: $\Delta G^{\dagger} = \frac{(\Delta G^o + \lambda)^2}{4\lambda}$. This gives the expected Arrhenius form for the rate constant of the electron transfer: $k = A\exp(\frac{(\Delta G^o+\lambda)^2}{4\lambda RT})$ as expressed in Equation 2.1. The transfer coefficient is a measure of the symmetry of the energy barrier (this can be considered as the geometry of the

intersection region of the graph in Figure 2.2). The force constant, $k_F$, describes reorganisation within the compound, controls the shape of the quadratic function. This can be modelled similarly to a harmonic oscillator ($F = -k_F x^2$). Normally the force constants are similar for both oxidised and reduced species (symmetric Marcus theory). Leading to the transfer coefficient typically being close to 0.5. It is also defined that $\alpha_{red} + \alpha_{ox} = 1$.[126, 127]

The theory was extended to include reactions where the inner-sphere was involved, these are the more closely held solvent molecules. These inner-sphere reactions involve a change in geometry or distance of co-ordination shell for example metal deposition and ion transfer reactions. The overall rate can depend on various reaction steps depending on the system under consideration. Examples of these include: adsorption of the reacting species, an electron-transfer step, a preceding chemical reaction, co-adsorption of a catalyst. Butler-Volmer type laws can still apply depending on the reaction controlling the rate. However, other laws may also apply for ion transfers and rates may be modified by apparent transfer coefficients for inner-sphere electron transfers from adsorbed species.[127]

An applied potential causes a chemical reaction to occur and the resultant current can be measured to give insight into the rate of the reaction. The partial currents for reduction and oxidation described by:[126]

$$i_{red} = -nFAk_{red}c_{ox} \tag{2.2}$$

$$i_{ox} = nFAk_{ox}c_{red} \tag{2.3}$$

with $c_{ox}$ and $c_{red}$ being the concentrations of the oxidised and reduced species respectively, at the surface of the electrode. The total current, $i$, is the sum of the partial currents. For an electrode of given area if the concentration was fixed only the rate of electron transfer would affect the measured current. However, as a reaction progresses the concentration of the reacting species can decrease at the electrode surface. For most systems the concentration can be influenced by mass transport and as the local concentration is depleted this can dominate the rate of the reaction.

### 2.1.2 Mass transport

The three potentially major contributions to mass transport are; diffusion, convection and migration. In practical electrochemical measurements it is desirable to avoid complexity by having only one of these be the main factor controlling local concentration. Often diffusion is the mass transport form of interest and efforts are made to reduce the influence of migration and convection to make this the predominant mechanism of transport to the electrode.

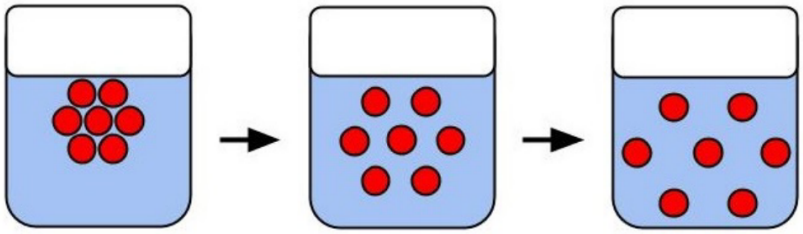

**Figure 2.3:** Schematic of diffusion causing movement down a concentration gradient to form a homogeneous solution.

Diffusion describes the thermal motion due to Brownian motion. If there is a region of high concentration diffusion will gradually cause this to become a homogeneous mixture as illustrated in Figure 2.3. The rate of diffusion depends on the concentration gradients, as described by Fick's first law:

$$j = -D\nabla c \tag{2.4}$$

where $j$ is the three-dimensional flux of a species, $D$ is the diffusion coefficient, $\nabla$ is the nabla operator (in Cartesian co-ordinates $\nabla = \mathbf{i}\frac{\partial}{\partial x} + \mathbf{j}\frac{\partial}{\partial y} + \mathbf{k}\frac{\partial}{\partial z}$) and $c$ is the concentration. Fick's second law of diffusion describes the variation of concentration in time across a 3D space:

$$\frac{\partial c}{\partial t} = D\nabla^2 c \tag{2.5}$$

where $t$ is the time and all the other variables are as described for Equation 2.4. For a process controlled by diffusion the biggest influences are the growth of the diffusion field and the diffusion coefficient. The diffusion field growth is dependent on the electrode geometry as well as any potential physical obstructions in the set up. This could be other electrodes in an array, which will influence

the shape of the diffusion field. The diffusion coefficient in aqueous conditions is typically between $10^{-5}$ and $10^{-6}$ $cm^2s^{-1}$, [129] and is approximated by the Stokes-Einstein equation:

$$D = \frac{k_B T}{6\pi\eta r} \tag{2.6}$$

where $k_B$ is the Boltzmann constant, $T$ is the temperature, $\eta$ is the dynamic viscosity and $r$ is the hydrodynamic radius.

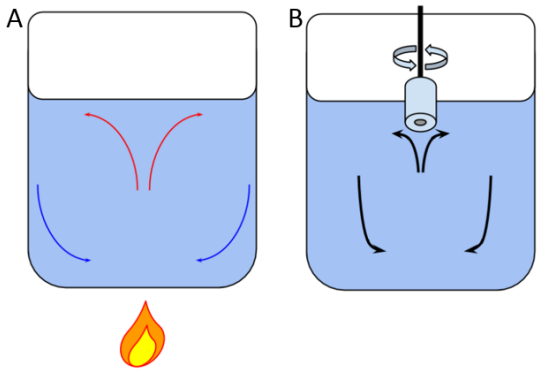


**Figure 2.4:** Schematic of natural convection due to temperature gradients within a solution (A) and forced convection with the use of a rotating disc electrode (B).

Convection describes mass transport caused by the macroscopic flow of the the solution. This can either occur naturally, for instance due to temperature gradients present, or it can be forced to occur if for example the solution is stirred, shown in Figure 2.4. In electrochemical processes natural convection often arises from density gradients due to electrolysis. Convection caused by natural forces can be difficult to mathematically model as it can be random or unpredictable, and often this is minimised during experiments by maintaining a constant temperature throughout the system by using a water bath. Alternatively forced convection can be used to control the mass transport of the system as this can be more easily mathematically modelled and thus accounted for. This is typically achieved with the use of rotating electrodes within experiments as mentioned in Section 1.7.3.1.

Migration describes the movement of charged ions due to the local electric field. An electric field will be present in a solution due to the applied potential on an electrode or an imbalance of charge distribution. The field will cause ions of opposite charge to be attracted towards the electrode and ions of like charge to be repelled as can be seen in the schematic illustration in Figure 2.5. The charge of the species and the electric field gradient balanced by retarding effects, such as

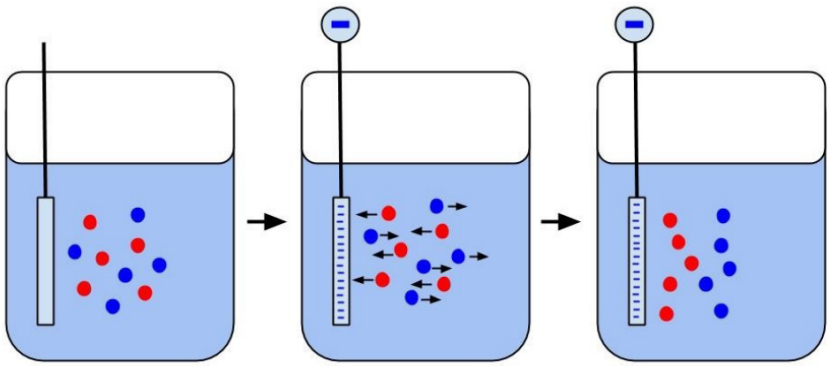

**Figure 2.5:** Schematic of the migration of charged species due to an applied negative potential on the electrode, red positively charged ions move towards the electrode and blue negatively charged ions are repelled.

the frictional forces experienced, will determine the flux of species to the electrode surface.[129] Migration is usually mitigated by the addition of a background electrolyte, which contains charged ions, at a higher concentration than the redox species. The background electrolyte should be chosen so that it does not undergo redox reactions within the electrochemical window of interest. This then acts to shield the redox species from the charges on an electrode or ions in proximity by the formation of an electrical double layer or by the formation of a counterbalancing charge cloud.

### 2.1.3 Electrical double layer

When a potential is applied to an electrode a double layer is formed which prevents further migration as shown in Figure 2.6. The modelled structure of the electrical double layer consists of a dense layer of oppositely charged background electrolyte ions adsorbed to the surface of the electrode by chemical interactions known as the Stern or Helmholtz layer and a diffuse layer of ions which are not adsorbed but are still attracted to the electrode because of the electric field.

The diffuse layer is attracted to the surface charge by the Coulombic force whilst the ions are still free to move in the solution under thermal motion. The separation plane between the two zones is called the outer Helmholtz plane (OHP). The thickness of the diffuse layer depends on the total ionic concentration of the solution. At a certain distance the ions exist as in the bulk, as they are completely shielded from the electric field at the electrode. The redox species experiences a steep potential gradient close to the electrode surface, indicated in Figure 2.6 by the solid black line.

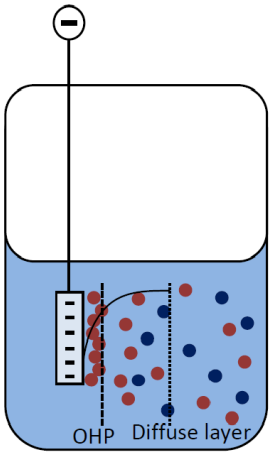


**Figure 2.6:** Schematic representation of the electrical double layer formed at the surface of the electrode in the solution with a dense layer of oppositely charged positive ions (red) and a diffuse layer. The solid black line indicates the potential experience by the ions in the solution, large close to the electrode surface and decreasing with distance from the electrode.

The possibility of electron transfer occurring via quantum tunneling with species further from the electrode surface is therefore prevented which ensures that the electron transfer follows Butler-Volmer kinetics. Typically the reaction occurs over distances under 5 nm.[128] The double layer capacitance and charging current can be important in electrochemical experiments. The capacitance of the double layer, $C_{dl}$, which determines the amount of charge within this surface layer typically has values around 10 $\mu Fcm^{-2}$when background electrolyte is present.

### 2.1.4 Three electrode cell

The measurement setup requires two main components to enable the study of a single working electrode, the application of a defined absolute potential and the recording of the current. A three electrode cell is often used to study a redox reaction which consists of a reference electrode (RE), a working electrode (WE) and a counter electrode (CE). This is illustrated in Figure 2.7.

The current is measured between the working electrode and the counter electrode. Historically, to ensure that the reaction at the working electrode is controlling the measured current, the area of the counter electrode is much larger than the working electrode. Electronics in the potentiostat ensure that is now the case and that the counter electrode passes the same current as the working electrode (with opposite sign). The reference electrode gives a fixed stable potential so that when

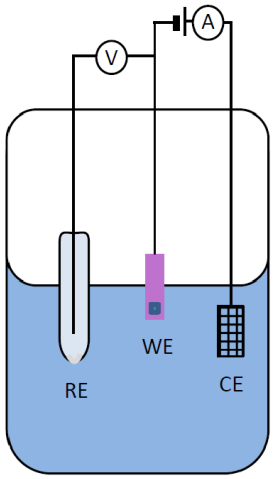


**Figure 2.7:** Three electrode cell schematic with a working electrode (WE), counter electrode (CE) and reference electrode (RE). The current is measured between WE and CE, the potential is measured between the WE and the RE.

a voltage $E$ (potential difference), is applied between WE and RE the working electrode potential is then known and varied in relation to this reference potential. As potential is a relative scale this allows the comparison between different experiments versus a constant reference electrode.

### 2.1.5 Reference electrodes

A reference electrode is an important part of an electrochemical set-up as it is used to give a stable potential to which other potentials can be referred or controlled by application of a potential difference. A good reference electrode will therefore have a potential that is stable with time, temperature and is not altered by small perturbations to the system e.g. drain currents. The reference electrode potential is usually fixed by the use of a redox system with constant activity of each participant of the redox reaction achieved often with the use of a saturated solution to maintain the activity. The electron transfer reaction must also be reversible. The Nernst equation describes the relationship between the concentration of oxidised and reduced species and the electrode potential for a reversible electron transfer under thermodynamic control.

$$E = E^{\theta} + \frac{RT}{nF} ln(\frac{a_{ox}}{a_{red}}) = E^{'} + \frac{RT}{nF} ln(\frac{c_{ox}}{c_{red}}) \tag{2.7}$$

where $E$ is the potential of the electrode, $E^{\theta}$ is the standard potential of the reaction, $E'$ is the

formal potential, $R$ is the gas constant, $T$ is the temperature, $n$ is the number of electrons in the reaction, $F$ is the Faraday constant and $a_{ox}$, $a_{red}$, $c_{ox}$ and $c_{red}$ are the activities and concentrations of the oxidised and reduced forms at the electrode surface. The formal and standard potentials are offset by a small value as the activity is equal to the concentration multiplied by a coefficient which depends on the electrolyte and concentration for a constant ionic strength.[126]

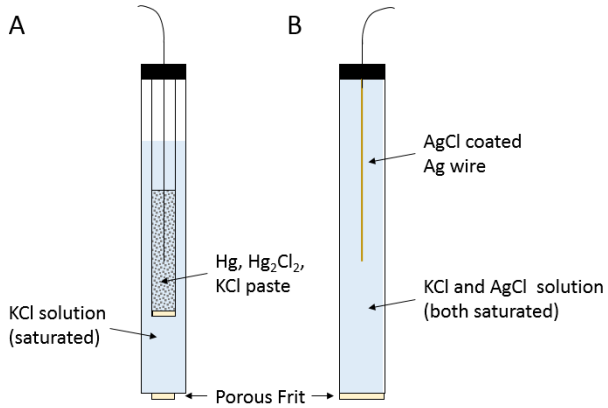


**Figure 2.8:** Aqueous reference electrodes, saturated calomel electrode (A) and Ag/AgCl electrode (B).

There are many different possible reference electrodes. For aqueous systems a saturated calomel electrode, which is a half cell (a structure which contains a conductive electrode and a surrounding electrolyte) composed of mercury (I) chloride in contact with a mercury pool, or a silver/silver chloride electrode which are often used which are both illustrated in Figure 2.8. Both types have a porous frit which allows ion exchange between the half cells and system under measurement so that the potential can be measured. The silver chloride reference electrode is a silver chloride coated silver wire in contact with a solution saturated with KCl and AgCl. The half reaction for the silver chloride reference electrode and the saturated calomel are respectively:

$$AgCl(s) + e^- \rightleftharpoons Ag(s) + Cl^-(saturated)$$

$$Hg^{2+} + 2Cl^- \rightleftharpoons Hg_2Cl_2(s)$$

For non-aqueous systems modifications need to be made as using an aqueous electrode introduces unmeasurable liquid-liquid junctions. In the case of the molten salt studied in this work, an aqueous

electrode clearly would not be suitable at the high temperatures involved. Most reference electrodes used in molten salts have been based on the $Ag/Ag^+$system with a porous frit.[130–132]

### 2.1.6 Macro-, micro- and nanoelectrodes

There are differences in the diffusion fields established at different sized electrodes as can be seen in Figure 2.9. It is clear from this that miniaturised electrodes experience enhanced mass transport in comparison to macroelectrodes.[97, 104] At a macroelectrode planar diffusion to the electrode surface occurs, the surface area of the diffusion remains constant as the field extends into the solution over time. This results in the mass transport limited current decreasing as the redox species has to diffuse from further away. At a microelectrode a hemispherical diffusion field is established due to the small size of the electrode. As this extends into the solution over time the surface area increases to counterbalance the distance the species has to diffuse from. So whilst the species still has to diffuse from further away there is an increasing volume of solution and hence number of species accessible. This means that a steady state is established as these two effects exactly counteract each other, creating a limiting current.


**Figure 2.9:** Schematic representation of the diffusion fields established at different sized electrodes. Planar diffusion at a macroelectrode surface (A) and hemispherical at a microelectrode surface (B). The colour gradient indicates the progression of the diffusion field extending into the solution with time.

Whilst radial diffusion also occurs at the edges of macroelectrodes the perimeter is small in comparison to the area of the electrode so the planar diffusion dominates. As the electrode size decreases from macro- to micro- or even smaller to nano-, the ratio between edge and surface increases causing the radial diffusion to dominate. This typically occurs when the radius is on a scale of tens of microns. The radial diffusion has the benefit of improved mass transport so that the current density is greater at smaller electrodes than at a macroelectrode.[133, 134]

This enhanced mass transport to micro- and nanoelectrodes also reduces the effect of unwanted convection on the response. The comparison of the convection velocity, $v$, and mass transport coeffi-

cient (which is given by $D/r$) demonstrates the relative contributions of each, so for microelectrodes where $D/r \ggg v$ there is no convective effect. This has enabled the use of microelectrodes in flowing or stirred systems.[135, 136] The time for the system to reach steady state is around $r^2/D$,which is very long for macroelectrodes so experimentally impractical whereas for microelectrodes occurs rapidly. The steady state response at micro- and nanoelectrodes results in a response which is significantly easier to analyse than for macroelectrodes, particularly as in addition it has been shown to produce additive responses for measurements on multiple analytes.[57] For macroelectrodes in order to extract a steady-state current mathematical techniques such as convolution have to be used.[126] This has been shown to have variable amounts of success e.g. within a molten salt system, when additional non-Faradaic charging currents cannot be neglected .[57, 137]

Although small electrodes have high current densities they exhibit low absolute currents due to their small size. There is also reduced voltage drop across the electroactive surface. Both of these effects lead to a lower voltage drop within the electrochemical cell (known as $iR$ drop) for micro- and nanoelectrodes in comparison with macroelectrodes. This has made it possible for microelectrodes to be used in resistive solutions and in the gas phase.[134, 138]

Micro- and nanoelectrodes additionally suffer less unwanted noise on measurements. Noise, such as capacitative and electrical noise, can hinder the measurement of Faradaic current (current due to redox process). Capacitive charging current arises because of the formation of a capacitative electrochemical double layer, as described in Section 2.1.3. The charging current, $i_c$, can be defined as the normal equation for charging a capacitor:

$$i_c = \frac{V}{R_s} e^{-\frac{t}{\tau}} \tag{2.8}$$

where V is the voltage applied, $R_s$ is the solution resistance between the working and reference electrode and $t$ is the time. The time constant, $\tau$, is defined as:

$$\tau = R_s C_{dl} \tag{2.9}$$

and the capacitance of the double layer, $C_{dl}$, is given by:

$$C_{dl} = \varepsilon_0 \varepsilon_r \frac{A}{d} \tag{2.10}$$

where $\varepsilon_0$ and $\varepsilon_r$ are the permittivity of free space and relative of the solution respectively. $A$ is the area of the electrode and $d$ is the double layer thickness. Therefore the charging (non-Faradaic) current is proportional to the area of the electrode for all sizes of electrode. The benefit lies within the relationship of the Faradaic current to the size of the electrode. For a macroelectrode the Faradaic current is directly proportional to the area of an electrode, as can be seen from Equation 2.12. Whereas for micro- and nanoelectrodes the current is proportional to the electrode dimension, dependent on the radius for a disc electrodes as evident from Equations 2.13 and 2.14. Therefore for a macroelectrode the ratio of the Faradaic to capacitative current is constant, irrespective of the electrode area. For a microelectrode or nanoelectrode the capacitative current decreases more rapidly than the Faradaic current as the electrode shrinks. Thus the ratio of Faradaic to capacitative current increases. The electrical noise also decreases significantly with a reduction in electrode area. This leads to a better signal to noise ratio for miniaturised electrodes, which is beneficial for the detection of redox species at low concentrations.[138]

#### 2.1.6.1 Geometry of electrodes

Microelectrodes of many different geometries have been used for investigating redox processes. Examples of common geometries are shown in Figure 2.10. Only the limiting current for inlaid disc and hemispherical microelectrodes have been analytically modelled to date, but this is bypassed with the use of numerical models for other geometries. Mathematical modeling is easier for symmetrical electrodes as this allows the reduction of the calculation. The general expression for the limiting current, $i_l$, for a microelectrode is:

$$|i_l| = BnFDcr \tag{2.11}$$

Where $n$ is the number of electrons transferred in the reaction, $F$ is Faraday's constant, $r$ is the radius of the electrode and $D$ is the diffusion coefficient as previously defined. $B$ is a constant which depends on the geometry of the electrode. For a disc electrode $B = 4$. Both the shape and whether the electrode is inlaid (flush with the surface of the insulator), recessed or protruded affects the prefactor. Previous computational and experimental studies have indicated that a small recess of around 500 nm does not cause a significant deviation from the inlaid square microelectrode

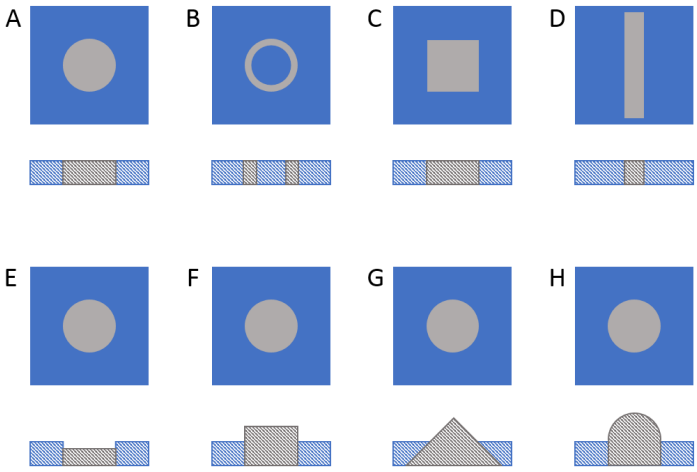


**Figure 2.10:** Schematics showing common microelectrode geometries, with grey representing the electrode and blue an insulator, viewed from above (solid colour) and the side (striped). The geometries shown are an inlaid disc (A), ring (B), square (C), band (D), recessed disc (E), cylinder (F), cone (G) and a hemispherical electrode (G).

response.[139, 140] In this thesis work solely recessed disc electrodes with a recess of 500 nm are used, as illustrated by Figure 2.10 E.

#### 2.1.6.2 Arrays

To overcome one of the limitations of low current measurements with the use of small electrodes, often groups of small electrodes are combined to amplify the current. If these groups are randomly positioned then they are normally known as ensembles; if the position is ordered then they are known as arrays. If a group of microelectrodes was considered rather than a single microelectrode, initially hemispherical diffusion occurs at each individual microelectrode element. However, as time progresses and the diffusion field grows these will start to overlap and a planar diffusion field will be established across the entire area of microelectrodes.[91] Ensembles are clearly harder to analytically model as the positions and inter-electrode distances are not well defined. Although groups of electrodes amplifies the measured current, diffusional overlap complicates the measured response. In this work arrays of electrodes are not used. For development of on-line sensors they could be of use to amplify the measured signal.

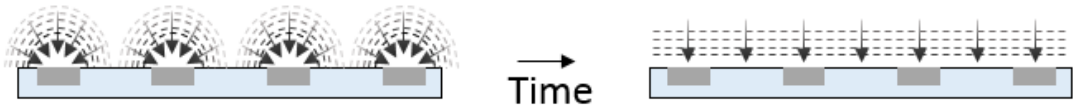


**Figure 2.11:** Schematic of the development of the diffusion field for an array of microelectrodes, changing from hemispherical diffusion to individual elements to planar diffusion across the array.

## 2.2 Electrochemical techniques and reactions

### 2.2.1 Redox couples

Figure 2.12 shows a typical reduction reaction at an electrode where both the oxidised and reduced species are soluble (soluble-soluble reaction). Mass transport controls the movement of the redox

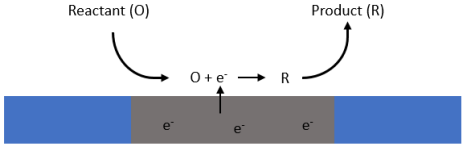


**Figure 2.12:** Schematic of a simple soluble-soluble reduction at the surface of an electrode.

species to the surface of the electrode where it undergoes electron transfer before the product travels away from the electrode under mass transport again. In some cases the product is not soluble in the solution, in this situation the reduced species remains on the surface of the electrode. If this is insulating it can passivate the surface of the electrode and prevent electron transfer. Alternatively the deposited species can be conducting, for metals this type of reaction is called a plating reaction for the metal in reduction and the oxidation of the metal is known as a stripping reaction.

### 2.2.2 Cyclic Voltammetry

Cyclic voltammetry is a common technique used to investigate a reaction at an electrode. This involves sweeping the potential of an electrode from an initial potential to an upper or lower vertex (depending on the direction of the scan) before scanning back to the initial potential. Normally the potential is scanned linearly at a constant scan rate, $v$, and the current is measured. The resultant plot of current against potential is known as a cyclic voltammogram (CV). In this work CVs are scanned negatively as 'first' direction on the forward scan unless otherwise stated.

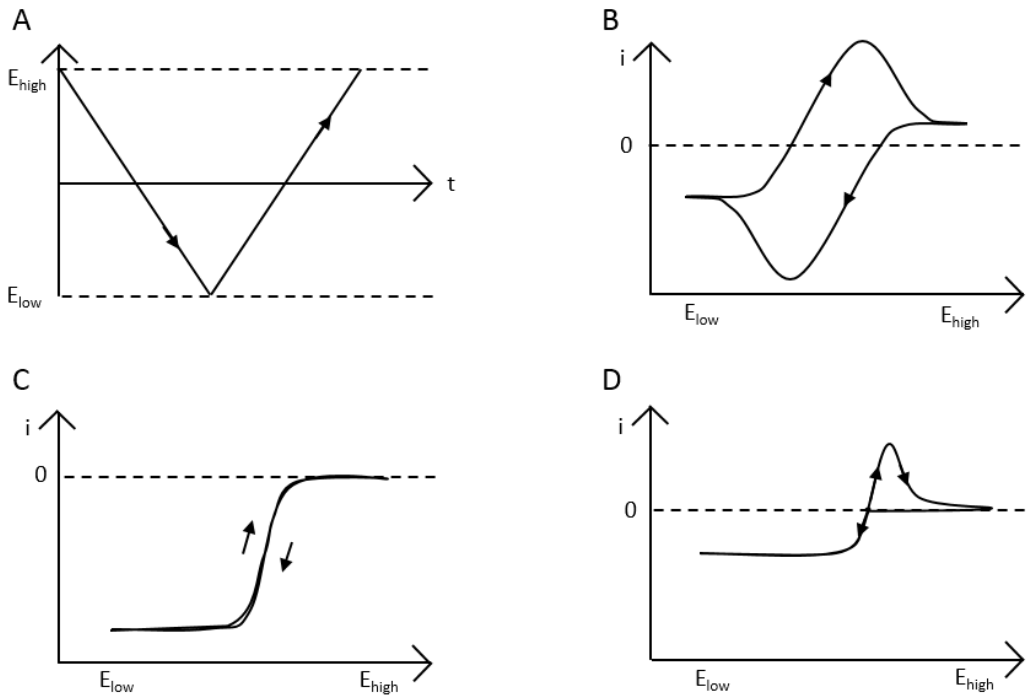


**Figure 2.13:** An example of a the voltage sweep applied to perform a cyclic voltammogram (A) and typical responses for a reversible electrochemical system using a macroelectrode (B), a microelectrode with a soluble-soluble couple (C) and a plating-stripping reaction on a microelectrode (D).

When a CV is performed across potentials at which a redox reaction can occur on a macroelectrode the typical response is shown in Figure 2.13. Initially the current is controlled by the potential and the kinetics of the electron transfer. The Nernst equation (2.7) describes the ratio of reduced and oxidised species (at the electrode surface) as a function of the applied electrode potential, $E$. Typically the formal potential is used for practical measurements as concentration is an easier function to measure and control in comparison to the activity of species. With changes in temperature or the concentration of the redox species there will be a shift at the potential at which the reaction occurs. As the concentration of reactant decreases at the electrode surface in comparison with the bulk, mass transport then starts to dominate the response which is evident in the CV with the peak being followed by a reduction in measured current for the macroelectrode response. As already discussed for a micro- or nanoelectrode soluble-soluble reaction a limiting current is established rather than a peak due to the enhanced mass transport to the electrode. For a plating and stripping reaction on a miniaturised electrode whilst the reduction results in

a limiting current as it is mass transport limited the oxidation reaction is different as the plated material is on the surface of the electrode so the stripping reaction is a sharp peak shape.

For a macroelectrode with diffusion as the dominating mass transport mechanism the peak current, $i_p$, for a reversible reaction is defined as:

$$\frac{|i_p|}{\sqrt{v}} = b(nF)^{\frac{3}{2}} Ac\sqrt{\frac{D}{RT}} \tag{2.12}$$

where $v$ is the scan rate, $b$ is a prefactor depending on the type of reaction, $A$ is the area of the electrode, $c$ is the bulk concentration and all other variables are as previously defined. For a soluble-soluble reaction $b = 0.4463$ and the equation is known as the Randles-Sevcik equation. For a plating reaction $b = 0.61$ which is known as the Delahay equation which is only valid for the peak observed in the reduction reaction.[126]

The analytical expression for the limiting current at a disc microelectrode, the Saito equation, is given as:[141]

$$|i_l| = 4nFDcr \tag{2.13}$$

where $r$ is the radius of the microelectrode. For a square band nanoelectrode, the expression for the limiting current is:[123, 140]

$$|i_l| = 0.98nFDcl \tag{2.14}$$

where $l$ is the length of a side of the square aperture. This equation is modified for a ring nanoband electrode with a geometrical factor $B = 1.46$ to give:

$$|i_l| = 1.46nFDcr \tag{2.15}$$

The measured current also depends on the reversibility of the reaction. Figure 2.14 shows an illustration of the change in expected CV response, for a macroelectrode, depending on the electrochemical reversibility of the system. The reversibility of the electrochemical system depends on the rate of electron transfer compared to the mass transfer. A reversibility parameter, $\Lambda$, is defined as:

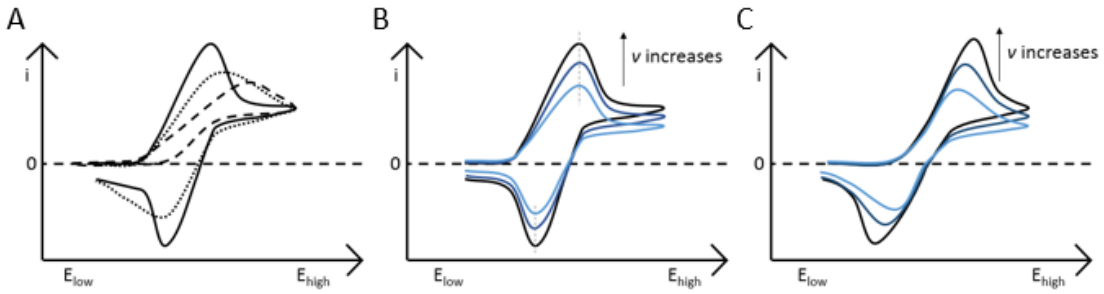


**Figure 2.14:** Schematic of typical CV responses (A) for reversible (solid line), quasi-reversible (dotted line) and irreversible (dashed line) electron transfer. Influence of scan rate on the cyclic voltammogram for a reversible (B) and quasi-reversible (C) redox couple.

$$\Lambda = \frac{k^0}{\sqrt{D\frac{nF}{RT}v}} \tag{2.16}$$

where $k^0$ is the rate of electron transfer, $D$ is the diffusion coefficient, $n$ is the number of electrons, $F$ is Faraday's constant, $R$ is the gas constant, $T$ is the temperature and $v$ is the scan rate.[126] A value greater than 15 is expected for an electrochemical reversible system and lower than 0.001 for an irreversible transfer.[126, 142] For rapid electron transfer kinetics Nernstian equilibrium is attained and the characteristic 'duck' shape is seen in the CV. In the quasi-reversible case the rate of electron transfer is comparable to that of mass transport and the peak potential depends on the scan rate. For the irreversible system the electron transfer is slower than mass transport and an appreciable overpotential is required to drive the reaction.[142] The variance with scan rate is also shown in Figure 2.14 for a reversible and quasi-reversible system. The important difference is that for a reversible system the peak current should be proportional to the square root of the scan rate and the peak potential at which this occurs is invariant with scan rate. A quasi-reversible case there is a clear dependence on scan rate for the peak potential and as scan rate increase the peak separation also increases.

### 2.2.3 Electrochemical Impedance Spectroscopy (EIS)

Another technique which can be utilised to garner information from a system is AC electrochemical impedance spectroscopy. Whilst in cyclic voltammetry the system is perturbed far from equilibrium through large applied potentials, in impedance measurements a small potential perturbation is

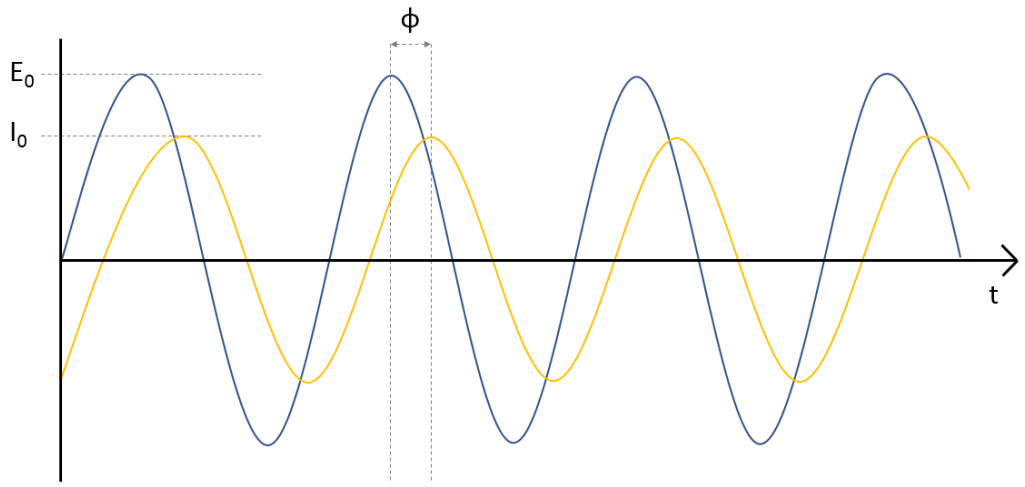


**Figure 2.15:** The applied sinusoidal potential (blue) and the measured current (yellow) which is reduced in amplitude and shifted in phase ($\phi$).

applied.[129] Both resistance and impedance are measures of the ability of a circuit to oppose the flow of electrical current when a voltage is applied. Resistance is used for DC (direct current) and impedance is the AC (alternating current) equivalent. An ideal resistor will meet the criteria of obeying Ohm's law, will be invariant with frequency and AC voltage and current signals must be in phase with one another. Impedance, $Z$, can be considered as complex plane resistance, for which the equivalent of Ohm's law can be written for non-ideal resistors:

$$Z = \frac{E}{i} \tag{2.17}$$

In EIS measurements an oscillating small sinusoidal AC potential, $E_{ac}$ (usually around 5-10 mV r.m.s. amplitude) is superimposed on a fixed DC potential, $E_{dc}$, which is imposed on the working electrode. The mean concentration in the electrode environment of the reduced and oxidised species is set by the DC potential. The response measured is the AC component of the current, $i_{ac}$ at different applied frequencies, $\omega$ (in radians $s^{-1}$). The applied AC potential is small in order to keep the response of the cell pseudo-linear. This means the observed impedance is independent of the magnitude of $E_{ac}$. There is a phase shift between the potential and current sinusoidal signal at any given frequency, as can be seen in Figure 2.15.

The applied potential, $E_t$ at time $t$, can be expressed as:

$$E_t = E_0 sin(\omega t) \tag{2.18}$$

where $E_0$ is the amplitude of the signal and $\omega$ is the frequency (in radians). In a linear system the measured current can be similarly described by:

$$i_t = i_0 sin(\omega t + \phi) \tag{2.19}$$

where $i_t$ is the current at time $t$, $i_0$ is the amplitude of the current and $\phi$ is the phase shift between the applied voltage and the measured current sinusoidal signal.

$$Z_t = \frac{E_t}{i_t} = \frac{E_0 sin(\omega t)}{i_0 sin(\omega t + \phi)} = Z_0 \frac{sin(\omega t)}{sin(\omega t + \phi)} \tag{2.20}$$

Using Euler's formula ($exp(j\phi) = cos(\phi) + jsin(\phi)$ where $j$ represents $\sqrt{-1}$), both $E_t$ and $i_t$ can be expressed as complex functions and the impedance at a certain frequency can be represented as a complex number.

$$Z(\omega) = \frac{E_0 exp(j\omega t)}{I_0 exp(j\omega t + \phi)} = Z_0 exp(j\phi) = Z_0(cos\phi - jsin\phi) = Z_{Re} - jZ_{im} \tag{2.21}$$

#### 2.2.3.1 Nyquist plots and equivalent circuit representation

An EIS measurement will record the current response at a range of frequencies (usually this is around 100 kHz to 0.1 Hz). Limited at the high frequency end by the charging of the double layer and at the low frequency end by the length of time and presence of noise (for example due to the convection). A Nyquist plot is normally used to display and analyse EIS data. This displays the imaginary component versus the real component of the impedance as is shown in Figure 2.16. Each point on the Nyquist plot is the impedance response at a set applied frequency. The real component ($Z_{Re} = Z_0 cos\phi = Z'$) is plotted on the x-axis and the imaginary component ($Z_{Im} = -Z_0 sin\phi = -Z''$) on the y-axis.

Comparison is usually made between the electrochemical response and an equivalent electrical circuit.[129] An ideal resistor has no frequency dependence so would be a single point on the x-axis at the value of the resistance. A capacitor is represented by a vertical line on top of the y-axis($Z' = 0$). Therefore, for a resistor and capacitor in series (the blue circuit in Figure 2.16) the result is a vertical line shifted by the amount of the resistance $R_1$ shown in Figure 2.16 by the blue line. For a resistor and capacitor in parallel a different response is obtained as the current can pass through either component. The result is a semicircle as the current flow follows the path of

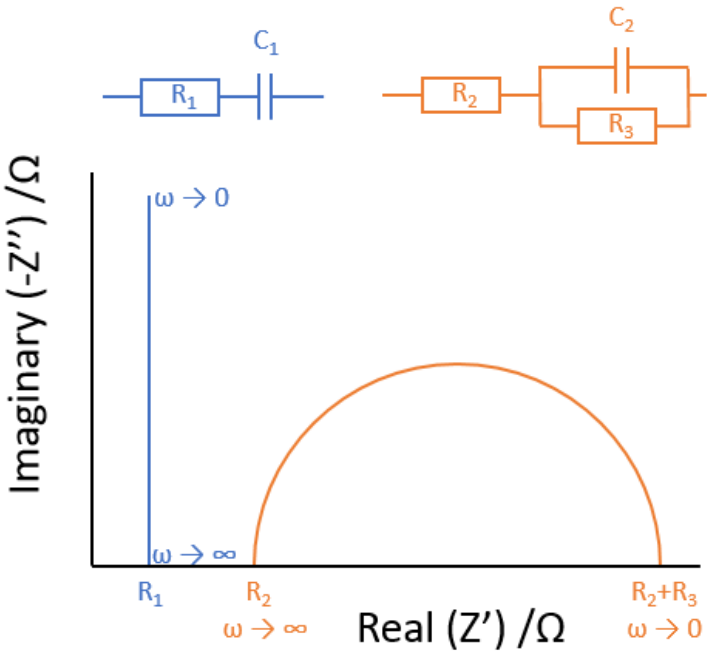


**Figure 2.16:** Illustration of a Nyquist plot and they typical response from a combination of circuit elements.

least resistance; at high frequency through the capacitor and at low frequency through the resistor (when the impedance through the capacitor is very large).

#### 2.2.3.2 Common Circuit Elements

These ideal circuit elements have been shown to have equivalent or near equivalent electrochemical analogues.[126] These are discussed below.

**Resistors (R)** Resistance is a measure of the opposition to current flow in an electrical circuit. Ideal resistors follow Ohm's law and there is no dependence on frequency so there is no reactive part (phase shift).

**Capacitors (C)** Capacitors store electrical charge, usually they are formed of two conducting layers separated with an insulator. They are common in electrochemical systems, mainly in places where an ideal (2D) interface is present. Farads are the units for the amount of charge stored. 1 Farad is equivalent to one coulomb of charge stored when one volt is applied across the capacitor. Capacitors are purely reactive impedance and an ideal one would have no

resistance. When an AC potential is applied across a capacitor, the current leads the voltage (the phase is shifted $-\frac{\pi}{2}$). The impedance of a capacitor increases with decreasing frequency, and the equation describing it is:

$$Z_c = \frac{1}{j\omega C} \tag{2.22}$$

Where $\omega = 2\pi f$ the radial frequency and $C$ is the capacitance.

**Warburg Element (W)** The Warburg element is the permittivity and is used as a model of linear diffusion of a redox species to the electrode (at longer times when the local concentration has been depleted). The Warburg element depends on both the surface area of the electrode as well as the diffusion coefficient of the redox species. On a Nyquist plot a Warburg element appears as a 45° line. The model for the Warburg impedance is:

$$Z_W = \frac{\sigma}{\omega^{1/2}}(1 - j) \tag{2.23}$$

where $\sigma$ is the Warburg coefficient.[126] Most equivalent circuit modelling programs give a value for the magnitude of the admittance $Y_0$ at the radial frequency $\omega$=1 rad $s^{-1}$. This is related to the Warburg coefficient by:

$$\sigma = \frac{1}{\sqrt{2}Y_0} \tag{2.24}$$

**Constant Phase Element (Q)** A constant phase element is a non-intuitive element which has been used to describe depressed semicircles (which have a centre some distance beneath the x-axis) by adding an additional variable $N$ which describes this shift. This is illustrated in Figure 2.17. Adding an additional variable will always improve the fit so care has to be taken when using a constant phase element so that it is physically realistic within the system, for example indicating inhomogeneous layers, rough surfaces or dispersion for a physical property. The impedance of a constant phase element is given by:

$$\mathrm{Z} = \frac{1}{Y_0(j\omega)^N} \tag{2.25}$$

For the physical situation of a roughened interface $N = \frac{1}{(D-1)}$, where $D$ is the fractal

dimensionality. A value of $N = 1$ represents an ideal capacitor, $N = 0.5$ is mathematically equivalent to a Warburg element and $N = 0$ is mathematically equivalent to a resistor.

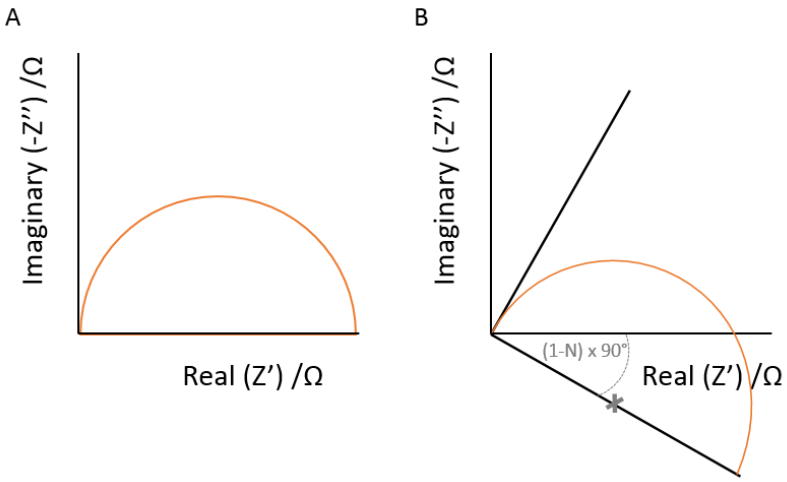


**Figure 2.17:** Illustration of a typical response of a resistor and capacitor in parallel in an ideal system (A) and how the constant phase element can be used to describe the shift of a semicircle (B) in actual measurements due to non-ideality within physical processes. The centre of the semicircle is depressed by an angle of $(1 - N) \times 90°$ visible in the diagram as the grey cross.

#### 2.2.3.3 Combination of circuit elements

As described usually a combination of components is used to model an electrochemical system. For reactions in series the impedances are additive:

$$\boldsymbol{Z} = \sum_n \boldsymbol{Z}_n \tag{2.26}$$

Thus the combination of a resistor and capacitor in series is the sum of both impedances which describes the vertical line with an offset on the x-axis (shown in blue in Figure 2.16). For reactions in parallel the admittances (inverse of the impedance) are additive:

$$\frac{1}{\boldsymbol{Z}} = \sum_n \frac{1}{\boldsymbol{Z}_n} \tag{2.27}$$

#### 2.2.3.4 Physical parameters in electrochemical cell

Solution resistance, $R_s$, is determined by the rate of ion migration through the electrolyte. When considering an applied alternating voltage between two plate electrodes a charged ion will alternate between being attracted then repelled to each electrode surface. The rate of resulting ion migration will depend on the concentration and their mobilities. As at a low enough frequency ions will build up at the electrode interface, the high frequency intercept on the x-axis is used to determine the solution resistance of a system.

The electrical double layer, discussed in 2.1.3, is a source of capacitance within the system - the double layer capacitance, $C_{dl}$. There is also an inherent resistance to the electron transfer reaction, $R_{ct}$. Typically the rate of electron transfer is very quick, compared to the mass transport, so is more easily measured with impedance techniques.[128]

As defined the Warburg element is used to model linear diffusion. This can be used to describe the diffusion to a macroelectrode and is generally dominant at lower frequency when this controls the rate of the reaction. However, as previously discussed in Section 2.1.6 the diffusion profile to micro- and nanoelectrodes becomes hemispherical. At these small scale electrodes a depletion zone of similar dimension to the electrode forms significantly faster (so will occur at higher frequency) than for a large macroelectrode. A resistance is used to model the resistance of transport for a redox species through the depletion zone to the Helmholtz plane. This is known as non-linear resistance, $R_{nl}$.

#### 2.2.3.5 Established circuits

Figure 2.18 shows an example of a typical Nyquist plot obtained during a reversible electrochemical process at macroelectrode. The equivalent circuit generally used to model electrochemical systems at macroelectrodes was developed by Randles in 1947, which is also shown in Figure 2.18.[143]

At very high frequencies the total impedance is dominated by the solution resistance. At high frequencies the charging of the electrical double layer acts as a pathway of low resistance to non-Faradaic current. As the frequency decreases (the double layer has become charged) the redox reaction occurs and the reaction is under kinetic control with the rate controlled by $1/R_{ct}$. This value can be extracted from the Nyquist plot by extrapolating the semicircle and subtracting the solution resistance. As the reaction progresses the analyte is depleted at the interface, establishing

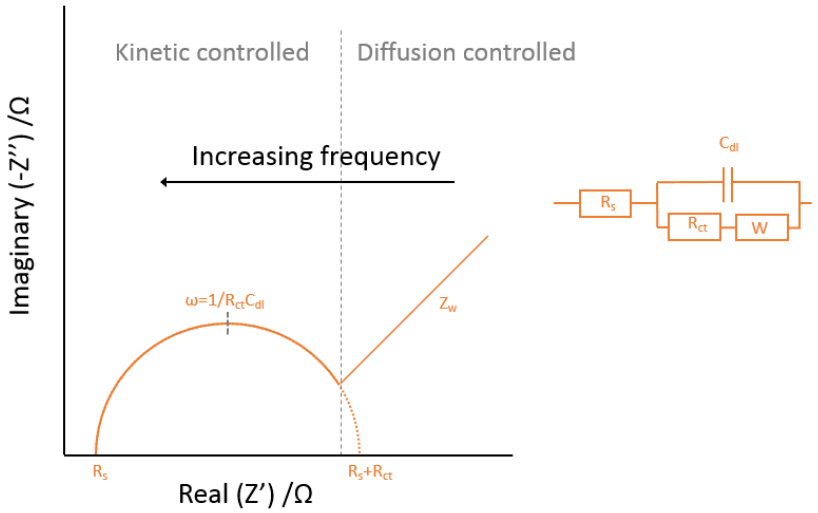


**Figure 2.18:** Schematic of a typical Nyquist plot obtained using a macroelectrode with a reversible electrochemical system and the Randles circuit (right) used to fit this response.

a diffusion gradient and the reaction is controlled by the diffusion regime. For the linear diffusion which occurs at a macroelectrode the Warburg element is used as a circuit element. The top of the semicircle occurs at the relaxation frequency and is related to the RC time constant, $\tau$, (the time required to charge the capacitor through the resistor). This is defined generally by:

$$\tau = \frac{1}{\omega} = \frac{1}{2\pi f} = RC \tag{2.28}$$

This provides information about the timescales for various processes and allows the calculation of the capacitance. Elements with higher relaxation frequencies (lower time constants) appear at higher frequencies in the Nyquist plot. If elements have very similar time constants then the observed features in the Nyquist plot will overlap and it becomes challenging to distinguish values for the individual elements.

The Nyquist plot obtained when using a microelectrode to probe a reversible electrochemical system looks markedly different to the macroelectrode response. The typical response is shown in Figure 2.19. As such it has been the subject of significant research to advance the theory to explain and analyse the system. Figure 2.19 also shows the modified Randles equivalent circuit which is frequently used to model the EIS response seen with a microdisc electrode.[119,139] The impedance response has been theoretically shown to vary with the positional geometry of the electrode with

respect to insulators.[144] However, the established circuits described here have been used to model electrodes of similar recessed geometry to those presented within this work.

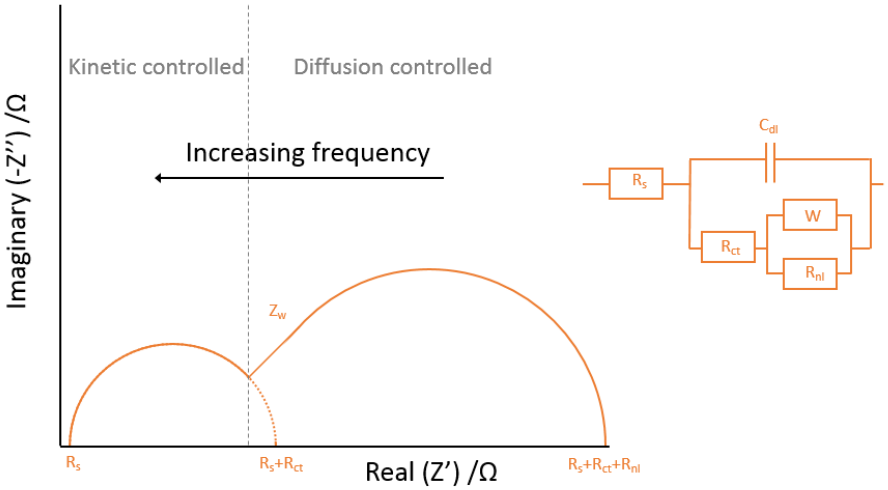


**Figure 2.19:** Schematic of a typical Nyquist plot from a microelectrode and reversible electrochemical system and the modified Randles circuit (right) frequently used to model the response of a microdisc electrode.

The response is initially similar to that from a macroelectrode. The modified Randles circuit which is frequently used to model this contains similar elements to the Randles equivalent circuit for macroelectrodes. When the system switches to a diffusion controlled regime a 45° degree line is observed which is modelled by the Warburg element. However a semicircle is then evident in the plot; this is modelled by a non-linear resistance, $R_{nl}$, in parallel with the Warburg. This resistance as discussed models the hemispherical diffusion established at the microelectrode and determines the steady state response.

For nanoband electrodes the equivalent circuit that has previously been used to fit a response from a single electrode within an array is shown in Figure 2.20.[125, 140] The kinetic response should be of similar form with a semicircular feature. The lower frequency region differs from a microelectrode response with the Warburg element being replaced by a redox capacitance, $C_N$. It was postulated that this was due to the increased non-linear diffusional transport to the nanoband edges and the capacitance gives a measure of the volume of solution above each microsquare aperture which underwent rapid redox conversion.

The situation is then the same as for a microelectrode with the steady-state hemispherical diffusional

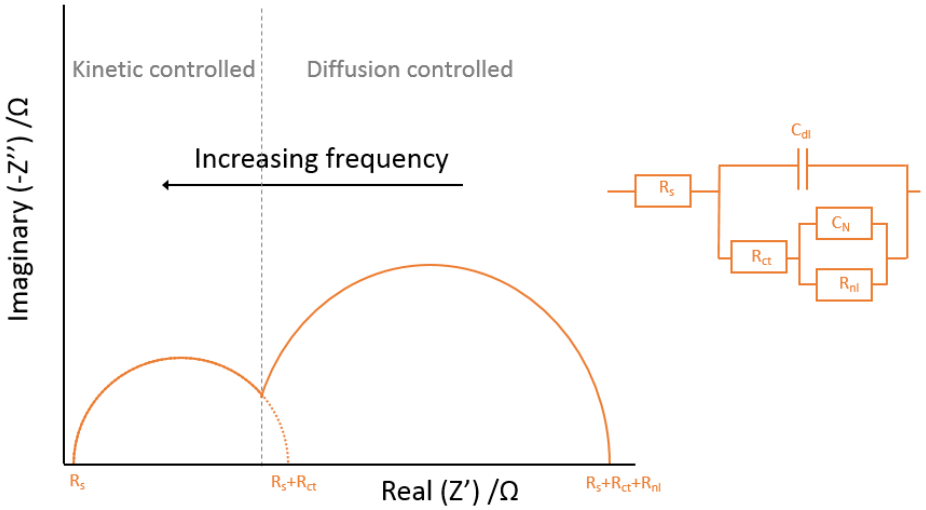


**Figure 2.20:** Schematic of a typical Nyquist plot from a nanoelectrode and reversible electrochemical system and the modified Randles circuit (right) frequently used to model the response of a nanoband electrode.

transport, defined by $R_{nl}$, occurring into this volume. The non-linear diffusion resistance is related to the current $i(E)$ in the steady state reversible voltammogram by $1/R_{nl} = \frac{\partial i(E)}{\partial E}$.

#### 2.2.3.6 Theoretical Variation of Circuit Elements with $E_{dc}$

Performing repeated EIS measurements at different DC potentials allows the interrogation of the system at a variety of fixed redox compositions. The variation of the various circuit elements has been previously determined for an electrochemical system from first principles.[139] For the charge transfer resistance the kinetic expression is:

$$R_{ct,k} = \frac{RT}{k^{\theta}AF^2c}[exp(\frac{-\alpha_{ox}nF(E_{dc}-E^{\theta})}{RT}) + exp(\frac{(1-\alpha_{ox})nF(E_{dc}-E^{\theta})}{RT})] \tag{2.29}$$

From this expression it can be seen that a minimum will be observed when $E_{dc} = E^{\theta}$when with the minimum value $R_{ct.min}$ described by:

$$R_{ct,min} = \frac{2RT}{n^2F^2ck^{\theta}A} \tag{2.30}$$

Where $k^{\theta}$ is the standard rate of electron transfer, $A$ is the electrode area and all other variables are as previously defined. If however, the process is thermodynamically controlled by Nernstian equilibrium at the electrode it has been shown that the expression would then be:

$$R_{ct,e} = \frac{R_{ct,min}}{4}[2 + exp(\frac{F(E_{dc} - E^{\theta})}{RT}) + exp(\frac{(-F(E_{dc} - E^{\theta})}{RT})] \tag{2.31}$$

Fitting the experimental response at different DC potentials enables these functions to be fitted to the extracted charge transfer values and the determination of the relative importance of kinetics and thermodynamics to the charge transfer process. The non-linear resistance should always be under thermodynamic control and should thus follow this functional form (with $R_{nl.min}$ replacing $R_{ct,min}$) and again show a minimum when the applied DC potential is equal to the standard reduction potential. Similarly the Warburg coefficient should follow the identical thermodynamic functional form (if the admittance is plotted this will be inversely proportional by the relationship $\sigma = 1/\sqrt{2}Y_0$). The functional form of these are:

$$\sigma = \frac{\sigma_{min}}{4}[2 + exp(\frac{F(E_{dc} - E^{\theta})}{RT}) + exp(\frac{(-F(E_{dc} - E^{\theta})}{RT})] \tag{2.32}$$

and

$$\frac{1}{Y_0} = \frac{4}{Y_{0,min}[2 + exp(\frac{F(E_{dc} - E^{\theta})}{RT}) + exp(\frac{(-F(E_{dc} - E^{\theta})}{RT})]} \tag{2.33}$$

## 2.3 Molten Salt Electrochemistry

When electrochemistry is performed within a molten salt the salt itself acts as the electrolyte, and offers the benefit of a very wide potential window. The LiCl-KCl eutectic is used in this work, which occurs at a molar ratio of 59.2 moles LiCl to 40.8 moles KCl. This corresponds to 45 g LiCl and 55 g KCl within an 100 g amount of the eutectic. When molten the viscosity is similar to that of water, however, unlike pure water the molten salt has a high ionic conductivity as it is comprised of ions (although many are paired). It should be noted that the theory of electrochemistry outlined in Section 2.1 is founded on ambient conditions in neutral solvents, predominantly water, with a dissolved background electrolyte at low concentrations. It is currently unproven for molten salt systems. There are several theoretical papers suggesting local order extending further into solution from the electrode surface, due to the liquid being comprised of many ions controlled by Coulombic forces.[72,145]

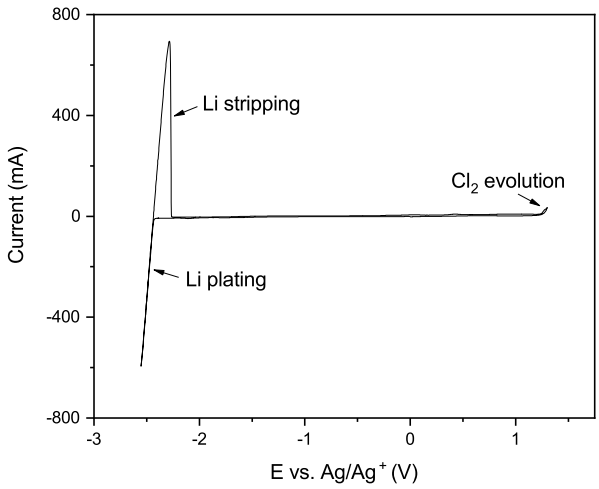


**Figure 2.21:** Typical CV showing the solvent window of LiCl-KCl using a tungsten macroelectrode as working electrode.

At the solvent limits with sufficient potential applied, the molten salt can undergo electrochemical reactions. Figure 2.21 shows the large solvent window of around 3.8 V for a LiCl-KCl eutectic melt. At the negative potential end around -2.6 V lithium ions are reduced to plate lithium metal, this can then be re-oxidised to form lithium ions seen as a stripping peak. At the positive potential end chloride ions are oxidised to form chlorine around +1.2 V. The chlorine produced can escape the system so no large reduction current is seen. Occasionally a small peak can be observed when chlorine gas adsorbed onto the electrode is reduced, although it is unclear why this sporadically occurs.

# Chapter 3

# Experimental

## 3.1 Introduction

The micro- and nanoelectrode devices in this work were fabricated at the Scottish Microelectronics Centre using standard microfabrication processes. This chapter details these processes, the electrode architecture at the start of this work, alongside a description of the functionality of the layers and the experimental set up for the testing of these devices. Significant work to establish devices which are suited to use in the harsh environment of the molten salt has been performed by previous members of the group, Brady and Blair. [120, 123] The layers have been previously optimised by Blair to provide both stress relief and corrosion resistance to the molten salt. However, there were still significant issues affecting the yield and lifetimes of devices when used in LiCl-KCl eutectic. The further development of single microelectrodes and progression towards nanoelectrodes which allow investigation into reactions in a molten salt will be covered in Chapter 5.

### 3.1.1 Microelectrode & Nanoelectrode design

The architecture of the microelectrode and nanoelectrode devices is a patterned metal layer on top of an underlying insulator, then a top insulating layer with patterned openings to define the microelectrode and the contact pad. A single microelectrode device was produced on a 35 mm long and 3.75 mm wide silicon chip, by dicing the silicon wafer upon which the layers were patterned. A schematic of a device is shown in Figure 3.1. The width of the contact pad was maximised to

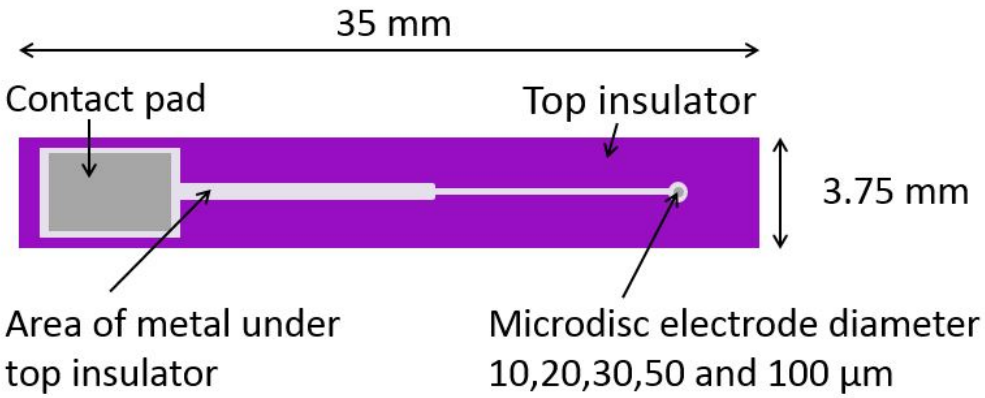


**Figure 3.1:** Sketch of the initial microelectrode showing the layout and dimensions. The exposed metal is shown in dark grey and areas of metal beneath the top insulator are lilac/white, the remaining area in purple is insulation without metal underneath. The width of the track reduces from the contact pad to the microdisc electrode. The microdisc size has been exaggerated for ease of visualisation.

enable easier connection to a crocodile clip, and the distance from the microelectrode was chosen to be sufficiently long to prevent salt reaching the contact pad and short circuiting the device or damaging the connection. Microdiscs were used as these were found to be more resilient to thermal stresses due to the elimination of corners, which were found to be a point of stress for square microelectrodes.[123] Five different diameters of microdisc electrodes were fabricated on each wafer: 10, 20, 30, 50, and 100 µm. There was space for a total of 40 chips on each wafer, eight of every diameter except 10 µm (of which there were seven), and also one test square which did not have an opening through the top insulator (as a test device which could be utilised to ensure the functionality of the top insulating layer). The layout of the devices on the wafer is shown in 3.2. The contact pads were located on the outside of the wafer and the microelectrodes were positioned towards the centre.

#### 3.1.1.1 Substrate

The substrates used for fabricating microelectrodes were four inch <n> silicon wafers (IDB). Silicon was used as a substrate due to established compatibility with the materials and processes; it is very commonly used as a substrate for micro-electro-mechanical devices.[146] At the elevated temperatures when used in the melt the silicon becomes electrically conductive as the intrinsic charge carrier concentration dominates, making any doping of the wafer irrelevant.[147] This

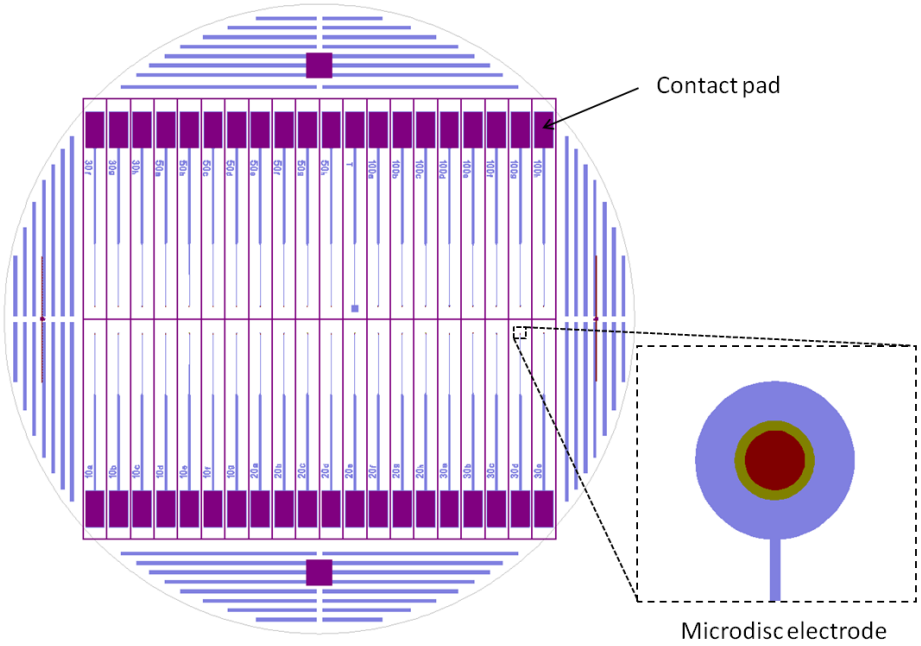


**Figure 3.2:** A layout showing the positioning of the micro- and nanoelectrodes on the four inch wafer. The lilac colour represents the metal layer, the purple areas show the openings which are created in the top insulating layer allowing access to the electrode metal and the yellow shows the top capping layer that may be used (when over the exposed metal this appears red).

necessitates an underlying insulator between the silicon substrate and the electrode metal to avoid shorting (Section 3.1.1.2). If not, the edges of the substrate which are exposed to the melt (from dicing) become active and dominate the response. It is also mechanically strong at the elevated temperatures, which is required both for processing steps and for the end use.

#### 3.1.1.2 Underlying Insulator

This layer is required to provide insulation between the conductive silicon substrate and the electrode metal. At the beginning of this work the underlying insulator was a 500 nm thermally grown layer of silicon dioxide. Although this is known to degrade in the molten salt, it is necessary to incorporate it into the architecture to act as a stress relief layer for the $Si_3N_4$ top insulating layer and prevent delamination.[123] Only a small area at the edge of the electrode is exposed to the molten salt and so, whilst it is highly desirable to be chemically inert in the molten salt, corrosion

was previously established to be a minor issue in comparison to the stress issues encountered without it.[123]

#### 3.1.1.3 Electrode metal layer

The metal is also required to be stable in the salt and not melt at the working temperature or during the fabrication processes, where the maximum temperature it will be exposed to is 800°C during the nitride deposition. In an ideal case it should be chemically and electrochemically inert, so that alloying does not complicate the analysis of the signal and the metal cannot be accidentally stripped off. Previous studies have used platinum or tungsten as suitable materials.[123] Tungsten is a refractory metal and platinum is a noble metal and hence both should be chemically inert. Melting points are 3422°C and 1768°C for tungsten and platinum respectively and so they are commonly used as electrode materials in molten salt studies. The thickness of the metal layer should be large enough to ensure it is conformal and preclude pinhole formation, whilst also providing sufficient conductivity without delamination due to stress (which increases with thickness). Tungsten and tantalum layers were 200 nm thick whilst platinum layers were only 50 nm thick, due to the higher cost of platinum. It is also known that platinum can be electrochemically stripped at around +1 V vs $Ag/Ag^+$, however, this is a higher potential than the redox active species of interest so can be avoided.[148–150] Both these metals do not adhere particularly well to non-metallic substrates, such as silicon, so require the use of a seed layer to enhance the adhesion.

#### 3.1.1.4 Adhesion layer

The adhesion or seed layer is used to improve the adhesion between some metals and non-metallic substrates. Titanium is a standard seed layer material in industry, however, it was seen that titanium was rapidly removed when immersed in the molten salt.[123] The loss of metal was found to contribute to device failure and alternatives to act as an adhesion layer were sought. Titanium nitride had previously been used as a corrosion barrier elsewhere so was tested and shown not to suffer from corrosion in the molten salt.[123, 151] A 20 nm layer of titanium nitride was therefore used as standard in this work to provide adhesion between the bottom insulator and the metal layer.

#### 3.1.1.5 Top insulator

This layer performs the function of separating the electrode metal from the molten salt. The contact pad and microelectrode are opened by etching a defined area in the layer. The layer is required to be an electrical insulator, mechanically stable at the elevated temperature under study and be chemically stable in the salt. Silicon nitride has a dielectric constant of 7.5 and is used as a dielectric in microelectronics.[139, 152–154] It is also considered to be resistant to chemical attack. From previous studies it was found essential to use LPCVD stoichiometric silicon nitride ($Si_3N_4$) to provide adequate corrosion resistance and non-permeability.[123] Issues were encountered with damage to silicon oxide and permeability of silicon rich silicon nitride, meaning they were unsuitable as materials for this layer.[123] The silicon nitride has a very high intrinsic stress so this needs to be relieved by other layers in the architecture, which is accomplished with the use of a silicon oxide layer for the bottom insulator to balance the stress.[123, 155] The top insulator needs to be thick enough to minimise parasitic capacitance between the salt and metal track and to prevent pinhole formation over the track, which would lead to a larger active area than expected. Increasing the layer thickness increases the depth of the cavity which increases the recess of the cavity, eventually leading to observation of diffusion into a pore. A balance between these competing factors is required. For Blair's final device design the top insulator was 500 nm thick, providing adequate insulation without affecting the mechanical and electrochemical performance.[123,156] This had previously been shown by numerical simulation not to adversely affect the diffusion profile significantly.[140]

### 3.1.2 Fabrication Process

The principles and details of the fabrication processes used to produce a wafer of devices are briefly outlined here. The run sheets for all devices are found in Appendix 1. The underlying insulator of silicon dioxide was thermally grown on the surface of a silicon wafer by exposing the wafers to a hydrogen and oxygen atmosphere, at high temperature, in a quartz furnace. The thickness of the oxide layer increased with time, although the rate slowed significantly with thickness as described by the Deal-Grove model.[157] The thickness and uniformity across a single wafer and between different wafers was measured using reflectometry. The rate of oxide growth was around 1.7 nm/min, which was calculated from the measured thicknesses of previous oxide growth measurements, and the process time was adjusted to give a layer of 500 nm, illustrated by Figure 3.3a).

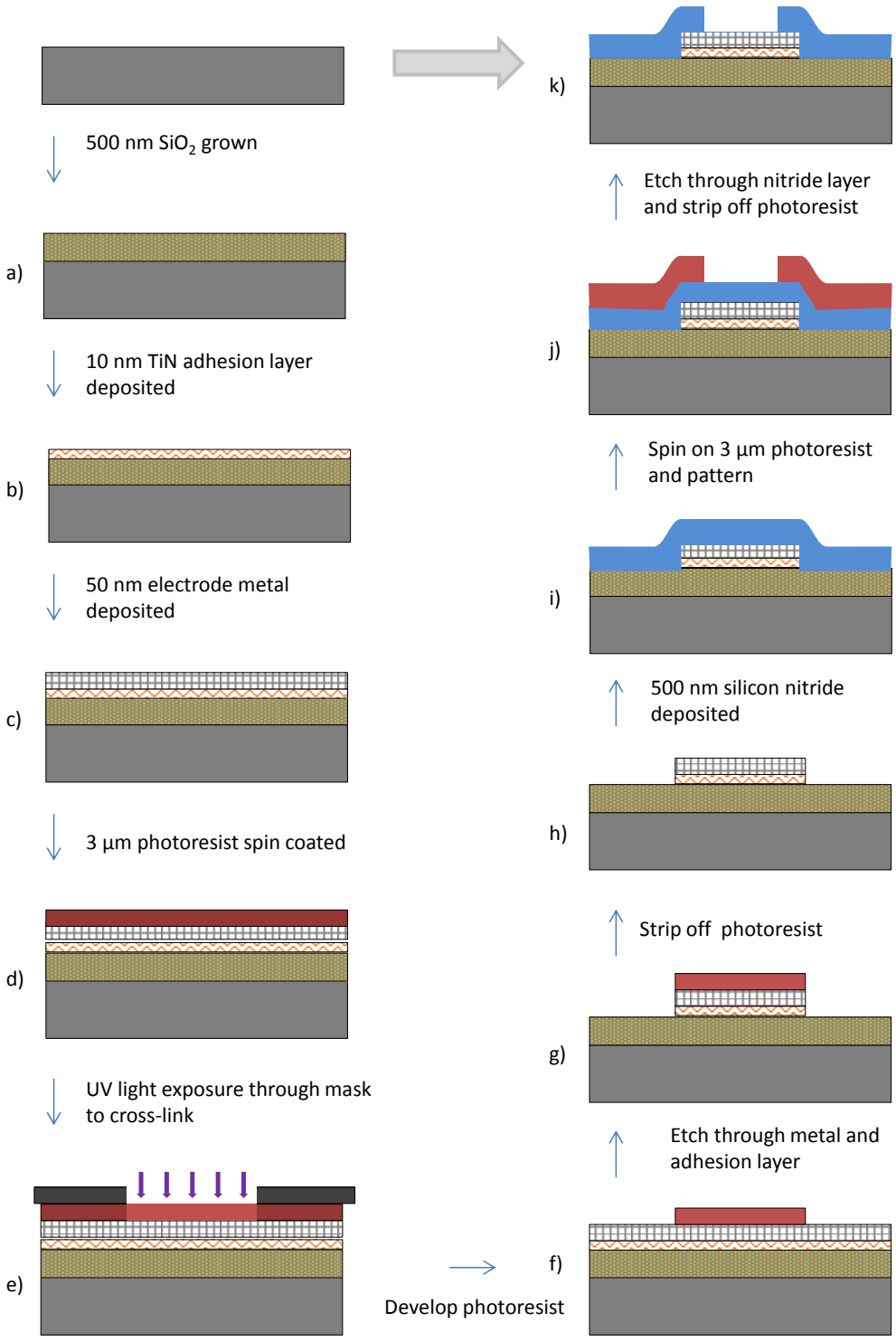


**Figure 3.3:** Cross-sections showing the fabrication procedure used to make microelectrode devices at the start of this work. Processes are a) forming SiO2 underlying insulator, b) and c) deposition of the adhesion layer and platinum metal layer respectively. d)-h) show the photolithographic pattern and etch process used to define the metal area. The stoichiometric silicon nitride deposition is shown in i) and then again the pattern and etch technique is illustrated by j) to form the openings in the top insulator to the contact pad and electrode to produce the final microelectrode device k).

A TiN layer of nominally 20 nm was then sputter deposited by sputtering Ti in an $N_2$ atmosphere, using an OPT Plasmalab System 400 sputter system (Figure 3.3 b). Sputter deposition is a process used to deposit thin films by positioning the wafer under a target of the desired material. A plasma is generated using an inert gas, ions are then accelerated into the target by applying an electrical field. The atoms from the surface of the target material are physically sputtered by this and land on the wafer beneath, building up a thin film. A 50 nm layer of platinum was deposited by electron beam deposition (Figure 3.3 c); this uses a magnetic field to direct a beam of electrons into hitting a crucible of the desired metal, which causes it to be heated and atoms to be released from a tightly controlled local environment. The deposition chamber is under high vacuum, so there is a long mean free path for the metal, which then condenses back to a solid on the surface of the wafer. E-beam deposition requires a smaller amount of metal than sputtering so is more suitable for platinum deposition due to the high cost of the metal. During deposition the film thickness was measured using a quartz crystal for the system used. Afterwards the thickness could be measured with profilometry or scanning electron microscopy measurements.

Standard photolithographical patterning and etching was used to remove material from selected areas. The wafers were cleaned, rinsed in a sequence of acetone (KMG Ultra pure chemicals semiconductor grade VLSI), isopropanol (KMG Ultra pure chemicals semiconductor grade VLSI) and deionised water. They were then dried under a nitrogen stream and dehydrated (on a hotplate at 90°C for 60 seconds) to encourage the adhesion to the surface. The wafers were then sat in an atmosphere of HMDS (hexamethyldisilazane, Aldrich 97 % purity), which is used as an adhesion promoter for photoresist, for 10 minutes. A 3 μm layer of positive photoresist (Megaposit SPR 220-3, Microchem) was spun on at 3500 rpm and softbaked for 60 seconds at 90°C, shown in Figure 3.3 d. It was then exposed to UV light for 12 seconds in contact mode through a photomask, which had transparent and opaque areas (defined by chrome on a quartz substrate for this work) which mirrored the pattern desired on the wafer, Figure 3.3 e. The light caused a photochemical reaction to occur in the photoresist exposed which changed the solubility of the material to a chemical developer, in this work MF26A resist developer (Microposit) for 60 seconds. Positive photoresist makes the areas of photoresist exposed to light more soluble. The developing solution removes these areas leaving a patterned mask on the surface of the wafer which protects selected areas from being etched, shown in Figure 3.3 f. The pattern in the photoresist was used as the etch mask in order to remove the exposed platinum and titanium nitride. This is necessary to make the patterned

metal smaller than the final chip to avoid exposing a band of metal at the perimeter of the chip, which would be electroactive and lead to a significant electrochemical response. The metal layer was etched using a reactive ion etcher JLS RIE. Reactive ion etching involves the generation of a plasma in which a mixture of chemical and physical etching occurs depending on the gases utilised. In chemical etching the gases used will react with the material to be etched thus removing it from the surface. Physical etching, seen for an inert gas such as argon, involves driving the ions into the surface by a DC bias, physically removing atoms from the surface of the metal. For these devices an Ar mill was used to remove the Pt (25 sccm Ar at 200 W) for 9 minutes exposed by the resist pattern. The TiN layer was removed using a $CF_4$ etch with Ar (60 sccm $CF_4$ and 4 sccm Ar at 75 W) for approximately 25 minutes. Once the metal was etched, Figure 3.3 g and the critical areas (around the electrode which will be immersed in the melt) were non-conductive, which was tested with a multimeter, the photoresist was removed using ACT-CMI (Versum materials) resist stripper at 50°C for 15 minutes or Microposit remover 1165 (Dow) for 15 mins with sonication, each were shown to be suitable for the stripping process. The wafers were then rinsed in isopropanol and deionised water to clean, and were dried with nitrogen.

LPCVD (low pressure chemical vapour deposition) stoichiometric silicon nitride was deposited in a horizontal tube furnace. The wafers were loaded into the furnace at 600°C, the temperature was then ramped up to 800°C. Dichlorosilane ($SiH_2Cl_2$) and ammonia ($NH_3$) gases were introduced at a ratio of 1:2 and pressure of 100 mT. The gases reacted on the surface of the wafer and the deposition rate was around 1.21 nm/minute (calculated from previous depositions). LPCVD is a type of chemical vapour deposition which uses a lower pressure, which results in fewer gas phase reactions. Pumps also circulate gases within the deposition chamber, the formation of the film is then limited by the surface reaction and results in a uniform and dense film. The process is operated at high temperatures to ensure a reasonable deposition rate. For the 500 nm thick layer the deposition process was five hours to create the layer as shown in 3.3 i.

The same pattern and etch process was repeated using a different mask to create the openings in the nitride layer to form the contact pad and electrode (Figure 3.3 j and k). The JLS-RIE was used to perform the same $CF_4$ and Ar etch (60 sccm $CF_4$ and 4 sccm Ar at 75 W) for approximately 18 minutes. The $CF_4$ chemically reacts with the silicon nitride to produce volatile Si and the argon present in the mixture of gases speeds up the exposure of unetched $Si_3N_4$to the $CF_4$by physical bombardment.[158] Once the nitride windows were etched the remaining resist was again removed

with warm resist stripper as described before. The wafer was diced into individual chips using a DISCO DAD-640 dicing saw, with a diamond impregnated saw blade. To protect the chips from debris the wafer could be coated in a layer of photoresist and softbaked prior to dicing. This was initially done for the first batch of wafers fabricated. Removing the resist was performed in a stream of acetone (Fisher, Analytical grade 99.8 %), isopropanol (Fisher, Analytical grade 99.8 %) and then rinsed with deionised water (Millipore Milli Q, 18.5 MΩcm minimum). Issues were found in ensuring that all the resist was removed (Chapter 6 & 7) so subsequently wafers were diced without a photoresist coating.

## 3.2 Experimental set up

Electrochemical measurements were carried out using Autolab PGSTAT30 and PGSTAT128N potentiostats (Ecochemie) which were controlled via a PC, and NOVA (version 1.11, Metrohm) was used for data collection of voltammetric and impedance measurements. NOVA was also used for data analysis including circuit fitting for the impedance spectroscopy which utilises the nonlinear least-squares fitting routine. A weight function can be utilised for the fitting, which multiplies each point by a weight factor equal to the inverse of the square of the impedance modulus when the weight function option is selected. If it is not selected all points will have the same weight factor. Origin (2015 and 2018) was used for further data analysis.

### 3.2.1 Aqueous electrochemical measurements

All solutions were prepared using deionised water (Millipore, >18.5MΩcm). Aqueous potassium chloride, KCl (Sigma Aldrich, >99% purity), or sulphuric acid (0.1 M) (Alfa Aesar) was used during electrochemical cleaning of micro- and nanoelectrodes. KCl was used as a background electrolyte for all redox couples. Redox measurements were performed using potassium ferricyanide, $K_3Fe(CN)_6$ [1 mM] (Sigma Aldrich, >99% purity) and potassium ferrocyanide, $K_4Fe(CN)_6.3H_2O$ [ 1 mM] (Sigma Aldrich, >98.5% purity) with KCl [ 100 mM] (Sigma Aldrich, >99% purity) background electrolyte. The fabricated micro and nanoelectrodes were used as working electrodes, with a saturated calomel electrode (SCE) (Fisherbrand accumet, Fischer Scientific) forming the reference electrode (RE) and a platinum gauze (Sigma Aldrich) attached to a platinum wire as the counter electrode (CE). All aqueous measurement potentials are quoted with respect to the SCE reference

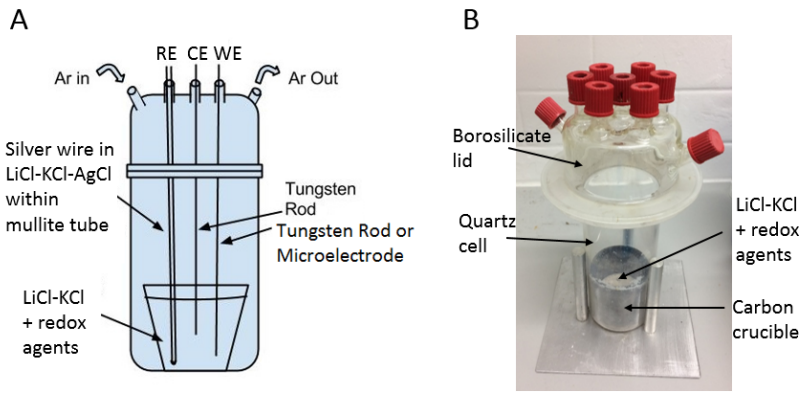


**Figure 3.4:** Schematic (A) and actual (B) set up employed for high temperature electrochemical measurements.

electrode. All experiments were performed in a Faraday cage to minimize the effect of noise from external electromagnetic radiation.

### 3.2.2 High temperature molten salt measurement

50 g of LiCl (Sigma Aldrich, >99% purity) and KCl (Alfa Aesar, >99% purity) in a 40.8:59.2 molar ratio was prepared inside a glassy carbon crucible (HTW), inside a glovebox with Ar atmosphere and placed inside a quartz cell with a borosilicate lid, manufactured by H Baumbach & Co. This set-up can be seen in Figure 3.4. Redox agents added to the LiCl-KCl included AgCl (Fisher Scientific, 99.999% purity) (usually unless stated otherwise 22 mg, 5 mMol equivalent to 3.01 moles $kg^{-1}$) and $EuCl_3$ (Alfa Aesar).

AgCl could be added directly to the LiCl-KCl prior to melting as it was found to be unaffected by small amounts of oxide and hydroxide in the melt. For $EuCl_3$ measurements both LiCl and KCl were heated to 250°C under vacuum, to reduce the amount of oxygen and water associated with the compounds. LiCl-KCl was then melted and sparge dried before the measured amount of europium (III) chloride was added to the re-solidified puck. This did not produce a measurable difference than sparge drying the prepared LiCl-KCl with added $EuCl_3$. Sparge drying the molten salt was performed by flowing argon (at a rate of approx 1 L/min) into the molten salt whilst electrochemical cycling between the positive and negative potential solvent limits was performed. This was based upon the procedure developed by Elliott.[137] An example of a CV from a molten salt which contained a significant amount of associated water is shown in Figure 3.5. The corresponding CV

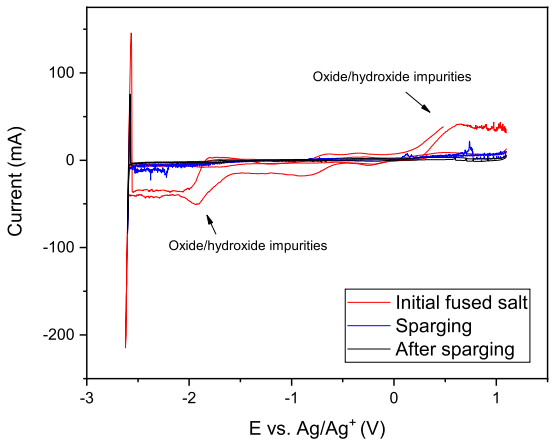


**Figure 3.5:** Comparison of CVs recorded when the salt contained water (red line) showing additional peaks evident between the solvent limits (+1.2 - -2.6 V) during sparge drying (red line) and the salt after drying (black) which is closer to zero current between the ends of the electrochemical window.

during sparging, and after using the procedure for approximately 10 minutes (30 full CVs) are also shown in Figure 3.5. This demonstrates the improvement that can be achieved with the use of the sparge drying process. Sparge cleaning was utilised to remove any contamination with associated water but the duration was minimised to prevent possibly unbalancing the salt if too much chlorine was evolved and lost from the system.

The lids have five vertical ports and two ports on the side for attachment of electrodes and gas lines. If used externally the cell was sealed using vacuum grease and was heated to 723 K inside an open tubular Carbolite furnace (Model GVA12/100/300) with a 300 mm heated zone. Dry Ar (supplied by BOC) flowed through the cell during the experiment in an attempt to maintain an oxygen and moisture free environment. If heated inside the glovebox (MBraun) the vacuum grease was not necessary as the entire glove box was maintained under argon. Both set-ups are shown in Figure 3.6. A metal gauze sheath around the cell was employed to act as a pseudo-Faraday cage to reduce noise due to electrical interference, particularly from the furnace heating coils.

The $Ag/Ag^+$ reference electrode, used throughout for molten salt electrochemical measurements, was a 1 mm Ag wire (Sigma-Aldrich 99.9% purity) in 1 g of LiCl-KCl + 1 wt% AgCl encased in a mullite tube (Multilab); a schematic of this is shown in Figure 3.7. The mullite is permeable to $Li^+$ at the operating temperature, which allows the ion permeability necessary to maintain the expected $Ag^+ + e^- \rightleftharpoons Ag$ potential. All potentials of molten salt measurements are quoted

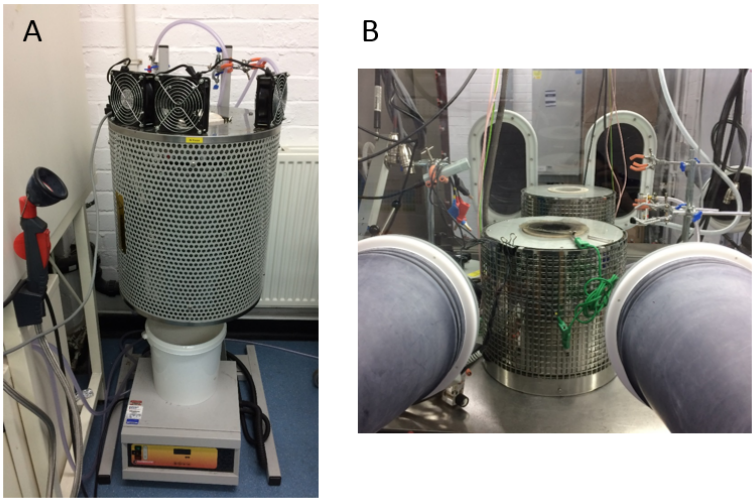


**Figure 3.6:** Vertical tube furnace (A) and bench-top furnace used within a controlled atmosphere glovebox (B).

with respect to this reference electrode. The macro working and counter electrodes used were 1.8 mm diameter tungsten rods (Goodfellow). Care was taken to position the counter electrode deeper than the working electrode, to ensure that the counter electrode had a larger surface area and the current through the cell was controlled by the working electrode. During measurements and tests of the developed micro- or nanoelectrode these were employed as the working electrode instead. The temperature of the melt was measured and continuously recorded with a Comark C28 K type thermocouple, inside a sealed mullite tube which was immersed in the salt. After any temperature increment the cell was then held for a minimum of 10 minutes at that temperature to ensure that the cell was evenly heated. Macroelectrodes, thermocouple and reference electrodes are shown in Figure 3.4. Connection of minituarised devices to the potentiostat was complicated by the high temperature and corrosive environment. Large nickel plated crocodile clips (Hirschmann test and measurement) crimped to a steel rod were used to provide electrical connection to the microelectrode, and also perform the function of mechanically supporting the device to suspend it in the salt. A small square of ceramic was positioned between the rear of the chip and the crocodile clip to prevent electrical connection to the silicon substrate. This connection is shown in Figure 3.14 (A).

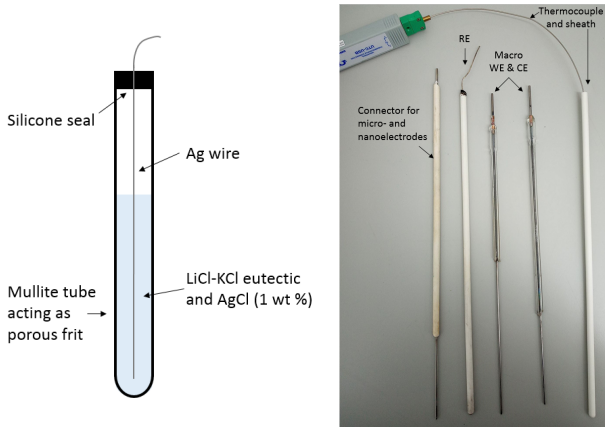


**Figure 3.7:** Schematic (left) of the reference electrode fabricated in house for use in molten salt measurements. Image of electrodes, including RE, and thermocouple connections (right).

## 3.3 Enhancements to experimental protocol for the high temperature measurements

During any experiment the rod was lowered until the micro- or nanoelectrode device was immersed in the salt. For micro and nanoelectrode devices the open circuit potential was observed and used as an indicator that the microelectrode had been lowered into the salt. The large separation between the contact pad and and electrode helped ensure only the microelectrode was submerged in the salt and prevent immersion of the larger contact pad.

### 3.3.1 Reducing noise in measurements

For all experiments performed within the glove boxes the potentiostat was connected via an extension cable, that was potted to provide the electrical connection and maintain the seal of the box. These were made in house with shielded wires (RS components) soldered to the corresponding pins in the connections (Binder). These were then potted by MBraun. The extension cable connects to the normal connection from the potentiostat for the Metrohm potentiostat, so the differential amplifier is located in close proximity to the furnace set up, this was considered to be important to minimise noise during the experiments. The extension cables were tested and compared to the normal configuration using a dummy cell to ensure fidelity of the measurements. The response using the extension cables was found to be identical to the standard set up and within specified tolerances for the potentiostat test procedures so could be employed in the set up without

negatively affecting measurements. One of the issues of using single electrode devices rather than arrays was the low currents which were measured making them more susceptible to noise (which was a considerable issue for high temperature measurements as there were many potential noise sources within the glove box). The pseudo-Faraday cages were still used to reduce noise during the measurements. Unfortunately measurements in the bench-top system still suffered from some noise during measurements. This was minimised by braiding the cables between the differential amplifier and the crocodile clips, as the common mode rejection system enables rejection of noise as long as it is the same for both measurement cables, which limited the impact of noise within the measurements.

### 3.3.2 Drift of reference electrode potential

As shown in Figure 3.7 the reference electrode used throughout this work was a silver wire immersed in LiCl-KCl eutectic with 1% weight AgCl added enclosed in a mullite tube, which were fabricated in house. The functionality of this is similar to a typical Ag/AgCl junction electrode, where a silver wire is immersed in a $Cl^-$ rich solution. However in this case the reaction which characterises the electrode is :

$$Ag^+_{(non-aq)} + e^- \rightarrow Ag_{(s)}$$

Therefore the Nernst equation for this reaction is:

$$E = E^0 + \frac{RT}{F} ln(a_{Ag^+})$$

This has been verified experimentally for a mixed LiCl-KCl-$CaCl_2$ melt.[159] A high concentration of AgCl is used in the melt to maintain a constant activity of silver ions. An Ag/AgCl electrode is well suited for use within a molten salt system as it is not affected by oxide ion contamination as silver oxide is unstable at temperatures below those used for most molten salt systems.[6, 131] Mullite, which has the structure $Al_{4+2x}Si_{2-2x}O_{10-x}$ (with x between 0.2 and 0.9), is known to form mixed crystals.[160] It has useful properties such as a high mechanical strength and thermal shock resistance. The electron transfer can occur due to the lithium ions' ability to diffuse across the mullite tube which is acting as a frit. The ionic conduction is thought to occur through the grain boundaries of the tube's thin walls. A wide variety of materials could be used as a sheath to contain the silver chloride containing melt including glass, quartz and ceramic materials such as

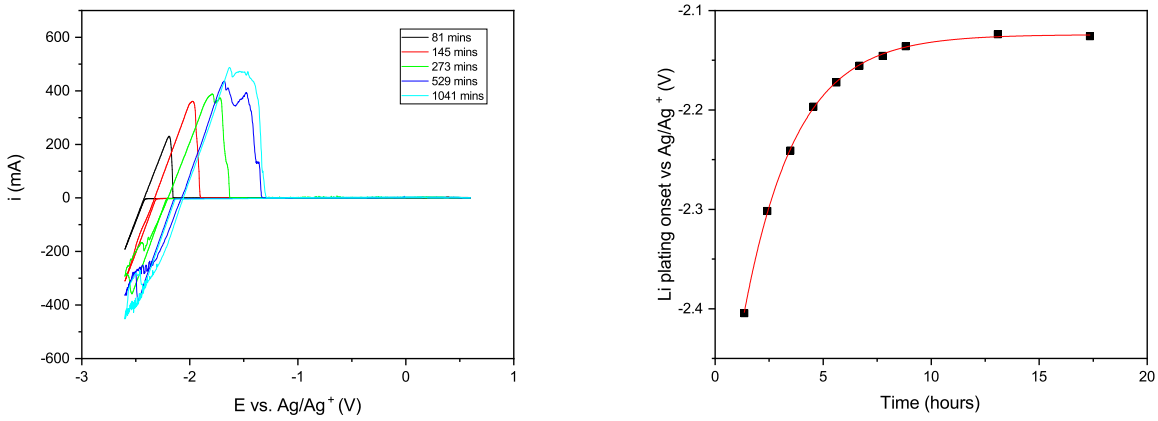


**Figure 3.8:** CV focusing on Li plating (cycling from 0.5 V to -2.5 V) in LiCl-KCl eutectic over time at $v$= 200 mV/s (left) and from this a plot of the onset of lithium plating versus time (right) fitted with a simple exponential function.

mullite which can conduct ions in different ways.[161] A similar reference electrode is described by Wang, but uses an alumina tube in place of mullite, although this necessitated thinning in order to provide the necessary ionic conductivity to be able to complete the electrochemical cell.[132]. A concern would be if the frit was permeable to the silver ion as this could contaminate the solution under investigation. However, in both eutectic LiCl-KCl and eutectic LiCl-KCl with added other redox agents, measurements have been performed with no observation of silver plating and stripping – which would be seen at the concentration of silver chloride present particularly with additional silver from the wire.[137, 162] Therefore the mullite frit is not permeable to silver ions and the solution will not be contaminated unless the tube suffers breakage.

It was observed within the group that over time and multiple usages of the fabricated reference electrodes the full window was observed to shift by approximately 0.2 V. Thus the potential limits needed to be adjusted to observe the complete electrochemical window (seen in Figure 3.5 with Li plating at the negative potential end). This was thought to be most likely due to a shift in the potential of the reference electrode and so long term stability testing of reference electrodes was performed. Experiments were performed to monitor and record if an observable shift in reference potential of the reference electrode over time occurred, by measuring a defined electrochemical window every hour over a long period of time in the same system. CVs were recorded using tungsten rods as the working and counter electrodes using a melt of dried LiCl-KCl eutectic. Figure 3.8 shows the change measured over an 18 hour time period using a newly fabricated reference electrode. A

clear shift in the onset of lithium plating was observable over time. The Li stripping peak grows in size as the same potential limits were used for each cycle recorded and as the plating onset has shifted to a more positive value there is more lithium plating onto the electrode. The plating current also shows some transient spikes, this could be an indication of dendritic plating, which may also explain the change of shape seen in the stripping peak which no longer looks like a sharp even peak but seems to contain multiple peaks. The other interesting observation is that the initial change in the shift of the solvent limits is far larger than the changes at later time. The time interval between scans shown in Figure 3.8 progressively doubles to emphasise the larger shift at earlier times, and adjustment to a more constant system. This can also be seen in the plot of applied voltage of the onset of lithium reduction with time which was found to fit a simple exponential with an $R^2$ value of 0.999. From this plot its clear that after a period of around 6 hours a near constant value for Li plating onset is observed.

For a reference electrode to maintain a fixed value of its potential relative to the solution phase requires that the chemical composition of the electrode and the solution to which it is directly exposed is fixed, as the potential depends on the relative activities of the species involved. This should remain constant in the fabricated reference electrodes as the fused LiCl-KCl will result in a large concentration of chloride ions, and the solution should be saturated with silver ions from the added silver chloride in equilibrium with the immersed silver wire. The fabricated reference electrodes were sealed so it is unlikely that the composition changed. For aqueous Ag/AgCl electrodes aging effects have been well documented. This is attributed to porosity of deposits on the electrode. Ag/AgCl reference electrodes were found to shift to more positive potentials and the aging period varied from a few minutes to 20 days.[161] At the elevated temperatures in the fused salt system, the silver ions would dissolve into solution more easily as there is more thermal energy. Another possible cause is attributed to a change in the frit of the reference electrode; a possible thinning of the mullite tube. A gradual deterioration of the mullite was observed over long time usage of the reference electrodes. Eventually cracks would appear and there was often discolouration on the exterior of the tubes. As it is known that silicon oxide can suffer material degradation in molten salt, it was theorised that this could cause aging of the sheath and potentially be contributing to a change in junction potential leading to the positive drift of the electrode potential over time.

To further test this theory and monitor the permeability of the mullite tube the resistance of the

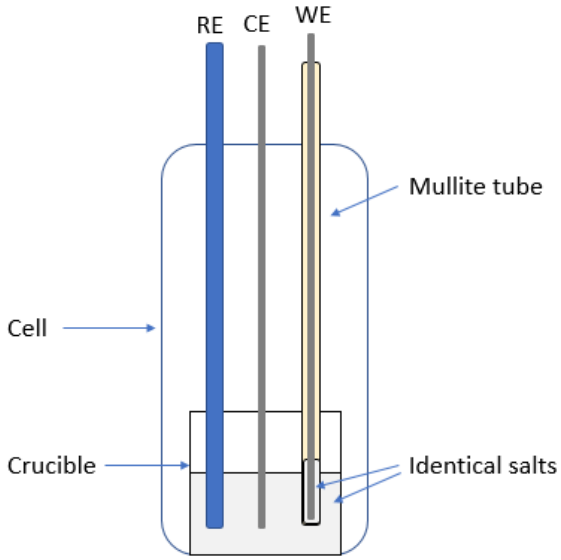


**Figure 3.9:** Schematic showing experimental set up for measurement of the junction potential

frit was measured from EIS measurements, with a tungsten rod inside the mullite frit acting as the working electrode along with 1 g of salt (the same as was in the crucible). The normal reference and tungsten counter electrodes were also used and the schematic of the setup is shown in Figure 3.9. This was performed initially using only using LiCl-KCl eutectic for both salts. It was then repeated with LiCl-KCl with 60 mM $EuCl_3$ added to clamp the open circuit potential of the molten salts. $EuCl_3$ was used as it was found to be a good soluble redox couple (Chapter 4). The salt was kept the same between the interior of the mullite tube and within the crucible in order to limit the number of factors affecting the junction potentials involved in the experiment. A difference in the concentrations or the presence of different ions across a membrane would contribute additional junction potentials, although any junction potential between different melts would be expected to be considerably lower than the resistance of the frit itself. This was a measurement of direct transfer across the frit induced by electrochemistry and not identical to the mullite performing as a reference electrode frit, and thus was a non-ideal measurement. However, only the EIS response for a small applied perturbation at OCP was applied to cause the direct transfer once every hour to minimise impact and attempt to monitor changes over time in the mullite frit.

The typical EIS response and circuit fit recorded in this system is shown in Figure 3.10, and it looked significantly different to the usual response for a tungsten rod in LiCL-KCl with europium

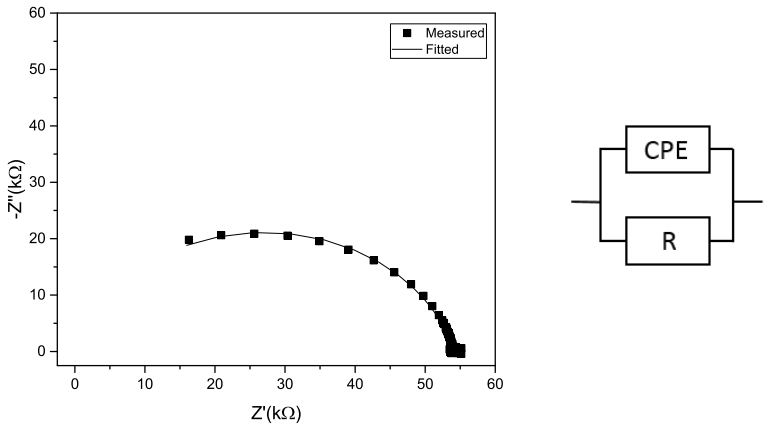


**Figure 3.10:** The typical Nyquist EIS response for a W rod housed in a mullite tube. The response shown was in LiCl-KCl eutectic after 6 hours.

as discussed in Section 4.2.2. In this system the EIS response seemed to be limited by a large resistance; this is not unexpected as the frit is 2 mm thick.

The impedance response did not fit well to the resistor and capacitor in parallel that was previously used to fit the typical response for a tungsten rod in LiCl-KCl eutectic. Instead a constant phase element was needed to improve the fit to the data. It is tempting to suggest that this could be due to the porosity of the mullite. This circuit, shown in Figure 3.10, fitted well with a $\chi^2$ value around 0.01 for all of the responses recorded. The EIS response over time is shown for the LiCl-KCl eutectic in Figure 3.11. There was a significant amount of noise on the OCP recording for the melt containing europium which may contribute to the discontinuities observed in the points over time. There was also a more negative OCP value recorded for the blank LiCl-KCl melt, which was surprising as the eutectic had been previously electrochemically cleaned by the standard procedure outlined in Section 3.2.2. It is reassuring that the EIS responses both with and without redox agent are consistent, with very similar values observed for both despite the large difference between the OCP values at which the measurement was performed (around 0.3 V difference). Both initially show a resistance value around 65 kΩ at the low frequency end of the Nyquist plot and reached a resistance value around 45 kΩ after 48 hours. Again a larger change is clearly observed in the EIS response over the initial time that the mullite tube is immersed in the melt, with a significantly larger decrease in the maximum resistance for the first six hours of the experiment. This is consistent with the cyclic voltammetric measurement across the solvent window indicating that this is indeed the period of greatest change for the mullite material.

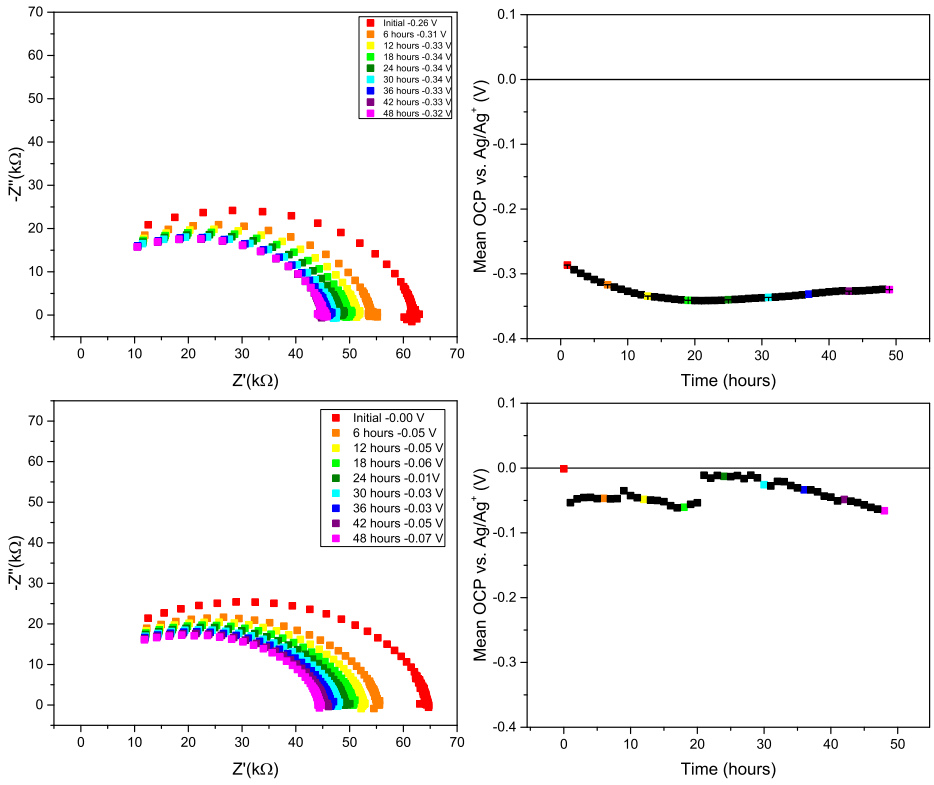


**Figure 3.11:** Change in EIS response over time for measurement behind the mullite tube frit (left) and the evolution of OCP value over time (right) for the measurements performed in LiCl-KCl eutectic (top) and in LiCl-KCl-$EuCl_3$ (bottom).

The fitted values for the equivalent circuit used to model the response are shown in Figure 3.12. Over time the resistance was observed to decrease, this is thought to be due to the corrosion occurring in the mullite - as it contains silicon dioxide which is known to corrode in the system,[122,123] which would then allow easier transport of ions through the frit. The fitted values were consistent for both experiments (with and without redox agents) and the resistance values are the same within error. Over a longer time period the change of the resistance gradually decreased as can be seen in Figure 3.12, an exponential curve fitted reasonably well to the observed resistance, except for the very early time values, with an $R^2$ value of 0.987. However in this measurement the resistance does not appear to decrease to a clear limiting value, but continues to decrease with longer times. An expression with the association of a double exponential improved the fit with an $R^2$ value of 0.996. This indicates that there could be two timescales associated with the equilibrium of the frit. The larger change was observable at earlier times on an apparently similar timescale to the observed change in the solvent window. The constant phase element values fitted were more constant, with

a change of less than 0.2 nMho, particularly with the larger errors associated with the values. This was particularly the case for after 15 hours when the fitted values appeared to reach a limiting value with some degree of fluctuation. This suggests that after a period of approximately 10 hours the reference was more constant, which corresponded well with the observations of the solvent window limits measured using a new reference electrode. This suggests that a conditioning step is important to reduce changes occurring in the frit during measurement. When reference electrodes are fabricated they should be 'conditioned' for approx 10 hours by immersing them in clean LiCl-KCl melt to induce this change in the frit. Care should be taken when heating and cooling the reference electrodes to avoid very fast freezing and melting of the internal salt, as this leads to cracking of the mullite tube most likely due to the stress induced. The tubes were also observed to break far more frequently in the presence of oxide and hydroxide, presumably as this increases the concentration of corrosive species within the salt.[163]

It would be possible to utilise alumina in place of mullite which would remove silicon dioxide from the frit. This has been shown to function by Wang for an alumina tube for use in fluoride salts, and chloride salts are considered to be less corrosive than fluoride melts.[56,132] Alumina is promising as it has been reported to be resilient to corrosion and thermal shock.[132] A non-ideal feature for the described alumina tube is the manual grinding to reduce the wall thickness of the tube from 1 mm to circa. 0.1 mm. As this is a manual process it would therefore introduce a large degree of error into the fabrication process and impact the reproducibility between different reference electrodes. The same experiment was conducted using an equivalent alumina tube in place of the mullite (without reducing the wall thickness) and measuring the impedance across the barrier. For this system only noise was recorded indicating there was a lack of ion transport through the alumina frit. Grinding was not performed as the aim was to improve the reliability of reference electrodes and it was undesirable to introduce human-caused variation into the fabrication process. If the grinding could be performed mechanically and hence reliably, then using alumina as the frit material could be further investigated.

#### 3.3.2.1 Improvements to fabrication of reference electrodes

The improvement in fabricating reference electrodes, by using pre-cleaned LiCl-KCl eutectic ground with AgCl (1 wt%) as the interior melt in the mullite tube and the use of a conditioning step where they are immersed in a clean melt for several hours prior to use resulted in smaller drifts

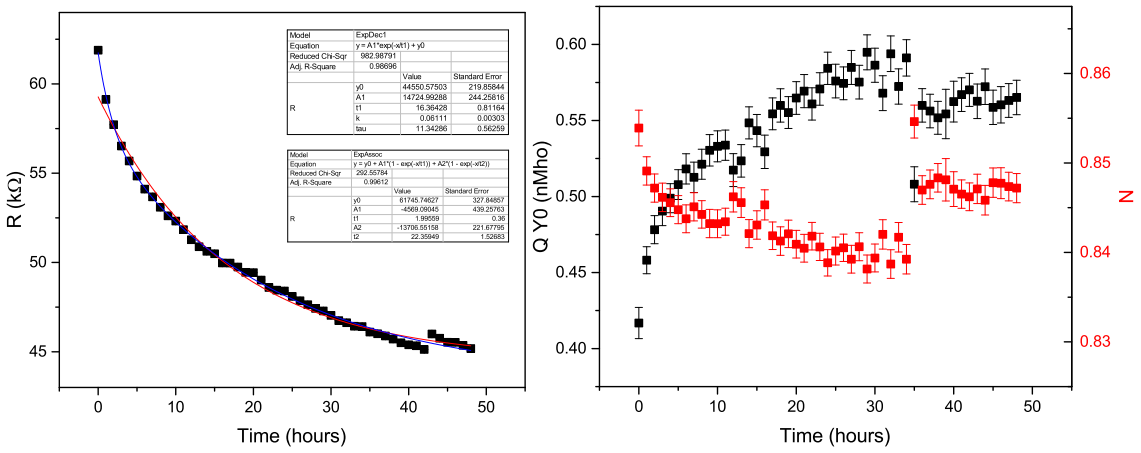


**Figure 3.12:** Fitted values for the EIS response to an (QR) equivalent circuit for the LiCl-KCl melt. The error bars on the resistance plot are too small to be seen.

observed within other experiments. This is shown by Figure 3.13 (left) where the electrochemical solvent limits were seen to be invariant with time, enabling confidence in measurements. With the reliability of the reference electrodes improving, it provides confidence that the reference potential isn't shifting within a measurement and enables easier comparison across experiments using different reference electrodes. This is exemplified by an experiment investigating the different alloying peaks of a platinum electrode with lithium and bismuth shown in Figure 3.13 (right), where despite the experiments being performed with different reference electrodes there is very good agreement with the corresponding peaks as the apex can be seen to align.

## 3.4 Improving the durability of reference electrodes and connection to microfabricated electrodes

The other issue encountered with the reference electrodes was the durability during experiments. This was a major issue encountered initially, as the mullite tube was often observed to have cracked during tests. This at worst contaminated a solution of a different redox couple such as europium or at best significantly increased the concentration of silver chloride, resulting in an unknown amount of silver present in the molten salt. This was a drain on both time and materials and ideally would be improved for a reliable reference electrode. Although this was found to occur with aging of the reference electrode, it most commonly occurred after removing the lid of the cell to replace a microelectrode. The breakage of the reference electrode was thought to be due to the large changes

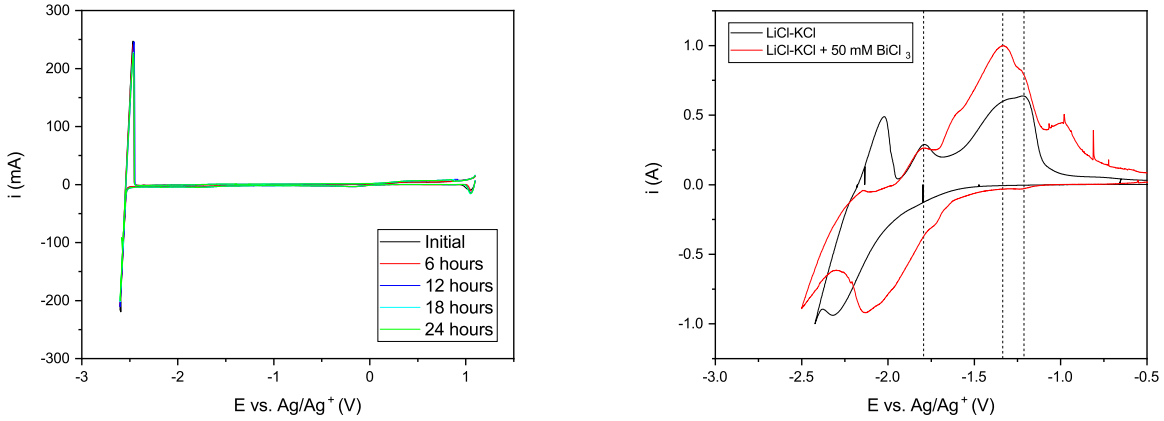


**Figure 3.13:** Figure showing CVs of the full electrochemical window for LiCl-KCl system showing the invariance over time using a W macroelectrode as WE at a scan rate of 200 mV/s. CV in LiCl-KCl eutectic (black line) and a separate experiment in LiCl-KCl with the addition of 50 mM $BiCl_3$(red line) both using a Pt wire as WE at a scan rate of 200 mV/s.

in temperature it was subjected to most likely causing rapid freezing and melting of the internal salt in the mullite tube.

At the start of this work large crocodile clips were used to connect to the contact pad of the electrode devices. The crocodile clip was physically crimped onto a tungsten rod. This seemed to produce a reliable connection and the single tooth was bent to only touch the contact pad of the chip and avoid contact with other layers, it could also be sanded for reuse. It did require the removal of the lid of the quartz cell to change electrodes (as the crocodile clip was larger than the diameter of the port) which opened the system and allowed the ingress of air for experiments performed in the external furnace. To improve this, mini crocodile clips were used which were also physically crimped to W rods. However, the shape of these did not match the area of the contact pad well (as the teeth were set wider than the contact pad) and the spring in these was found to corrode quickly, often resulting in the device falling into the molten salt during a measurement or when removing the device, which was also undesirable as it prevented analysis of the device after use. An alternative connection method was found with dolphin clips. The dolphin clips required the use of a thicker backing plate to reduce the diameter of the clip when in use so that it could pass through the ports; machinable ceramic (Macor) was made into a customised backing plate, this was designed with grooves each side to prevent rotation of the clip and the device, whilst being thick enough to allow the device and connection to fit through the ports on the lid. Figure

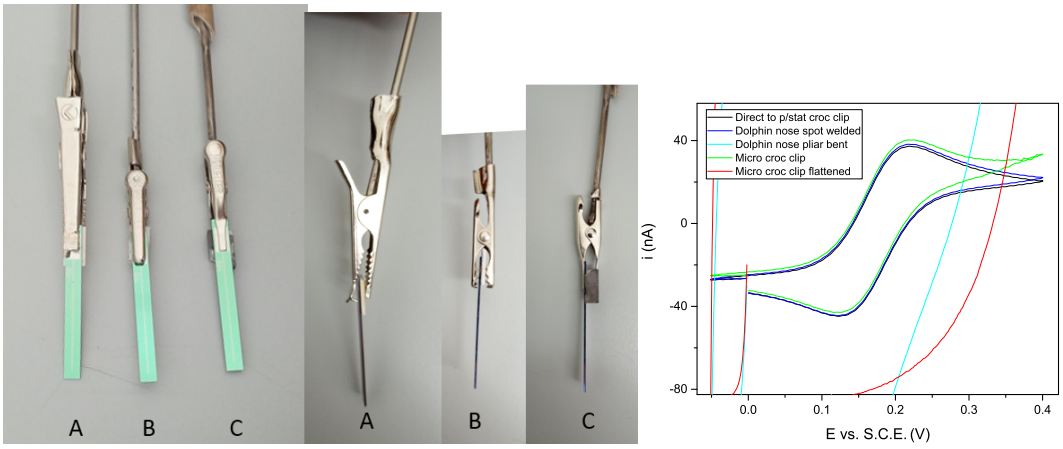


**Figure 3.14:** Optical images of different connections (front and side); macro croc clip (A), micro croc clip (B) and dolphin croc clip (C) (left image). Comparison of the various connection methods to analyse performance of the connection to a microelectrode device using the standard redox couple of ferri/ferro aqueously with a platinum microelectrode of 100 µm diameter (right).

3.14 shows a comparison of the various connections attempted for the high temperature set-up. A test of the various connection methods was performed aqueously to check the connection to the microelectrode, and test whether the micro croc clip could be flattened to improve the contact. From the various options available a dolphin clip was found to offer better contact to the contact pad, as can be seen in Figure 3.14. The surface area for electrical connection to the contact pad was larger, and the lack of teeth prevents the possibility of punching through to a different layer.

The dolphin clips could not be physically crimped to a rod of metal reliably (as can be seen from the aqueous test), so were instead spot welded to steel rods. Spot welding the connection was found to provide both a strong physical structure and ensure the electrical connection was good. It could also be performed in-house so this improvement was used for both dolphin clips and the micro croc-clips. The dolphin clips were also found to show a better response than the mini croc-clips, even when they had been flattened to provide a better contact. The dolphin clips were spot welded onto steel rods sealed into a ceramic sheath with putty as can be seen in Figure 3.14.

The other improvement was an adaption to the lid of the cells with the replacement of one of the ports (GL14 connection) with a larger quick fit port (B14) which had a diameter larger than the microfabricated electrode, to enable switching of devices with greater ease. This is shown in Figure 3.15. Both the mini croc-clips and the dolphin clips could be inserted through this as they were smaller than the avoiding the requirement to remove the lid. A quick-fit adapter to screw thread

**Figure 3.15:** Image of the improved cell lid allowing easier exchange of microfabricated electrodes for testing.

could still be attached to the rod prior to assembly, enabling the positioning of the device within the cell. This resulted in easier switching of devices and, as the reference electrodes were no longer exposed to sudden thermal shock, resulted in an improvement in the durability of the reference electrodes with fewer occurrences of the mullite tube cracking. Unfortunately reference electrodes were employed by multiple users and at the start of this work no record was kept so the lifetime improvement could not be quantified. These enhancements led to a large improvement in the yield of initially functioning devices, and indicates that some of the low yield figures for molten salt microelectrodes were likely due to poor connection to devices.

# Chapter 4

# Fundamental Characterisation of $EuCl_3$ on Macroelectrodes

## 4.1 Introduction

Lifetime results for microelectrodes have been characterised using silver chloride as a model plating and stripping system, both previously and in this study (Section 5.2.5).[123] Although this exemplifies a typical plating and stripping reaction, silver is unlikely to be a constituent part of a spent fuel stream and not all redox species present in waste fuel will undergo plating/stripping redox reactions. In addition, to demonstrate the optimised micro- and nanoelectrodes suitability for extracting information about the processes (particularly the electron transfer reaction) occuring at the electrode interfaces, a suitable soluble and electrochemically reversible one-electron redox couple was required to be identified. To address all these requirements, measurements were performed in LiCl-KCl eutectic containing europium (which is a nuclear relevant species) model lanthanide metal and established soluble/soluble redox couple.[78, 164–166]

Europium is a well studied redox species in LiCl-KCl eutectic.[78, 79, 164–169] However, there is some disagreement regarding the electrochemical reversibility of the Eu(III)/ Eu(II) couple in the molten salt media, with some reporting it as reversible and others reporting it as quasi-reversible (as described in Section 2.2.2) on typical measurement timescales.[78] Europium chlorides have also been noted to coexist in both divalent and trivalent states, as Eu(II) and Eu(III) in

varying proportions within an LiCl-KCl melt.[164, 169–171] The exact speciation is also unclear with some literature reporting that they exist as $[Eu(II)Cl_4]^{2-}$ and $[Eu(III)Cl_6]^{3-}$.[164, 170] A computational study suggests that the average coordination number in the bulk melt is six, however, the coordination shell is affected by the proximity to the electrode with the smaller Eu(III) ion coordination dropping to around 3-4.[172] After addition of europium (III) chloride to a molten chloride salt it has been reported that it can immediately be reduced to Eu(II) by the reaction $2EuCl_3 \rightleftharpoons 2EuCl_2 + Cl_2$ .[52, 164] Kim had previously reported that around 20 % was converted when using absorption spectroscopy to measure the reaction. Park et al. reported when using electron paramagnetic resonance spectroscopy that around 50 % was reduced to Eu(II) in frozen samples of the molten salt.[171] This chapter therefore considers these observed variations by characterising the electrochemical response of europium in LiCl-KCL eutectic using a tungsten macroelectrode as the working electrode and comparing the resulting responses with literature. The experimental characterisation will first be performed using cyclic voltammetry and electrochemical impedance spectroscopy, followed by discussion of the results of these measurements. A particular focus, given the need to determine the suitability of the redox system, is the electrochemical reversibility of the system and whether both the divalent and trivalent europium ions are stable in the solution.

## 4.2 Characterisation of europium as a redox agent in LKE using macro tungsten rods

### 4.2.1 Voltammetric measurements

The blue line in Figure 4.1 shows the typical CV in dry LiCl-KCl eutectic melt containing 60 mM $EuCl_3$ recorded on an inert tungsten electrode. Tungsten was chosen as it is inert in LiCl-KCl and has not been found to form intermetallic compounds with europium at elevated temperatures.[137, 162, 173] Reassuringly, the expected solvent window limits are seen in the CV, with chloride oxidation at the positive potential end occurring at approximately 1.2 V and lithium plating and stripping at the negative potential end at approximately -2.5 V. The other feature seen in the CV is the expected oxidation (α') of Eu(II) to Eu(III) and on the reverse scan the reverse reaction of the reduction of Eu(III) to Eu(II) (α). The black line shows why care had to be taken to ensure

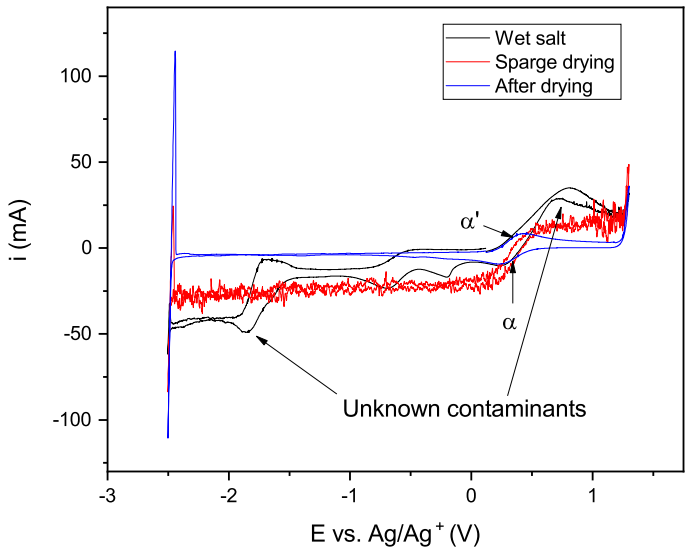


**Figure 4.1:** Full window CVs of LiCl-KCl-$EuCl_3$ (60 mM $EuCl_3$ added) solution at 698 K using a tungsten macroelectrode at a scan rate of 200 mV/s. The black line shows the overlap of oxide/hydoxide impurities with the europium signal, the red line is the CV during sparge drying of the melt (the fifth scan out of ten) and the blue line shows the typical response of europium after drying.

that impurities were excluded from the melt as these were found to have several electrochemical signatures. This includess an oxidation around 0.5 V, also shown in Figure 3.4, which complicates or at worst precludes measurement of the europium redox species. This was consistent with previous measurements of wet salts, which was overcome by Elliott, using a technique of flowing argon through the fused salt whilst cycling to the solvent limits known as sparge drying.[137] Figure 4.1 shows the sequence of an initially wet salt, a sparge drying CV and the resultant CV after cleaning. It is clear that sparge drying the melt successfully dries the salt as the waves due to the electrochemically active water contaminant were removed whilst leaving the electrochemical signature of europium. This signature is certainly due to the presence of europium as comparison of the blue line with the CV shown in Figure 3.5 (which shows the typical CV obtained after sparge drying the LiCl-KCl eutectic) where there is no evident electrochemistry around 0.3 V. Sparge drying for this case was performed for 10 complete CVs and sparged with argon for approximately 10 minutes. One potential issue identified with europium was the formation of europium oxychloride, previously observed by Bermejo,[167] on heating europium chloride hexahydrate. Therefore the size of the europium peaks was measured and using an approximate size of the immersed electrode was

found to correlate with the known amount of europium trichloride added (using literature values for diffusion coefficients).It can then be concluded that the europium signal can be recovered from a wet salt, indicating that insoluble europium oxychloride is not produced - even at elevated temperatures in the molten salt. Although every effort was taken to reduce the amount of impurities, particularly water associated with the salt, this provides confidence that the europium signal could be recovered if impurities were found.

Figure 4.2 shows the typical response for the investigation of the potential region where europium electrochemistry was observed for dry salt. A single set of redox peaks was observable. As expected the cathodic and anodic peaks attributed to Eu(III)/Eu(II) were characteristic of a soluble-soluble redox couples and consistent with that reported for this system.[87,167] The scan was started in the direction of increasing voltage so Eu(II) would first be oxidised to Eu(III). This was the first scan performed after the system sat at OCP for 10 minutes to allow equilibration. Clearly there was a negative current observed indicating that there was Eu(III) in the solution. In the CV shown in Figure 4.2 the CV appears to be evenly positioned about the x-axis of zero current, with the peak current associated with oxidation of Eu(II), $\alpha'$, and the reduction of Eu(III), $\alpha$, being approximately equal. Assuming that the diffusion of the product away from the electrode is similar to the diffusion of the reactant species to the electrode during the scan, this suggests that there was a near equal distribution of Eu(II) and Eu(III) species present within the melt, consistent with the sparging CV in Figure 4.1. Similar diffusion coefficents is reasonable for the reversible reaction (discussed in section 2.2.2) for the interconversion of the species, and consistent with other work.[174]

Figure 4.3 shows the result of a scan rate study on the europium system at 60 mM concentration in LiCl-KCl employing a tungsten macroelectrode as the working electrode. In this case, very little current is observed at the start of the CV when the scan is swept in the positive direction. This is entirely different to the CV shown in Figure 4.2, when initially a negative current was observed. In this instance it shows that there is little to no reductive current at the start of the CV, which indicates that there is very little Eu(III) in the melt. This demonstrates almost complete reduction of the Eu(III), which was the form originally added to the melt.

Examining the backround current within a dry and clean melt, around the potential region the CVs were started (-0.1 to 0 V), there is not a huge variation in the value of the background current, certainly not to the level of 4 mA current difference seen in comparison of Figures 4.2 and 4.3, indicating that this observable shift in the position of the CV is shows varying proportions of

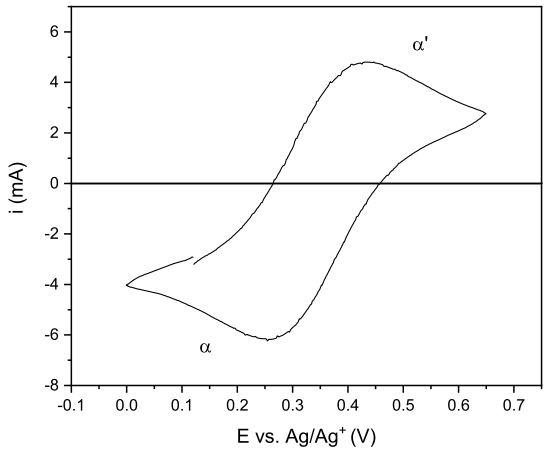


**Figure 4.2:** First scan CV of $Eu^{3+/2+}$ couple in molten LiCl-KCl containing 60 mM of $EuCl_3$at 425°C. CV started at 0.08 V in the positive direction at a scan rate of 100 mV/s.

the Eu species within the melt. This shows that the reduction of Eu(III) within the melt is not due to thermodynamics, but rather is a kinetic reaction. There is significant discussion of this in the literature debating the amount of each europium species present within molten LiCl-KCl eutectic reinforcing the idea that there is variation in the amount of Eu(II) and Eu(III) in different melts.[52, 78, 164, 168, 171] Interestingly it has also been noted that on addition of Eu(II) to the melt as an initial material, no oxidation to Eu(III) was observed.[171] Kim previously reported, using absorption spectroscopy that around 20 % was converted from Eu(III) to Eu(II). Park et al. reported that around 50 % was reduced to Eu(II) in electron paramagnetic resonance spectroscopy which was performed on frozen samples of the molten salt.[171] The variation has been attributed to the oxide concentration within the molten salt.[164] For the data shown here all the measurements were performed in a glovebox under an argon atmosphere to limit the amount of oxygen present. The variation in proportion of Eu(III)/(II) is likely due to the presence of reducing species within the melt, which could change the redox state of the europium. It was visible that different salts had varying amounts of water associated with them, which was evident in the appearance of the initial whole window CVs. This also led to changes in the level of electrochemical drying of the salt required, which could affect the quantity of reducing species in the melt. During the drying process both $H_2$ and $O_2$ would be generated from water. Another possibility is the formation of Li from lithium reduction at the edges of the entire potential solvent window. The opposite reaction, occuring on either the WE or the CE, produces $Cl_2$ which could escape the solution and thus leave

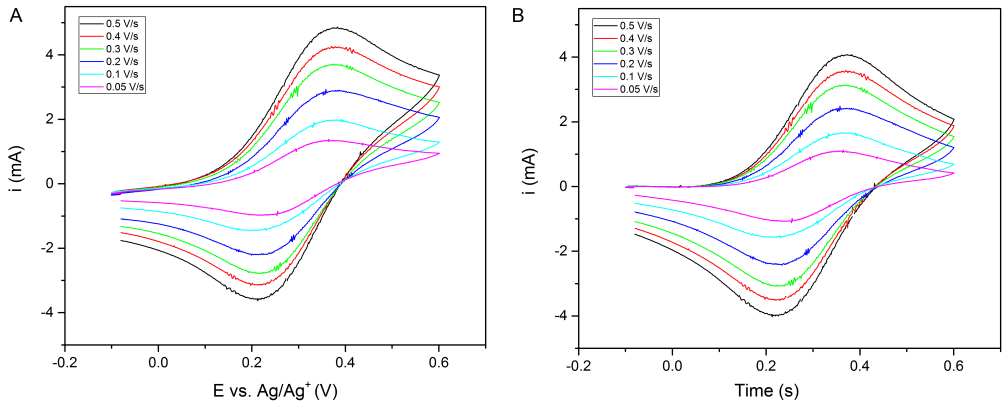


**Figure 4.3:** Scan rate study performed on Eu(III/II) couple in molten LiCl-KCl eutectic at a concentration of 60 mM with the scan beginning at -0.08 V at 375°C, the raw data is shown in A and the background corrected CV is shown in B.

some Li remaining near the electrode. The presence of a lithium colloidal suspension within LiCl has been noted by Merwin *et al.*.[175] The reducing environment is also corroborated by Park's measurement of no conversion to Eu(III) when Eu(II) was added to LiCl-KCl eutectic. This also provides useful evidence that the reaction is not thermodynamically controlled.

For the scan rate study shown in Figure 4.3A the negative current at the start of the 200 $mVs^{-1}$ scan was found to be -0.174 mA. This is within the range of the background current observed in just the pure eutectic and is obviously different from the CV shown in Figure 4.2 where the current was around -4 mA at the start of the positive sweep. The current also doesn't change with the scan rate for the start of the CV in the raw data in Figure 4.3, therefore the small amount of current is background. This is for this case only as there was near complete reduction of Eu(III). For CVs such as in Figure 4.3 where it is plausible that the background current is solely due to a reaction other than Eu(III)/(II), a background correction can be performed. The background correction was performed using the region where there should be little to no Faradaic current (this was taken as the region between -0.05 and 0.05 V for each CV), and subtracting the linear fit of this region across the entire CV. The result of this is shown in Figure 4.3 B.

Figure 4.4 shows a comparison of the peak current to the square root of scan rate for both the raw data and the background corrected data. The peak current was found to correlate directly with the square root of the scan rate, as can be seen with the linear regression fitted in Figure 4.4, showing the current was under diffusional control. This is consistent with that previously reported.[167] The main influence of the background correction was centering the intercept around

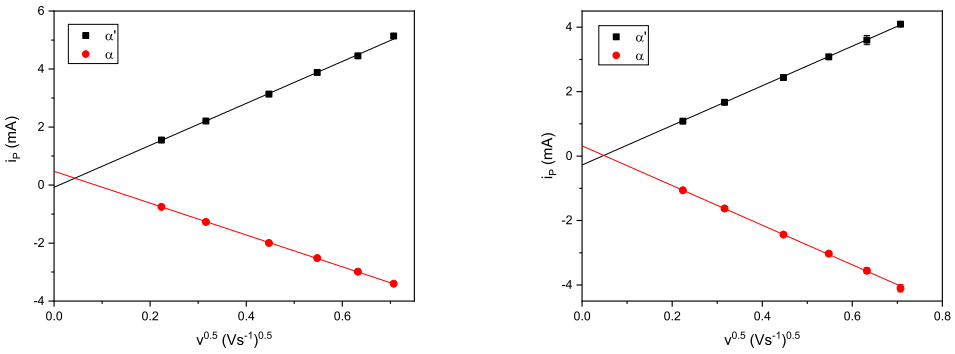


**Figure 4.4:** Peak current versus the square root of the scan rate for europium reaction α/α' seen in Figure 4.2 for the raw data (left) and the corrected data (right). The solid lines are the fitted linear regressions which have been extrapolated to $v^{0.5}$=0. Error bars are 1σ.

| | α' | | α | |
|---|---|---|---|---|
| | Raw | Corrected | Raw | Corrected |
| Intercept /mA | -0.0761 ± 0.0031 | -0.278 ± 0.021 | 0.475 ± 0.009 | 0.316 ± 0.014 |
| Slope/ $mAV^{-1}s^{1/2}$ | 7.23 ± 0.09 | 0.615 ± 0.006 | -5.49 ± 0.03 | -0.615 ± 0.004 |
| $R^2$ | 0.99919 | 0.99942 | 0.99988 | 0.9998 |

**Table 4.1:** Comparison of the raw and corrected linear regressions for the reactions α' and α at 375°C

zero current. Compensating for the apparent resistance obviously caused the magnitude of the gradients of the reduction and oxidation to be equal. From the raw data although there is a slight discrepancy between the magnitude of the gradients obtained by linear regression on the data, this is reasonably small (around 24% difference) indicating that the Eu(II)/Eu(III) reversibility is high. This also confirms that the diffusion coefficients for each of the charged europium species are very similar and can be considered as approximately the same. The gradient of the regression shows an improvement in the error level with background correction. The intercept instead shows a slight increase in the error of the linear regression fit. It is not entirely clear why this is the case, however it is only a small difference and all of the linear fits provided a good fit to the experimental data.

Figure 4.5 shows the variation of the cathodic and anodic peak potentials with the logarithm of the scan rate. Whilst there is a slight divergence this is very small, suggesting that peak potential is near independent of $\nu$. This invariance is similar to that presented by Bermejo for the LiCl-KCl-EuCl system for this range of scan rates, whilst there was a clear divergence at a scan rate of 600 $mVs^{-1}$.[167] For this study at all sweep rates recorded the current is therefore controlled by the rate of mass transport.

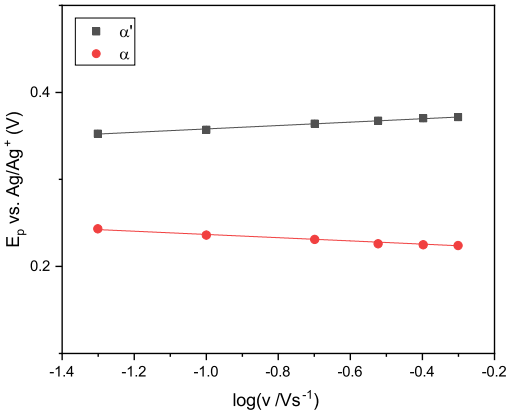


**Figure 4.5:** Variation of the peak potential for α and α' with the logarithm of the sweep rate.

Scan rate studies were also performed on the Eu couple at 60 mM concentration at higher temperatures of 400°C, 425°C and 450°C. The results of this are shown in Figure 4.6. It should be noted that these data sets were collected together, but separately to the one performed at 375°C. The scan rate study was also performed over a slightly wider potential window as well as at higher temperatures. The CVs were started at the upper potential limit and scanned negative so the reduction was the first reaction. Current was observed when CVs were started at the positive end, indicating that Eu(II) is converted into Eu(III), again this data set suggests that a large amount of the $EuCl_3$ has been reduced in the melt.

As expected the macroelectrode peak shaped response is seen. In these measurements the influence of convection is seen to be less as the current approaches the zero current axis, indicating that the flux of species to the electrode surface is still decreasing as the depletion zone around the electrode grows with time. However, the window is wider so it is harder to infer whether this would happen for the system at 375°C. No real influence of convection is apparent for both data sets as the intercepts are near zero (or opposite sign), for the plots of peak current variation with the square root of scan rate. The magnitude of the current is larger, which is most likely due to a larger active electrode area (as the immersed area of the macroelectrode was not well controlled). This illustrates why the data collected could not be used to extract accurate values for the diffusion coefficient with the Randles-Sevcik equation, as the exact immersed area of the electrode was unknown. The variation of peak current with the square root of scan rate is shown for the data sets collected at 400°C, 425°C and 450°C in Figure 4.7.

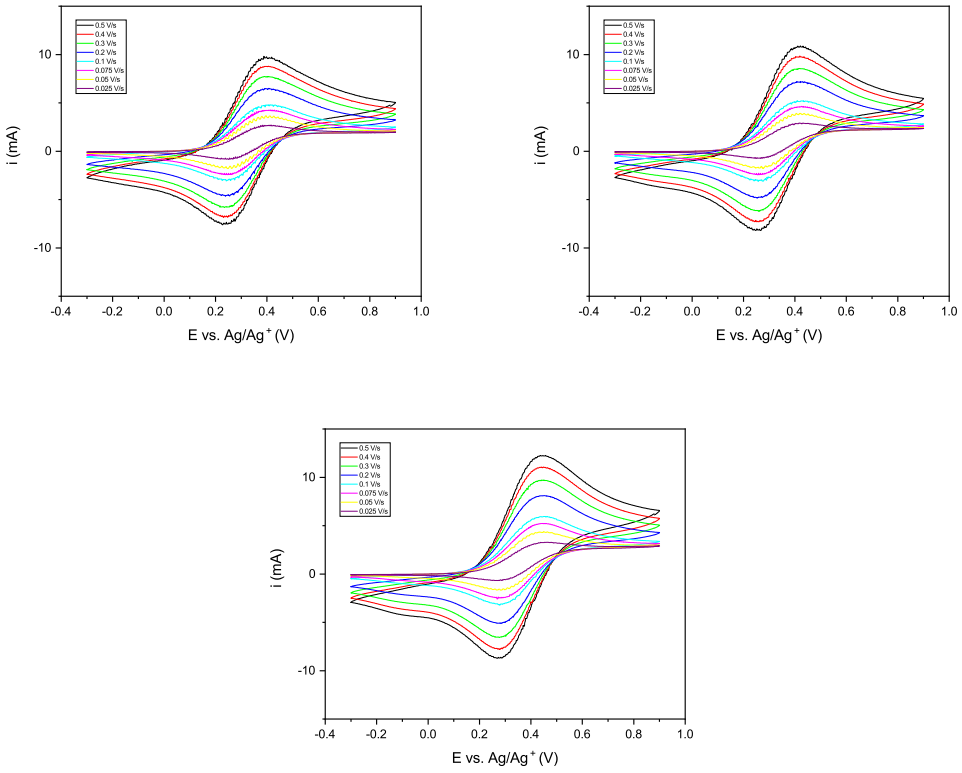


**Figure 4.6:** Scan rate study CVs at 400°C (top left), 425°C (top right) and 450°C (bottom), the scan was started at the 0.88 V and scanned negatively.

Clearly across all data sets there is a very strong linear correlation of peak current with the square root of the scan rate as would be expected for linear diffusional control occuring at a macroelectrode as described in Section 2.2.2. Table 4.2 shows the values extracted from these scan rate studies. The very high $R^2$ value for all data sets shows the linear regressions fit very well to the data reinforcing the clear linear dependency of the peak current with $v^{0.5}$.

The intercept values are reasonably small for all of the experiments performed; as would be expected if these were reasonable background subtractions. The similarity between the extracted values for the different temperatures which were recorded in the same melt is evident.

The assumption is that the reaction is reversible and therefore should follow the Randles-Sevick equation;$|i_p| = 0.4463(nF)^{\frac{3}{2}}Ac\sqrt{\frac{Dv}{RT}}$ . For a plot of $|i_p|$ vs. $v^{0.5}$ the magnitude of the peak current should also change with the area of the electrode and the square root of the diffusion coefficient. From the equation the greatest effect will be due to the area of the electrode. This is clearly reflected in the results where the gradient of the plot is very similar for those recorded

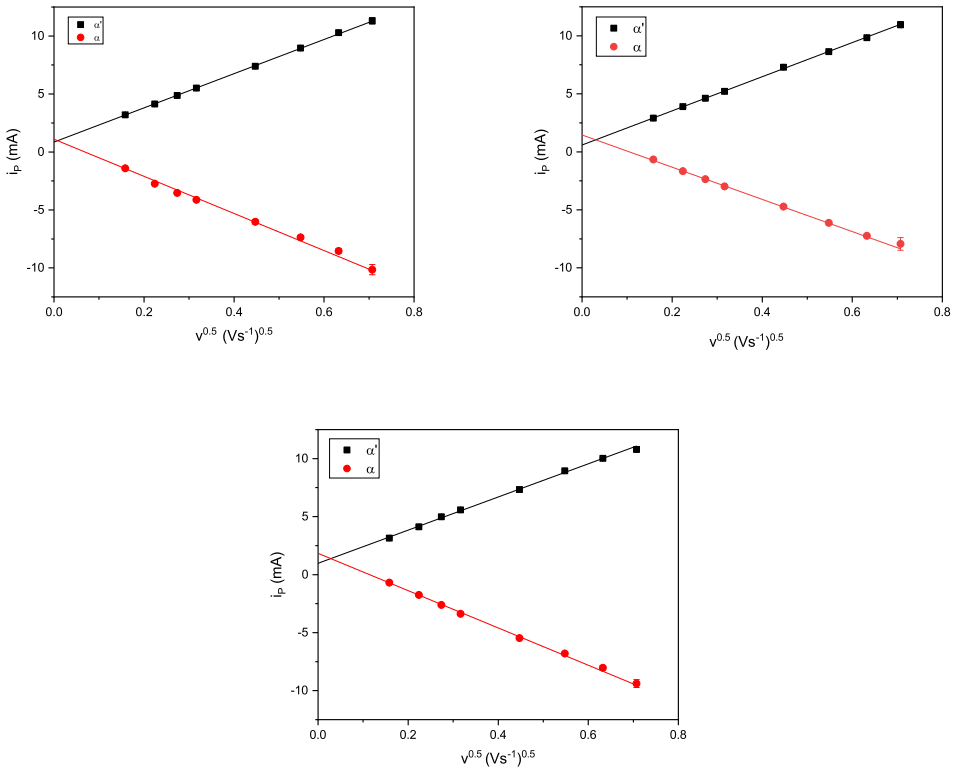


**Figure 4.7:** Peak current versus the square root of the scan rate for europium reaction α/α' from the raw data seen in Figure 4.6 at 400°C ( top left), 425°C (top right) and at 450°C (bottom). The solid lines are the fitted linear regressions which have been extrapolated to $v^{0.5}$=0 and error bars are 1σ.

in the same experimental set-up, and very different from the lower temperature which had been recorded separately. For the measurement in the same set-up at higher temperatures the electrodes were neither adusted nor moved during the collection of the data; thus the active area should be constant. For the data set collected at the lower temperature it is likely that the electroactive area was much smaller. Interestingly the gradient decreased as the temperature increased which is not as would be expected with aqueous measurements, since the diffusion coefficient depends on the temperature, dynamic viscosity $\eta$ and the hydrodynamic radius $r$ as defined by the Stokes-Einstein equation:[176] $D = \frac{kT}{6\pi\eta r}$. Normally for aqueous conditions $\eta$ decreases with increasing temperature, so the gradient would be expected to increase with temperature. So whilst this is interesting it cannot be considered conclusive given the unknown areas of the macroelectrodes. Indeed, the measurement of different systems highlighted the complication of using macroelectrodes with a poorly known active electrode area, particularly as there is a lack of knowledge around the wetting

| Reaction | Temperature /°C | Intercept /mA | Gradient /mA$(Vs^{-1})^{-0.5}$ | $R^2$ |
|---|---|---|---|---|
| α' | 375 | -0.076 ± 0.003 | 7.23 ± 0.092 | 0.99919 |
| | 400 | 0.853 ± 0.027 | 14.75 ± 0.090 | 0.99974 |
| | 425 | 0.703 ± 0.025 | 14.71 ± 0.066 | 0.99986 |
| | 450 | 0.978 ± 0.089 | 14.29 ± 0.250 | 0.99875 |
| α | 375 | 0.475 ± 0.009 | -5.49 ± 0.027 | 0.99988 |
| | 400 | 1.100 ± 0.115 | -16.01 ± 0.599 | 0.99029 |
| | 425 | 1.454 ± 0.064 | -15.98 ± 0.193 | 0.99864 |
| | 450 | 1.800 ± 0.058 | -15.92 ± 0.192 | 0.99897 |

**Table 4.2:** Extracted values from the raw data of the scan rate studies at different temperatures.

properties of molten salts on various materials.[123, 167, 177, 178] Despite efforts to overcome this, including the manufacture of fixed area electrodes as well as gradual increments of the immersion depth and analytical comparison of the resultant electrode response, the use of macroelectrodes is still hampered by the issue of unknown electroactive area.[137, 167]

### 4.2.2 Electrochemical Impedance Spectroscopy

The one electron transfer was further investigated with the use of electrochemical impedance spectroscopy around $E_{1/2}$. The typical response is shown in Figure 4.8, this is the response at an applied DC potential of 0.16 V. At high frequencies the results are spurious as there appears to be some cell inductance.

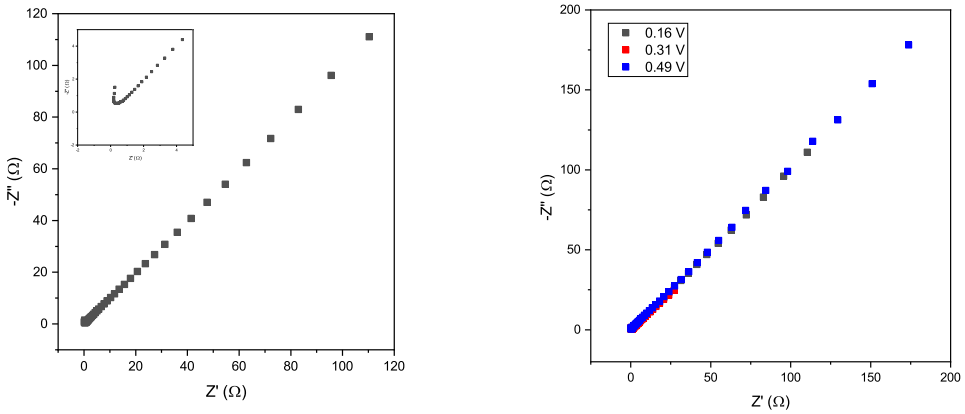


**Figure 4.8:** Nyquist plot of the EIS response of LiCl-KCl-EuCl system at 375°C at an applied DC potential of 0.16 V (left) with the inset showing the highest frequencies magnified. The Nyquist plot of the response at three different applied DC potentials around $E_{1/2}$ (right)

Therefore very high frequency data (above 2.6 kHz) was discarded from subsequent analysis. For the low frequency data a 45° line was observed, typical of the Warburg element. This is not surprising

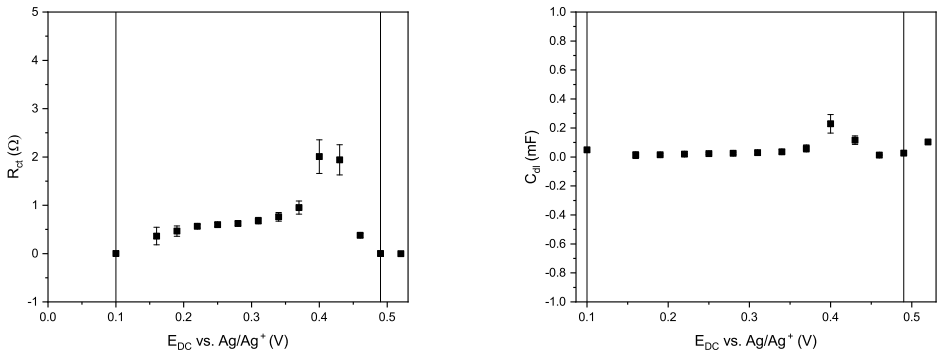


**Figure 4.9:** Fitted $R_{ct}$ (left) and $C_{dl}$ (right) values with change in applied DC potential for the LiCl-KCl-EuCl system at 375°C.

as this is typical of the low frequency end of the Nyquist plot of a macroelectrode response where linear diffusion dominates. Somewhat more surprisingly, there appears to be little evidence of the semicircular feature expected at high frequencies. This suggests that electron transfer was a very rapid process and therefore the charge transfer resistance was low in this system and thus that semicircle was merged into the response due to diffusion at high frequencies.

The response at different applied DC potentials is also shown in Figure 4.8, this is only shown for three potentials due to the similarity between the plots and overlap making it hard to distinguish them separately. The total impedance clearly decreases at the DC potential closest to $E_{1/2}$ (0.31 V) and is larger for both potentials either side. This is the typical behaviour expected. It is evident at all applied DC potentials that the response is dominated by diffusion as the main feature of the response. To fit the response to an equivalent circuit the established Randles' circuit for macroelectrodes was used. The solution resistance was set to zero as after disregarding the highest frequencies, the intercept was very small (between 0 to 0.5 Ω) and could only be fitted with a large error. The low solution resistance was consistent with previous voltammetric measurements in LiCl-KCl eutectic.[137,162] To reduce the error on the rest of the fitted parameters it was therefore necessary to fix the solution resistance parameter to zero. The Randles' equivalent circuit fitted the data well with the $\chi^2$ value always lower than 0.2. The variation of $R_{ct}$ and $C_{dl}$ with DC potential is shown in Figure 4.9.

As would be expected the $R_{ct}$ value was found to be very small and there was no clear variation with applied potential. This is probably due to the difficulty of fitting the response without a clear semicircular feature evident in the Nyquist plot. The $C_{dl}$ values were reasonably consistent. Fixing

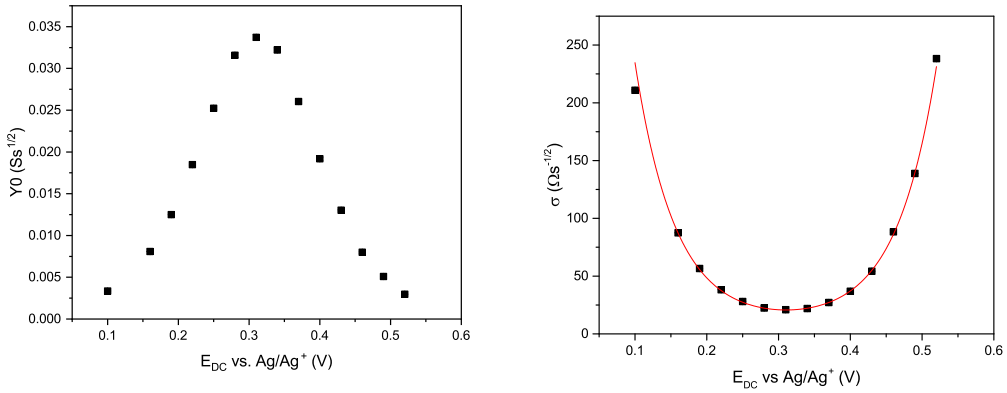


**Figure 4.10:** Y0 (left) and sigma (right) variation for fitted EIS responses of W macroelectrode in LiCl-KCl-EuClsystem. Error bars of 1$\sigma$ are too small to be seen on the plot.

$R_{ct}$ to the average value of 0.667 Ω resulted in a reduction of the average value of $C_{dl}$, however it was still difficult to fit it accurately.

Fixing $R_{ct}$ resulted in an increased percentage error on the fitted value of $C_{dl}$ to over 100%, from around 30% for the circuit fitted allowing $R_{ct}$ to vary. Therefore the capacitance values shown in Figure 4.9, extracted whilst allowing $R_{ct}$ to vary, is likely to be a more accurate representation of the physical double layer capacitance. The capacitance appeared constant within error across the range of applied potentials measured. For aqueous measurements the typical value of $C_{dl}$, is around 10 μF/cm$^2$. With an approximate area of 1.5 cm$^2$ with the measured immersion depth of 2.5 cm and taking the average $C_{dl}$ value the normalised capacitance was found to be 6.7 ± 2.1 μF/cm$^2$, which is reasonably similar to aqueous values, especially considering the large errors with fitting to the high frequency region. The estimated area seems reasonable but should not be considered reliable.

As would be expected from the appearance of the Nyquist plot the fit for the low frequency region using a Warburg element was significantly better. The fitted data gave rise to the expected shape for the Warburg element and the error on this was very small (maximum of 1 % of fitted value), this is not unexpected as the diffusion is expected to dominate the response on a macroelectrode. The Warburg admittance Y0 and impedance $\sigma$ for the system is shown in Figure 4.10. The extracted values from the system very clearly fit the expected thermodynamic response (red line) as would be expected, with an $R^2$ value of 0.997. Using the fitted value of $\sigma_{min}$ from the thermodynamic fit, equation 2.2.3.6 and a literature value for the diffusion coefficient the area of the electrode looks

likely to have been smaller than that estimated from the geometric calculation, and was found to be 0.63 ± 0.20 $cm^2$. Without having an accurate and reliable value for the area it is not possible to use the fit to the Warburg impedance for the calculation of other values such as the diffusion coefficient. It is clear from these measurements with the dominating feature due to diffusion, that the charge transfer is taking place too quickly and cannot be accurately measured even with the use of EIS on a macroelectrode. It is therefore desirable to utilise smaller electrodes to gain more insight into the processes occuring and this will be the objective in subsequent chapters.

### 4.2.3 Reversibility and uncompensated resistance

Similarly to the work performed by Elliott and Reeves the iR drop in the system could be calculated by comparing the peak current and the peak voltage at which it occured for the scan rates investigated.[137, 162] An uncompensated resistance can then be calculated with the gradient of this plot. Figure 4.11 shows this plot for the study performed at 375°C and 425°C. The plots for 400°C and 450°C are not shown but were very similar to that shown for 425°C. These values are summarised in Table 4.3.

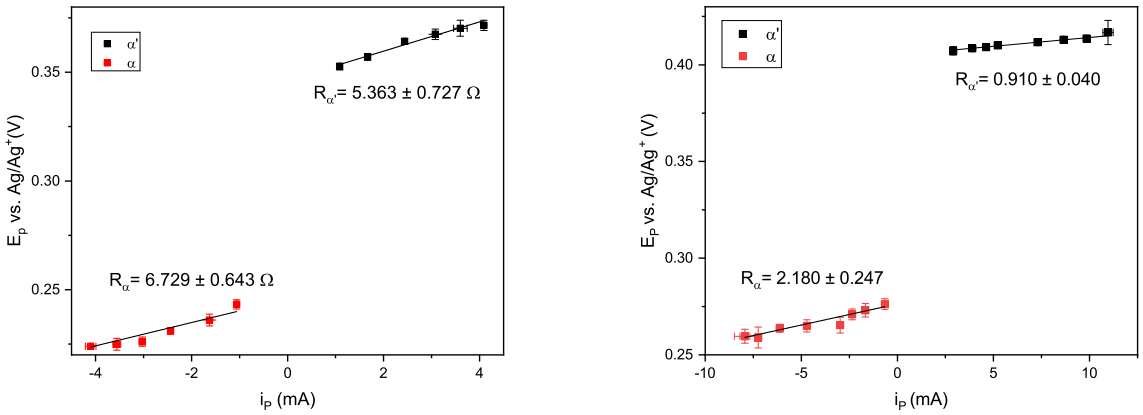


**Figure 4.11:** Uncompensated resistance calculated for the scan rate study performed at 375°C (left) and 425°C (right).

The resistance was higher than that observed by Elliott (which was typically around 0.15 Ω) when investigating bismuth and cerium alloying. It was, however, of similar magnitude to some of those calculated by Reeves; for example aluminium plating on a tungsten macroelectrode where the apparent resistance of the plating reaction was 3.54 Ω. For the data sets collected at the higher

temperatures there is less apparent resistance and the values are more typical of those reported previously by Elliott and Reeves.[137, 162] The high resistance observed especially in the 375°C

| Reaction | Temperature /°C | $R_u/\Omega$ |
|---|---|---|
| α' | 375 | 5.363 ± 0.727 |
| | 400 | 0.896 ± 0.232 |
| | 425 | 0.910 ± 0.040 |
| | 450 | -0.571 ± 0.194 |
| α | 375 | 6.729 ± 0.643 |
| | 400 | 2.00 ± 0.412 |
| | 425 | 2.180 ±0.247 |
| | 450 | 1.563 ±0.086 |

**Table 4.3:** Table showing the calculated uncompensated resistances for the different temperatures.

system could be due to possible contamination on the tungsten macroelectrodes. Perhaps due to the presence of oxides on the surface (tungsten is known to form a stable oxide). Although a high resistance at the electrode surface would be expected to change the charge transfer resistance measured, the resistance is still quite low and $R_{ct}$ was difficult to accurately measure with the macroelectrodes. For the soluble-soluble redox couple the surface of the electrode should remain unchanged during the measurement whereas for plating and stripping reactions including alloying, the surface of the electrode could be affected during the process. Alternatively the spread of peak potentials at different scan rates could indicate that the system is quasi-reversible. However, the EIS measurement indicated that the solution resistance or any uncompensated resistance was very low (under 0.5 Ω), suggesting that the uncompensated resistance extracted from the voltammetric data were a little high. As there was noise within the measurements this could have contributed to some uncertainty in the determination of peak current and potential. Interestingly, the resistance for the reduction was always found to be higher than the uncompensated resistance for the oxidation reaction $\alpha$'.

Clearly the reaction is chemically reversible, but to conform to the electrochemical definition of a reversible system the electron transfer kinetics need to be sufficiently high as discussed in Section 2.2.2. Therefore the reversibility parameter, $\Lambda$, was calculated for the scan rates investigated. The diffusion coefficient was calculated using the gradient from Figure 4.4 and an approximate area calculated from a measured immersion depth of the macroelectrode after use of 2.15 cm for a 4 mm diameter W rod. From this the diffusion coefficient was calculated to be (4.34 ± 0.07) x $10^{-6}$ $cm^2$ $s^{-1}$, which is consistent with literature values considering experimental errors and

differences in the temperatures under investigation.[87,167] Using the average value of $R_{ct}$ from the impedance fits as the minimum it was possible to find an approximate value of the electron transfer rate $k^0$ = 0.658 cm $s^{-1}$, which could be used to calculate the maximum and minimum values of the reversibility parameter, $\Lambda$, for the scan rates investigated. Table 4.4 summarises the values calculated in comparison with other reported electron transfer rates.

| $k^0$/$cms^{-1}$ | 0.003 | 0.26 | 0.658 |
|---|---|---|---|
| Source | Bermejo[167] | Corrigan[87] | estimated from EIS |
| $\Lambda_{500\ mV/s}$ | 0.519 | 41.7 | 106 |
| $\Lambda_{25\ mV/s}$ | 2.32 | 187 | 472 |

**Table 4.4:** Reversibility parameter calculated for different rate constants, from the EIS data and values reported in literature.

The approximated electron transfer rate from the impedance response was higher than both previously reported values. However, the value calculated is also reliant on extracted values with significant errors and no clear expected bowl for the charge transfer resistance. So whilst it can guide calculation of an approximate rate constant it is desirable to probe this further. This could be achieved with the use of micro- and nanoelectrodes and is further investigated in Chapters 6 and 7. The reversibility parameter for both the approximate rate constant in this study, and that reported by Corrigan, was greater than 15 at all scan rates investigated positioning it as a reversible couple. Using the rate constant reported by Bermejo the reversibility parameter at all scan rates was within the quasi-reversible definition.[126, 167] It is important to note that Bermejo's study used glassy carbon electrodes and this work used tungsten so it is possible that the carbon electrodes caused some other reaction or surface layer to be formed. It should also be noted that there was evidence of a secondary peak in the voltammetry presented within their work.

The peak separation was measured to be $\Delta E_P$ = 0.128 V (at $v$ =100 mV/s) for the data set collected at 375°C which is 3.6 % different to the expected value of 0.124 V calculated using the equation $\Delta E_P = 2.2\frac{RT}{F}$. Schroll, who investigated the LiCl-KCl-EuCl system, found a higher value of 0.16 V and indicated that this could be due to slow heterogeneous electron transfer.[78] However, there was also evidence of two oxidation peaks in the reverse scan which could be evidence of impurities in the fused salt or another reaction occuring. This study seems to suggest fast electron kinetics but the measurement of the electron trasnfer rate was very limited with the use of macroelectrodes.

### 4.2.4 Effect of temperature

A slight positive shift in the half wave potential was observed with an increase in temperature as can be seen in Figure 4.12, although there are only three data points and the CVs are quite noisy which made the determination of the peak voltages more challenging. A linear trend was found which indicated an increase in $E_{1/2}$ of $6.4x10^{-4}V/K$ which was consistent with that seen in literature (Schroll found it to be $5x10^{-4}V/K$[78] ). The change in standard potential is expected to follow $\frac{\partial E^o}{\partial T} = -nF\frac{\partial \Delta G^o}{\partial T}$. Therefore would be expected to increase with more entropy within the system, as demonstrated by this measurement.

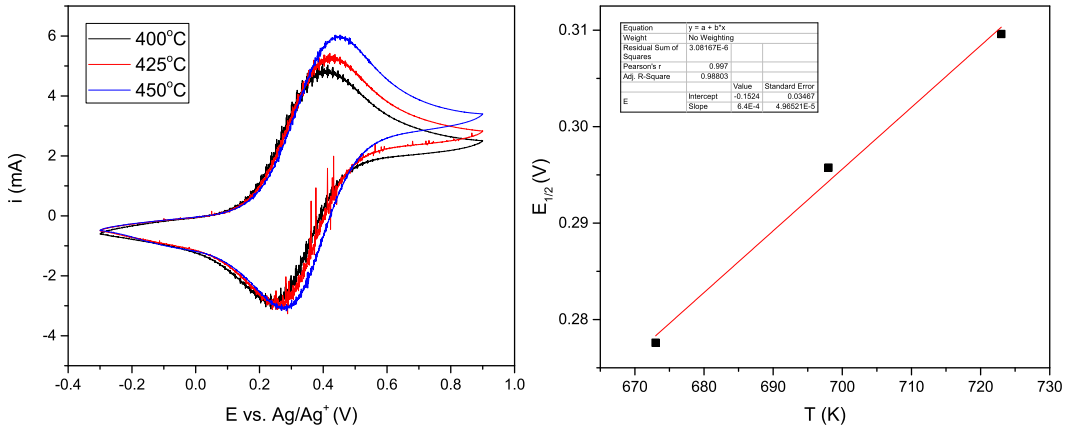


**Figure 4.12:** CV of Eu(II)/Eu(III) at 100 $mVs^{-1}$at different temperatures. Scan is the second CV of a set which starts at 0.88 V and is scanned in the negative direction.

### 4.2.5 Conclusions

Europium chloride gave a clear measurable response in LiCl-KCl on a tungsten macroelectrode which was indicative of a soluble-soluble couple. Eu(II)/(III) was found to be most likely electrochemically reversible or at the very least quasi-reversible. As the species is non-radioactive and will be present in spent nuclear fuel it is therefore a suitable species to use as a redox couple to investigate the response on a variety of electrodes. On a macroelectrode it was found to conform well to theory and the values obtained were in agreement with literature values. The EIS and CV measurements were consistent. Previously low kinetics described in literature are likely to be due to some other reaction or surface layer on the electrodes.

The proportions of Eu(II)/(III) were found not to be fixed by the thermodynamic reaction but by reduction of Eu(III) due to the presence of electrochemically (or chemically) generated reducing

agents. Within measurements perfomed in this study variations were observed within the proportions of each species, which is also reflected in the wide range of reported ratios in the literature.

Limitations were encountered in measurement and extraction of parameters at high frequency in EIS measurement of the reaction. This precluded a clear measurement of the charge transfer resistance and the capacitance of the double layer. Both this, and the difficulty of a poorly known area of the electrode, demonstrate the motivating factors that have driven the creation of minituarised electrochemical sensors to probe reactions further in molten salt systems.

# Chapter 5

# Improving Miniaturised Electrodes for Molten Salts - Identification and Elimination of Failure Mechanisms for Improved Devices

## 5.1 Introduction

For sensors to be suitable for use in a molten salt environment they are required to withstand elevated temperatures (around 450°C for the LiCl-KCl eutectic) and be corrosion resistant, as there are many corrosive species present in the melt. These include both oxidising and reducing agents such as redox species and oxygen gas.[56, 73, 163] Significant work has previously been carried out within the research group to develop microelectrode devices for use within a fused salt.[57,87,120–123] These have been microfabricated in-house, and the architecture may be tailored to improve the suitability of them for use in harsh conditions. Brady initially demonstrated the use of these, mainly in acidic aqueous media but also showing the proof of concept for use in a molten salt.[120] These were then further improved by Blair to increase the lifetime to approximately 4.9 hours and yield of devices to about 65%.[123] Although for the lifetime measurements Blair noted

that they were still highly variable between different devices, the error on this average value for his final device design was 6.7 hours (for a small number of devices). It is clearly necessary to improve the lifetime of devices in order to utilise these sensors for more extensive quantitative analysis of reactions in molten salts. This is particularly the case for EIS measurements as each individual measurement at an applied DC potential takes approximately 5 minutes to complete. This chapter will first detail the functionality of the electrodes at the start of this work, and their limitations together with the systematic work undertaken to address these issues. The techniques which have been used within this work to characterise the devices are then discussed before analysing failed microelectrodes with the aim of identifying the failure mechanisms. This was performed by examining both the complete devices and the materials individually. Modifications to improve the architecture of devices to prevent failures were then evaluated, with the aim of developing more reliable devices capable of performing fundamental measurements within the molten salt system. Once this was achieved they were to be utilised to gain fundamental insight into charge transfer kinetics.

## 5.2 Improvement of the microelectrode devices

### 5.2.1 Performance of benchmark microelectrodes at start of this work

The start of this current work is Blair's final device.[123] Figure 5.1 shows the design of the electrodes and this is the device that all subsequent designs were benchmarked against. The microelectrode technology developed comprised of a device with reduced critical area referred to as a super thin track electrode. The electrode shape was improved by changing from the initial microsquare to a microdisc, thus minimising potential points of stress. The architecture used a silicon substrate, a stress relief layer of silicon dioxide (500 nm thick), and a titanium nitride adhesion layer (20 nm thick) below the electrode metal. This metal was either platinum (50 nm thick) or tungsten (200 nm thick). Both adhesion and metal layers were patterned using reactive ion etching to create a very thin track, minimising the critical area where defects could cause device failure. A layer of stoichiometric silicon nitride (500 nm) protected all non active areas with windows patterned to provide access the electrode and the contact pad.

The main factors analysed by Blair for the functionality of devices were the yield and the lifetime.[123] The yield in manufacturing is the fraction of units which function correctly out of those

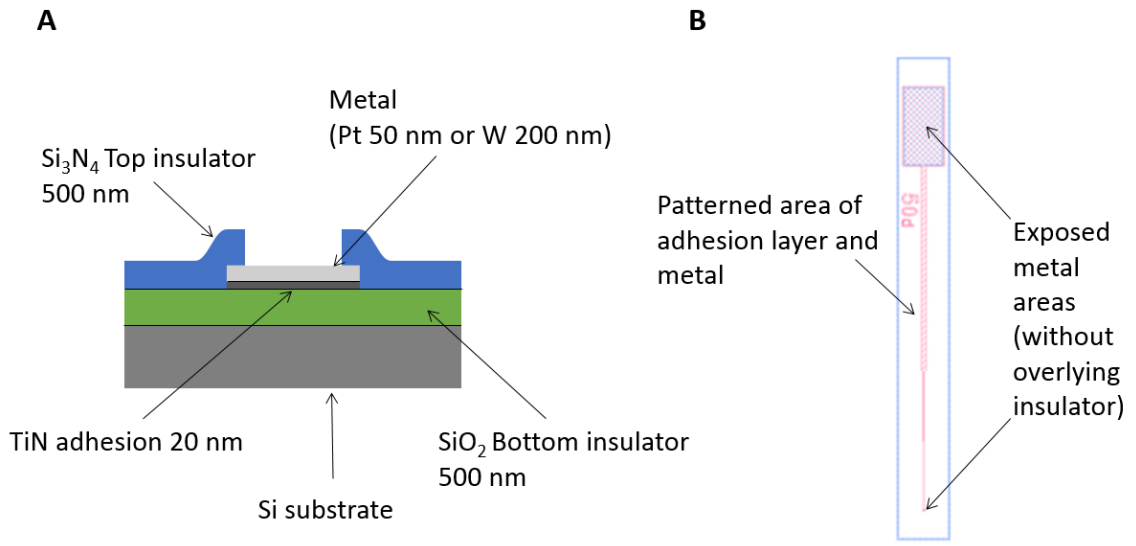


**Figure 5.1:** (A) Cross-section of in-house fabricated microelectrode at the start of this current work. (B) Layout of electrode.

produced.[179,180] In this and previous work on microelectrodes the yield is defined as the number of functioning devices after the microfabrication process.[123] Yield figures are reduced by devices either failing completely or not functioning to the required specification. This is typically due to defects, which may be systematic within the design or random (typically this can be due to particulate contamination).[179] It is interesting that the yield for the microelectrodes was significantly lower when they are used in molten salt instead of aqueous media (where the engineering yield is close to 100 %).[140] For Blair's final design (the super thin track platinum electrode) the yield when used in molten salt was 65 %.[123] The lower yield of functional microelectrodes suggests that the molten salt provides a more challenging environment than aqueous solutions and therefore the consequences of any defects were greater in the molten salt. The definition and test for a functioning electrode used by Blair was adopted by this work in order to provide a meaningful comparison between generations of electrodes. For an electrode to be deemed functional in the molten salt environment, it was required to produce a response that was typical for a microelectrode with a limiting current and a stripping peak (when silver plating and stripping was measured in a potential window between 0 V to -0.5 V), in addition the measured limiting current must be within error of that predicted by $i_{lim} = 4nFDcr$, as discussed in Section . This potential window is smaller and more positive than the window which would be required for sensing species in pyroprocessing. [6,181]

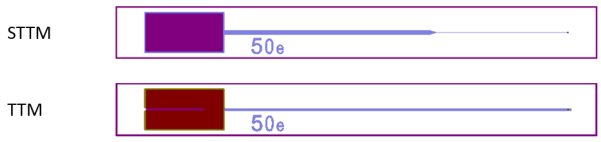


**Figure 5.2:** Schematic of the thin track (TTM) and super thin track (STTM) electrode designs. Taken from [123].

Devices which have "fatal defects" never function properly directly add to the yield figures. Defects that cause a device to fail after a period of time are known as "latent defects", these reduce the longevity of the device. The lifetime of devices is defined as the length of time that the device demonstrates the expected response. For dedicated measurements of lifetime continuous cyclic voltammetry of $Ag^+$ plating and stripping was performed using a concentration of approximately 5 mM to remain consistent with the previous work done within the group on lifetime characterisation.[123] The objective of this work was to establish the defects and causes that lead to failure of devices in order to increase the yield and extend the lifetime. As no wafer level test has been established to identify the defects causing failure in the molten salt this is particularly important, as identification of a faulty electrode was not possible before use in molten salt.[182,183] Only obvious defects such as a poorly defined electrode area due to an issue in lithography could be detected with inspection methods within fabrication. At the end of Blair's work although many devices gave the desired quantitative response there was a large number of microelectrodes which did not function. The causes of failure were not identified and therefore this thesis focused on determining other failure mechanisms and overcoming them to allow reliable measurements.

### 5.2.2 Identification of Connection to Silicon Substrate as a Failure Mechanism

A common feature of the failed benchmark devices was very high currents observed in measurements (in the micro-amp range rather than nano-amps) and a signal which was highly variable.[123] Even at the largest size of microelectrode (100 μm diameter) and with a concentration of $Ag^+$ of 5 mM the maximum expected limiting current would be 250 nA. Measurements in the micro-amp range are at least an order of magnitude larger suggesting a significantly larger electrode area. Blair had already improved the top insulator in the design to use stoichiometric silicon nitride (above the metal of the track) to prevent leakage current and silver plating in this area. In Blair's work the

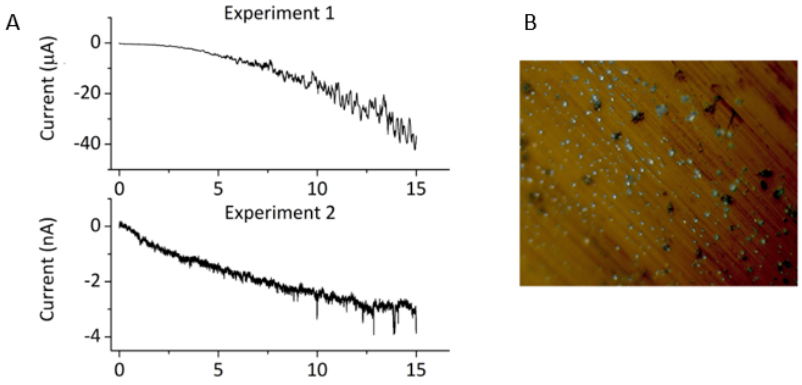


**Figure 5.3:** Blair's results of leakage current (A) for a 4 $mm^2$ test square buried beneath $Si_3N4$ insulator and silver deposits (B) observed after the measurement on the silicon substrate (x100).[123]

area of metal patterned on the device was also reduced in order to limit the critical area where if a defect was located it would result in failure, which led to an improvement in yield.[123] The final benchmark design is referred to as the 'super thin track' (STTM) shown in Figure 5.2 and has a critical area of metal calculated to be 22 $mm^2$ assuming 1 cm immersion into the melt. Within this work it will be compared to another design referred to as the 'thin track' (TTM) which has a larger critical area of metal of 30.8 $mm^2$ at the same immersion depth into the molten salt.

However, even with this improvement a large number of devices (45%) did not function. As metal loss was also a common feature, neither an increase in the exposed metal area or failure of the top insulator could have caused the larger currents observed. One possibility is a connection between the metal to the silicon substrate. At the high temperatures used in the molten salt silicon is conductive due to the thermal excitation of intrinsic charge carriers into the conduction band.[147] Clearly this is not the case in aqueous measurements due to the low temperature of the solutions (around 25°C) as the silicon has a much higher resistance. The exposed silicon around the perimeter (of the region of the chip which is submerged in the melt) would create a significantly larger electroactive area, and could cause the high currents observed. This is also likely to cause variation between experiments, as the positioning of the device is performed manually and relies on monitoring the OCP until a steady and expected value is detected, leading to variation in the immersion depth. Blair investigated whether this was the cause with test structures consisting of buried metal plates which should have no exposed area and thus no measured current would be expected. Instead he found that for many of the devices, tested by holding at a silver plating potential for 15 minutes, a

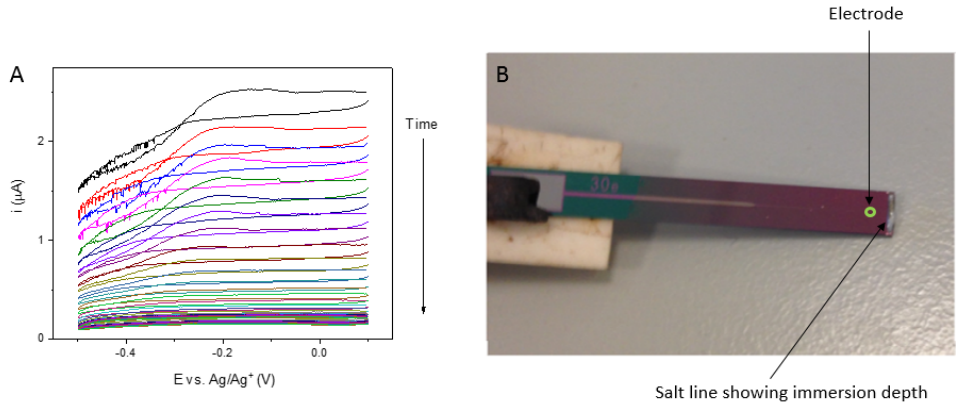


**Figure 5.4:** (A) Electrochemical signal measured with only the very tip of the diced chip immersed into the salt (without the electrode contacting the molten salt). Every tenth scan at a scan rate of 0.2 V/s in LiCl-KCl eutectic with 5 mM AgCl starting at 0.1 V is shown on the graph. (B) shows the optical image of the electrode with the immersion depth indicated by the solidified salt remaining at the bottom of the chip (white material at the end of the chip) and the location of the exposed active electrode highlighted.

large leakage current was observed with significant variation between nominally identical samples. He also observed silver deposits on the perimeter of the silicon substrate and no evidence of silver on the top $Si_3N_4$ insulator.[123] An illustration of his results is shown in Figure 5.3.[123]

This was still under study at the start of this work so further investigations were undertaken to confirm that the silicon was the source of these large currents. Devices were positioned so that there was none of the metal electrode area immersed in the molten salt whilst performing the standard measurement. Figure 5.4 shows an example of the cyclic voltammograms recorded and the appearance of the chip after 15 minutes measurement. These CVs have a very large current (in the micro-amp range), significantly above the 80 nA that would be expected for the 30 μm diameter electrode according to Equation 2.13. There is also evidence of nucleation loops and initially significant plating although this may not all have been stripping on the return sweep. The measured current could not have been from any electrode metal as this was not immersed in the molten salt, instead there must be some connection to the conductive silicon which had a large area in contact with the melt around the perimeter of the chip. It is proposed that there is a failure of the underlying silicon dioxide insulator. The ceramic plate positioned between the crocodile clip and the back side of the device prevents contact at the rear of the chip and it is unlikely that the crocodile clip had pierced through the contact pad on the top and contacted the silicon as this would require piercing the metal, the adhesion layer and the bottom insulator and no damage was apparent for the devices characterised. From these tests to discern the defects causing

| Critical area /mm$^2$ | Top insulator | Bottom insulator | Metal layer |
|---|---|---|---|
| Thin track (TTM) | 1.2 | 20.3 | 9.6 |
| Super thin track (STTM) | 0.1 | 22.1 | 10.8 |

**Table 5.1:** Critical areas of layers in the microelectrode architecture calculated assuming 10 mm immersion into the melt and possible connection to a contact pad length of 2 mm.

microelectrode failure it is clear that there is a connection between the silicon substrate and the adhesion/metal layers, most likely occurring through the underlying $SiO_2$ insulator.

Measured currents vary over time and show large differences between nominally identical devices. Large variability was also observed between devices fabricated from the same wafer where this failure has been observed for some electrodes and others have functioned well, suggesting that these stem from random defects most likely within the silicon dioxide underlying insulator separating the metal and substrate. Particulate contamination leading to random point failures in the oxide layer are thought to be unlikely as the layer was 500 nm thick and thermally grown. Chemical attack or corrosion of the oxide (observed for other oxides) could create conduction pathways, but again this seems unlikely as the metal pattern is centred on the chip and measurements have shown a leakage current very rapidly after immersion into the melt. Another possibility is that $Li^+$ diffusion in the silicon and silicon oxide, which have both been investigated as anode materials for batteries as they can intercalate lithium,[184–186] could be creating conduction pathways. The diffusion coefficient of $Li^+$ in Si has been determined to be on the order $10^{-12}$ cm$^2$ s$^{-1}$.[187] Electrochemical reactions of $SiO_2$ with the electrolyte has been observed to make the film less dense and cause the bonds to become disordered, which would impact the barrier properties of the layer.[188, 189] Connection to the substrate is a major issue as the current would swamp any signal from the microelectrode, and thus cause devices to fail immediately, reducing the yield. Prior examination of the electrodes at room temperature in aqueous experiments does not allow for the identification of devices which have connective pathways to the substrate, as the silicon isn't conductive enough in these low temperature measurements, thus the yield of devices in aqueous experiments is typically $> 99\%$.[123, 182] This complicates testing of fabricated devices as it means practically they must be used in the fused salt to check functionality.

#### 5.2.2.1 Critical areas of electrodes

The measurement of a large current with no patterned metal area immersed in the molten salt (Figure 5.4)also demonstrates an important point; that the critical area for the different layers in the architecture varies depending on their function. The critical areas for the different layers are presented in Table 5.1. For failure of the underlying bottom insulator the critical area is the total area of the patterned metal, as any failure in this region leading to connection between the layers would cause total failure of the device. Defects in the top insulator would only lead to electrode failure if they are located above the patterned metal area which is immersed in the melt, and thus cause a change in electroactive area. The metal layer is critical for the electrical connection along the length of the chip (value presented in Table 5.1) and for a precise electrode area. Although the design was changed from thin track to super thin track to reduce the area of metal immersed in the melt, this actually slightly increased the total area of metal on the entire device.

### 5.2.3 Elimination of connection to silicon substrate

It was important to eliminate or significantly address this failure mechanism as it reduces the yield of functional devices. Two methods were considered feasible solutions by either; using a non-conductive substrate in place of the silicon, or improving the bottom insulator layer in the structure. Both were evaluated to see if they could be successfully employed.

### 5.2.4 Feasibility of using a non-conductive substrate

Assuming the electrical conduction of silicon is the problem the most obvious change to eliminate the issue would be to use a non-conductive substrate. Although this appears to be an ideal solution, there are several potential issues. The list of suitable substrates is quite limited as the majority of semiconductor fabrication is based on silicon,[190] and any alternative needs to be resilient to the harsh environment of the molten salt. A change of materials could also require the complete development of a new fabrication procedure. A problem Blair encountered with previous designs was delamination due to stress,[123] so stress must be carefully considered for any adjustment in design. Typically this occurs for thin films when the deposited film expands or contracts relative to the substrate. The two types of stress that can occur are: compressive when the film is held under compression or tensile when the film is held in tension relative to the substrate which it is

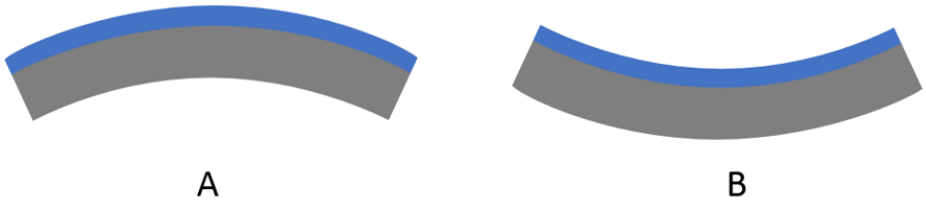


**Figure 5.5:** Cross-section through a wafer which is under compressive stress (A) and tensile stress (B).

fixed to.[191, 192] Both of these cause characteristic wafer bows which are illustrated in Figure 5.5. One of the most commonly encountered causes of stress is due to changes in temperature.[193] This arises when films, which have differing coefficients of thermal expansion, are heated and expand or cooled and contract different amounts.

Significant work had gone into balancing the stress in the benchmark electrode when used at the elevated temperatures.[123] The thermal expansion of the silicon substrate and silicon based insulating layers are similar and are commonly used at the SMC which means fabrication hurdles can be avoided. Potential materials for an insulating substrate include: quartz, diamond and sapphire. All of these are significantly more expensive than silicon.[194] Table 5.2 shows the thermal expansion coefficients of different materials that could be used (as substrates, metals and insulating layers) to fabricate micro and nano-electrodes. A likely candidate could be diamond, as the thermal expansion coefficient is much more similar to the insulators used in the current structure (silicon oxide and silicon nitride). There is precedence for using diamond in a molten salt however, diamond wafers are very expensive.[195] Another issue is diamond is not commonly used in-house, so the process flow would likely need redevelopment and there are several potential hurdles (including the possibility that the diamond could oxidise at high temperatures similar to the furnace loading temperatures).[196] Both sapphire and quartz would be likely to be suitable as a substrate material as the materials have been seen to be resilient in the molten salt environment. Aluminium oxide has been used for reference electrode sheaths, so it is likely that sapphire would be resilient.[132] Quartz is already used in-house for the cell containing the melt for its resilience. Both aluminium nitride and boron nitride have very similar thermal expansion coefficients so may provide viable microelectrode devices with sapphire. Unfortunately it is not possible to deposit either of these insulators in house so these insulators were not examined in this work. An initial feasibility trial was

performed using quartz wafers which had demonstrable corrosion resistance in molten salt and a coefficient of thermal expansion which was more similar to the silicon based insulating layers than sapphire. Quartz wafers were also cheaper than the alternative insulating substrates and easily available.[197]

| Function | Material | Thermal expansion coefficient at 20°C ($10^{-6}$/K) |
|---|---|---|
| Substrate | Silicon | 2.4 |
| | Quartz | 0.5 |
| | Diamond | 1.0 |
| | Sapphire | 6.7 |
| Insulator | $Si_3N_4$ | 3.2 |
| | $SiO_2$ | 0.6 |
| | Aluminium nitride | 4.5 |
| | Boron nitride | 8 |
| Adhesion layer | Titanium nitride | 9.4 |
| Metal | Platinum | 8.8 |
| | Tungsten | 4.5 |

**Table 5.2:** Thermal expansion coefficients of materials used in microelectrode devices and various possible other materials for use in future designs. Values from [198–201].

The feasibility study on quartz wafers used tungsten as the electrode metal, because it is commonly used in molten salt measurements,[123, 202, 203] The electrodes on the quartz substrates were fabricated following the standard procedure detailed in Section 3.3. The standard $CF_4$/Ar dry etch was used to pattern the tungsten and the TiN adhesion layer (38 minutes). The deposition of the adhesion layer and metal presented no difficulties and the wafers passed visual inspection under the microscope. The increased fragility of the quartz wafer compared to silicon was noted and created challenges, with one wafer shattering during processing. Fabrication was continued with the other tungsten coated metal wafer and stoichiometric silicon nitride was deposited onto this following the standard procedure. After removal from the nitride furnace the wafer appeared satisfactory at macro-scale. However, after cooling the nitride layer was observed to have cracked, as can be seen in Figure 5.6. The channeling cracks which were observed are consistent with a film under tension, as has been previously measured for stoichiometric silicon nitride deposited at the SMC.[123, 192, 193, 204, 205] Some loss of adhesion was also noted which was most likely due to the generation of shear stresses along the interface of the cracks.[206] The electrode area was not well defined as can be seen in the zoomed in image of the patterned metal area in Figure 5.6. Although more visually apparent on some metal areas, cracking was apparent across both the metal regions and the quartz wafer. The metal layer itself showed no evidence of cracking despite differences

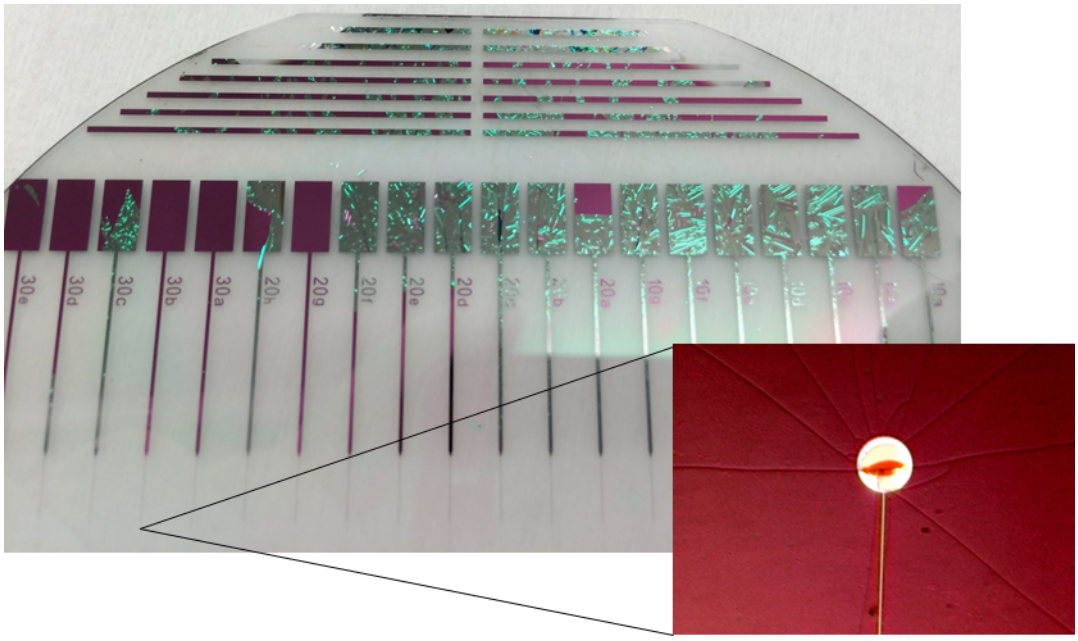


**Figure 5.6:** Insulation layer of stoichiometric silicon nitride layer on quartz wafer patterned with tungsten showing evident damage, cracking and delamination across wafer. Inset shows a 500x zoomed image across an electrode which appeared to have a uniform covering when visually examined but is also clearly cracked upon closer inspection.

in thermal expansion coefficients between the tungsten and both the adhesion layer and quartz wafer. Tungsten electrodes were previously fabricated on silicon wafers without the problem of stoichiometric silicon nitride cracking, so it is unlikely that this stress would be the sole cause of the cracks.[123] It is more likely that differences in the thermal expansion coefficients between the quartz wafer and the silicon nitride, as the much thicker substrate sets the stress.[193]

It may be possible to achieve a uniform film of stoichiometric silicon nitride on a quartz substrate by adjusting temperature and pressure settings in the furnace used for deposition. However, this might not solve the issue as the thermal expansion of silicon nitride is more than double that of the quartz. Different substrate materials with better matched thermal expansion coefficients could be an avenue of potential future research. This could be worth further research, however, it is highly probable that optimising fabrication procedures would be very time consuming, with the possibility of further problems being encountered with differences in thermal expansion coefficient, stress and other possible material damage in the molten salt. The current device fabrication procedure and architecture had taken significant work previously both with materials and device architecture to develop microelectrodes suitable for quantitative measurements.[120, 123]

### 5.2.5 Improving the underlying insulator

As a cause of microelectrode failure was established to be connection to the silicon substrate through the $SiO_2$ bottom insulator, it was found not to be performing well as an insulator under these harsh conditions. The feasibility of improving the bottom insulator with the inclusion of a thin layer of silicon nitride was evaluated. Silicon nitride is known to produce a denser film, is a good barrier to lithium ions and LPCVD stoichiometric silicon nitride had been shown to be a chemically resistant barrier to the LiCl-KCl eutectic.[207] It was undesirable to completely remove the oxide layer, as it is known to be an effective stress relief layer and the work with quartz highlighted the importance of stress in the design of the electrodes.[123] Stoichiometric silicon nitride is known to have tensile stress.[208–210] Thermally grown silicon oxide typically has the opposite compressive stress and is used in microelectronics and MEMS devices as a stress relief layer, as incorporating it results in a reduced net stress in the device architecture.[155, 211] This is a common method used to control stress in thin film stacks.[212]Previous work by Blair switched the lower insulator to thermally grown silicon dioxide, as a stress relief layer for the top silicon nitride layer.[123]

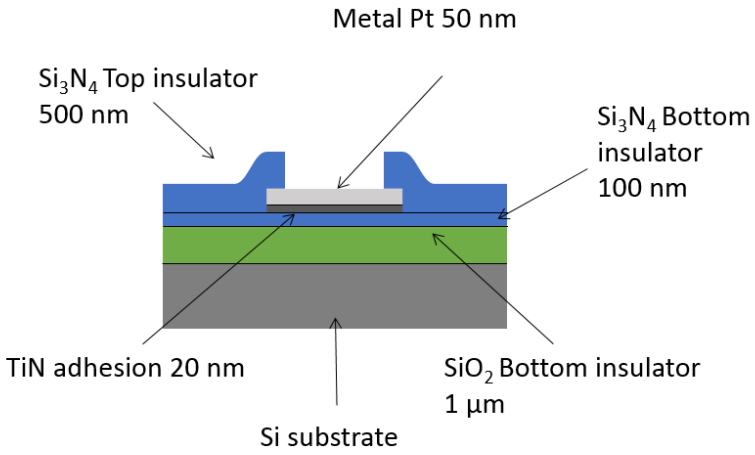


**Figure 5.7:** Schematic of the new device architecture including an additional layer of stoichiometric silicon nitride beneath the metal.

Figure 5.7 shows the layer structure evaluated with an enhanced bottom insulator. As the top insulator was functioning adequately for insulation, it was decided not to change the thickness of this layer. An additional 100 nm thick stoichiometric silicon nitride layer was included beneath the

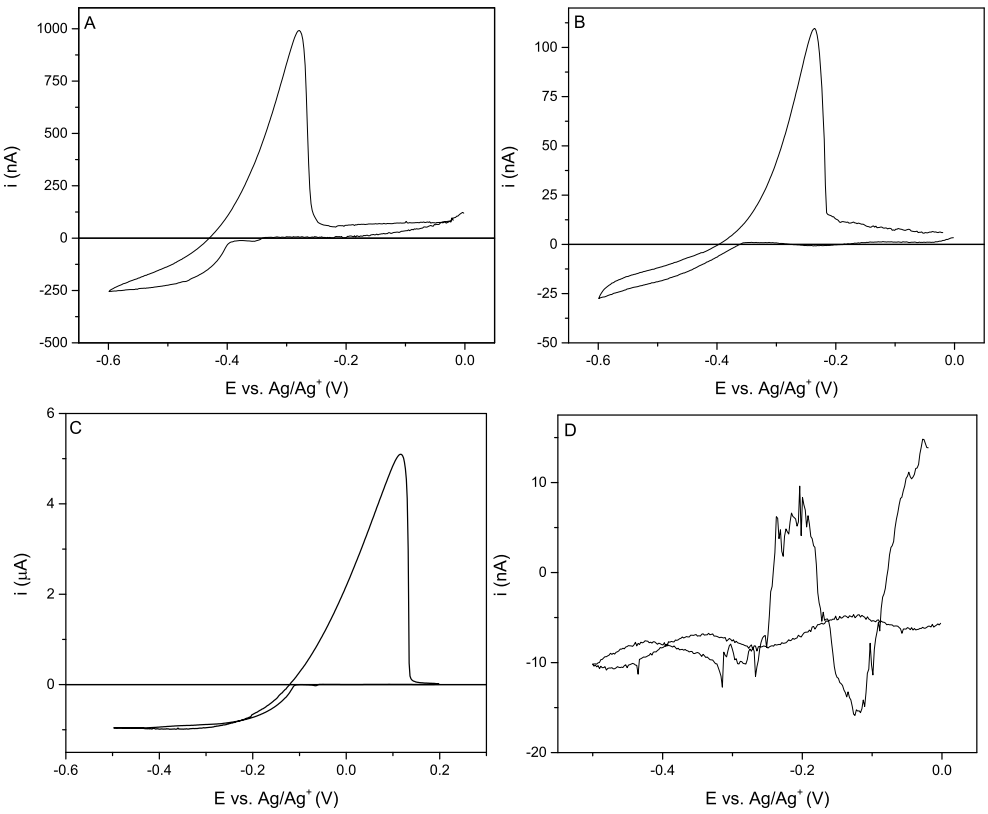


**Figure 5.8:** Typical CVs of disc microelectrodes fabricated with silicon nitride underlying insulator in LiCl-KCl with 5 mM AgCl at 450°C and a scan rate of 100 $mVs^{-1}$. (A) Shows the response for a 100 μm diameter electrode, (B) a 10 μm diameter electrode (C) is a different 100 μm diameter electrode and (D) a 30 μm diameter electrode which was deemed non-functional.

metal. To compensate for the additional tensile stress from the extra $Si_3N_4$ layer, the thickness of the oxide was increased to 1 μm.

The improved bottom insulator was evaluated by measuring the current for a buried plate of metal beneath the top insulator at a voltage where silver plating should occur, and by measuring silver plating and stripping in LiCl-KCl eutectic for fabricated microelectrodes. Figure 5.8 shows the typical response seen for microelectrodes with the improved bottom insulator. Most electrodes functioned (77 %) and gave limiting currents very close to those expected for the size of active electrode, calculated using Equation eq: micro current ($i_l = 4nFcDr$) and a literature diffusion coefficient of silver at this temperature of D = 2.44 x $10^{-5}$ $cm^2s^{-1}$.[57] The comparison of the measured currents and those recorded experimentally are presented in Table 5.3.

There was little evidence of the traits considered to be associated with electrical connection to the underlying silicon, such as silver deposits on the side of the silicon chips and higher magnitude

| Microelectrode diameter / μm | Graph | Expected $i_{lim}$ / nA | Measured $i_{lim}$ / nA |
|---|---|---|---|
| 100 | A | 259.06 | 248.5 ± 3.2 |
| 10 | B | 25.91 | 24.10 ±1.8 |
| 100 | C | 259.06 | 957.8 ±0.6 |
| 30 | D | 77.72 | No limiting current |

**Table 5.3:** Table showing comparison of expected and measured limiting currents using the microelectrodes used in Figure 5.8.

of measured currents.[123] When electrodes failed to produce a typical microelectrode response very low currents were recorded, such as in Figure 5.8 D. This is more indicative of a different issue: a poor connection rather than the large currents observed when connection to the silicon substrate was encountered.[123] One issue encountered was the reference electrode breaking during the measurement, as was the case for the CV in Figure 5.8 C, where the device produced a response that was characteristic of a microelectrode but with a current far larger than the 259 nA expected. Upon removal of the device it was discovered that the reference electrode sheath had broken exposing both LiCl-KCl eutectic with a higher concentration of AgCl added (1 wt % in 1 g) and the silver wire. The silver wire was then acting as a quasi-reference electrode. There is a shift observable in the onset of the plating potential which would be affected by the shift in equilibrium at the reference and also the change in concentration of $Ag^+$ in the solution. The increase in concentration of $Ag^+$ in the solution expected with the mullite sheath breaking equates to 14.2 mM, which is roughly three times the initial value. From the measured limiting current the current was approximately four times the expected value correlating with an $Ag^+$concentration of 19.9 ± 0.3 mM, which is a similar order of magnitude to that expected but could indicate a slight possibility of a marginally higher local concentration and not effective mixing. The improvements in the set-up implemented to reduce the breakage of reference electrodes are discussed in Section 3.4

A comparison of the yield figures for these designs with the improved STTM is shown in Table 5.4.

| Layout and architecture | Total yield / % | Number tested |
|---|---|---|
| Thin track | 60 | 41 |
| Super thin track | 65 | 40 |
| Super thin track with improved bottom insulator | 77 | 26 |

**Table 5.4:** Comparison of yield figures for benchmark electrodes in comparison with new design of improved bottom insulator. Yield figures for thin track and super thin track are taken from [123].

Care should be taken in comparing these figures as these statistics are from many different users

and therefore the yields are difficult to directly compare due to the influence of variables such as the redox couple/concentration and size of the device not being controlled in yield figures. Also it should be noted that for the improved insulator the yield figure is for fewer devices examined. However, it is promising that a significantly greater number of devices characterised function well enough to show the expected microelectrode response, 77%, compared to previous batches of electrodes where the yield was between 40-65% for different architectures.[123,213] A larger improvement in yield was observed for the implementation of an extra $Si_3N_4$ bottom insulator (in this work) compared with a reduction in the area of metal on a chip (in Blair's work). Additionally the signatures thought to be due to connecting to the silicon substrate, such as significantly larger currents and high capacitance, were not observable for the CV response of any devices characterised with the improved bottom insulator. Both of these indicate that the inclusion of an additional insulating layer of silicon nitride beneath the metal alleviates the issue of conduction paths through the oxide layer. The electrodes still showed a much higher failure rate in the molten salt than for aqueous characterisation. However, the yield of devices was characterised prior to the improvements implemented for connection to the microfabricated electrodes discussed in Section 3.14. It is likely that some of the failed devices may have suffered from poor connection which would be consistent with the low current measured and the sinusoidal noise evident in Figure 5.8, leading to a reduced yield being recorded. This was consistent with the set-up Blair used so the connection should not have impacted a comparison of the yield figures.

The improvement in shorting defects to the silicon substrate was also confirmed by the measurement of buried test squares (a metal plate underneath the top insulator) which yielded no current observed in chronoamperometry at -0.5 V for the three test structures incorporating an underlying nitride layer. There was some noise and variance in the current measured on the buried test square, however, this was in the nano-amp range and should be negligible for measurements on devices. This is an improvement on the large currents observed for the measurement of a range of buried test squares for the original architecture at the start of this work.[123,213] For all of the electrodes characterised there was no evidence of delamination within the insulating layers, therefore the additional layer of stoichiometric silicon nitride in the bottom insulator is a positive improvement to the architecture of micro- and nanoelectrodes. After this study the design improvement of an additional insulating layer was incorporated into all electrodes microfabricated for molten salt use.

## 5.3 Lifetime of devices with improved underlying insulator

The operational lifetime over which electrodes perform to specification is another important aspect of device functionality, that requires optimisation both for measurement (to gain time varying insight into the processes occurring at electrodes), and for the design of sensors for use in an online monitoring process. The definition to assess the functionality of an electrode and determine a lifetime was, again, the same as the one used by Blair to enable comparisons to be drawn.[123]. This was that the current response was typical and agreement with the theoretical limiting current for the silver plating and stripping reaction.

The lifetime of these improved devices is shown in Figure 5.9 and were found to be highly variable. The majority of electrodes showed a response which was typical for a microelectrode with a lifetime between 1 to 2 hours. However, a small number of electrodes functioned for significantly shorter time periods; of the order of minutes. Often a noisy signal was evident on the plating current

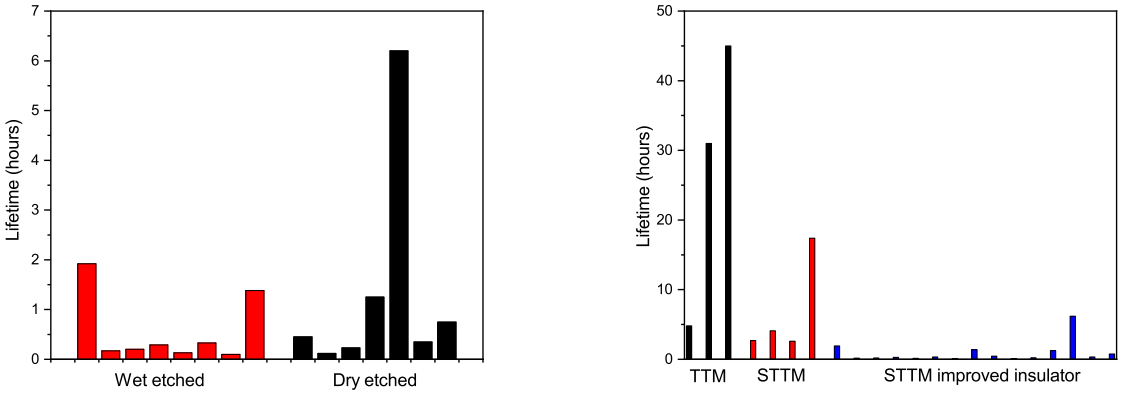


**Figure 5.9:** Lifetime of platinum microelectrodes characterised in this work (left). Comparison with the thin track (TTM) and super thin track (STTM) versions in Blair's work for the improved STTM produced in this work.[123]

after several scans, suggestive of dendrite formation. The limiting current would also typically increase. There was no clear difference between the fabrication methods employed for patterning the metal layer, with a high variability between all microelectrodes. The average lifetime was 0.9 $\pm$ 0.7 hours, which was shorter than some of the benchmark devices (one of which functioned for over 50 hours).[123] However, statistically relevant comparison is challenging as clearly there is a large variation in lifetimes of all the electrodes, and only a few lifetime values characterised for

the benchmark devices. It appears that the median values were similar across different devices with some exceptions which survived longer time periods. The reason for the decreased average lifetime is unclear, but a contributing factor may be the determination of when a limiting current is no longer observed as although efforts were made to be consistent the interpretation of when a limiting current failed to be established could be different. It is also possible that the stress has been increased by the inclusion of the additional silicon nitride layer. This was not apparent in the same fracturing of devices as seen in those fabricated with too much nitride for the top insulation layer, Figure 5.10 for inspection of the failed devices. Interestingly the larger area of metal pattern appeared to give rise to some electrodes demonstrating longer operational lifetimes in the melt. For this reason and the track resistance discussed in Section 5.5.5 a return was made to the thin track metal pattern.

## 5.4 Stress in new architecture and the importance of silicon nitride thickness

The silicon oxide layer thickness was increased in the improved architecture (Figure 5.7) to compensate for the additional stress from the 100 nm layer of stoichiometric silicon nitride. This was evaluated to be adequate, except for when electrodes were produced with a slight increase in nominal top insulator thickness. When this deviated slightly from the target value of 500 nm due to a slight difference in deposition rate, resulting in the top layer of stoichiometric silicon nitride being measured as 551.5 ± 6.4 nm (using reflectometry) all electrodes characterised showed evidence of cracking, as shown in Figure 5.10. This was also apparent through larger currents than expected in the electrochemical measurements, which was evidently due to larger areas of exposed metal when the insulator cracked.

The electrodes fabricated with the underlying nitride are thus suspected to be very close to the upper limit for stress. In the current microelectrode architecture the 1 μm $SiO_2$ layer is providing just enough stress relief for 100 nm layer of underlying and 500 nm of top $Si_3N_4$. It is critical that this silicon nitride thickness is not exceeded otherwise the devices will fail in the MS environment. This was confirmed by a wafer fabricated in the same batch undergoing an additional dry etch process prior to patterning and opening up windows in the insulator for the electrode and contact pad. This thinning of the top insulator by approximately 52.7 ± 2.9 nm (measured with reflectometry) was

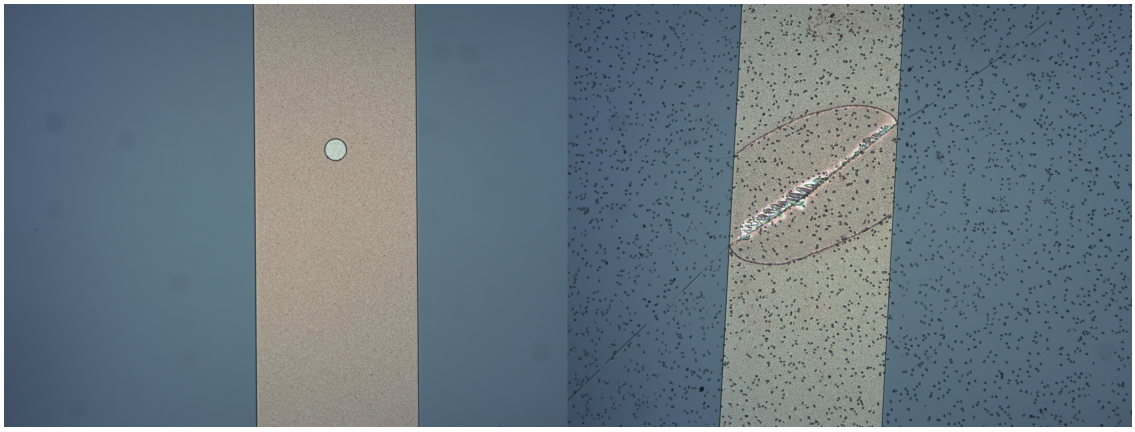

**Figure 5.10:** Optical image of the electrode and track after fabrication and before immersion into the melt (left) and cracking evident of the top insulating silicon nitride layer after immersion in LiCl-KCl eutectic (right), alongside salt remains which appear as black specks in the image.

adequate to prevent cracking in the MS. Subsequently all silicon nitride depositions were performed to give slightly less than the 500 nm and thus prevent this issue occurring. It was undesirable to make the top $Si_3N_4$ insulator much thinner as it was still required to isolate the metal from the salt.

## 5.5 Analysis of device failure for electrodes with improved bottom insulator

### 5.5.1 Electrochemical signature of microelectrode failure and analysis after removal

During the measurement of silver plating it was often observed that there were transient spikes in the limiting current and it had an increased average value, which is exemplified by the pink line in Figure 5.11. This response is an example of the electrochemical signature of the microelectrode failing in the molten salt and is identical to the failure Blair observed during measurements.[123] The charge passed in the stripping peak was also seen to decrease when the spikes in current were observed. As the plating current was also observed to increase this indicates that there may be detachment of silver from the microelectrode surface.

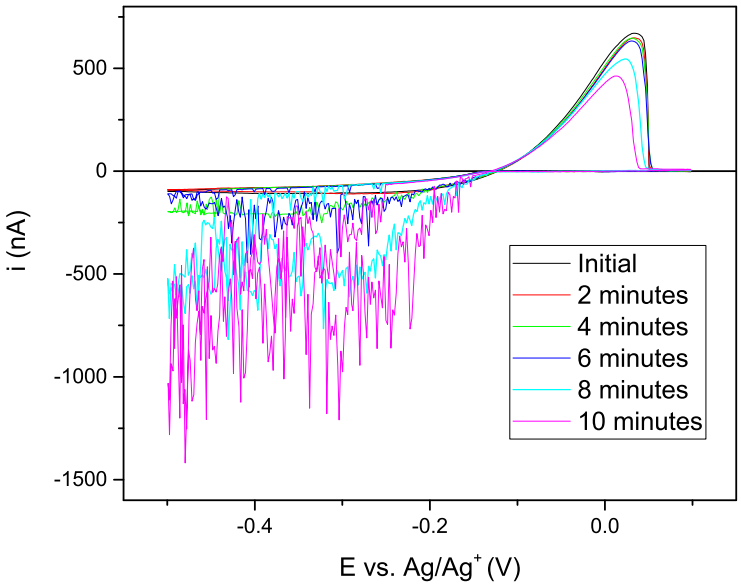


**Figure 5.11:** CV of 10 µm microelectrode scanned at 100 $mVs^{-1}$ in LiCl-KCl containing 5 mM AgCl, showing change in limiting current signal over time.

The microelectrodes were optically examined after use and removal from the molten salt. Signs of failure in the devices were manifold. A change of colour was often observed in the nitride covered area, both the areas with underlying metal and those without. This would appear to indicate that the nitride has been changed by exposure to the molten salt, possibly by thinning of the layer by chemical attack or due to thermal effects. Thinning could not be directly measured due to the structure of the devices. The reflectometry measurement used to measure the thickness of silicon nitride layer was not capable of providing a reliable measurement due to the optical similarity of the underlying silicon oxide layer. A common feature observed on platinum microelectrodes after removal from the LiCl-KCl eutectic was that areas of metal were missing. This typically appeared to begin with small sub-micron regions that with time merged into larger areas. An example of this is shown in Figure 5.12 for an electrode which was tested in LiCl-KCl with silver plating and stripping. The platinum appears to have developed a large number of holes in the layer and also looks to have been undercut. This electrode also demonstrates some other damage; including a crack emanating from the electrode and also a hole in the top insulator (most evident in Figure 5.12 of the SEM image of the electrode after use), along with large amounts of salt ingrained into the top insulator. Cracks and holes in the insulator were unusual when electrodes were inspected after use, however, metal loss was apparent in most of the devices utilised in molten salt measurements. All of these would contribute to a change in the active electrode area of the device, most likely

an increase of exposed metal which would be consistent with the increased current. Any change in active area would interfere with measurements of fundamental processes at an electrode in the molten salt. As the metal loss was observable after many yield and lifetime evaluations it was decided that it warranted investigation to eradicate this failure mechanism.

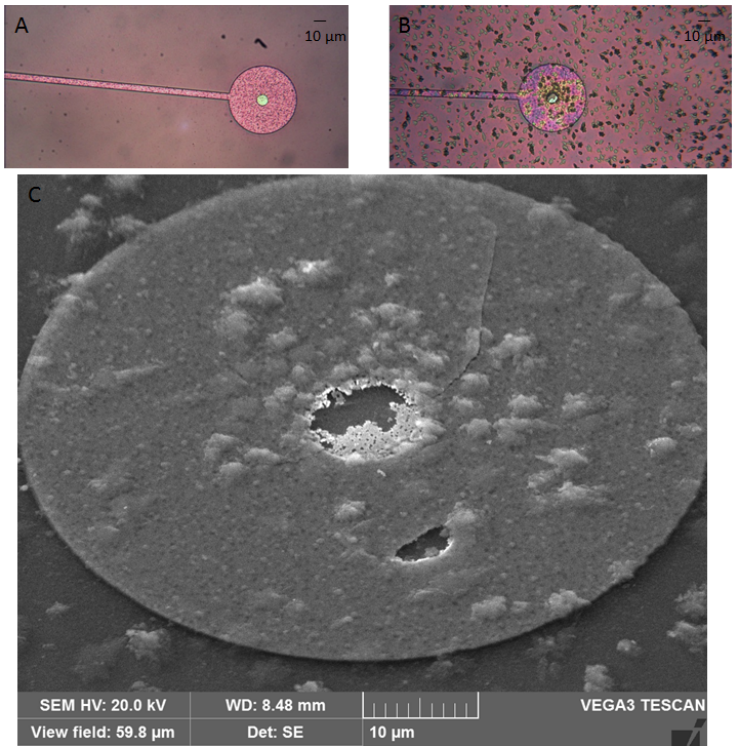


**Figure 5.12:** Optical image of a platinum microelectrode before (top left) and after (top right) being immersed in LiCl-KCl and silver plating and stripping for 12 minutes. The SEM of the same electrode (bottom) from which EDX measurements were taken, showing damage including metal loss and cracking.

The EDX (energy dispersive x-ray) analysis showed an absence of both the platinum metal and titanium making it likely that the adhesion layer of titanium nitride had also been lost from the surface of the microelectrode. This was confirmed by AFM measurements of electrodes after failure, showing a height difference of around 70 nm between the top insulator and regions where metal was lost which corresponds to the thickness of both the metal and the adhesion layer.

### 5.5.2 Investigation into the cause of metal loss

Both micro- and nano- (Section 7.1.3) platinum electrodes were observed to suffer from metal loss during lifetime measurements involving silver plating and stripping on the surface of the

electrode. As this changed the surface area of the electrode, and thus the electroactive area, this makes the sensors unsuitable for use in a quantitative monitoring system, and casts doubt on any fundamental measurements performed to further understand the processes occurring at the metal electrodes. Thus it was necessary to reduce and ideally eliminate this failure mechanism, which required understanding what factors were causing this observed metal loss. Two possibilities were chemical loss due to the salt environment or, alternatively, harsh mechanical treatment of the electrode with the plating and subsequent stripping of silver.

An analogue to platinum stripping was the stripping of aluminium which has previously been found to occur if aluminium were immersed in molten LiCl-KCl eutectic. Both platinum and aluminium can be electrochemically stripped inside the electrochemical window of the LiCl-KCl eutectic. This suggests that chemical species could be a possible cause of the metal loss. Aluminium can be stripped at a much lower potential (around -1.2 V) and it was found that aluminium loss could be prevented by holding at a more negative potential (where aluminium plating should occur).[162] Several experiments were performed to observe if the same would be true in this case - if holding the electrodes at a potential of -0.2 V between scans would prevent the metal loss observed. This value was selected for silver plating measurements as it was above the potential where silver should plate but more negative than the potential where the platinum would strip. The holding potential was around 1.2 V lower than the platinum stripping potential ( platinum is known to strip at a positive potential around 1 V vs. $Ag^+$),[123, 214] so even with any variance in the reference electrode potential, the working electrode would always be at a platinum plating potential.

To determine if metal loss was caused by the silver stripping electrodes were also tested in LiCl-KCl eutectic with a soluble-soluble redox couple performing measurements, and solely with immersion into LiCl-KCl eutectic. Microelectrodes were used for this investigation as it was easier to image the electrode surface and the conditions were imposed for a period of one hour. Figure 5.5 shows typical examples of the optical results. Although the different electrodes tested appear very different colours this can be caused by a small variation in thickness of the layers of the device so should not be over-interpreted. Care was taken to ensure that microscope settings were identical for the images taken of the initial and final appearance of the electrode so a comparison could be made between them.

Metal loss was apparent across the devices immersed in the salt, to varying extents. The only condition where metal loss was not observed was heating the electrode to 450°C with no salt present.

| Test performed | Initial appearance | Appearance after test |
|---|---|---|
| Measured Eu in LiCl-KCl $EuCl_3$ | 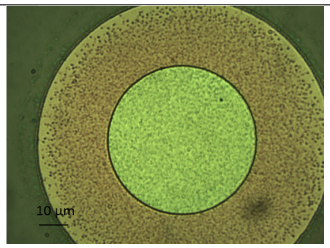  | 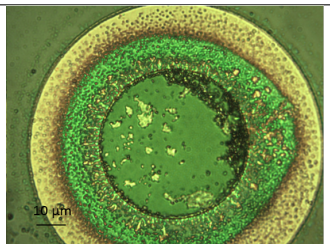  |
| Held at -0.2 V in LiCl-KCl | 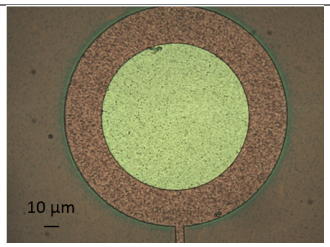  | 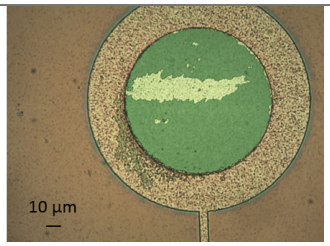  |
| Immersed in LiCl-KCl | 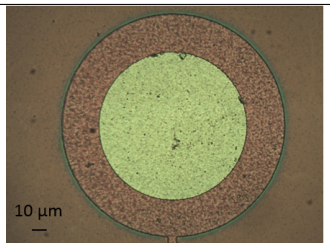  | 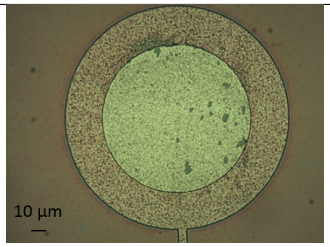  |
| Heated to 450°C not in molten salt | 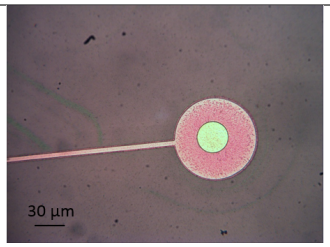  | 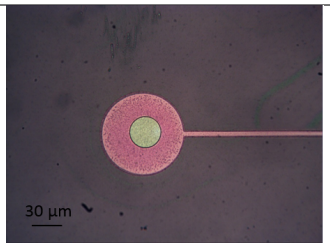  |

**Table 5.5:** Optical images of electrodes before (left) and after (right) different molten salt conditions to elucidate the cause of metal loss observed.

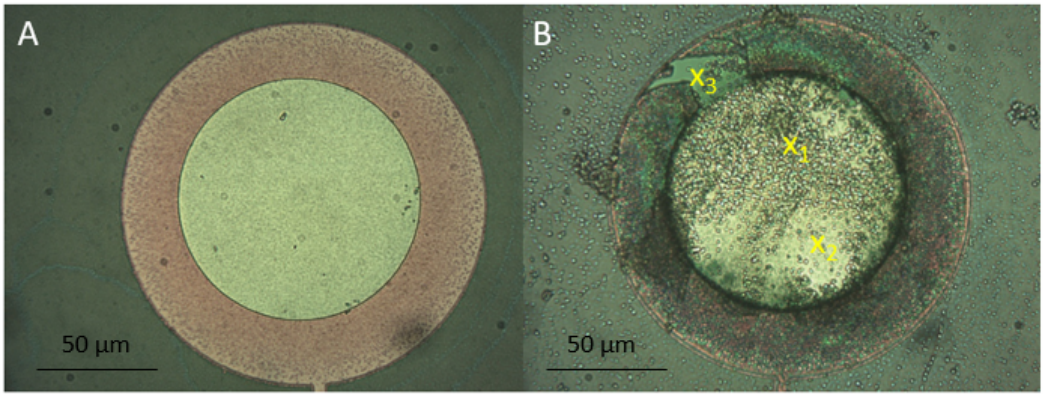


**Figure 5.13:** Optical image of a 100 µm diameter platinum microelectrode before (A) and after (B) cycling for 30 minutes in melt containing 52 mM $EuCl_3$ .

Although it was suspected that the elevated temperature was not causing the metal loss (as during fabrication the metal is heated to 800°C for the deposition of the silicon nitride), this confirms that the metal loss is due to the interaction with the molten salt. The most damage was observed for the electrode cycled around the europium redox reaction, with likely metal loss extending from the electrode to underneath the insulator. The electrode immersed in the eutectic showed small regions of metal loss (the green regions on the electrode) which are not present on the initial image. It was found that holding at a platinum plating potential didn't prevent the metal loss occurring on the platinum electrode, in a similar manner as that achieved for aluminium electrodes.[162] There was a high degree of variability between different electrodes tested and there was no indication of correlation with applied potential. This indicates that although the process might be assisted by electrochemistry, the mechanism behind this is likely to be physical in origin. It is challenging to know when this damage occurred as imaging of the microelectrode necessitated freezing of the salt on the surface of the chip and then rinsing with deionised water. As the rapid freezing is a particularly harsh process for the device it could be contributing to the metal loss observed. However, the optical visualisation of metal loss coupled with the spiky limiting current indicates that there is likely to be some surface change during the measurement itself. This characteristic metal loss was observed in the absence of redox species in the molten salt, and was seen to occur irrespective of whether electrochemistry was performed using the microelectrodes. Metal loss was also evident on tungsten electrodes in other molten salt work.[123]

The electrodes were investigated after failure by inspecting visually and also using SEM to analyse damaged areas. Figure 5.13 shows a comparison of the visual appearance of an electrode before use

| Position | 1 | 2 | 3 |
|---|---|---|---|
| Si | 71.6 | 74.3 | 66.8 |
| O | 14.5 | 14.9 | 27.2 |
| Pt | 6.7 | 4.9 | 0.0 |
| Ti | 0.6 | 0.6 | 0.0 |
| N | 0.5 | 1.9 | 5.9 |
| Eu | 1.7 | 0.6 | 0.0 |
| Cl | 0.1 | 4.4 | 3.5 |

**Table 5.6:** Normalised atomic percentages from EDX measurement at various positions of the used platinum microelectrode (Figure 5.13).

and after measurement in a melt containing $EuCl_3$. The proportions of elements detected by EDX measurement of the electrode after use are summarised in Table 5.6 for the positions indicated in Figure 5.13. The area showing delamination was found to contain no measurable Ti or Pt, (nitrogen is still observed as the underlying insulator is $Si_3N_4$). Clearly both the adhesion layer and the platinum metal have been lost in areas that appear green in the visual image. There is also evidence of Eu remaining on the electrode metal, as expected on drying. Similarly for the platinum electrodes EDX measurements did not detect platinum or titanium on regions where suspected metal loss had occurred on the active area of the electrode.

### 5.5.3 Investigating the materials used in microfabricated electrodes

As metal loss was observed across a range of different salts and could not be prevented by applying a plating potential to the devices. A thorough investigation was performed on the materials used for each of the layers in the microfabricated electrodes stack as failure of any layer could cause metal loss.

#### 5.5.3.1 Electrode metals

Metal loss was observed when the sample was immersed in the fused salt and even when not subjected to electrochemical reactions at the metal interface. This suggests that the mechanism for the metal loss observed is mechanical or physical in nature and not chemical, particularly as it was seen to occur for different metals [123]. To confirm that this was the case the durability of the electrode metals in LiCl-KCl melt was investigated. This necessitated the use of bulk materials to avoid the requirement of an adhesion layer to attach the metal to a dielectric, ensuring that this couldn't be a cause of failure. Materials considered for use as the metal layer in the electrode

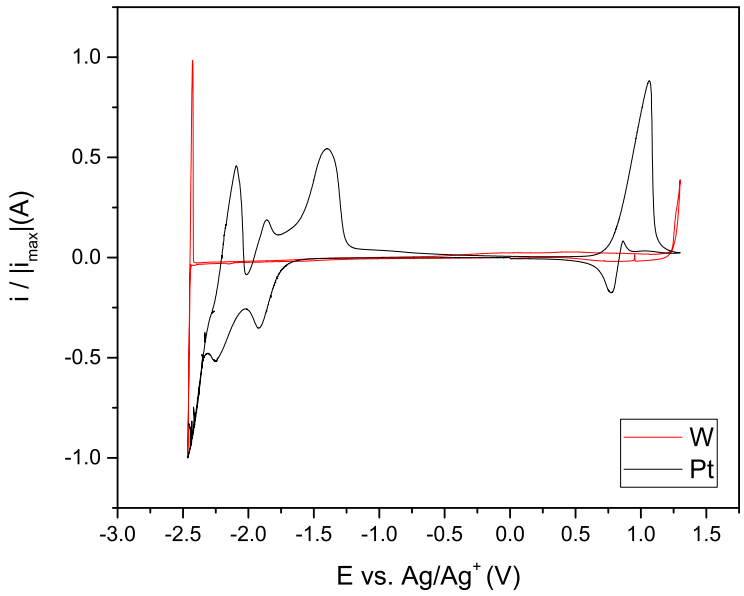


**Figure 5.14:** CV response for a macroelectrode of tungsten and platinum at 0.2 V/s in dry LiCl-KCl. The current has been normalised to the lithium plating peak.

architecture were evaluated including: platinum, tungsten, molybdenum and tantalum. Testing the bulk materials was achieved by immersing wires of each metal simultaneously into clean LiCl-KCl for 300 hours. No electrochemistry was performed and the temperature was maintained at 450°C throughout the experiment with the wires immersed and withdrawn whilst the salt was molten. The mass of the wires were compared but there was no observable change for any of the metals. The frozen salt was analysed by ICP-MS to determine if the metals were present in the melt. There were trace amounts of some metals present in the salt, however, the amounts were very low. Considering the long length of immersion and negligible amounts detected, it is unlikely that chemical removal is the cause of platinum loss from microelectrodes where metal loss was observed to occur within minutes for multiple devices. Although bulk metals are likely to behave differently from a thin film of the material, it would be expected that chemical corrosion would be similar for films and the bulk material.

The electrochemical response for each metal was also recorded within the solvent window of a clean LiCl-KCl salt. The comparison is shown in Figure 5.14, the current was normalised to the lithium plating peak potential for easier comparison as the current magnitude was significantly larger for the CV employing platinum as the WE.

As can be seen in Figure 5.14 tungsten shows the expected response of lithium plating and stripping

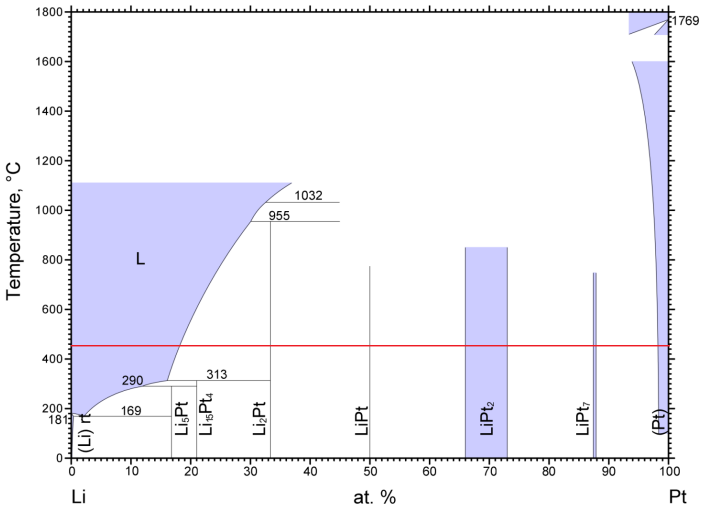


**Figure 5.15:** Phase diagram for platinum-lithium adapted from ASM.[215]

at the negative end, and chlorine evolution at the positive end of the solvent window. This is unsurprising as tungsten is a refractory metal and W rods are employed as the standard working and counter electrodes within molten salt research within the group and have extensively been used in literature. [57] For the response recorded on the platinum wire there are several peaks within the expected solvent window. At negative potentials these are likely to be due to the platinum alloying with lithium. From the phase diagram shown in Figure 5.15 it is clear that at 450°C there are numerous platinum- lithium alloys that can be formed. When the potential is swept positively the platinum starts stripping around 0.7 V. The current initially increases as the potential is swept positive. However, then it suddenly falls to zero which suggests the surface becomes passivated preventing further platinum stripping, causing chlorine gas evolution to be suppressed with a peak only visible at a higher potentials (around 2 V although this is not shown in this CV). The return sweep is very interesting as this shows an oxidative peak on the reduction sweep. This could be linked to the passivation of the surface as this is removed and then platinum can be plated.

This was further investigated using LiCl-KCl with 20 mM $PtCl_2$. Figure 5.16 shows the plating and stripping reactions on both a W rod and Pt wire in this solution. There are subtle differences between the two CVs starting at the same potential (the grey line showing the response with a tungsten WE and red line showing the response with a platinum WE), such as the appearance of two peaks in the plating of Pt on the reductive sweep. This is attributed to the Pt plating onto W initially and then a Pt surface. The similarity can be explained by the plating of Pt through

the reductive sweep for the tungsten electrode thus the alloying reactions will most likely be the same in both systems. When the CV was started at a potential positive of platinum stripping, the response is more similar to that observed for a tungsten rod in just the eutectic LiCl-KCl, showing a clear Li plating and stripping peaks, as well as the start of chlorine evolution at the positive potential end of the window. Small peaks are evident of Pt-Li alloying as throughout the scan platinum will be plating onto the electrode. Peaks were very similar for the Pt wire in clean LiCl-KCl and $PtCl_2$ salt (Figures 5.14 and 5.16), the only real difference is the shape of the reduction peak during alloy formation. The alloying and passivation of platinum wire were also confirmed using the optical furnace to visualise the processes occurring at the electrodes. During the reductive period beneath -1.75 V, supposedly due to alloying, the platinum wire became darker in colour and increased in size. The electrode then decreased in size during the corresponding oxidation peaks. There were far fewer bubbles evolved on the Pt wire at positive potentials compared to a W rod in LiCl-KCl. Again, confirming that the surface of the electrode is passivated or coated preventing the evolution of chlorine at the expected potential. It is unclear what is causing the surface to become passivated. Literature suggests that this is due to platinum oxide forming. However, although this may be possible these experiments were performed in a glove box to minimise the presence of oxygen and the salt was thoroughly dried before experiments were performed. Other possibilities are forming hexachloroplatinate. Certainly in the optical measurements a brown colour is visible around the liquid gas interface which would correspond with the colour of this compound.

The alloying of platinum has been shown to occur with bismuth in LiCl-KCl.[137] Although platinum is commonly used as an inert metal at standard conditions in molten salt environment it is clearly not acting as an inert metal. This could be an interesting phenomenon and could be used to provide a series of signals as a fingerprint of an analyte which could help to identify components. However, this would likely need to be incorporated with inert electrodes in a monitoring system. This is because the platinum alloying with the solvent would severely limit the useful electrochemical window, and thus reduces the utility of this as the sensor metal. Also alloying could cause damage to the material and cause changes in the electroactive area so quantitative analysis could be precluded.

The same features were observable on platinum microelectrodes. At the positive end this was very clear but the current decreased significantly after each scan. After removing the electrode having performed only 5 CVs it was clear that the platinum had been removed and not replated. The negative scan also showed significant damage. This shows that platinum microelectrodes can only

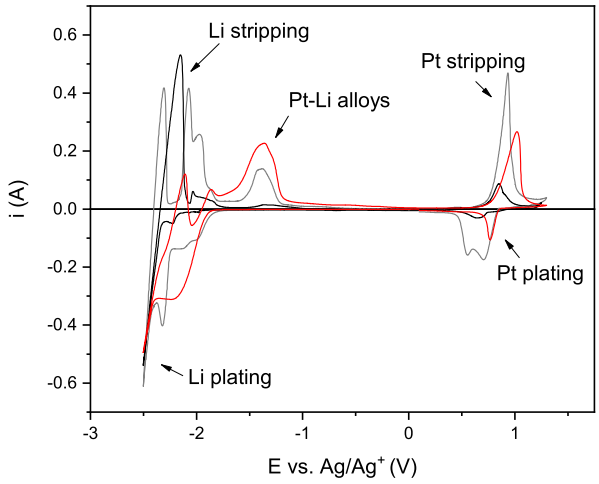


**Figure 5.16:** Comparison of CVs initially scanning in the negative direction at a scan rate of 200 mV/s on tungsten and platinum in LiCl-KCl with 20 mM $PtCl_2$ added at 450°C. The red line is platinum wire WE and the grey line is tungsten rod WE both starting at 0.08 V. The black line is the response of the tungsten rod WE with the scan starting at 1.1 V.

be used in a narrower window of around 2 V where the platinum is inert and provides motivation to use alternative metals for the fabrication of a microelectrode sensor to function over a wider solvent window.

#### 5.5.3.2 Adhesion Layer

Previous studies showed that titanium nitride was a chemically stable adhesion layer as it did not appear to be removed when samples were immersed in molten salt.[123] This was in preference to other possible materials such as titanium, which was removed by electrodissolution upon immersion and cycling in the salt.[123] To confirm that the titanium nitride is adequately resistant to corrosion dedicated test structures were fabricated with TiN layers of two thicknesses; 20 and 200 nm on 100 nm stoichiometric silicon nitride. The 20 nm corresponded to the thickness used within the electrode architecture and 200 nm was a more visually apparent layer. The TiN was deposited by sputtering Ti in an $N_2$ atmosphere using an Oxford Plasma Technology Plasmalab System 400 sputterer. This was then patterned into test squares and Greek crosses by a wet etch using hydrogen peroxide at 50°C following photolithography.

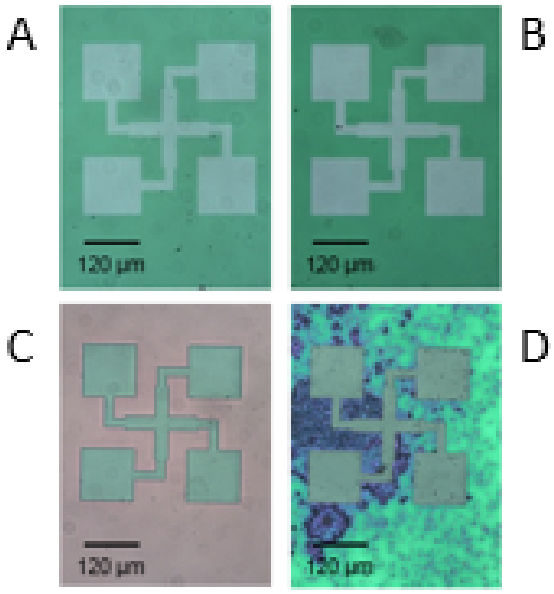


**Figure 5.17:** Optical image of titanium nitride test structures before (A & C) and after immersion in LiCl-KCl eutectic for 35 hours (B) and immersed in a different melt for 10 hours (D).

The Van der Pauw method was used to measure the sheet resistance of the test structures using the crosses. There was found to be a very large variation in the sheet resistance measurements across the wafer indicating some non-uniformity of the layer. The deposition process is known to have some variability, and with the 20 nm layer being very thin it is unsurprising that variation was observed across the wafer. To overcome this limitation several measurements were recorded for each chip both before and after it was immersed in the salt for a period of time, to gain an accurate measurement of any changes occurring. Recording multiple measurements and examining the change in sheet resistance for a single chip allowed a clearer picture of the effect on the titanium nitride.

As can be seen in Figure 5.17 the titanium nitride did not optically appear to suffer damage from immersion in the salt. This was the case for multiple samples. However, after immersion in a corrosive salt the silicon nitride layer appeared changed by the immersion, as seen in Figure 5.17 D. After immersion the silicon nitride visibly looked very patchy, this was corroborated by reflectometry measurements showing a clear linear decrease in thickness with time, as shown in Figure 5.18. The corrosion of the silicon nitride was found to vary in different batches of salt. It is known that impurities, particularly oxides and hydroxides, increase the rate of corrosion within

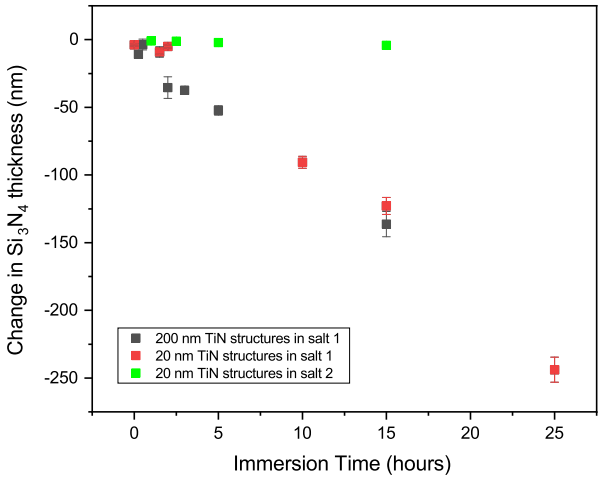


**Figure 5.18:** Measured change in silicon nitride layer thickness by reflectometry as a function of immersion time in the molten salt.

molten salts.[56] The average rate of silicon nitride layer thickness decrease was found to be 8.58 ± 0.88 nm/hour in salt 1 which was more corrosive, most likely due to oxide or hydroxide impurities present in the melt. In salt 2 the rate of decrease was found to be 0.24 ± 0.01 nm/hour as the salt contained fewer corrosive species. This demonstrates the importance of a dry and impurity free salt for measurement to limit corrosion. However, from all immersion studies (even in the more corrosive salt) the TiN layer did not appear optically changed.

Figure 5.19 shows the change in sheet resistance measured for the 200 nm thick TiN test structures immersed for different times in a dry LiCl-KCl eutectic melt. The sheet resistance measurements also confirmed that the TiN was not being attacked in the molten salt, as over time they did not show an increase in resistance. The sheet resistance would be expected to increase in magnitude with a thinning of the TiN layer as resistance is inversely proportional to thickness. It was surprising that after immersion the sheet resistance decreased linearly with time for the samples measured for both layer thicknesses. A similar phenomenon was observed for the 20 nm thick TiN test structures. The likely explanation for this is that the TiN is deposited by sputtering Ti in an atmosphere of $N_2$, thus it is likely that the layer is annealing in the high temperature environment of the molten salt (450°C). This was corroborated by a similar decrease in the sheet resistance of a TiN sample that was annealed under argon. Literature also indicates that titanium nitride layers can be porous and that annealing affects the sheet resistance.[216] The annealing time is slightly different to the

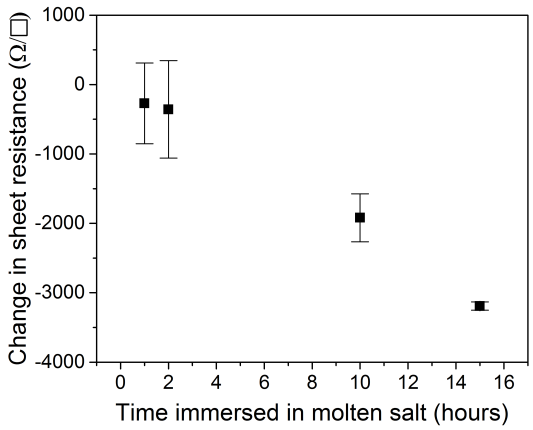


**Figure 5.19:** Change in measured sheet resistance for Greek cross structures of 200 nm thick TiN with immersion time in LiCl-KCl eutectic at 450°C. Each point represents measurements of eight separate Greek crosses on a sample immersed in the salt.

immersion time as the sample remained in the furnace during the slow cooling process, which accounts for minor differences between the values. This indicates that no chemical change to the TiN layer is responsible for the metal loss observed as it is clearly stable even in relatively corrosive salts. Therefore the metal loss is likely attributable to a physical process occurring. It seems likely that the adhesion between the TiN and the platinum is superior to the adhesion onto the silicon nitride, which would explain why titanium nitride is also found not to be present in cases of metal loss from the electrode surface.

### 5.5.4 Eliminating the adhesion layer

The physical restructuring of the TiN identified earlier could be contributing towards the observed metal loss by exerting force on the thin layer of deposited platinum. Another motivation for removing the adhesion layer from the architecture of the electrode is for the development of MNEE nanoelectrodes, where the TiN edge is exposed to the melt. In this case the TiN contributes to the signal recorded, as shown in Figure 7.6. This complicated the measurement with two different responses evident, and this feature could be exacerbated if one layer undergoes an alloying reaction and the other metallic layer does not. Hence the motivation to work towards achieving an architecture that did not require an adhesion layer. A possible metal candidate which does not require an adhesion layer is tantalum, as it can be used as adhesion layer itself.[123,217] It has also been reported that tantalum has very good resistance to corrosion.[218]

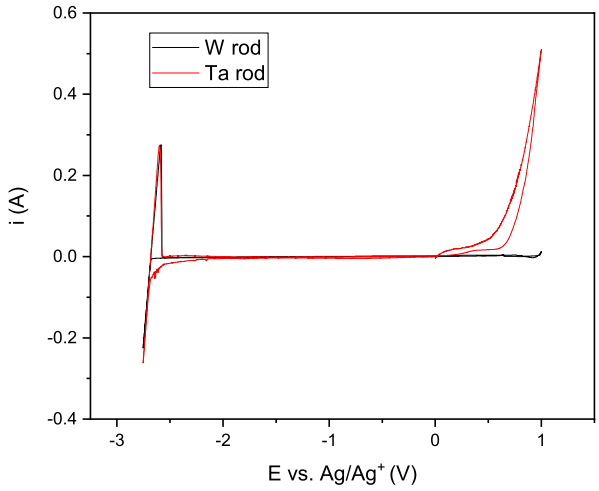


**Figure 5.20:** Typical CV within LiCl-KCl eutectic using tantalum rod at a scan rate of 0.1 V/s.

However, it is first important to establish whether tantalum is suitably inert electrochemically. A CV using a macroelectrode using a 2 mm diameter tantalum rod as the working electrode in the electrochemical system is shown in Figure 5.20. There was no evidence of alloying within the electrochemical window of the LiCl-KCl eutectic. Thereby demonstrating suitability of tantalum as an inert electrode to investigate fundamentals of electrochemical reactions within the melt.

Tantalum electrodes were fabricated and characterised for heat and corrosion resistance to LiCl-KCl eutectic. A concern was that oxides are known to form on tantalum and there were further concerns over the fidelity of the connection to the devices.[219,220] These tantalum electrodes were fabricated with an aluminium capping layer, which was deposited after argon milling the surface whilst under vacuum to remove the top surface oxide. The structure of the capped microelectrodes is shown in Figure 5.21. Aluminium was used as it is known to be removed from devices without applying a

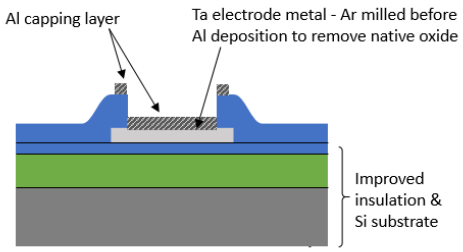


**Figure 5.21:** Cross-section of tantalum microelectrode with aluminium capping layer.

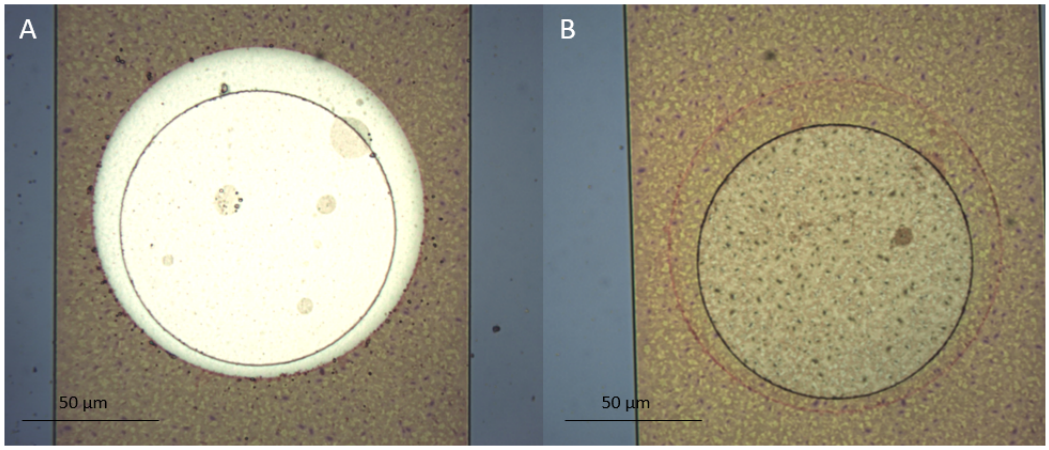


**Figure 5.22:** Comparison of a tantalum electrode before (A) and after (B) use in LiCl-KCl at 450°C for 10 hours.

holding potential so could easily be stripped *in-situ* once immersed in the melt. Figure 5.22 shows a comparison of tantalum electrodes with immersion into the melt, the aluminium capping layer was fully removed and a ring artefact can be seen after immersion where this was positioned on the electrode. The tantalum itself does not appear different than underneath the insulator. Neither heat or immersion into the salt seemed to significantly damage the tantalum and no loss of metal was observed over similar time periods of immersion to the platinum electrodes.

### 5.5.5 Track resistance

Previously the width of the track had been reduced to decrease the critical area of the devices.[123] This was done in order to improve the yield of devices which showed the expected microelectrode response.[123] A comparison between the thin track (TTM) and super thin track (STTM) designs is shown in Figure 5.2. However, looking again at the lifetime data in Figure 5.9 it does not appear that this resulted in an improvement in lifetime, and this suggests that the $Si_3N_4$ is robust with a low defectivity.

During this work decreasing the width of the track had a deleterious effect on the resistance of the track in the devices. This was particularly the case for the 50 nm thick platinum micro- and nanoelectrodes, where the track resistance increased from 1475 ± 23 Ω for the thin track to 14325 ± 1111 Ω for the narrower super thin track design. This was most evident in the electrochemical impedance spectroscopy performed with the microelectrodes, the analysis of which is covered in greater depth in Section 6.3.2.3. The track resistance of various microelectrode designs were

measured with a probe station using two probes; positioned at the centre of the contact pad and the electrode. Table 5.7 shows the measured values. While nanoelectrodes cannot be measured in the same manner, these would be expected to have very similar track resistances to the microelectrode equivalent design. The thin track design has a smaller resistance for both metals by an order of magnitude, which is a significant decrease and is consistent with the decreased number of squares in the design. As the stoichiometric silicon nitride top insulator was performing adequately and no evidence of silver plating on the top of the covered metal was evident in the evaluated devices (which would have been evidence of pinholes in the insulator), it was decided to return to the 'thin track' design. This had the added benefit of not having a sharp corner at the base of the track where the enlarged disc of metal with the central microelectrode was located, which should help minimise stress at this location in subsequent devices.

For the tantalum electrodes, both with and without the aluminium capping layer at contact pad and electrode, the influence of contact and track resistance were investigated further. Table 5.8 shows a comparison of the measured resistance across the contact pad (approx 0.5 cm separation between probes) and between the contact pad and the electrode (approx. 3 cm separation between probes). Clearly there is a large track resistance of around $10^5\Omega$ inherent in all of the devices, two orders of magnitude above the Ta contact resistance measured across the contact pad. The aluminium

| Microelectrode device | Metal thickness (nm) | Measured track resistance ($\Omega$) | Calculated iR drop (mV) |
|---|---|---|---|
| Platinum STTM | 50 | 14325 ± 1111 | 1.43 ± 0.11 |
| Platinum TTM | 50 | 1475 ± 23 | 0.15 ± 0.01 |
| Tantalum TTM | 50 | 147009 ± 86000 | 14.70 ± 8.60 |
| Tantalum TTM (loaded into furnace at room temp) | 200 | 631 ± 1 | 0.06 ± 0.01 |
| Tungsten STTM | 200 | 1710 ± 43 | 0.17 ± 0.01 |
| Tungsten TTM | 200 | 333 ± 8 | 0.03 ± 0.01 |

**Table 5.7:** Measured track resistance of platinum, tantalum and tungsten microelectrode devices (with metal layer thicknesses of 50 nm and 200 nm) and the calculated iR drop assuming a current of 100 nA for all designs.

capping layer significantly reduced the contact resistance measurement across the contact pad of the device where there is a slab of aluminium between the probes, which is fully expected as the aluminium is deposited as a contact because it acts as a good conductor. Also as expected affirming it is a track resistance, this clearly hasn't caused a change in the measured resistance between contact pad and electrode for the tantalum devices with a capping layer. In the deposition

process an argon mill process is used to remove the oxide from the surface of the tantalum before the aluminium is sputtered onto the wafer (both under vacuum), and the track resistance for the tantalum electrodes with and without an Al capping layer has been shown to be equivalent within error. Thus it can be concluded that the milling process is not adequate to remove all of the tantalum oxide present on the devices. Clearly there is a large track resistance present in these devices which is not due to the formation of an oxide at the contact pad and electrode causing contact resistance between the device and the probe. Interestingly, the high temperature anneal

| Electrode | Resistance across contact pad /Ω | Resistance between contact pad and electrode /Ω |
|---|---|---|
| Ta | $3.14 \times 10^3 \pm 848$ | $1.47 \times 10^5 \pm 0.86 \times 10^5$ |
| Ta with Al capping layer | $1.66 \times 10^1 \pm 2.08$ | $1.23 \times 10^5 \pm 0.002 \times 10^5$ |
| Ta with Al capping layer annealed for 1 hour in Ar | $4.75 \times 10^1 \pm 1.07$ | $1.33 \times 10^5 \pm 0.01 \times 10^5$ |

**Table 5.8:** Comparison of the measured track resistance for various tantalum microelectrodes.

(450˚C) under argon of the Ta electrodes with high resistance has only slightly increased the track resistance. This suggests that there is little physical restructuring of the devices which was observed for the TiN adhesion layer. Therefore the resilience of the devices would be expected to be improved.

The sheet resistance of a 50 nm tantalum layer after deposition was measured to be $27.9 \pm 0.9\ \Omega/\square$ using a Veeco FPP 5000 four point probe. For the thin track design there are 165 squares leading to an expected track resistance $4598 \pm 141\ \Omega$. This is two orders of magnitude lower than the measured track resistance of the devices when fully fabricated, so there has clearly been a change to the metal during the fabrication process. The high resistance measured for the tantalum TTM was thought to arise from the formation of a stable oxide layer on the surface of the tantalum, as tantalum pentoxide is often used in capacitors because it has a high dielectric constant and can easily be formed by anodization.[219, 221] Although the measurements indicate that oxide formation must be occurring across the entire length of the track, rather than just at the electrode and contact pad which are left exposed. During the fabrication process the devices are not exposed to an oxygen plasma, an alternative cause of oxidation to the tantalum could be during the process used for nitrogen deposition. The wafers are loaded into the nitride furnace whilst it is at 600°C, causing the tantalum to be exposed to oxygen in the atmosphere at elevated temperature before the furnace is purged with nitrogen. This was confirmed with an increased sheet resistance measurement of 449

$\pm$ 177 $\Omega/\square$ for a 50 nm Ta layer after a $CF_4$ blanket etch of deposited silicon nitride compared to an initial value of 27.9 $\pm$ 0.9 $\Omega/\square$ after Ta deposition.

To reduce the amount of oxide formed on the entire tantalum pattern, the fabrication process was adjusted so that the wafers were loaded into the nitride furnace at room temperature, and only heated when the chamber had filled with nitrogen to limit the exposure to oxygen at high temperature. The measured resistances are shown in Table 5.7. This adaption to the fabrication process (along with an increase in track thickness) resulted in a decrease of the resistance by three orders of magnitude, and a track resistance value which was more consistent with other electrode metals.

The measured sheet resistance for the 200 nm thick layer of tantalum was 6.97 $\pm$ 0.21 $\Omega/\square$ after metal deposition. It can be clearly seen that as would be expected the track resistance decreases with both increasing thickness of the track and width. With a four times thicker track the measured sheet resistance decreased by roughly a factor of four. The adaption to the fabrication procedure had the desired effect of decreasing the track resistance, as the reduction in track resistance was more than expected for an increase in the thickness of the metal. This is a significant reduction that would help distinguish parasitics arising from the track and charge transfer characteristics in impedance spectroscopy. Clearly increasing the thickness of the track is also beneficial in reducing the track resistance. However, for the fabrication of nanoelectrodes the layer thickness is the

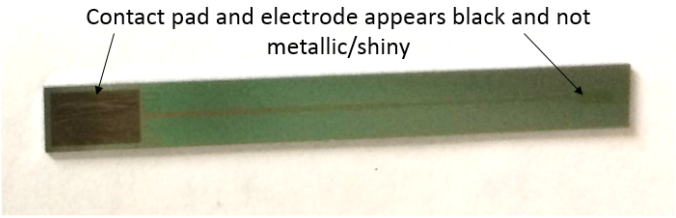


**Figure 5.23:** Example of the typical discolouration of the tantalum electrodes observed during etching the top insulator.

critical length scale of the device so it is not desirable to increase the thickness. Therefore a trial was performed of thickening the track over a few centimetres above the electrode. This design would mean the majority of the track would be significantly thicker thus helping limit the overall track resistance. A concern was that this could cause stress and poor coverage over the step change in metal thickness. This was simply done with the use of a shadow mask during deposition of the

tantalum in the sputter deposition system. All devices immersed and held in LiCl-KCl with 5 mM AgCl did not show any evidence of cracking due to stress or silver plating on the insulator. Thus it was concluded that this would be a viable method of ameliorating the track resistance.

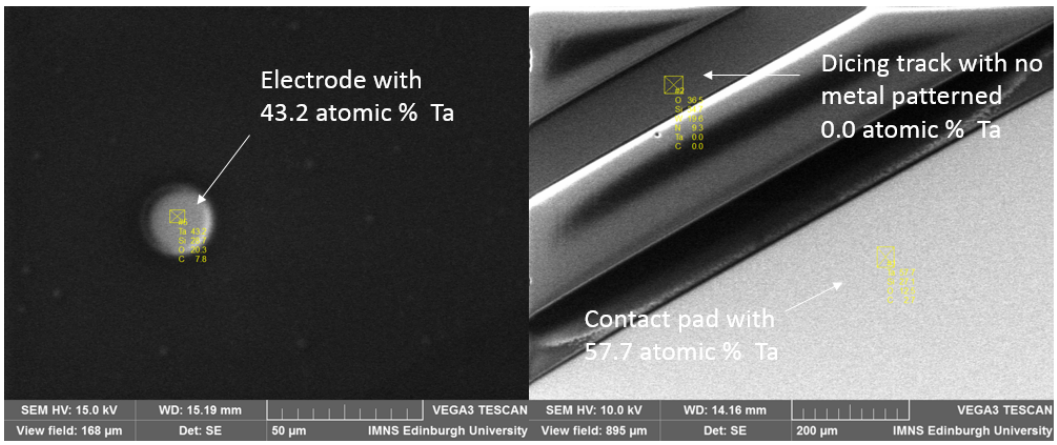


**Figure 5.24:** SEM images and EDX measurements of Ta electrodes fabricated to check whether Ta was present on the contact pad and electrode after etching windows into the top insulator.

Unfortunately issues were encountered during the fabrication of the devices using low temperature loading of the furnace. During the final etching step the metal was observed to become discoloured - although this could merely be an optical feature with a very thin layer on the surface. This can be seen in Figure 5.23. As the etch used to create windows in the top silicon nitride insulator is also known to etch tantalum, there was a concern that the thin 50 nm layer of tantalum was being removed.[222,223] This was checked using EDX to investigate the surface of the electrode and contact pad, the results of which are shown in Figure 5.24. It was determined that tantalum was still present on all the devices, with an atomic percentage of Ta between 35-60 for areas of exposed tantalum (electrode and contact pad) although the roughness of the layer showed some variation. An example of the electrochemistry observed when these devices were used for measurements in LiCl-KCl with europium is shown in Figure 5.25. The electrochemical response showed many peaks which seemed to change over time and could be indicative of contamination of the electrode surface. Interestingly the EDX measurements show the presence of carbon, which could have contaminated the surface from the $CF_4$ etch. This could be contamination within the instrument or from the photoresist which was still present on the wafer. However, it was not detectable on the dicing tracks which only showed the expected elements present in the dielectric layers in these areas. It is also unlikely to be photoresist as the removal steps were the same as for other metal electrode fabrication

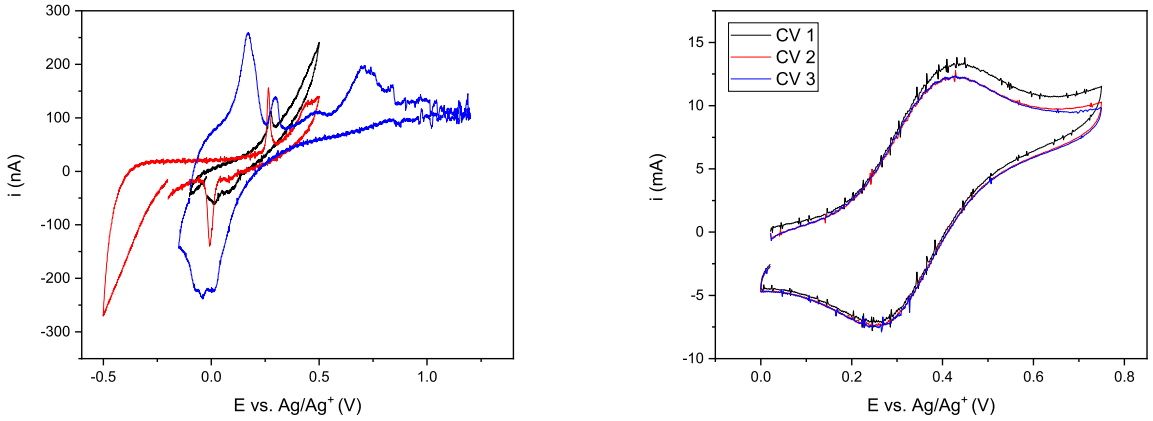


**Figure 5.25:** Electrochemistry of the first CV observed over different windows for Ta electrode with apparently black surface (left) and the W macroelectrode respones in the same melt (right) which contained 60 mM $EuCl_3$ at the same temperature (375°C).

and this issue wasn't encountered during fabrication. Tantalum carbide and fluorocarbon residue has been observed by Kuo for plasma etched sputtered tantalum, using electron spectroscopy,[224] whilst Martz *et al.* attributed slow etch rates to fluorocarbon deposition.[225]

Unfortunately scarcity of time prevented a more thorough investigation of this phenomenon and investigation of different processes to overcome this observed issue. Although the high track resistance of tantalum microelectrodes could not be overcome without adversely affecting the electrochemical measurement in the time available, the tantalum microelectrodes (with high track resistance) demonstrated very good functionality in the molten salt environment.

The lifetimes of devices in comparison to the platinum electrodes measured with the same silver plating and stripping reaction is shown in Figure 5.26. The average lifetime of the Ta electrodes was 13.5 ± 3.5 hours. Only four devices were evaluated due to the available time so statistical conclusions are limited. Despite the observation of variability in the lifetime of the devices the electrodes were consistently reliable for 9 hours, a time which allows meaningful measurement and analysis of reactions. This is discussed further in Chapters 6 & 7. The new design of tantalum microelectrodes is a suitable pathway for the production of nanoelectrodes, as there is no adhesion layer requirement.

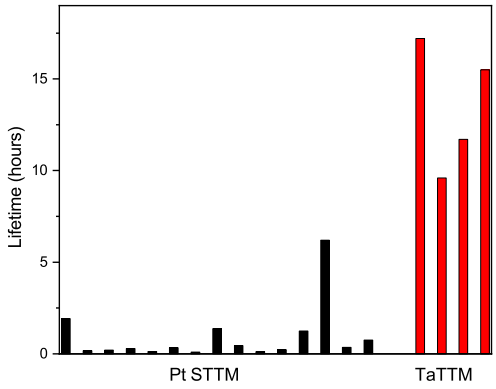


**Figure 5.26:** Comparison of the lifetimes of tantalum microelectrodes in comparison with the platinum microelectrodes measured in this work.

## 5.6 Conclusions

Within the group issues with the yield and lifetime of devices used in the harsh environment of the molten salt have been encountered, and efforts to improve these for devices have been sought.[122, 123] For the device at the start of this work, possible shorting to the silicon substrate was identified as a possible critical failure mechanism for devices. Two different approaches to overcome this issue were evaluated; firstly using a quartz substrate as it would be non conductive, and then improving the insulator between the metal and the silicon substrate. Major issues were encountered in fabricating microelectrodes using a non-conductive substrate which would require complete redesign of the devices requiring significant time and effort.

Electrodes fabricated with a silicon nitride layer underneath the metal layer performed to a high standard, whilst only requiring minor additional fabrication steps. The yield of functioning devices significantly improved with the added layer in the structure. This is most likely due to it acting as a better insulator and covering any pinholes in the silicon oxide layer, which thus reduced the likelihood of critical failure of connecting to the conductive silicon substrate. The inclusion of a silicon nitride layer was judged to be beneficial in preventing connection between the metal and silicon substrate, and thus was incorporated into all subsequent batches of devices fabricated to improve the yield of devices functioning in the molten salt environment. The lifetime of microelectrodes was highly variable and typically functioned for under an hour, the common observation after utilising the platinum microelectrodes was the loss of metal from the surface

of the electrode. This was investigated and found to occur due to physical changes occurring within the adhesion layer of TiN although this itself was found to be chemically resilient to the molten salt. This motivated the adaption to the architecture of the devices to remove the adhesion layer from the structure of the device. A completely new system compatible with nanoelectrode production based on tantalum as an electrode metal has been designed and fabricated. The tantalum microelectrodes were found to withstand the harsh conditions reliably. Although these devices still require further optimisation to reduce the track resistance without impacting the final etch to expose the tantalum, which unfortunately due to time constraints could not be completed within this work. The development of resilient tantalum electrodes enables the investigation of fundamental processes occurring with the use of micro- and nanoelectrodes.

# Chapter 6

# Microelectrode Characterisation

## 6.1 Introduction

Significant work has been performed to develop minituarised sensors to enable the fundamental processes occurring during electron transfer reactions to be studied. The previous chapter focused on the development of devices so that they were resilient to the high temperature molten salts of interest for nuclear pyroprocessing. This chapter now considers the analysis of microelectrode measurements. The fabricated microelectrodes were first characterised in aqueous media to ensure that they behaved as expected; the results for the platinum devices are presented. The nuclear relevant soluble/soluble europium (III/II) redox system, which was studied with macroelectrodes in Chapter 4, was then used for further investigation of the enhanced microelectrodes developed.

## 6.2 Aqueous characterisation of microelectrodes

### 6.2.1 Cleaning Pt microelectrodes

The microelectrodes were first tested aqueously and were found to need electrochemical cleaning, as can be seen in Figure 6.1. When characterised using $[Fe(CN)_6]^{3-/4-}$ without electrochemical cleaning the electrodes were generally found to be highly resistive and the expected 'wave' response was not evident. Although a few electrodes showed a reasonable microelectrode response with both shape and magnitude similar to those expected for the buffer solution with potassium ferricyanide and

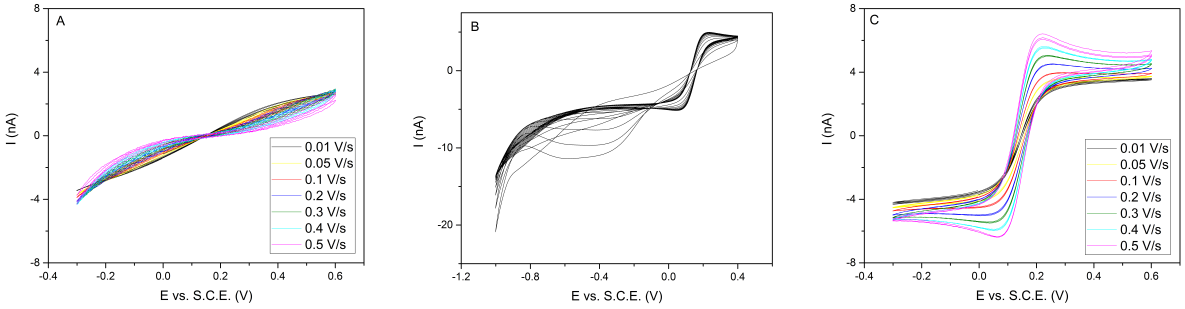


**Figure 6.1:** (A) Comparison of resistive response when tested without electrochemical cleaning, and (C) after, for a 30 μm diameter microdisc electrode in 1 mm FFC in 0.1 M KCl. (B) shows the rapid change to a 'wave' response during the cleaning cycling at 200 $mVs^{-1}$ in the same solution.

ferrocyanide redox agents, the majority ($> 90\%$) of those tested without electrochemical cleaning did not. As the currents observed were markedly smaller than expected, it also indicated that not all the electrode surface was active. Ensuring the entire area of the electrode is clean and accurately known is important for electrodes, so that the current can be related to the concentration,[226, 227] and essential for the production of sensors which necessitate a quantitative measurement.

There are many methods employed for cleaning electrodes; a typical protocol for cleaning macroelectrodes typically includes polishing to produce a fresh surface, but this is not feasible for microfabricated electrodes.[228, 229] A common method of cleaning very small electrodes is electrochemical cycling in sulphuric acid between the solvent limits.[85] This was not employed in this instance as potassium ferricyanide/ferrocyanide (FFC) was used as the redox couple for testing the electrodes. It is known that potassium ferricyanide reacts with ferrous ($Fe^{2+}$) ions in acidic solutions to form an insoluble blue complex known as 'Prussian Blue', which has been widely used in histology and blue printing.[230] A similar side product of electrochemical cycling in FFC has also been observed and investigated within the group; this formed an insoluble film on the electrode surface.[231] As there were concerns over the thoroughness of rinsing all of the acidic solution off the electrodes, and for rapid use when the electrode was clean, all electrochemical cleaning was performed in the FFC measurement buffer. The cleaning protocol used was cycling between -1 V and + 0.4 V for 15 cycles at a scan rate of 0.2 $Vs^{-1}$. It was seen that the wave due to the FFC grew in size, and a characteristic microelectrode response was typically observed after 5 complete scans. The typical responses for unclean, cleaning cycles and clean microelectrodes are shown in Figure 6.1. It is likely that the reduced active electrode area initially seen is due to some contamination on the surface. It is possible

this is from incomplete removal of the photoresist deposited for dicing the wafers. It has been seen within the group previously that contamination can be easily removed by scanning to negative potentials in aqueous KCl,[231] which was also seen to be the case for the microelectrodes tested here. All electrodes were therefore cleaned with this procedure, immediately prior to recording the fundamental response in the FCC solution. The limiting currents were measured and compared to those expected for the electrode size, calculated from Equation eq: micro current using literature diffusion coefficients of ferrocyanide, D = 7.7 x $10^{-6}$ $cm^2s^{-1}$ and ferricyanide, D = 6.2 x $10^{-6}$ $cm^2s^{-1}$ at 25°C.[232,233] After these initial results showed issues with ensuring all of the resist was cleaned from the active surface wafers were not coated with photoresist prior to dicing in the fabrication process discussed in Section 3.1.2. This would also likely be more of an issue for molten salt measurements, where there is no established electrode cleaning protocol. It was also undesirable to aqueously test each electrode in aqueous media, to establish cleanliness, prior to use within a melt.

### 6.2.2 Cyclic voltammetry analysis

The majority of the electrodes functioned well in aqueous media. 91% of electrodes tested from the dry etched wafer and 94% from the wet etched wafer gave the characteristic sigmoidal microelectrode response and limiting currents after electrochemical cleaning. The small number of electrodes that didn't work showed a resistive response, which could either be due to a poor connection to the device or remaining contamination on the surface of the electrode. Figure 6.2 shows an example of the scan rate study performed on the smallest, 10 μm diameter, and largest, 100 μm diameter, platinum microelectrodes following cleaning.

Reassuringly it was possible to measure currents at standard concentrations for single microelectrodes with accuracy, even at very low currents of only single nanoamps. Interestingly, for smaller diameter electrodes at low scan rates, less noise was evident on the measurements compared to faster scan rates, as can be seen for the 10 μm diameter data in Figure 6.2. This was due to the interval time (which is the step potential divided by the scan rate) being longer for slower scan rates. This could be optimised, if required, for future measurements at faster scan rates, but the data recorded at slow scan rates were good and could be used to take the limiting current value at a set potential for comparison with theoretical values.

The measurements were generally in good agreement both with others of the same size, which is

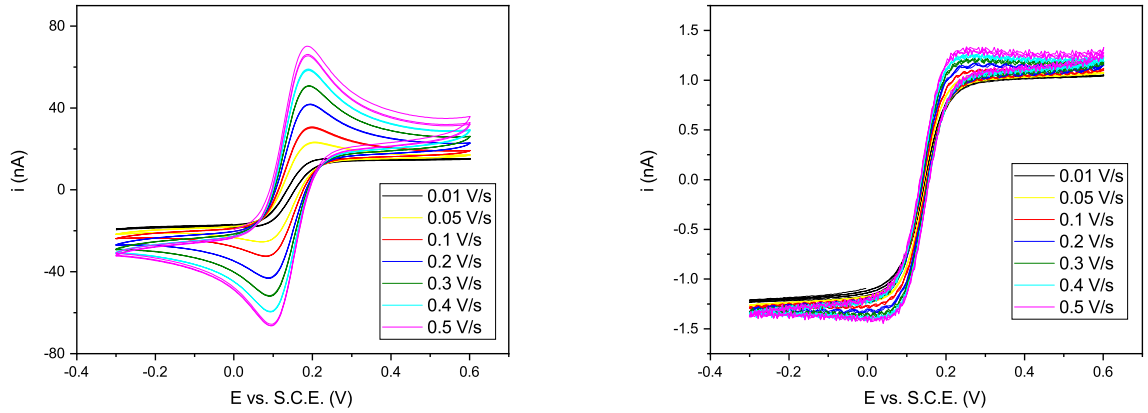


**Figure 6.2:** Scan rate study for 100 µm diameter (left) and 10 µm diameter (right) platinum microdisc electrodes in 1 mM FFC in 0.1 M KCl aqueous solution.

apparent from the small size of error bars in Figure 6.3 and the predicted limiting current from Equation eq: micro current, $i_{lim} = 4FnDcr$.

The literature diffusion coefficients of ferrocyanide, D = 7.7 x $10^{-6}$ $cm^2s^{-1}$ and ferricyanide, D = 6.2 x $10^{-6}$ $cm^2s^{-1}$ in water at 25°C were used to calculate the expected limiting current. The measured currents are all within error, in agreement with those predicted by the modelled microdisc response except for the 100 µm diameter microelectrodes. It is interesting that the measured currents for the 100 µm diameter electrodes are more variable and consistently slightly larger than the expected current. The higher current seems to indicate a larger active area, however, this is highly unlikely. Any deviations in electrode area would be more likely to be seen in smaller electrode sizes than the 100 µm electrodes and no issues in fabrication were apparent in inspections carried out during the fabrication process. The larger and more variable currents therefore indicate that the largest electrodes are not true microelectrodes and are sensitive to additional convective transport. This is consistent with relevant literature, which suggests that at this size such electrodes are expected to produce a quasi- macroelectrode response.[234][235] It is also evident at these large diameter microelectrodes that even at the slowest scan rates used in the study (10 mV/s) a peak is still observable, as can be seen in Figure 6.2, which is more indicative of a macroelectrode response. Clearly at fast scan rates the largest diameter microelectrodes are not behaving as microelectrodes with deviation from the expected limiting current for the 100 µm diameter electrodes. Thus there is a clear agreement with theory and established similar responses for these microfabricated devices.

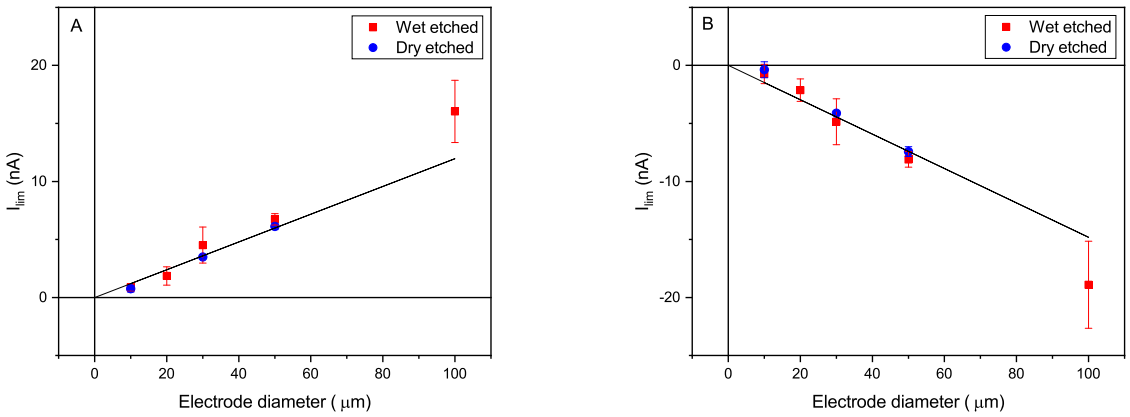


**Figure 6.3:** Comparison of aqueous results (at slowest scan rate) from all platinum microelectrodes tested ($n \geq 4$ for each size on the wafer) and the expected limiting current (shown by the black line) calculated from Equation eq: micro current for (A) the oxidation of ferrocyanide and (B) the reduction of ferricyanide in 1 mM FFC and 0.1 M KCl solution.

### 6.2.3 EIS analysis

The EIS response for each electrode was also measured at OCP (approx + 0.14 V) for the 1 mM FFC in 0.1 M KCl aqueous solution. Figure 6.4 shows the Nyquist plot of the resulting response for three individual 100 μm diameter electrodes.

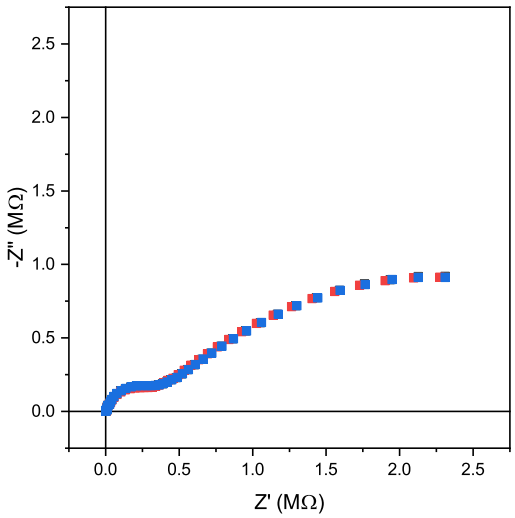


**Figure 6.4:** Demonstration of good reproducibility for the EIS response of three different 100 μm diameter microelectrodes in 1 mM FFC, 0.1 M KCl aqueous solution. The responses are shown in three different colours; blue, red and black.

The devices showed good reproducibility across different electrodes as would be expected from the microfabrication of devices which enables the reliable production of nominally identical electrodes. The Nyquist response shows a clear semicircular feature at high frequencies, interpreted to be due to $R_{ct}$ and $C_{dl}$ described in Section 2.2.3.4. Then as would be expected a 45° line is apparent, which is indicative of planar diffusion and can be modelled with the use of a Warburg element. It fitted well to the modified Randles circuit for microelectrodes shown in Figure 2.19. A comparison

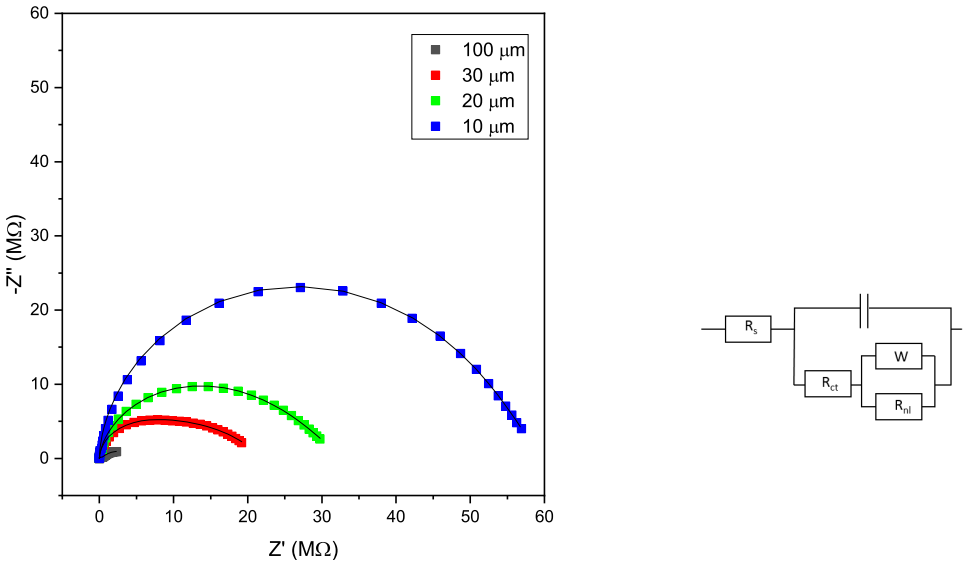


**Figure 6.5:** Comparison of the Nyquist response (left) for different diameters of platinum microelectrodes for the FFC aqueous system and (right) the modified Randles circuit used to fit the data.

of the response at different diameters of electrode is shown in Figure 6.5. As the electrode diameter decreases a more semicircular feature becomes apparent at the low frequency end of the Nyquist plot characteristic of the typical microelectrode response. It also appears that the expected two semicircles have significantly merged in this measurement, which indicates that the time constants for the charging time of the double layer and the Warburg element must be similar. Also as expected the total impedance increases as the electrode size decreases. The modified Randles circuit, which is the established circuit for fitting microelectrode responses, provided a good fit at all diameters of devices characterised aqueously using FFC. The 100 µm diameter microelectrode shows less of a circular feature at low frequency and therefore less influence of $R_{nl}$ which is consistent with the non-microelectrode behaviour at slow scan rates discussed in Section 6.2.2.

### 6.2.4 Tantalum electrodes

Tantalum microelectrodes could not be directly compared by aqueous characterisation, as only a resistive response was observable. This is due to the insulating tantalum oxide formed on the surface of the electrode by fabrication or further ambient oxidation preventing a measurable current being passed. The effects of this oxide in molten salt is discussed in Sections 5.5.5 and 6.3.2. Tungsten shows similar behaviour where electrodes are unsuitable for aqueous measurement but have been used successfully within the LiCl-KCl eutectic.[87, 123]

## 6.3 Microelectrode measurements of europium in molten salt

As described above, very high fidelity and high yield platinum microelectrodes were produced for aqueous measurements. The next step was to test whether similar enhancements were found in molten salt. Thus the improved microelectrodes were used to study the macroelectrode-characterised europium redox system in molten salt to help gain further insight into the electron transfer process.

### 6.3.1 Pt microelectrodes Cyclic voltammetry

The typical CV response for a 30 μm diameter platinum thin track microelectrode is shown in Figure 6.6. The response appears more spread out in voltage than the equivalent aqueous CVs due to the elevated temperature at which the measurement was performed. There appears to be a small amount of resistance in the measurement causing the limiting current to not be perfectly flat. This most likely occurs due to resistance in the connection to the microfabricated device. Current above and below the axis indicates that both Eu(III) and Eu(II) are present. This has previously been observed and discussed in Section 4.2 and literature.[78, 87]

Taking the limiting current, $i_l$, as the difference between the oxidation and reduction mass transport limited current and assuming a global diffusion coefficient, D, this can be compared to the expected value using equation eq: micro current. The diffusion coefficient of $Eu^{2+}$ and $Eu^{3+}$ have been shown previously to be similar and a global value has been calculated experimentally to be 5 x $10^{-6}$ $cm^2s^{-1}$.[87] Using this value an expected limiting current of 173.7 nA would be expected for a 30 μm diameter microelectrode with a concentration of europium of 60 mM. Clearly the CV in Figure 6.6 shows a significantly higher value than this, with a limiting current of 2 μA which would correspond

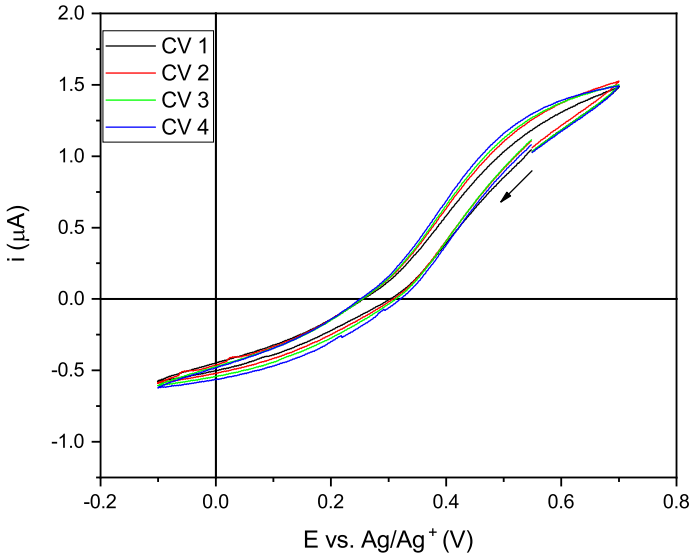


**Figure 6.6:** CV from a Pt 30 µm diameter microelectrode in LiCl-KCl with 60 mM added $EuCl_3$ at 425°C. The scan started at 0.5 V with the arrow indicating the start and direction of the first scan at a scan rate of 100 mV/s.

to an active electrode area of 93,740 $\mu m^2$. This correlates to a microdisc of 345 µm diameter which is over a factor of 10 bigger than the fabricated size of the electrode. However, despite the larger than expected active electrode area the typical microelectrode wave response is still observable in the CV.

Despite the larger current the impedance response was then measured with the same 30 µm platinum microelectrode at a various potentials around E'. The Nyquist plot of the response is shown in Figure 6.7. Initially a similar response to that observed in aqueous solution was observed with a typical microelectrode response apparent. The semicircle at high frequencies is small and merges into the second apparent semicircle. As would be expected the non-linear resistance decreases as the applied DC potential in the EIS measurement approaches E' for the reaction $Eu^{3+} + e^- \rightleftharpoons Eu^{2+}$. From the CV this is expected to be around 0.4 V, however, during the measurement at 0.3 V applied DC potential there is a clear change in the response. Initially the impedance response seems to be following the same functional form as previous EIS measurements but at a certain point during the measurement (at the applied DC potential of + 0.30 V) the response changes and a very low and noisy impedance response was observed, most likely indicating an change in the electrode during

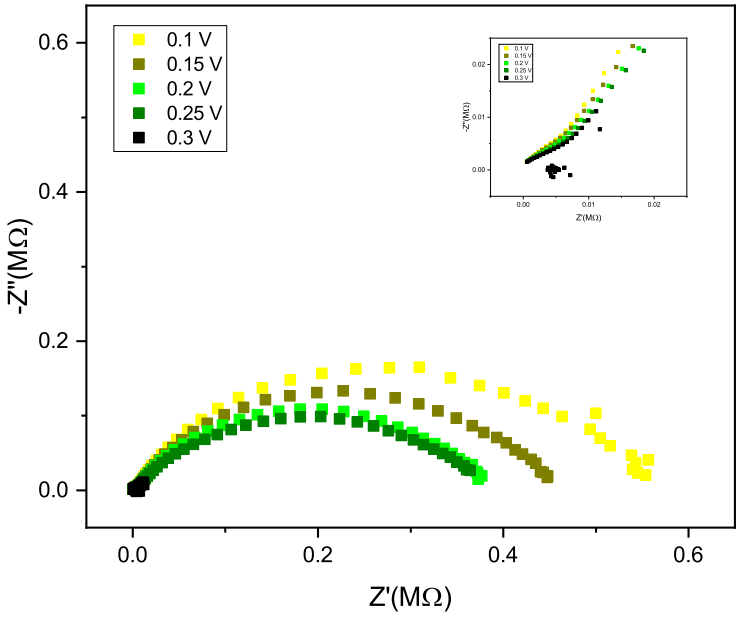


**Figure 6.7:** EIS response around E' for a 30 μm platinum microelectrode in LiCl-KCl with 60 mM $EuCl_3$.

the measurement. This was confirmed as upon inspection after removal of the device from the melt it was clear that the electrode had been damaged during the measurement.

A comparison of the appearance of the platinum electrode before and after measurement is shown in Figure 6.8. The electrode was removed from the melt after observation of loss of signal. There is a large amount of salt remaining on the chip after washing in deionised water. There was significant damage to the device as was expected from the clear change in EIS response. Significant metal and top insulator loss was observed after removal from the molten salt, which was confirmed with EDX analysis. In the image of the electrode after use it is difficult to even distinguish the area where the 30 μm diameter electrode was patterned. There are islands of exposed metal remaining; a loss of insulator could account for the larger magnitude of limiting current recorded in the CV. Either subsequent loss of metal with the insulator leaving disconnected islands of exposed metal or significant changes of active electrode area could account for the clear change in the impedance response. For this device the damage was more severe than for most other devices tested, with large degrees of metal and top insulator loss suggesting that there could have been some increased stress within the device. However, this result although more extreme, is illustrative

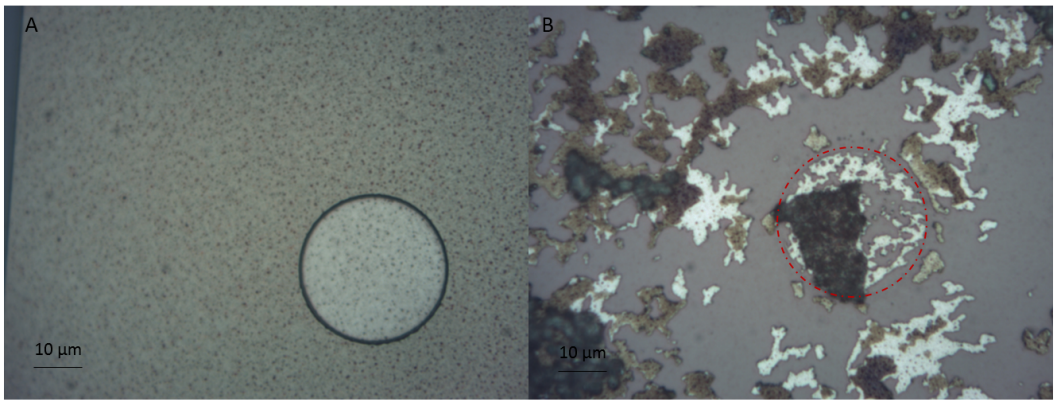


**Figure 6.8:** Optical images of 30 µm diameter platinum microelectrode used for CV and EIS measurement of 60 mM Eu in LiCl-KCl at 425°C before use (A) and after (B). The initial electrode diameter and position is outlined by the dashed red line in the optical image of the device after use.

of the difficulties encountered during attempts to use the platinum microelectrodes with changes to the active electrode area precluding reliable measurements being recorded over a period of time. Thereby, demonstrating the need for development of robust microelectrodes suitable for reliable long-term measurement.

Whilst platinum microelectrodes have been shown to function in molten salt measurements there are clear limitations over of the devices for measurements over long periods of time. It is clear from this example that midway through an EIS measurement around the formal potential that the electrode failed. This is consistent with the previous results of damage observed for microelectrodes in LiCl-KCl with different redox agents, and from the tests in Chapter 5 it was found that it was not possible to prevent the metal loss observed for the platinum microelectrodes. The demonstration of changes to electroactive area occuring when in the melt precluded quantitative measurement of the system.

### 6.3.2 Ta microelectrodes

#### 6.3.2.1 Cyclic Voltammetry

Unlike platinum, the tantalum electrodes developed in Section 5.5.4 were tested and found to be suitable for high temperature molten salt measurements as they did not suffer from metal loss damage causing variation in the active electrode area of the device. Despite the difficulties encountered with substantial track resistances for tantalum electrodes, the resistance in measurements is

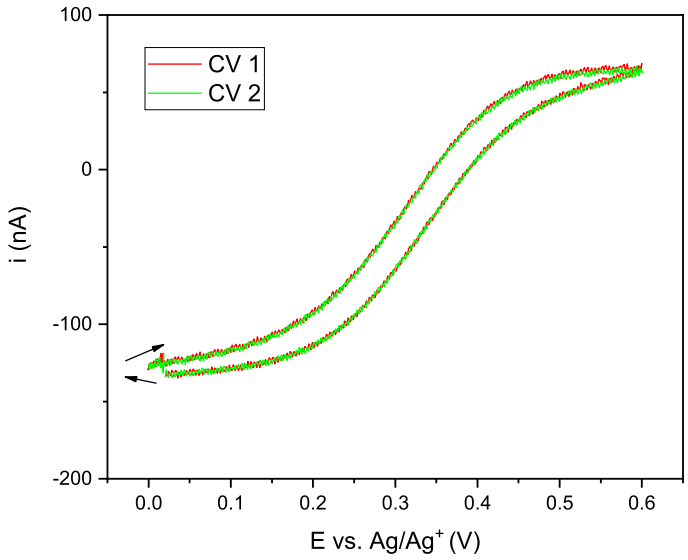


**Figure 6.9:** Typical CV of 30 µm electrode showing consistent CVs in LiCl-KCl with 60 mM $EuCl_3$ at 375°C with arrows indicating that the scan started at 0 V with a small part in the negative direction before the oxidative sweep at a scan rate of at 100 mV/s.

comparable to the platinum devices. This is because all of the Ta devices fabricated used the thin track design whereas the majority of platinum devices were super thin track, thereby mitigating the differences between the metals. The initial response for a 30 µm tantalum microelectrode is shown in Figure 6.9. Consistent CVs were recorded, which was typical of Ta microelectrodes. Even despite the likely presence of an oxide layer on the tantalum thin track electrodes they function well in molten salt, giving the expected microelectrode sigmoidal CV response with expected limiting currents. It is interesting that the CV is more equally centred about the zero current indicating a more equal distribution of $Eu^{2+}$ and $Eu^{3+}$ in this melt.

Figure 6.10 shows a scan rate study performed on two different sizes of tantalum microelectrodes: 30 µm and 100 µm diameter. From the study performed on the 30 µm Ta microelectrode the response was very consistent, with the repeat of the 500 mV/s scan rate identical to the first scan measured. This indicates that the device is functioning as expected and therefore the microelectrode is not undergoing any changes or deterioration in the harsh conditions of the molten salt. The response asymptotically approaches a sigmoidal response as the scan rate tends to zero. The increasing peaks with increasing scan rate is particularly apparent with the larger diameter electrode. Although the capacitance looks reassuringly low, there is also evidence of an increase in capacitative current with

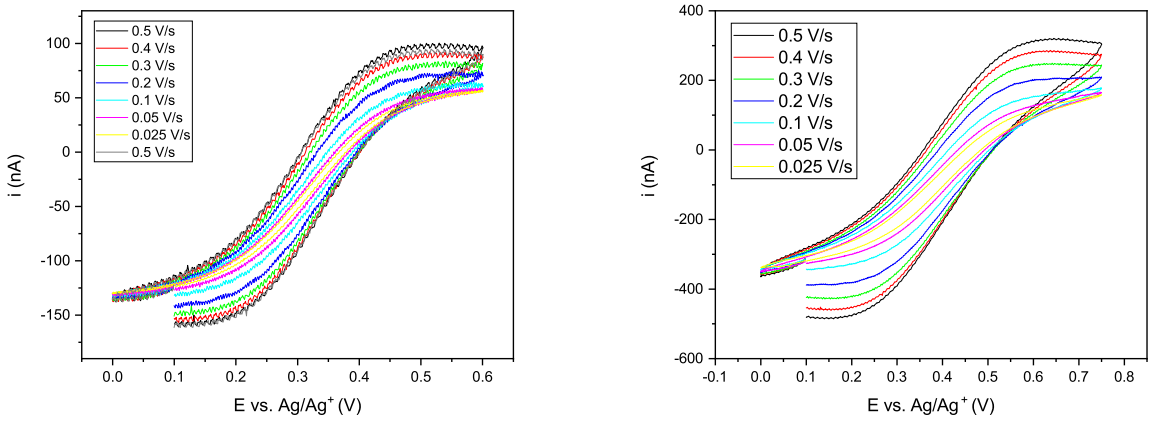


**Figure 6.10:** CVs at different scan rates with 30 µm (left) and 100 µm (right) diameter Ta microelectrodes in LiCl-KCl with 60 mM $EuCl_3$ at 375°C.

increased scan rate as would be expected due to the charging current described in Section 2.1.6. Interestingly despite the increased track resistance present in these electrodes the CVs shown in Figures 6.9 and 6.10 do not show any evidence of resistance. The extracted diffusion coefficient from the measurement using Equation eq: micro current was (4.99 ± 0.09) x $10^{-6}$ $cm^2$ $s^{-1}$, which is in very good agreement with literature values from various techniques where D was found to be (5.0 ± 0.2) x $10^{-6}$ $cm^2$ $s^{-1}$ at 430°C using microelectrodes.[87] Additional current is shown again for the 100 µm diameter Ta microelectrode due to peak shaped response and likely convection. This is consistent with the expectation that with the larger diameter electrodes there is more divergence from theory with a larger amount of less efficient planar diffusion present in the measurement.

#### 6.3.2.2 EIS measurements with Ta microelectrodes

From the consistency of the CVs and the improved reliability of Ta microelectrode lifetimes shown in Section subsec:Eliminating-the-adhesion there is confidence that these electrodes may be most suitable for impedance measurements in the molten salt environment. The typical EIS response is shown in a Nyquist plot for a 30 µm Ta microelectrode at E' (approximately +0.30 V vs. $Ag/Ag^+$) in LiCl-KCl with 60 mM added $EuCl_3$. E' was taken from the midpoint of the sigmoidal CV recorded using the tantalum microelectrode in the LiCl-KCl-EuCl system. Clearly the response is different from the typical response expected for a microelectrode which would be expected to have one semicircle and one near semicircular features. Instead for these measurements there were

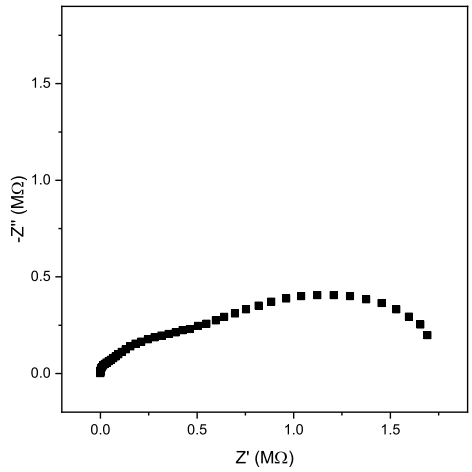


**Figure 6.11:** EIS response of 30 µm Ta microelectrode at E' in LiCl-KCl with 60 mM $EuCl_3$.

always three features evident in the Nyquist plot of the response. There appears to be an additional unexpected semicircular feature in the Nyquist response for these Ta microelectrodes. It seems likely that two of these observed semicircles will be the typical features of a microelectrode response with the $R_{ct}$ and $R_{nl}$ semicircular features present, however there seems to be an additional resistance and capacitance in parallel leading to a third feature in the EIS response at the highest frequency. As it is known that these electrodes suffer from a high track resistance it seems likely that this may be giving rise to this feature in the Nyquist plot.

Measurements on track resistances were performed as discussed in Chapter 5 using a probe station, and the Ta electrodes were found to have a large track resistance. Section5.5.5 discusses the origin of this; which was identified to be due to high temperature loading of the nitride furnace when the wafer was heated in the presence of air which likely converted a certain thickness of the tantalum to insulating tantalum oxide. Attempts were made to overcome this (also detailed in Section 5.5.5), but efforts to produce functioning Ta electrodes with a lower track resistance were unsuccessful within the time frame of this work. Despite the likely presence of an oxide layer on the microelectrodes, the devices were shown to function well in molten salt and could be used reliably to perform EIS measurements without the concern of electroactive area changes within the timeframe of the measurement. The magnitude of the resistance that affected the EIS measurements should be constant and could be compensated for in the equivalent circuit fit of the impedance response. The highest current recorded in the CV measurements on the functioning Ta microelectrodes was 150 and 400 nA for the 30 µm and 100 µm diameter electrodes respectively, the voltage drop over

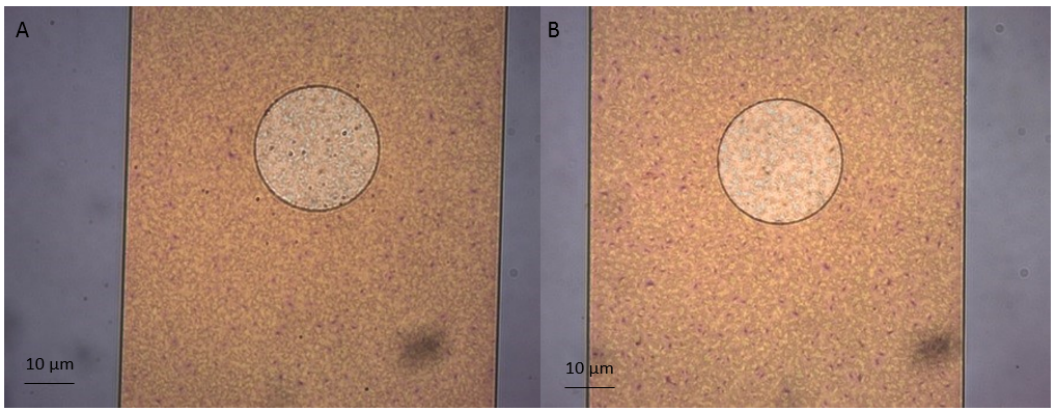


**Figure 6.12:** Comparison of 30 µm diameter Ta microelectrode before (A) and after (B) measurements of Eu in LiCl-KCl eutectic which was used to perform cyclic voltammetry, impedance spectroscopy and chronoamperometry for a period of 18 hours.

the length of the track is therefore is between 22.1 ± 12.9 mV to 58.8 ± 34.4 mV. As the track resistance was found to be consistent across different devices and the diameter of electrode should have no impact on the track resistance, the voltage drop is more apparent at the larger electrode diameters due to the increased limiting currents established. Previously a voltage drop of 18.4 ± 11.8 mV had been calculated for thin track platinum microelectrodes, which was considered small enough to not adversely affect the response too much.[123] It would be expected to lead to a reduced gradient around E', although this feature could also arise due to the high temperature of the measurements. It is interesting that this was a similar value to those calculated here and was previously neglected in molten salt measurements with microelectrodes. Clearly, although the calculated values of voltage drop are similar to previous values, there is evidence that track resistance contributes to the response of the device and is more apparent in the EIS measurements performed. Despite this voltage drop, the typical microelectrode response is still observable. As the Ta microelectrodes with high inherent resistance were shown to withstand the harsh environment of the molten salt well and could be used to reliably measure the system, they were used for further investigation of the europium reaction.

Figure 6.12 shows the comparison of a Ta electrode before use and after CV and EIS measurements of the europium couple for 18 hours. There was no apparent damage and it was clear that there was no metal loss. There is no observable difference between the images, lending confidence that the electrode area remained constant during the measurements performed.

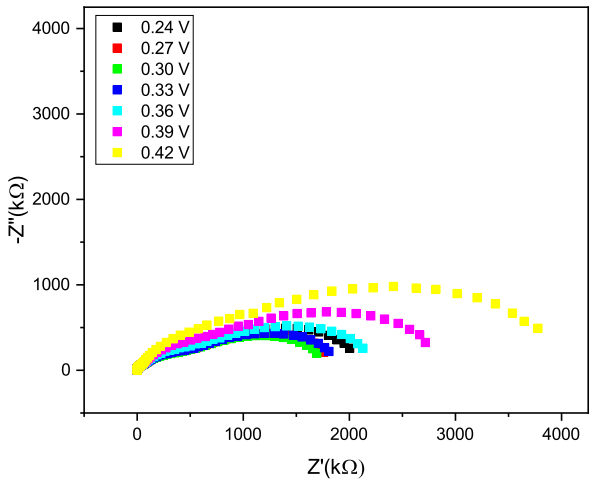


**Figure 6.13:** EIS response of 30 µm electrode in LiCl-KCl + 60 mM $EuCl_3$ at 375°C

#### 6.3.2.3 EIS fitting

The EIS response at different applied DC potentials around E' is shown in Figure 6.13. There is evidence that the impedance response changes across the range of applied potentials and appears to reach a minimum impedance at the value of E' determined from the cyclic voltammetry measurements. A wider step size between the applied DC potentials was used due to the elevated temperature the measurements were performed at, which would cause the expected bowl to widen.

The equivalent circuits were fitted for the responses at different applied DC potentials taking into account the influence of parasitic resistance (which is far more evident in EIS measurements than CVs). Thus the modified Randles circuit was required to be adapted to include the track parasitics. The circuit used to fit the response is shown in Figure 6.14. Parasitics have previously been used to modify equivalent circuit fits for impedance measurements to good effect by Schmueser.[140]

This modified Randles circuit with a parasitic resistance and capacitance was used to fit the EIS responses using NOVA without constraints. Except for imposing zero solution resistance, because the x-intercept was very small and this parameter could not be fitted without a very large error (in similarity with the macroelectrode analysis). An issue encountered was that the software could struggle to distinguish between the capacitance due to the double layer and the capacitance arising from parasitics, as they were of similar magnitude (both were single nanofarads). Care therefore had to be taken to prevent a switch in frequency of $Cdl$, $R_{ct}$ and $C_{para}$, $R_{para}$ from happening

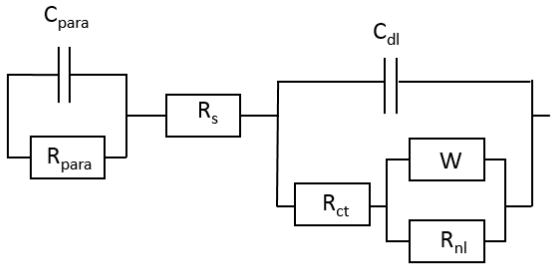


**Figure 6.14:** Modified Randles circuit with track parasitics used to model the tantalum microelectrode response.

when performing circuit fits; this could be achieved by switching the values and re-performing the iterative fit.

The values extracted from the circuit fits for the parasitics are shown in Figure 6.15. The errors shown are those associated with the fit of the model to the data. The fitted values for the parasitic elements are constant within error across the range of applied DC potentials where the EIS response was recorded. This is expected as the parasitics should not be dependent on the potential applied to the system. There is quite a large error on the values extracted for the parasitics and the best estimation for the circuit element was found by calculating a fixed mean value across applied DC potential, particularly when there were any outlying data points. The value of the parasitic resistance was found to be 76.06 $\pm$ 1.98 k$\Omega$ from a linear fit to the values. This was within error of that measured across the microelectrode devices using the probe station in Section subsec:Track-resistance. It is surprising that the extracted parasitic resistance was not higher as the EIS measurement was performed at an elevated temperature. There was variation in the sheet resistance measurements for the Ta wafer and measured track resistances which could account for a difference. This could be due to non-uniformity in the amount of Ta oxidised, variation within the etch process or removal of oxide within the melt.

A comparison of the fitted values on the charge transfer and non-linear resistance is shown in Figure 6.16. Fixing the values of the parasitics did not cause a large change in the extracted values, which was reassuring that it is a reasonable approximation of no change to the electrode within the measurement. It was found to have most impact on the second semicircular feature visible in the Nyquist plot, which was attributed to the charge transfer resistance and the double layer capacitance. The errors on the charge transfer resistance fitted values were reduced far more

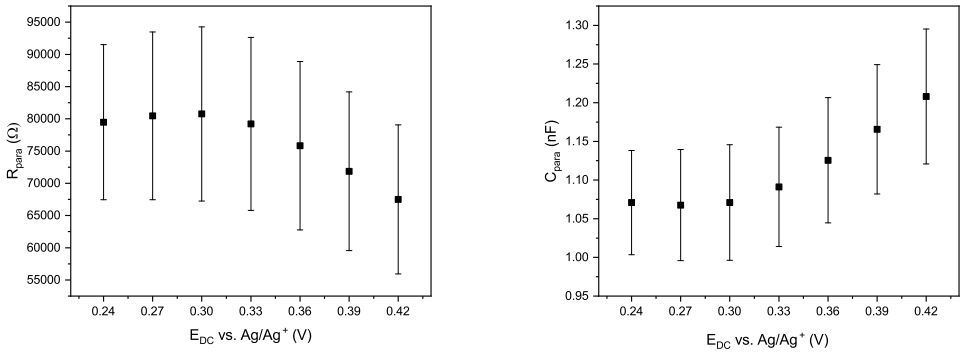


**Figure 6.15:** Fitted values for track parasitics in EIS response for 30 µm electrode in LiCl-KCl + 60 mM $EuCl_3$ at 375°C

than the error on the non-linear resistance. This is expected because the effect of the parasitics are observed in the highest frequency region of the Nyquist plot and thus there is more overlap with the charge transfer semicircle. Whereas the Warburg and non-linear resistance features are in the lowest frequency region and are better resolved from the parasitic semicircular feature. The characteristic shape of the $R_{ct}$ values with variation of applied $E_{DC}$ around E' is more observable in the fit when the parasitics were fixed as constant. This is consistent with previous work using background subtraction to account for parasitics within the measurement system.[140] Extracting a mean value for the parasitic resistance and imposing this fixed value on equivalent circuit fits was therefore determined to provide the clearest picture of the values. The iterative fit was then performed to extract the values for the other circuit elements, which are of more interest to provide information about the electrochemical reaction occurring.

Adaptions to the fitting process for the response at E' were explored to find the optimal fit for the response, including the weight factor. This weight factor multiplies each data point by the inverse square of the impedance modulus (rather than inverse of the square root of the average of the impedance modulus which multiplies each point by the same value) so that the fit is weighted to the highest frequency data points. Deselecting this means the software attempts to fit with equal weight to all points on the Nyquist plot. The software could not iteratively fit well to the data without using the weight factor unless the initial values for each circuit element were reasonably close to the likely true value. The constant value for the parasitics, particularly for the parasitic resistance, needed to be fixed when the weight factor wasn't used as otherwise physically unrealistic values such as a negative resistance could be output from the circuit fit. A complicating factor is

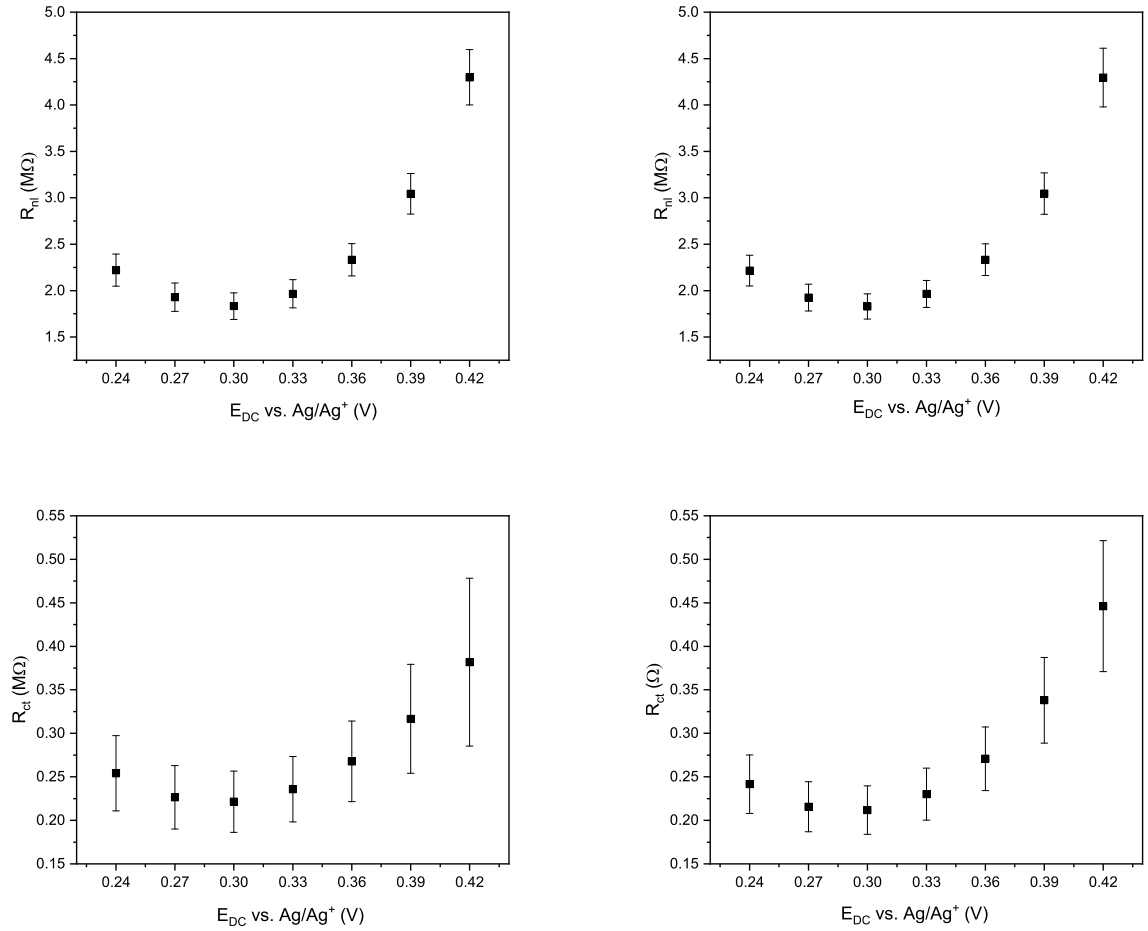


**Figure 6.16:** $R_{nl}$ (top) and $R_{ct}$ (bottom) values from the equivalent circuit fit allowing the parasitics to vary (left) and using a constant value (right) from all the fitted parasitics in Figure 6.15.

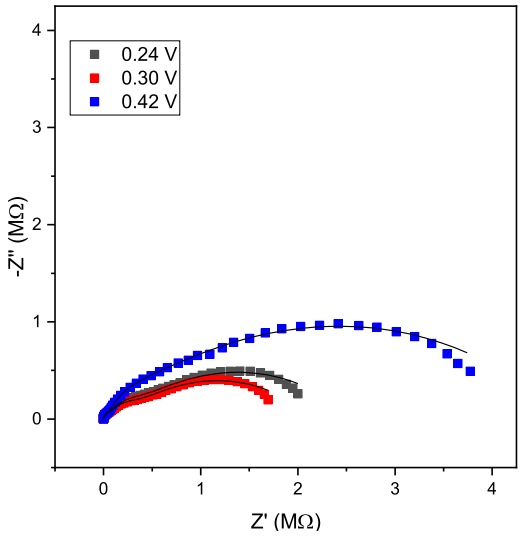


**Figure 6.17:** EIS response fitted with the circuit shown in Figure 6.14 for different applied DC potentials around E' = 0.30 V.

that the reported $\chi^2$ value with and without using the weight factor cannot be directly compared due to the difference in weighting each data point. The $\chi^2$ value was 0.04767 for the fit without the weight factor and 0.55482 when the weight factor was used. However, visually the fit looked better when the weight factor was used, although there was more deviation at the few last points at the lowest frequency (where typically convection can cause deviation). For the fit without the weight factor there was more deviation between the high frequency charge transfer region and the lower frequency diffusive region. Most of the values were not significantly different between the two fitting methods suggesting either could be used to model the system. The weight factor gave a better fit to the high frequency data, where noise and deviation due to convection is usually less of an issue. Therefore the weight factor was used for all subsequent fits shown in this thesis work.

The modified Randles circuit with parasitics was found to fit well using the weight factor to the recorded data. Although there was deviation for few the last few points the Warburg type response was still seen and the fit spans the entire frequency range. The equivalent circuit fits are shown in Figure 6.17 for applied DC potentials below E' (0.24 V), at E' (0.30 V) and above E' (0.42 V vs. $Ag/Ag^+$). For all the applied DC potentials where the EIS response was measured the circuit shown in Figure 6.14 fitted well as demonstrated below.

For previous measurements using platinum microelectrodes to measure the EIS response in LiCl-KCl with 19 mM $EuCl_3$ a constant phase element was required in order to fit the observed gradient

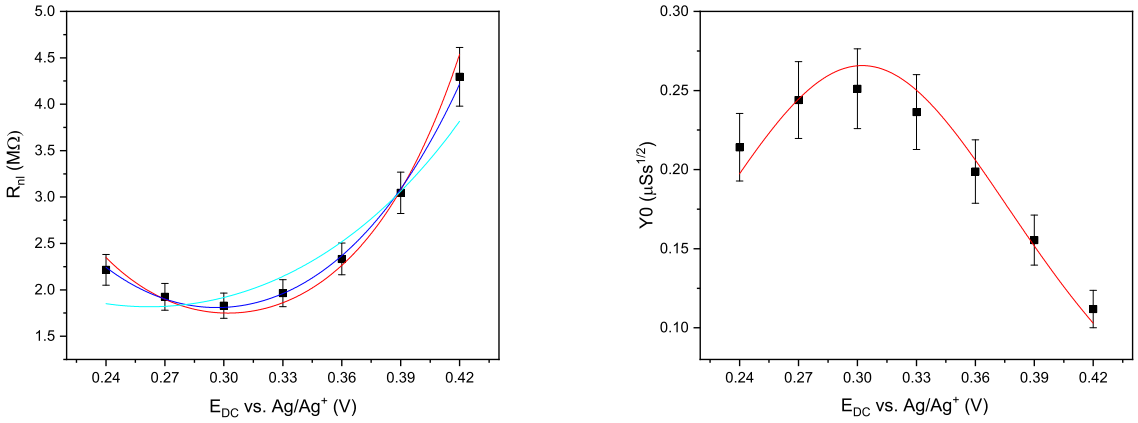


**Figure 6.18:** (Left) The non-linear resistance extracted from the EIS data presented in Figure 6.17 with fits to the thermodynamic (red) and kinetic (blue) models. The light blue line is forcing the transfer coefficient for the oxidation to be 0.5 whereas the dark blue allows all parameters to vary freely. (Right) The Warburg admittance extracted from the EIS data with the fit to the thermodynamic expression.

at higher frequencies which was greater than 45°.[87] Care should be taken in direct comparison with this data set as these measurements were performed on a platinum STTM electrode, which still has a relatively high track resistance (noted in Chapter 5). This was not accounted for in the analysis of the data. For the data collected with the tantalum microelectrodes the EIS response fitted well with the use of a Warburg element, as would be expected for a typical microelectrode with the establishment of planar diffusion initially. This suggests that the diffusional response is similar in aqueous and molten salt measurements. As diffusion coefficients for redox couples in the two solvents are very similar then this is understandable.

Figure 6.18 shows the variation of the extracted values of non-linear resistance and Warburg admittance from the EIS data presented in Figure 6.17. As already described in Section 2.2.3.6 $R_{nl}$ is expected to follow the thermodynamic expression: $R_{nl} = \frac{R_{nl,min}}{4}[2 + exp(\frac{nF(E_{dc}-E')}{RT}) + exp(-\frac{nF(E_{dc}-E')}{RT})]$, where $R_{nl,min} = \frac{RT}{nFi_l}$. Both the thermodynamic and kinetic expressions fit well within error to the extracted values from the EIS response. The parameters for all of the fits are summarised in Table 6.1. The kinetic fit first appears to fit better to the extracted data from the impedance response. However, there is an additional parameter in this fit with the transfer coefficient for oxidation, $\alpha_{ox}$, thus it is likely the introduction of an additional parameter which allows this to fit the data better. The fitted value for $\alpha_{ox}$ of 0.693 ± 0.014 is reasonably high. Although the reaction was found to be reversible with macroelectrode investigation and there is

little evidence of a clear difference in the cyclic voltammetric response, so it is unlikely that the $\alpha_{ox}$ value should be so far from 0.5. When the value of $\alpha_{ox}$ is constrained to be 0.5 the kinetic fit was found to offer a significantly worse fit with a $R^2$ value of 0.868. Therefore it can be concluded that the thermodynamic expression provides a better fit to the extracted $R_{nl}$ values.

An apparent transfer coefficient could be indicative of double layer effects. If reactants are adsorbed in an electrode reaction, this can affect the rate of reaction. Non-specific adsorption of reactant at the outer Helmholtz plane (start of the diffuse layer) is usually known as the Frumkin effect.[126, 236, 237] This causes an extended double layer (the structure of which is discussed in Section subsec:Electrical-double-layer) over which the electrode potential gradually decreases. In this situation the potential at the outer Helmholtz plane is a function of the applied potential, and not close to the zero potential experienced in the bulk solution. This can lead to deviations in the rate constant, exchange current and the apparent transfer coefficient. The measured rate constants and exchange current can be corrected for the Frumkin effect ($K^o = k_t^o \exp(\alpha(n-Z)F\phi_2/RT)$). Where $k_t^o$ is the true rate constant from the apparent one, $K^o$, $z$ is the charge on the species undergoing reduction and $\phi_2$ is the potential at the OHP. The effect on the transfer coefficient can be understood by considering the ratio between the Stern layer and Debye length. Deviations from the classical Butler-Volmer approach are likely to occur at small electrode potentials, in combination with small Stern layer thickness to Debye length ratios. Although the Frumkin correction can account for deviation of the transfer coefficient from 0.5, careful consideration of when it should be applied is important. There could be other causes perturbing the value such as large reorganisation of the species involved leading to multiple reaction steps.[126] Historically the correction was easiest for application with liquid electrodes due to the insufficient data to model the double-layer structure at solid electrodes. Specific adsorption of electrolyte, reactants and products is a common occurrence and with different ions there can be uncertainty in the $\phi_2$ value which can hinder corrections. Most electrochemical measurements utilise high concentrations of background electrolyte to ensure sufficient screening to minimise the potential experienced at the OHP.[126]

The double layer in a molten salt is thought to be similar in composition to those established in aqueous conditions with compact and diffuse layers. Many computational studies have been performed to investigate the structure.[238–241] Some of these suggest there could be longer ranged order in a molten salt which comprises many charged ions and the inorganic species as the solvent.[72, 145] The experimental study of the double layer within a molten salt has been

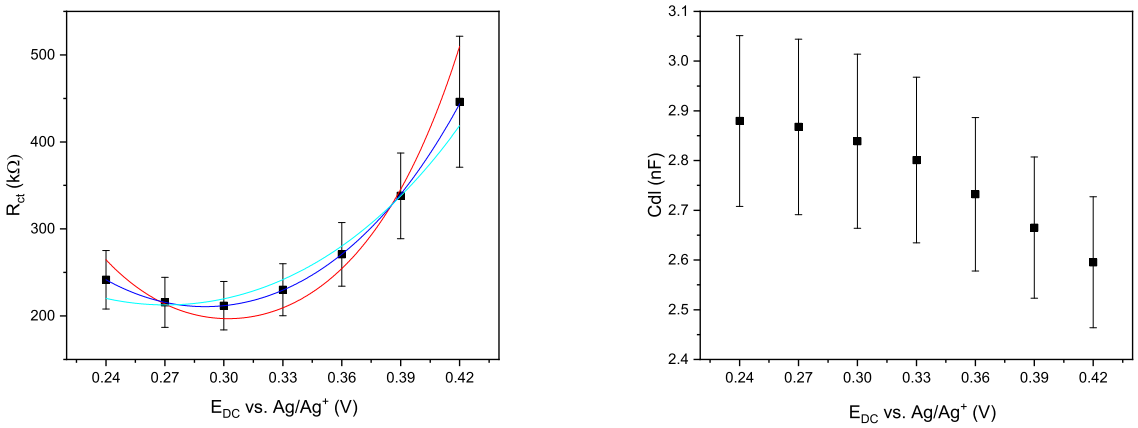


**Figure 6.19:** The charge transfer resistance extracted from the EIS data presented in Figure 6.17 with fits to the thermodynamic (red) and kinetic (blue) models. The light blue line is forcing the transfer coefficient for the oxidation to be 0.5 whereas the dark blue allows all parameters to vary freely. The lower graph shows the double layer capacitance extracted from the EIS data with the errors associated with the fit.

frustrated by the high temperatures and challenging experimental conditions. A notable mention is Fellner's work which used an a.c. bridge and liquid electrodes as well whose work showed large dependence on temperature, and a minimum value close to the radius of a potassium ion in the melt.[242] From the values extracted from impedance spectroscopy within this work the thickness of the double layer is similar to the values extracted in aqueous systems, suggesting that adsorption and an extended double layer is unlikely. Correcting for the Frumkin effect therefore would not seem to be suitable for these measurements. Instead it seems likely that deviation from the expected value for the transfer coefficient is due to other physical factors in the melt.

When the diffusion regime was investigated using a constant phase element the mean n value was found to be 0.543, which was remarkably similar to that found for the aqueous investigation of MNEE arrays (0.542) performed by Schmueser for frequencies describing planar diffusion to individual array elements. For purely planar diffusion and a description of the Warburg element the n value would be 0.5. The very similar values indicate that planar diffusion is a good description of the physical response occurring in the local volume of the microelectrode. The modified Randles circuit was found to fit a single microdisc response in molten salt well.

Turning to the higher frequency region and the second semicircular feature observable in the Nyquist plot where $R_{ct}$ and $C_{dl}$ control the impedance response, Figure 6.19 shows the $R_{ct}$ values extracted from the EIS response and the errors associated with the fit. Although the $R^2$ value for the

thermodynamic fit is lower than for the kinetic fit (as can be seen from Table 6.1) both the kinetic and the thermodynamic model fit the data within one standard deviation. From previous aqueous work on microsquare electrodes it has been shown that the charge transfer resistance can be modelled by the thermodynamic model.[120, 139] This has been of subsequent interest in the determination of whether the electron transfer is limited by mass transport or kinetics. Comparison of the $R_{nl}$ and $R_{ct}$ functional forms indicates that there is more divergence between the kinetic and thermodynamic models for the $R_{ct}$ extracted values. It is also noticeable that constraining $\alpha_{ox}$ does not result in a fit that deviates within the experimental error. From this data set it is inconclusive which fit best represents the physical reality of the system due to the relatively large errors associated with the data points, although this has been greatly reduced from previous measurements.[87] This could be due to the parasitics present in the system making it difficult to reliably fit the high frequency impedance response due to overlap between the semicircular features. In the fit of the models to the extracted values at applied potentials around $E'$ the added parameter of the transfer coefficient causes the kinetic model to fit the extracted data better than was seen for the non-linear resistance. Previous measurements of europium in LiCl-KCl eutectic by Corrigan demonstrated that the established EIS theory for aqueous conditions can be used to extract quantitative information from microelectrode measurements within a molten salt environment.[87] However, in this case although the non-linear resistance was seen to follow the expected form with variation in the applied DC potentials, the charge transfer values extracted were shown to be discontinuous. This could be due to a small influence from parasitics within the system, which were not accounted for and would affect the high frequency region of the impedance response. This work reduced the mean error on measurements. It is reassuring that with this improvement the typical variation in $R_{ct}$ with applied DC potential is observed for molten salt measurements as has been shown for aqueous measurements. This corroborates the fact that impedance spectroscopy can be a useful tool for the extraction of quantitative information about the reactions occurring in molten LiCl-KCl eutectic.

The double layer capacitance is seen to be constant within the limitation of error across the variation of applied potentials. The mean value of the double layer capacitance was calculated to be 381.9 $\pm$ 1.2 $\mu Fcm^{-2}$ which is two orders of magnitude higher than that seen in aqueous measurements with platinum microelectrodes.[140] It was also larger than that extracted by Corrigan for the measurement of europium in molten salt with platinum microelectrodes, which was 86 $\mu Fcm^{-2}$,[87]

| | Fit notes | |
|---|---|---|
| $R_{ct,\ min}$ | kinetic | 210.7 ± 7.2 kΩ |
| E' | | 302.2 ± 4.3 mV |
| $R^2$ | | 0.999 |
| $R_{ct,\ min}$ | thermodynamic | 196.9 ± 7.2 kΩ |
| E' | | 302.2 ± 4.3 mV |
| $R^2$ | | 0.811 |
| $R_{nl,\ min}$ | | 1.750 ± 0.361 MΩ |
| E' | | 302.1 ± 2.3 mV |
| $R^2$ | | 0.962 |
| $Y_{0\ W,\ max}$ | | 0.266 ± 0.007 $\mu Ss^{1/2}$ |
| E' | | 302.4 ± 3.2 mV |
| $R^2$ | | 0.958 |

**Table 6.1:** Regression parameters for the 30 μm diameter microdisc tantalum electrode EIS fits.

although in his measurement the $R_{ct}$ was not seen to follow a clear bowl shaped functional form suggesting that the high frequency region was difficult to fit accurately. This may be due to a slight influence of parasitics which wasn't clearly distinguishable from the impedance response. It is interesting that his measurement is also higher than typical aqueous values, which are usually around 10 $\mu Fcm^{-2}$. This suggests that the double layer in the molten salt system could be thinner than that for an aqueous solvent. This is plausible as the entire solvent in the molten salt is of charged ions in comparison to the background electrolyte present for screening charges in aqueous measurements. Alternatively it could hint that there is more structure or a feature of surface screening. $R_{nl,\ min}$ is slightly higher than the value extracted from the CV measurements which give a value of 1.117 ± 0.625 MΩ, although only 34.3% different and within error of each other. Assuming that $R_{ct,\ min}$ follows the kinetic model the rate of electron transfer can be calculated as $k^0$=0.013 cm $s^{-1}$(using the literature value of 5 x $10^{-6}$ $cm^2s^{-1}$. This is interesting as it is between the values published for this LiCl-KCl-EuCl system, with a value of 3.31 × $10^{-3}$ cm $s^{-1}$ (on a glassy carbon macroelectrode) and a value of 0.26 cm $s^{-1}$ (on a platinum microelectrode).[87,167] It has previously been demonstrated that in aqueous measurements using microelectrodes the enhanced mass transport rates enable the measurement of faster charge transfer rate constants which are more realistic. The microelectrode used here was smaller than that used by Corrigan for the platinum microelectrode measurement. Although the measurement published is 55°C higher and the concentration was about a third of the value used within this thesis work the order of magnitude difference could indicate that the parasitics are still complicating the measurement of the true rate

constant. The values of E' are consistent across all the extracted parameters and also in the CVs both for macro- and micro-electrodes and with literature values.

## 6.4 Conclusions

Platinum microelectrodes have been shown to be suitable for quantitative measurements in aqueous conditions. In aqueous systems the platinum microelectrodes produced reliable measurements demonstrating that the fabrication was reliable. However, the platinum devices were shown to suffer damage in the molten salt environment and EIS measurements showed an evident change in the impedance response. Platinum microelectrodes were only able to provide good initial results in the molten salt. This was consistent with the work performed to optimise devices discussed in Chapter 5. This along with the desire to remove the adhesion layer motivated the work performed to create more resilient devices to enable reliable measurements to be performed for a longer period of time, leading to the fabrication of tantalum microelectrodes.

The high resistance of the tantalum electrodes was determined to be dominated by the resistance of the track. Because of the high resistance the devices were found to be incapable of performing aqueous measurements. However, in molten salt measurements, despite the high parasitic resistance present in the devices, a characteristic response was observable in all of the measurements performed using the tantalum microelectrodes. Quantitative parameters could be extracted from the impedance response utilising these devices as working electrodes by incorporating the parasitic features into the equivalent circuit. The modified Randles circuit with parasitics was shown to provide a good fit to the EIS response. The tantalum electrodes were found to be resilient and capable of performing long term measurements within a molten salt enabling investigation using techniques such as EIS.

The molten salt measurements showed similar features to aqueous measurements. A thermodynamic model was concluded to best fit the $R_{nl}$ feature when measured using impedance. The higher frequency region was more challenging to measure due to the ratio of the response to the parasitic feature. It could not reliably be determined whether the impedance feature fitted better to the thermodynamic or the kinetic model. Coupled with the lower rate constant measured for the europium system the charge transfer rate should be further investigated. To probe this further and gain a better measurement of the rate constant for the reaction it is desirable to improve the ratio of the

response due to the charge transfer to the parasitics. One way of achieving this is to further decrease the size of the active electrode area. Moving towards using nanoelectrodes to gain more insight into the processes occurring during the reaction, the demonstration of tantalum microelectrodes enabling the system to be probed reliably encourages the use of tantalum nanoelectrodes, which will be discussed in the next chapter.

# Chapter 7

# Nanoelectrode Characterisation

## 7.1 Introduction

Nanoelectrodes have been shown to offer advantages in measurement sensitivity compared to microelectrodes due to the further enhancement of diffusion as a result of the larger diffusion fields generated.[95, 97, 104] Within the research group nanoelectrode arrays have been developed by cutting through a deposited thin metal layer to expose a band of metal around the edge of the microscale aperture. The resulting band nanoelectrode thus has a critical dimension on the nanoscale. This harnesses the benefits offered by microfabrication such as control over the dimensions and production reliability without the need for serial costly processes such as e-beam lithography to create nanoscale patterns.[107, 124, 140, 243] These nanoband electrodes have been shown to function well in aqueous solutions as biological sensors and offer insight into processes occurring at the nanoelectrode interface.[119, 125, 139, 140, 231, 244] These have been produced as nanoelectrode arrays to overcome the issue of low signal and are known as microsquare nanoband edge electrodes (MNEE).[124, 140, 231] The schematic of this design is shown in Figure 7.1, which shows the historic design which has been optimised for aqueous measurements. The nanoelectrodes are produced by continuing to etch through the metal and the adhesion layer, after opening up windows in the top insulating layer to expose the active metal electrode. Etching completely through the metal leaves a band exposed at the edge of the aperture, which is of nanometre dimension and thus has a critical length on the nanometre scale and functions as a nanoband electrode. The vertical positioning of the nanoelectrode band within the stack (near the middle or at the bottom

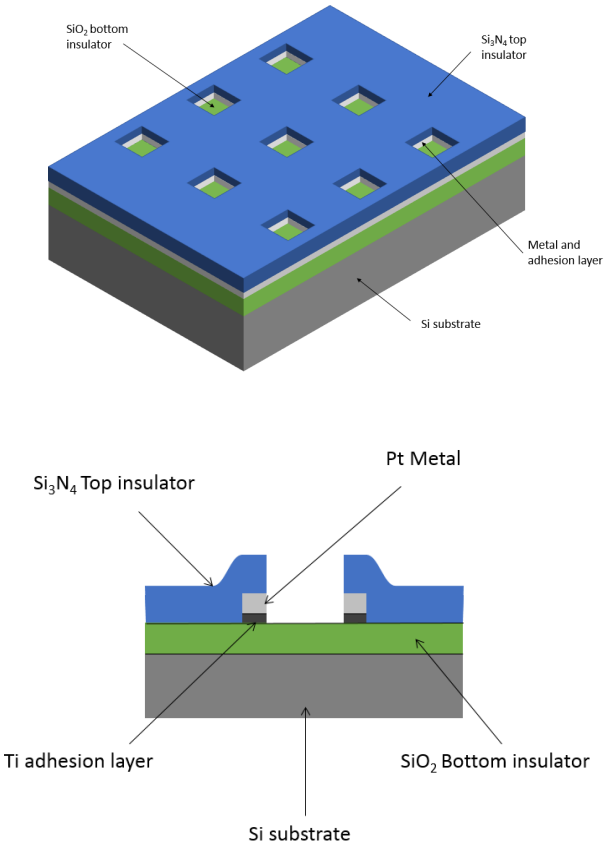


**Figure 7.1:** Schematic (top) and cross section through (bottom) part of the MNEE nanoelectrode arrays that have previously been used for aqueous electrochemical measurements (not to scale).

of the aperture) has been shown not to have a large influence over the sensing capabilities of the electrode.[124, 140]

This historic design of nanoelectrodes within the research group ensures arrays of individual nanoelectrodes with specified separations between each electrode. Although this offers the beneficial property of amplifying the total current (signal) measured, as each nanoelectrode will contribute to the measurable current, it can also complicate the response signal with diffusional array overlap occuring at longer times.[245, 246] For example in impedance spectroscopy this can complicate the analysis of the response of the system, as diffusional array overlap will occur eventually leading to planar diffusion and a Warburg type response. Unfortunately, it is not possible to fit both the response from the individual nanoelectrode and the overlap with a single equivalent circuit. This

has previously been tackled by separating the two different regimes and independently fitting to them.[140] Depending on the spacing between the individual nanoelectrodes in the array the onset of array overlap will change, occur at increasing frequency with a decrease in spacing, and this can interfere with the individual nanoelectrode response. This could be avoided by developing single nanoelectrodes.

The MNEE devices have been designed and utilised as arrays for for enhanced redox sensing and analysis within the group.[124,125,244] These devices have been optimised for and used in relatively mild aqueous conditions. For example, the nanoelectrodes were developed with an adhesion layer of titanium as when these were used in aqueous conditions the titanium would spontaneously oxidise and form surface $TiO_2$ as insulation, ensuring the adhesion layer would not contribute to the electrochemical signal. This was shown to function well for aqueous experiments which were performed with platinum as the active metal on titanium. Such an approach would not apply in molten salt, as the adhesion layer would remain conductive and active. There are also larger thermal stresses due to the higher operating temperature range and a greater materials challenge due to the corrosive environment. A titanium adhesion layer would likely also suffer damage in the molten salt, as it had previously been shown not to be resilient in the LiCl-KCl melt.[123] It would be desirable to produce molten salt compatible nanoelectrodes which would help elucidate processes occurring at electrode interfaces. Using the information gained from materials optimisation to create molten salt compatible microelectrodes it should theoretically be possible to fabricate nanoelectrodes which function in the melt. This chapter details work to develop molten salt compatible nanoelectrode systems, building on the microelectrode development work in Chapter 5.

Although the majority of previous work within the group has utilised square nanoband electrodes within this thesis work only ring nanoband electrodes were developed. This was chosen since the end goal was the development of molten salt compatible nanoelectrodes, the corners on square electrodes have been shown to be a point of failure due to stress, and the electrodes should experience more thermal stress at higher temperatures.[123] Previously only arrays of nanoelectrodes have been utilised for analysis so an additional aim is to test whether it is possible to accurately and quantitatively measure the low currents produced by single nanoelectrodes.

### 7.1.1 Improvements to design for molten salt nanoelectrode measurements

Although arrays have been used successfully to increase the measured signal there is still the possibility of overlap of the diffusion fields which complicates the signal and transitions into a macroelectrode type response.[95, 109, 140] This will affect the response at lower scan rates for cyclic voltammetry and at lower frequencies in EIS measurements. The response of an individual nanoelectrode has been analysed as has the overlapping macroelectrode response region, however, there is no analytical expression to model the transition region between these regimes.[125, 140] Thus, the response from a single nanoelectrode is easier to model and would be desirable to use for EIS measurements as long as the low currents produced can be reliably measured and give acceptable signal to noise ratio.

The titanium adhesion layer was suitable for aqueous measurements due to the spontaneous formation of an insulating oxide layer which meant contributions to the current from the adhesion layer were negligible. However, it is known that alkali salts can dissolve oxide films.[56, 163] This is corroborated by the demonstration that metals such as tungsten and tantalum, which typically have oxide layers preventing their use in aqueous systems, function as electrodes in molten salt systems. [57, 87] The adhesion layer would then be acting as an exposed conductor so the electrode critical dimension would be that of the metal and the adhesion layer together, but the influence of this could be limited by reducing the thickness of the metal and the adhesion layer deposited to the total desired critical dimension. This assumes that the response of both metals is equivalent (they act as inert electrodes) which may not be the case if they were to form alloys or specifically react with any of the redox agents or the salt itself. One piece of evidence which suggests this may not be the case when titanium was used previously as an adhesion layer in molten salt is that the titanium was found to be chemically removed, and led to electrode delamination.[123] This would be expected to be a critical issue for a nanoelectrode, because the adhesion layer would be exposed to the melt. So delamination is likely to be more severe for nanoelectrodes in comparison to microelectrodes where presumably pinholes were the access point for the salt. The solution for the adhesion layer in microelectrodes suitable for molten salt measurements was found to be replacing the titanium with titanium nitride.[123] This could also be a possible adhesion layer to produce molten salt compatible nanoelectrodes as in Chapter 5 TiN was found to be resilient in the LiCl-KCl eutectic. Titanium nitride is used as a metal in the semiconductor industry, thus would

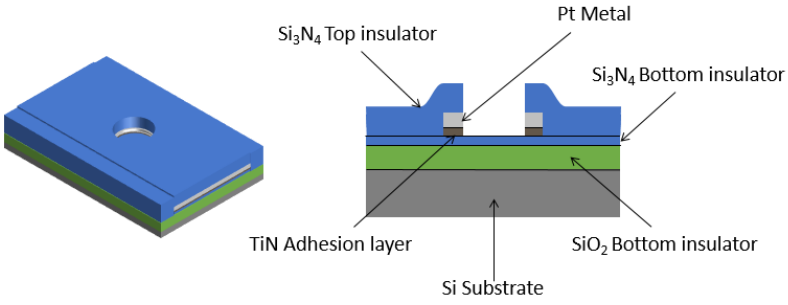


**Figure 7.2:** Schematic (left) and cross section through (right) molten salt compatible nanoelectrode design, with improved sandwich insulator and adhesion layer. (Not to scale).

likely be electroactive and contribute to the critical vertical dimension in the nanoelectrode design and hence the measured signal. Indeed, Blair's attempt at conversion of a microelectrode into a nanoelectrode demonstrated the proof of principle but had a significantly higher current, which could be consistent with an electrochemically active TiN adhesion layer.

It is also known that the silicon oxide can be damaged and undergo thinning within the molten salt.[123] For the nanoelectrodes the underlying insulator is exposed to the melt at the base of the nanoelectrode aperture (apparent in Figure 7.1) and thus it is considered likely that this exposed oxide might be attacked and removed by the melt. Therefore more of the adhesion layer could have been exposed to the melt leading to the possible increase in active electrode area for Blair's device. As stoichiometric silicon nitride was found to offer better resilience in the harsh environment of the molten salt,[123] and be beneficial in alleviating the possibility of shorting to the silicon substrate as discussed in Section 5.2.5, all nanoelectrode designs incorporated a nitride sandwich structure to prevent shorting and diminish likelihood of undercut. $SiO_2$ was essential to keep within the architecture as it offered important stress relief within the structure. A schematic and cross section through the architecture of these platinum nanoelectrodes initially fabricated for use in the molten salt is shown in Figure 7.2.

The nanoelectrodes were fabricated in a similar manner to microelectrodes (detailed in Chapter 2), apart from the final step of deeper etching through the microelectrode. Once the metal was exposed the etch was continued to remove the metal and adhesion layer from the opening, whilst masking the bond pad to ensure that this wasn't damaged and ensure a good connection could be made to the nanoelectrodes. It should be noted that the initial devices still used the super thin

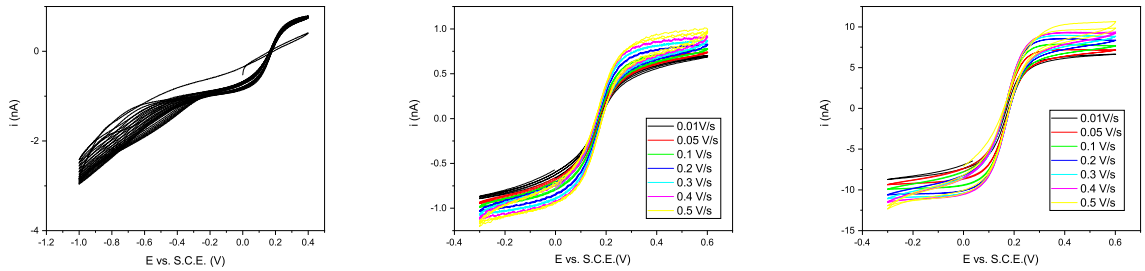


**Figure 7.3:** Cleaning CVs at a scan rate of 100 $mVs^{-1}$ of a nanoband electrode of 10 μm aperture (left) and subsequent for CVs at different scan rates (centre) in 1 mM FFC in 0.1 M aqueous KCl solution. Equivalent scan rate study with a ring nanoband of 100 μm aperture (right).

track design (discussed in 5.X) as they were fabricated before the decision to change to a larger area for the track to reduce the amount of track resistance encountered. The first Pt devices fabricated in this work were nanoband rings with a TiN adhesion and platinum layers of 20 nm and 50 nm respectively. Their response was then tested.

### 7.1.2 Aqueous performance of Pt nanoband rings

As previous work has predominantly focused on square nanoband arrays the single platinum nanoelectrodes were first tested aqueously to ensure they were performing as expected prior to testing the devices in the LiCl-KCl eutectic molten salt. It was also important to establish if the response could be reliably measured with commercial potentiostats, which is a particular challenge when using a single nanoelectrode as the current measured is likely to be very low. Additionally as the proof of principle square nanoband device had shown a much larger current,[123] it was particularly important to establish that these nanoelectrodes functioned quantitatively in aqueous conditions. CVs were measured at different scan rates for each electrode using 1 mM ferri/ferro in 0.1 M KCl, in the same way as for the microelectrodes in Chapter 6. Similar to the microelectrodes tested aqueously, the nanoelectrodes required several wider cleaning CVs before the expected nanoelectrode response was observed (Figure 7.3 (left)). After a couple of cycles the resistive response changes to show a near sigmoidal response with clear limiting currents characteristic of the steady-state response from a micro- or nanoelectrode. This rapid change from a resistive response is most likely to be due to the mechanical and chemical cleaning effects of gas evolution due to potential excursion past the limits of the solvent window. This could remove contamination on the

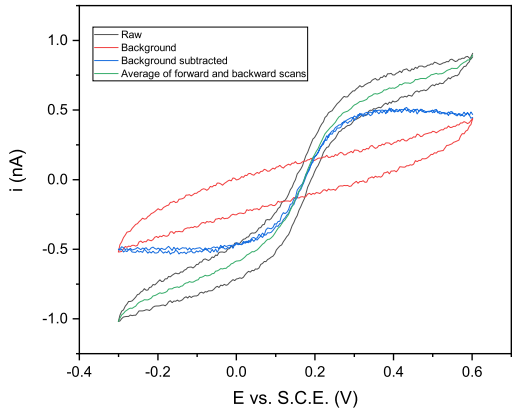


**Figure 7.4:** Graph showing the typical CV of 10 μm diameter electrode (as shown in Figure 7.3) at $v$=500 $mVs^{-1}$ in 1 mM FFC with 0.1 M KCl background electrolyte, the parasitic capacitance measured without redox agent and the difference between them (blue), also shown is the mean of the forward and backward scans (green). The onset potential was 0 V with the initial direction of scan in the positive direction.

active metal surface of the nanoelectrode, such as any residual photoresist coating. The response at different scan rates (10-500 $mVs^{-1}$) are shown for a nanoband ring electrode at the smallest and largest diameter aperture, 10 μm and 100 μm diameter, respectively in Figure 7.3 (centre and right). On the CVs (particularly at faster scan rates) there is some noise evident, similarly to the single microelectrodes measured aqueously in Section 6.2. However, the slower scans were of high quality and could be used to extract limiting currents. It is encouraging that the observed currents, even for the fastest scans and smallest diameter nanoelectrode for which the response is shown ( 10 μm), is significantly larger than the noise level. With these measurements it can be concluded that the response can be readily measured for such single nanoelectrodes with a critical dimension of 70 nm and therefore single devices can indeed be used to analyse reactions and avoid the possibility of complication due to diffusional overlap when using an array. This is especially promising as the concentration of the redox couple ( 1 mM each of ferricyanide and ferrocyanide) is reasonably low and significantly lower than the concentrations used for typical analytical measurements in this molten salt in the literature.[57, 79, 87]

At faster scan rates a small amount of resistance and capacitance can be observed in the voltammetric measurements. Previously, observations of capacitance in data from square nanoband MNEE arrays has been attributed to the parasitic capacitance that arises from non-Faradaic charging of the dielectric layers between the metal plane and the solution.[125, 140] (An additional source of

capacitance could be the influence of the TiN metal adhesion layer as spontaneous thin oxide layer could form on the TiN upon exposure to air.[247]) Parasitic capacitance shows insensitivity to the potential and increases with $v$. As can be seen in Figure 7.3, in this data set the influence of capacitance is more apparent at faster scan rates and appears to be independent of potential. The effect of parasitic capacitance should be removed by background subtraction of the measurement in background electrolyte as the charging current is in parallel with the redox current. An example of this is shown in Figure 7.4 for the 10 μm diameter nanoband ring electrode. The parasitic capacitance is relatively invariant with the applied potential which is consistent with a non-Faradaic process, although there is also evidence of resistance in the background measurement. For the measurement at a single nanoelectrode in comparison with an array, the parasitic capacitance has a greater effect on the measured current. This is understandable as the measured current from an array is amplified with the number of independent electrodes in the array. It is also apparent in comparison of the scan rate study shown at different sizes of electrode in Figure 7.3. The parasitics cause a greater effect on the response measured for the 10 μm diameter nanoring in comparison with the 100 μm diameter nanoring which has a significantly larger redox response. In the case of the single nanoelectrode background subtraction gave an extremely good CV response of the characteristic sigmoidal response from a nanoelectrode. The simple averaging of the forward and backward scans, which had been shown to approximate the redox response with nanoelectrode arrays did not result in such a characteristic sigmoidal response for the single nanoelectrode. This is most likely due to the background resistance also present in the data which was better accounted for with the background subtraction. Whilst the impact of the parasitics is larger for the single nanoelectrode response these results have the benefit of avoiding array diffusional overlap which causes the time independence of the redox response to be lost. Interestingly although the data collected with platinum nanoelectrodes is approaching invariance with scan rate, there is still some evidence of decreasing redox current with decreasing scan rate. For the nanoelectrode arrays this had been attributed to the array overlap.[125] That is clearly not the case for this data set which employed single platinum nanoelectrodes and whilst in this data set is significantly smaller variation than that seen with nanoelectrode arrays, it is unclear why this feature is evident. One possibility is that it could occur due to the structure of the recessed nanoband which is not an ideal planar nanoelectrode.

A plot of the average measured limiting current versus the diameter of the nanoband ring electrode

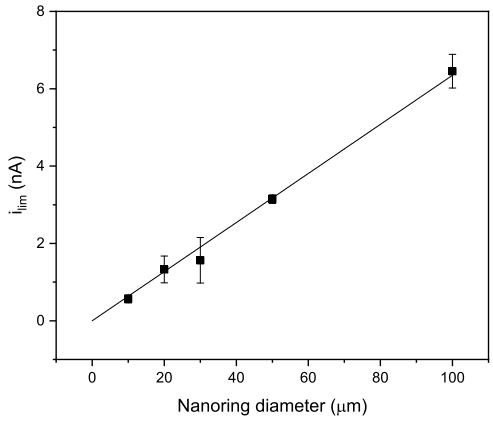


**Figure 7.5:** Comparison of background subtracted limiting currents from at least 3 electrodes of each size with the expected steady state current for various sizes of nanoelectrodes rings measured for the oxidation of ferrocyanide (left) and the reduction of ferricyanide (right). The theoretical current is shown by the red lines (solid line B=1.46, dashed line B=1.6) and the solid black line is the linear fit for the experimental data and the dashed black lines the linear fit with an intercept of zero.

is shown in Figure 7.5 for the oxidation of ferrocyanide. A linear regression was fitted to the values which gave a gradient of 6.35 x $10^{-5}$Am$^{-1}$. Using Equation eq: nano current for the limiting current of a nanoring band electrode ($i_l = 1.46nFDcr$) gave a diffusion coefficient of 4.51 x $10^{-4}$ cm$^2$s$^{-1}$. The experiment wasn't thermostatted, so this could account for some deviation but does not seem likely to account for a difference of this magnitude.

Reassuringly there is a clear linear trend observable for the measured limiting current confirming that it is directly proportional to the radius of the electrode. The $R^2$ value for the linear regressions performed on the experimental values were all $> 0.998$. The prefactor extracted for the theoretical limiting current of a nanoband ring electrode was modelled using the assumption that the adhesion layer was not contributing to the measured current. Whilst this was applicable to the historic architecture of nanoelectrodes using titanium in aqueous measurements it was a concern that the TiN adhesion layer may be increasing the size of the nanoband by approximately 20 nm (two fifths of the assumed nanoelectrode. The higher measured current than expected from the equation suggests a larger active electrode area, this is consistent with the TiN adhesion layer contributing to the measured signal thus increasing the critical dimension of the nanoelectrode. The difference between the linear regression with and without a fixed intercept of zero is minimal. The prefactor was extracted from the gradient of the linear regression with fixed intercept as 2.123$\pm$ 0.001 and

2.176± 0.050 for the oxidation and reduction respectively. Within experimental error these values are consistent. Although there was a larger deviation from the theoretical limiting current across all measured sizes of electrode, the 100 µm (largest aperture) ring electrode seemed to follow the linear trend well. This is clearly different from the largest diameter microelectrode which diverged from the linear trend. This is reassuring since the critical width should be the thickness of the metal layer in the nanoelectrode structure. This was consistent for all the devices, so only the area of the electrode should increase with a change in the diameter of the recess for the nanoelectrode, which should result in an increase in measured limiting current rather than a change of the characteristic type of response.

### 7.1.3 Silver measurement in molten salt with Pt nanoelectrodes

The nanoelectrode devices tested were found to function initially in the melt and gave clear limiting currents within experimental error of those predicted by Equation eq: nano current. The current typically increased over time during the measurement, this is shown for a 100 µm diameter nanoband electrode in Figure 7.6. For this nanoelectrode initially the expected limiting current was observed in the early scans, but this rapidly increased to over six times the expected value, suggesting a large increase in electroactive area.

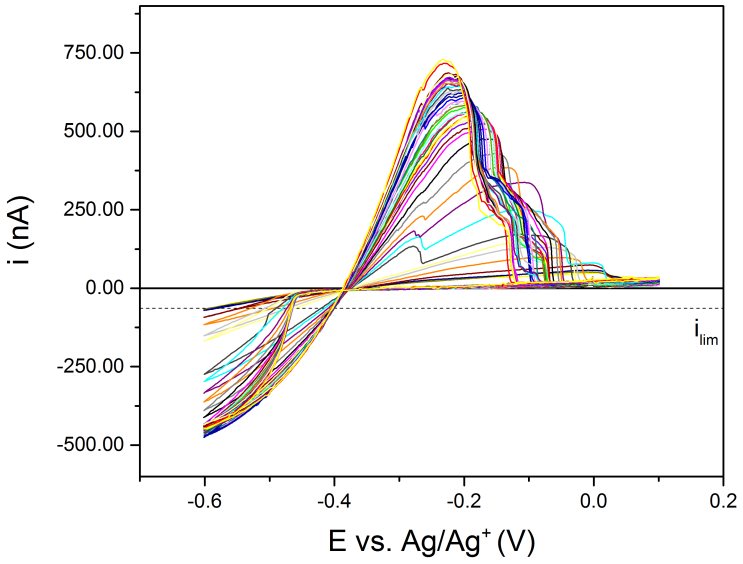


**Figure 7.6:** Graph of 100 µm nanoelectrode response over time at 0.1 V/s in LiCl-KCl eutectic with 10 mM AgCl, showing increasing current with immersion time.

This could be explained by the ring of buried metal becoming exposed to the melt and hence electrochemically active illustrated in Figure 7.7. The expected current for this scenario can be calculated as a microelectrode missing the central region $i_{lim,ring} = i_{lim,total\ diameter} - i_{lim,nanoring\ diameter}$. The total diameter of the buried metal disc is 200 µm missing an 100 µm disc, thus this would give rise to an expected magnitude of limiting current of $i_{lim} = i_{lim,200} - i_{lim,100} = 941.69 - 470.85 = 470.84$ nA. This value is very similar to the final current. Interestingly, the current spikes previously seen on the microelectrodes was not evident. Instead at intermediate times there are two clear stripping peaks. This could be indicative of removal from two different surfaces, perhaps from the platinum and the TiN adhesion layer.

After removal from the melt clear delamination of the nanoelectrode was confirmed, as can be seen in Figure 7.7. Analysis with reflectometry and EDX confirmed that the exposed area was insulator and that both the TiN and platinum had been removed. This had previously been seen by Blair for test chips of TiN and Pt where delamination occurred for a minimum of 5 hours.[123] A very small amount of delamination was also observed for the trial nanoelectrode, although this was only cycled for 10 minutes.[123]

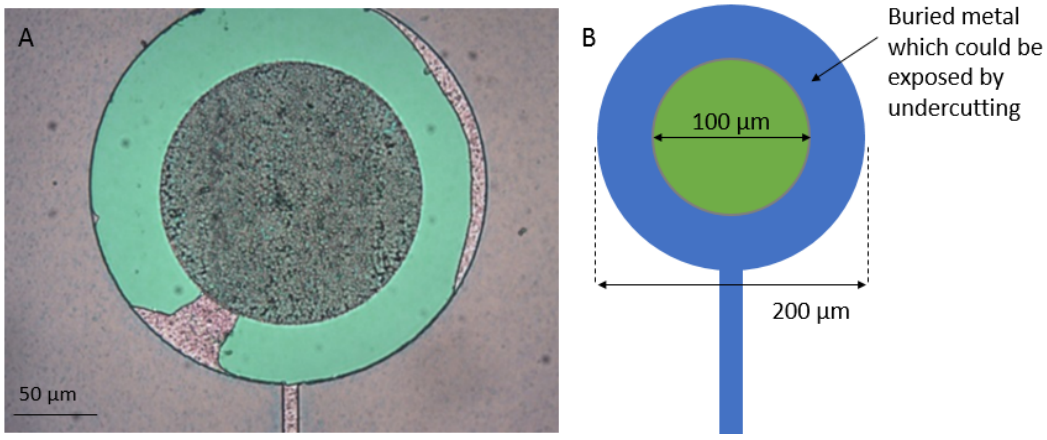


**Figure 7.7:** Optical images showing the appearance of the 100 µm nanoelectrode after testing with constant cycling of silver plating and stripping for over 48 hours. The green regions are where damage has occurred and the insulator and metal have been lost.

For this device as the magnitude of the current increased during the measurement the active area of the electrode must have been growing. The magnitude of the increase of current was large and similar to the buried metal ring, suggesting that this was active and thereby must have still been connected to the track. This therefore suggests that the final delamination damage which occurred for the device happened as it was removed from the fused salt. This is a harsh mechanical process

for the device as it results in it being exposed to thermal shock as well as the stress induced by the salt freezing on the surface and subsequently being washed off from the electrode then dried with nitrogen or argon. Nanoelectrodes tested for shorter timescales in the molten salt did not always show such clear delamination. Figure 7.8 shows a comparison of the optical appearance

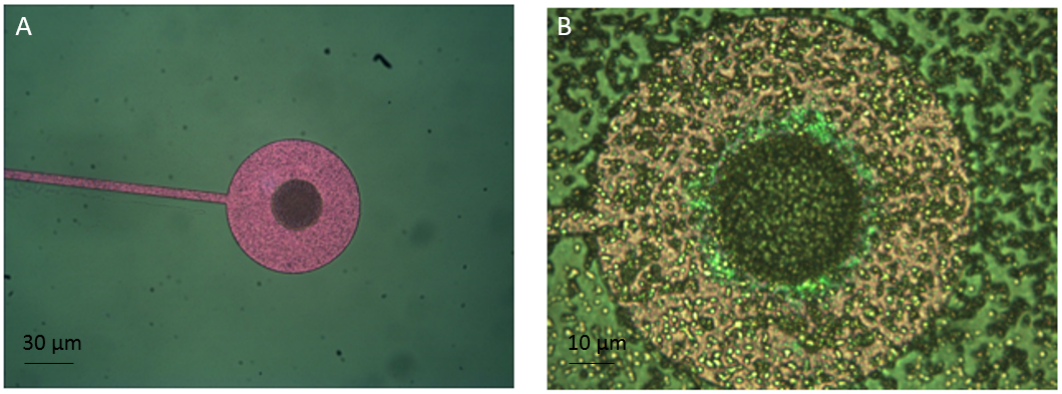


**Figure 7.8:** Images of platinum nanoband electrode before (left) and after (right) silver plating and stripping in LiCl-KCl eutectic.

of nanoelectrodes before and after testing lifetimes in LiCl-KCl-AgCl. After removal from the melt nanoelectrodes typically had a ring surrounding the electrode where the insulator appeared a slightly different colour than the rest of the buried metal area. This is indicative of a localised change. The devices generally showed a colour change radially around the nanoelectrode. Although colour changes should be treated with caution: only a small change of thickness for a thin film, or changes in refractive index can result in a large degree of colour change. There is a clear difference observable across the ring of buried metal in the used electrode. Profilometry measurements to determine if this was a raised or depressed area were limited by salt crystals ingrained into the surface which was significantly higher than the layers inspected and caused huge spikes on the measurement, making an accurate measurement impossible. The nanoelectrode architecture means that the adhesion layer is exposed to the melt. Although the titanium was replaced by TiN to offer improved robustness, it is considered that this may be causing the delamination observed. Blair had also observed metal loss and concluded that this architecture would not be suitable for long term use.[123] This has emphasised that these devices are suitable for use in a molten salt environment but suffer from lifetime issues, and require improvement in order to offer long term monitoring and insight into the processes occurring within reactions of interest.

### 7.1.4 Europium measurements in molten salt with Pt nanoelectrodes

A scan rate study performed with a 50 μm diameter Pt nanoelectrode is shown in Figure 7.9. Whilst a sigmoidal response was measured which would be expected from a nanoelectrode, there was some evidence of resistance within the measurement. There is an obvious change observed over the scan rate study performed on the 50 μm diameter Pt nanoelectrode resulting in an increase in the measured limiting currents. During the measurement the active electrode area must have increased as for the repeat of the 500 mV/s scan rate there was an increase of around 50 nA which essentially doubled the measured current. The expected limiting current for a nanoring of 50 μm diameter in this system would be between 35 nA for the theoretical limiting current or 51 nA for the calculated value with the aqueous experimentally derived prefactor. The 100 μm diameter nanoring was more consistent but the limiting current was significantly higher than the 70 or 102 nA expected values. From these measurements there is little evidence of differing responses from the two exposed metallic layers within the nanoelectrode structure. This suggests that multiple electroactive layers would not be such a large impediment to the investigation of soluble-soluble reactions. However, it is important to account for the increased nanoband thickness which could potentially be contributing to increased values of limiting currents measured. For a real molten salt reprocessing system plating and stripping reactions will certainly occur, so for nanoelectrode sensors it would be essential to avoid the complications from a dual layer electrode as peaks are already likely to overlap and will be challenging to individually distinguish. It should be noted that the response from electrodes of different metals could be used to help analyse a system by computational analysis from the known fingerprint responses of each metal with the various elements present in reprocessing systems.

Damage was still evident on all nanoelectrodes which were used to measure the europium reaction in molten salt. An example of this is shown in Figure 7.10. Typically a ring was seen originating at the ring of the exposed electrode metal and extending further into the buried metal plate surrounding the electrode. Whilst colouration of thin films rapidly changes even with small changes in layer thicknesses and it is a multilayer structure so care is required in the analysis of the optical image. There is a pink ring surrounding the nanoelectrode and a white/yellow colour radially spreading into the area of buried metal. It is interesting that this is occurring in a very localised area, suggesting damage is originating in this area. It is likely that this indicated the region where molten salt has penetrated the layers either above or below the metal and/or adhesion layer, which is consistent

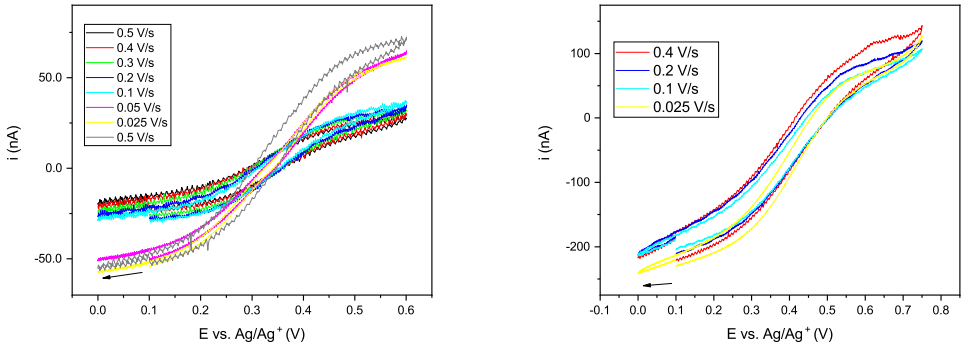


**Figure 7.9:** Scan rate study on 50 µm with 20 mM $EuCl_3$(left) and 100 µm with 60 mM $EuCl_3$(right) diameter Pt nanoring electrode at 450°C in LiCl-KCl eutectic showing the first scan beginning at 0.1 V and travelling in the direction indicated.

with an increase in the electroactive area of the device. There were concerns over the longevity of the platinum nanoring electrodes within the molten salt with evident damage on all devices used and changing voltammetric responses. This is consistent in the lifetime measurements performed with silver plating and stripping. Thereby making the nanoelectrode devices unreliable for further investigation of the europium reaction.

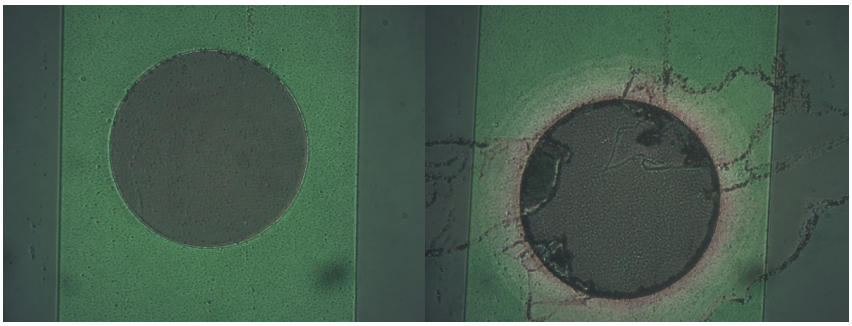

**Figure 7.10:** Comparison of the optical appearance before use (left) and after use (right) of the 100 µm Ta thin track nanoelectrode, which was used to perform voltammetric measurements on the Eu(II)/Eu(III) redox couple in molten LiCl-KCl eutectic.

## 7.2 Development of nanoelectrodes without adhesion layer

Although these devices can in principle function as nanoelectrodes, in an ideal case the nanoelectrode design would not include an active adhesion layer which could contribute to the measured signal. This was found to be particularly important with the observations that for nanoelectrodes

used for lifetime testing (discussed in Chapter 5) with silver plating and stripping, the CV response showed distinguishable peaks due to differences in the response from the two metals. An example

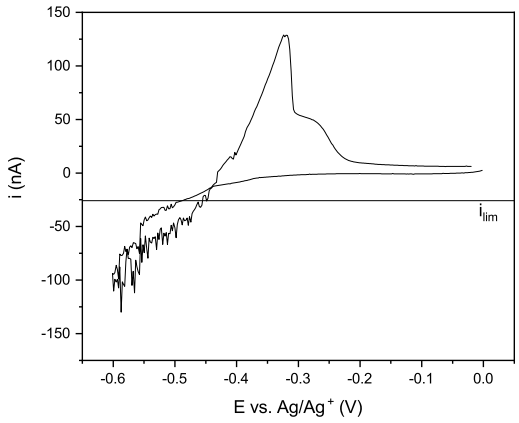


**Figure 7.11:** Background corrected tenth CV showing the typical response of silver plating and stripping in LiCl-KCl eutectic with 5 mM AgCl using a Pt nanoelectrode (with TiN adhesion layer) with a diameter of 30 µm with the architecture shown in Figure 7.2.

of this is also shown in Figure 7.11 for the CV from a platinum nanoelectrode with $Ag^+$ plating. There was clear evidence of two stripping peaks which is likely due to the differences in stripping behaviour from the adhesion layer of TiN and the electrode metal platinum. It's also possible to distinguish a change in gradient in the reductive sweep which could be under potential deposition or indicative of plating onto different surfaces as reduction potentials will also be different on each material. Reassuringly the limiting current seems to correlate well with the end of the smooth reductive current. Blair took this as the determination of the measurement of the limiting current to determine the lifetime of devices.[123] Beyond this, spikes are evident in the measured current which has been linked with damage to the device. With the evidence of differing contributions to the signal from the metallic layers in the nanoelectrode structure it would be highly desirable to remove the adhesion layer and ensure that the response observed is solely due to the electrode metal. For this to be achieved it is necessary to use a metal which adheres well to the dielectric layers in the electrode sandwich architecture. This was investigated using tantalum as an alternative metal to produce nanoelectrodes, as Section subsec:Eliminating-the-adhesion established this electrode metal does not require a seed layer for adhesion to the underlying insulator. Microelectrodes were demonstrated to function well in molten salt and allow analysis of the europium reaction which creates a pathway to the production of molten salt compatible nanoelectrodes with no adhesion

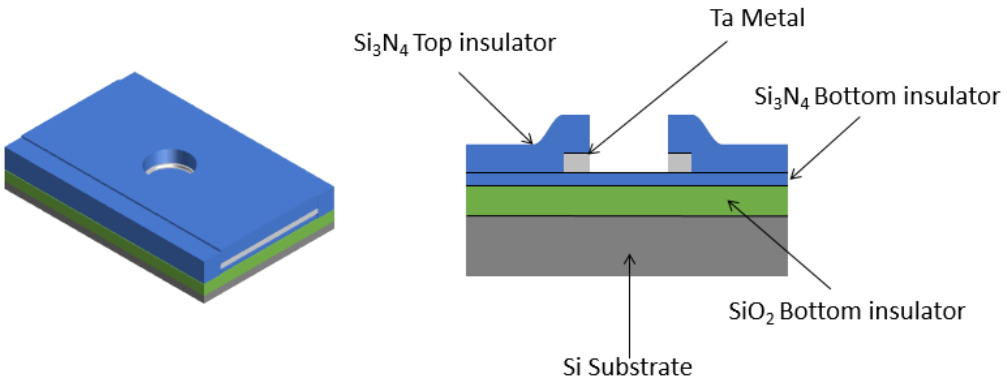


**Figure 7.12:** Schematic (left) and cross section through (right) molten salt compatible tantalum nanoelectrode design without an adhesion layer. (Not to scale).

layer. The architecture of this design is shown in Figure 7.12 and is broadly similar to that for the nanoelectrodes previously fabricated but without the adhesion layer. The other benefit of this design is that it removes the need to etch through two different layers thereby avoiding the possibility of etching variation between the layers and/or the required need for different reactive ion etches.

The scan rate study performed using a Ta nanoring electrode with 100 μm aperture is shown in Figure 7.13. There is evidence of influence of capacitance within the voltammetric measurement similar to that seen in the aqueous characterisation of platinum nanoelectrodes. It was not feasible to perform a background subtraction for the molten salt measurements due to experimental constraints (difficult to add europium accurately to the molten salt and challenging to rely on nanoelectrode functionality for multiple immersions in the melt). However, due to the reasonably high concentration of europium present (60 mM) and the order of magnitude increased diffusion coefficient (of europium compared to ferri/ferro) the currents measured are significantly larger than the 100s of pA to single nA which were measured in the aqueous system. Therefore the parasitic capacitance should have less affect on the results. The CVs again approached invariance with scan rate (at all scan rates measured) as would be expected for a nanoelectrode response. The limiting current was not so clearly defined at the positive potential end of the cyclic voltammogram and instead seems to be linearly increasing with voltage. This is not solely resistance within the system as the currents are lower for the nanoelectrodes than the microelectrodes therefore there should be less voltage drop down the track and this was not observed using tantalum microelectrodes. It is

also more apparent at the positive potential end in comparison with the negative potential end of the cyclic voltammogram. This CV is markedly different from that recorded using the Pt nanoring of 100 μm diameter where there was clearly an influence of some resistance in the system. This is interesting and seems to either occur with the tantalum devices but not the platinum or at higher concentrations of europium (this measurement was at three times the concentration of europium for the measurements using platinum electrodes). A similar linear increase with potential in the region of mass transfer limiting current was seen in aqueous nanoelectrode measurements of 50 nm thick metal.[125, 140] This was attributed to migration effects and found for 50 nm bands as the highest current densities are at the band edges and at relatively high ionic strengths. This hints at the possible influence of either migrational effects or a field effect on the charge transfer rate constant.

As was the case for the tantalum microelectrodes the measurement of ferri/ferro using Ta nanorings resulted in a resistive response. This unfortunately prevented the same measurements being performed in order to determine whether this provided a better fit to the nanoring equation for the expected limiting current.

### 7.2.1 Europium measurements in LiCl-KCl with optimised Ta nanoelectrodes

Approximating the limiting current from the start of the linear increase at the positive potential end of the CV the diffusion coefficient was calculated as $(6.33 \pm 0.81) \times 10^{-6} cm^2 s^{-1}$ which is a little greater than some of the values quoted in literature. Part of this deviation might be due to the estimation of the limiting current at the positive potential end. Despite this the extracted diffusion coefficient is similar to those reported within the experimental error.

The EIS response of the system at the 100 μm diameter nanoelectrode is shown in Figure 7.14. There was evidence of variation in the response with the applied DC potential. Given the longevity of these tantalum devices, the response should be representative of the system without the concern of changing electrode area. There seemed to be three features still part of the EIS response although this was less apparent than for the microelectrode response (Section subsec:Ta micro EIS-fitting).The first feature is expected to be due to parasitics is at very high frequency and is far smaller than the second high frequency semi-circular feature(which is clearer on the Nyquist plot).

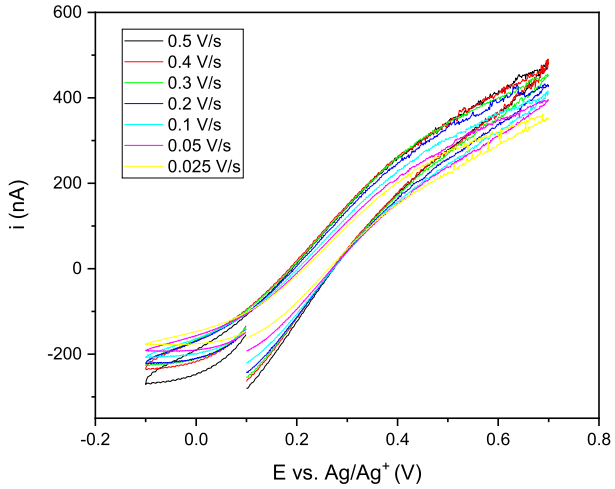


**Figure 7.13:** Scan rate study for Ta nanoelectrode of 100 µm cavity at 375°C in LiCl-KCl eutectic with 60 mM $EuCl_3$

The next high frequency semi-circle can be attributed to the electron transfer. The third feature is far smaller than the charge transfer semicircle (in comparison to microelectrodes) and is attributed to the steady-state diffusion established at the nanoelectrode.

In the Nyquist plot of the EIS response the trend with applied DC potential is difficult to distinguish. Attempts to normalise this plot against the maximum (either in the imaginary or real part) in the major semicircular feature are shown in Figure 7.15. Both normalisations indicate that there are clear trends with the applied DC potential. The response looks quite different to the typical aqueous nanoelectrode response. Although, again this has been investigated primarily with the use of nanoelectrode arrays where array overlap complicates the low frequency region with the occurrence of array overlap. In the response of the Ta single nanoelectrode this certainly isn't the case. In the Nyquist plot at very high frequencies there is a slight semicircular feature observable which appears to be independent of the applied potential with the various responses overlaying each other which suggests this feature is due to the parasitic resistance known to be present in the electrode devices. The next feature is semicircular and would be expected to be due to the charge transfer characteristics as it is occurring at reasonably high frequencies. The charge transfer feature is considered to have more influence at smaller electrode sizes and the 100 µm nanoelectrode has about 4.4 % of the active electrode area in comparison with the 30 µm microelectrode for which the response was analysed in Section subsec:Ta micro EIS-fitting. The third feature at the

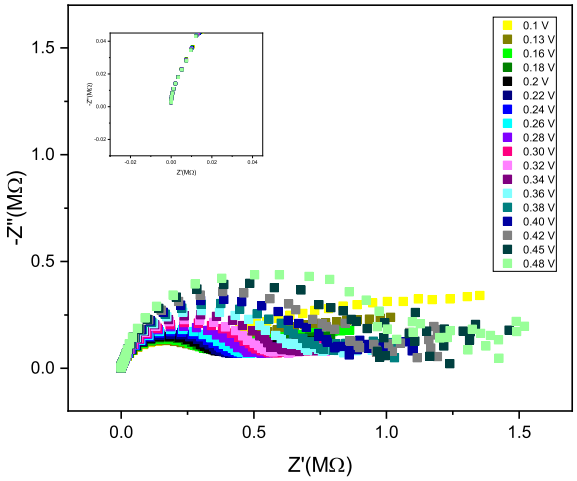


**Figure 7.14:** EIS response raw data for Ta nanoelectrode with 100 µm cavity in LiCl-KCl with 60 mM $EuCl_3$.

lowest frequencies is more linear and quite an uncharacteristic shape for nanoelectrode responses. Examining the lowest frequencies the response appears to be highly dependent on the applied DC potential. It also seems to become noisier at increasing applied potentials above E', which reflects the linear increase seen in the voltammetric response. This feature must be the response of the electrode at steady state; since it occurs at the lowest frequencies when the system should have enough time to establish the mass transfer limiting steady state observed in the voltammograms. As there was only a single nanoelectrode, the feature must be due to the diffusion field established.

As can be seen in Figure 7.14 the x-intercept was very close to zero so for fitting purposes the solution resistance was set to zero. This is reassuring as the solution resistance is expected to be low for molten salt systems. Elliott and Reeves estimated it to be less than one ohm from their data.[137,162] The third feature in the impedance response can be modelled by an element (due to diffusional transport) and a resistance due to non-linear diffusion. Previous work demonstrated that a capacitor gave the best fit for nanoelectrode EIS responses.[140] The physical interpretation of this was the rapid depletion of redox species near the electrode in the establishment of hemispherical diffusion. The charging of the capacitor corresponding to the hemispherical depletion zone for the redox species above each cavity. Interestingly other work, using slightly larger diameter (30 µm square length) cavities, found that a Warburg element instead of the capacitor provided a better

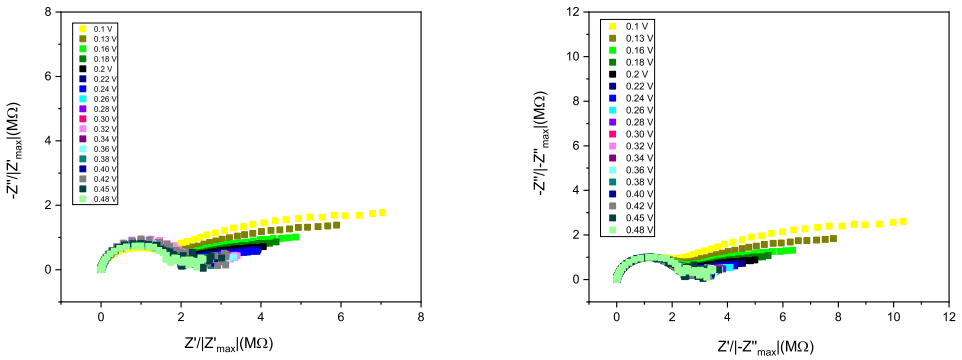


**Figure 7.15:** Normalised Nyquist plot to the maximum of the main semicircular feature for the real part (left) and the imaginary part (right) of the impedance.

fit. This was interpreted as linear diffusion to the nanoband within the cavity being the dominant physical process.[231] There was no clear semicircle observed in the low frequency diffusional region for any impedance response with the Ta nanoelectrode measurements, so as might be expected, the equivalent circuit with a capacitor did not produce a good fit to the data. Instead the Warburg element in parallel with the non-linear resistance (which applied for the microelectrodes) was found to provide a good fit to the entire data set. These nanoelectrodes are 100 μm diameter cavities so it would be understandable that the situation with linear diffusion dominating is the physical reality for the system. The fitting procedure used was similar to that described for microelectrodes; allowing the circuit to fit freely before calculating a mean value for the parasitics present in the circuit. Attempts were made to investigate different methods of fitting including only fitting to the main semicircular feature using a resistor and capacitor. However, this didn't significantly change the fit as this feature dominated the response at many applied potentials. The fit for the impedance response around E' is shown in Figure 7.16.

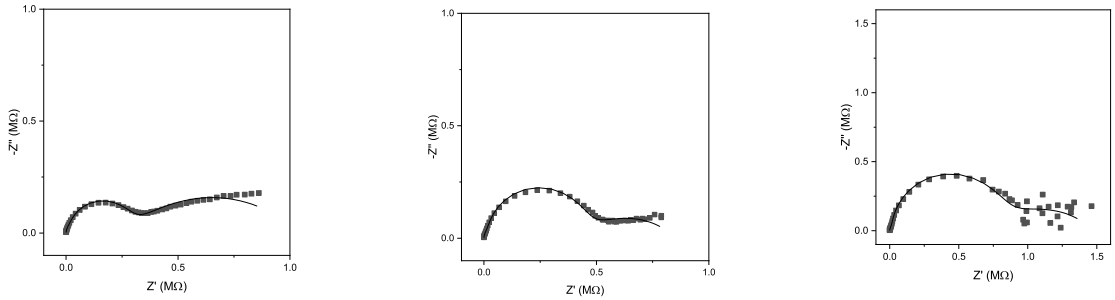


**Figure 7.16:** Impedance response and fit for the 100 μm Ta nanoring electrode at 0.16 V, 0.32 V and 0.45 V (from left to right).

There is more scatter in the low frequency data at higher applied potentials. This was observed across measurements performed across different sizes. The occurrence of noise at low frequency indicates a difference in the steady state mass transport limiting current. It was also in this potential region that contaminant species were observed to show a signal on macroelectrodes. All experiments were performed in the controlled environment of a glove box with oxygen and water contents <0.1 ppm. The salt was also pre-dried to minimise possible sources of contamination such as water, and all measurements were performed only within LiCl-KCl-$EuCl_3$ systems which appeared clean, dry and contaminant free in macroelectrode measurements. Therefore the most likely influence is due to field effects or changes to the charge transfer kinetics. The response around E' (approx 0.3 V) and had an almost flat impedance response at low frequency. The values for the parasitic resistance and capacitance across all the applied potentials from freely fitting the circuit are shown in Figure 7.17.

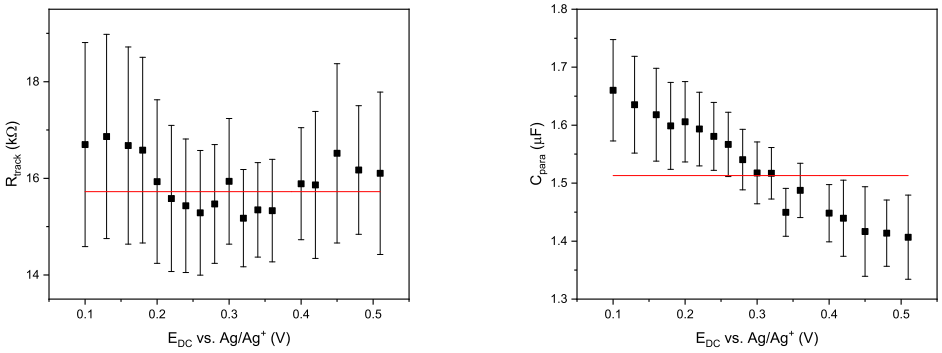


**Figure 7.17:** Fitted track parasitic resistance (left) and capacitance (right) for 100 μm diameter Ta nanoring electrode

The track resistance extracted from the EIS measurements was constant with applied potential which is reassuring as the parasitics would not be expected to show potential dependency. The best constant linear fit value of 15725 Ω is significantly lower than that extracted from the microelectrode measurements. As the currents measured are lower, the nanoelectrodes should show less voltage drop across the resistance of the track, or there could be a difference with connection. The capacitance seems to decrease with an increase in applied potential. Although the variation between the values is very small, around 0.25 μF, and all of the extracted values are constant within two sigma. The best linear fit with zero gradient was taken as the a good representation of the fitted values similarly to the analysis performed on microelectrodes, this gave a value of 1.51 μF. Using

these values the modified circuit with parasitics was fitted to the data set. Turning attention firstly to the low frequency region (which should be describing the steady state response of the electrode), Figure 7.18 shows the fitted values of $R_{nl}$ and the Warburg admittance variation with the applied DC potential.

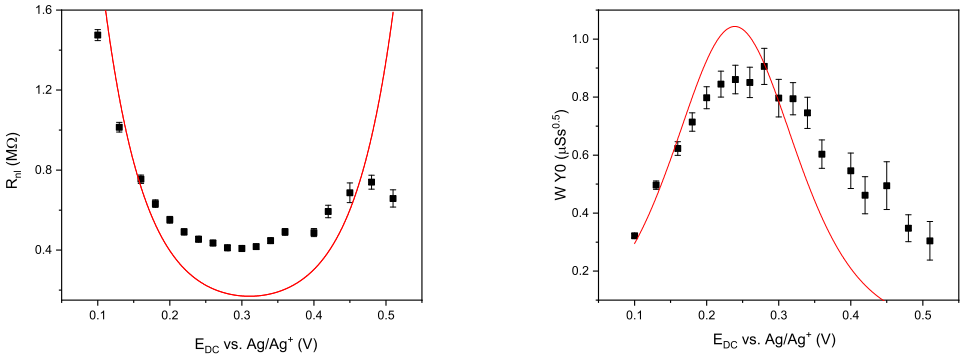


**Figure 7.18:** Extracted values of non-linear resistance and the Warburg admittance for 100 μm diameter Ta nanoring electrode showing the fit to the thermodynamic function.

The typical bowl shape is apparent for the non-linear resistance as would be expected from aqueous measurements. The Warburg impedance also shows a typical variation with applied DC potential. Both $R_{nl}$ and the Warburg admittance would be expected to follow the thermodynamic model and cannot be kinetically controlled. Clearly the thermodynamic model does not provide a good fit to either the non-linear diffusion or the Warburg admittance. This is obvious from Figure 7.18 and also Table 7.1 which summarises the extracted values from the non-linear fits. The negative value reported by Origin for the $R^2$ value for the thermodynamic fit for $R_{nl}$ demonstrates that the model clearly does not fit the data. There was scatter in the impedance response at the higher applied potentials away from E' which can be seen in Figure 7.16. This led to higher error as it was difficult to fit the low frequency region at potentials above E' and likely explains some of the deviation observed at the higher voltages. The errors are significantly reduced in comparison with the microelectrode data.

Figure 7.19 shows a comparison of the fitted values of non-linear resistance and Warburg impedance (calculated from the fitted admittance values) which were normalised to their respective minimum values. They are of very similar shapes, except for a couple of points at higher frequency where fitting to the low frequency region was challenging. This deviation is particularly evident for $R_{nl}$. Suggesting the same sub-Nernstian thermodynamic response for both features. The non-linear

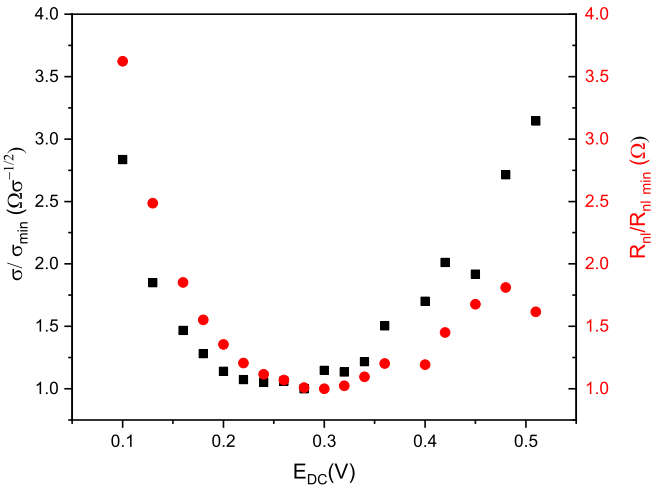


**Figure 7.19:** Comparison of normalised Warburg impedance $\sigma$ (shown in black) and non-linear resistance (shown in red) fitted values for the 100 µm diameter Ta nanoring electrode. Both were normalised to their respective minimum values.

resistance is shifted slightly more positive than sigma. This is interesting and unexpected. It could potentially be explained by a difference between exchange occurring at the surface or an extension further into the solution. It is challenging to understand why this would be the case for the two features dependent on the diffusion to the electrode. The deviation shown at higher potentials on the non-linear resistance could be indicative of the field effects of which there was also evidence in the voltammetric measurements. The bowl shape appears symmetrical for the diffusional element. This is confirmed with Tafel slope analysis of the voltammetric data shown in Figure 7.20 for the slowest scan rate of 25 mV/s with the Ta nanoelectrode of 100 µm cavity at 375°C. The clear linear regions provided very good fits with $R^2$ values of 0.999. The gradients were found to be $-9.25 \pm 0.01$ $V^{-1}$ and $-9.15 \pm 0.02$ $V^{-1}$ for the reductive and oxidative scans respectively. The gradients were nearly identical and from the equation $m = \frac{\gamma nF}{RT}$ the spread parameter, $\gamma$ was found to be $0.510 \pm 0.001$. The thermodynamics must therefore be sub-Nernstian for the europium one electron transfer reaction.

Agreement between experiment and theory has been achieved previously by taking into account non-ideal behaviour in the application of the Nernst equation to reactants.[248–250] This has predominantly been the case for reactants which are confined to the surface of the electrode for instance a polymer film on the surface of the electrode. Albery *et al.* used a development of a Guassian

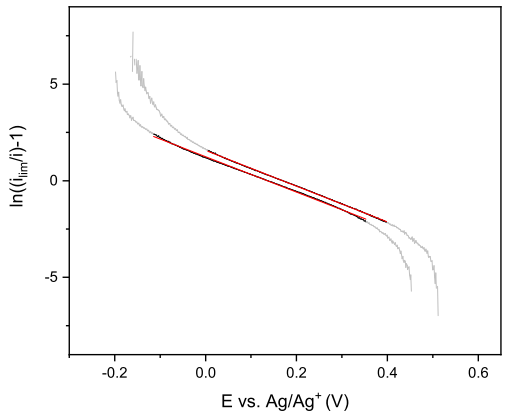


**Figure 7.20:** Tafel plot of CV of Ta nanoelectrode with 100 µm cavity at 375 °C

model to describe the dispersion of the redox change with potential from spectroelectrochemical measurements of thionine films, relating this with a dispersion of free energy change.[250, 251] For the nanoelectrode data the sub-Nernstian behaviour could similarly be modelled using a Gaussian distribution about the average value of the formal electrode potential $E'$. The distribution is given by:

$$\left(\frac{dc}{c_{tot}}\right)_{\triangle P} = \pi^{-1}\xi \exp(-\xi^2 \triangle P^2) d\triangle P \tag{7.1}$$

where $P = (E - E')F/RT$, $\left(\frac{dc}{c_{tot}}\right)_{\triangle P}$ is the fraction of species in the interval $d\triangle P$ that have an electrode potential of $E'$ and $\xi$ represents the spread of the Gaussian distribution. This corresponds to a modification for the thermodynamic fit with a prefactor multiplying both exponential terms;

$$R_{nl,th} = \frac{R_{nl,min}}{4}(2 + \exp(\frac{\gamma nF(E - E')}{RT}) + \exp(\frac{-\gamma nF(E - E')}{RT}) \tag{7.2}$$

In Albery's published paper this prefactor which is related to the spread of the Gaussian distribution was termed $\alpha$, however, to prevent confusion with the kinetic transfer coefficient in this work it shall be referred to as $\gamma$. All other variables have the same definitions as previously described.

Figure 7.21 shows a comparison of the modified thermodynamic fit (assuming a distribution about the formal potential of the europium reaction) to the thermodynamic plot with no spread if all had the same redox potential. Clearly the modified function was a far better fit for the extracted values.

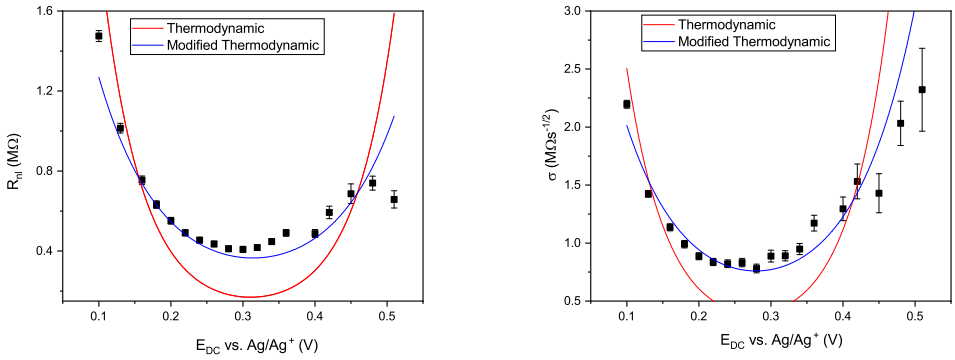


**Figure 7.21:** Comparison of thermodynamic and modified fits for the extracted values of non-linear resistance and the Warburg impedance for 100 µm diameter Ta nanoring electrode.

| | Normal thermodynamic | Modified 1 |
|---|---|---|
| $R_{nl,\ min}$ /kΩ | 169 ± 25 | 365 ± 1 |
| E' /mV | 311 ± 9 | 313 ± 1 |
| γ | 1 | 0.645 ± 0.001 |
| $R^2$ | -0.577 | 0.998 |
| | | |
| $\sigma_{min}$/kΩs$^{-1/2}$ | 393 ± 4 | 760 ± 33 |
| E' /mV | 276 ± 8 | 279 ± 5 |
| γ | 1 | 0.666 ± 0.028 |
| $R^2$ | 0.104 | 0.924 |

**Table 7.1:** Regression parameters for the various fits shown in Figure 7.21 for the Ta nanoring electrode.

The fit parameters are summarised in Table 7.1. This reinforces that the sub-Nernstian feature in the impedimetric response and illustrates the huge improvement in fits allowing a Gaussian distribution of redox potentials.

The best fit for both the non-linear resistance and sigma was found with $\gamma$ around 0.65. The plot includes The Gaussian model used relates $\gamma \approxeq erf(\zeta)$. From this a similar Gaussian can be constructed describing the spread of redox potentials at the surface of the nanoelectrode and accounting for the temperature of the experiment (648 K). Figure 7.22 shows the Gaussian functions constructed showing the spread in redox potentials using the average value of $\gamma = 0.65$. This corresponds with a value of $\zeta = 0.27$. The full width half maximum measurement of this corresponds to a spread in E' of ±239 mV. This is quite large in comparison to the width of the bowl for both $R_{nl}$ and $\sigma$. A modified fit showed better agreement between the experimental data and theory, which is evident from the significantly greater $R^2$ values.

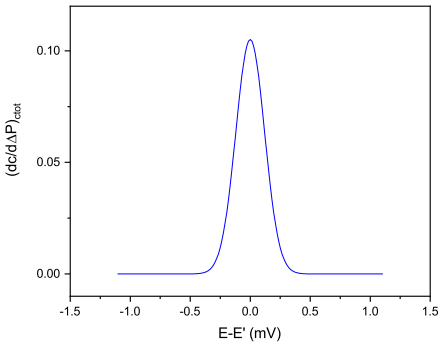


**Figure 7.22:** Plot of the Gaussian distribution of the formal electrode potentials of the Eu species at the surface of the nanoelectrode for $\gamma = 0.65$

Moving on to consider the charge transfer semicircle, which is at higher frequencies in the Nyquist plot. The extracted values for the double layer capacitance and charge transfer resistance across the range of applied potentials are shown in Figure 7.23.

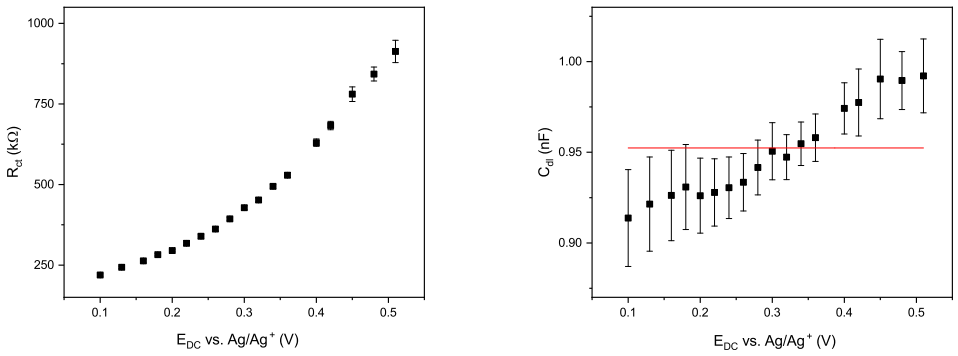


**Figure 7.23:** Extracted values of charge transfer resistance and the capacitance double layer for 100 μm diameter Ta nanoring electrode.

The double layer capacitance appears to increase across the applied potentials although this is only to a very slight degree as there is only a variation of 0.06 nF between all the extracted values suggesting that is could be approximated as constant as would be expected. The double layer capacitance should be largely independent of $E_{DC}$. A linear fit to this data was within two standard deviations of all values. The mean value of this corresponds to a double layer capacitance of 60.8 $\mu F/cm^2$. This was significantly smaller than that observed for microelectrodes discussed in Chapter 6. However, it is more similar to the value extracted from platinum microelectrode measurements by Corrigan which had a value of 85.54 $\mu F/cm^2$.[87] Again, this could indicate a thinner double layer

in molten salt than in aqueous conditions. A lower value for the capacitance double layer has also been noted for nanoelectrode arrays in aqueous conditions compared to macroelectrodes.[125] This would relate to a thicker double layer characterised by the Debye length. A plausible explanation for this is that the reduced electrode size appears more rounded.

The charge transfer resistance did not show the expected bowl shape and instead seemed to increase with applied potential. This is very different from aqueous measurements where a kinetic response was observed giving rise to the typical bowl shape.[139, 140] At an electrode in aqueous media the charge transfer typically dominates the response, if certain conditions are imposed such as the redox couples are at very low concentrations and there is no interaction between species at the electrode surface. For the molten salt system there is more thermal energy due to the elevated temperature. So, whilst there could be more interaction with the ions within the metal it would be expected to increase the rate of electron transfer. This increase with potential, which is a clear deviation from theory, could indicate a change of the electrode over time. However, the nanoelectrodes were found to be reliable over time and the nanoelectrode was not observed to be damaged after the measurement. It could indicate that europium is more stable in the oxidised form close to the electrode surface where field effects may be more dominant. This is interesting as this system has been computationally modelled to investigate the Eu redox reaction at the interface of a molten salt and metallic electrode by Pounds *et al.*.[172] Their study claims that Eu(III) ion is destabilised relative to Eu(II) close to the electrode surface. It is possible that the bowl shape would start to appear if impedance responses were collected and analysed at lower applied $E_{DC}$ potentials. However, if this is the case, it must happen at potentials significantly lower than 0.1 V. This is considerably lower than the standard potential previously observed for this system, both for all the other parameters investigated in this work and also literature values.[78, 87, 167] Therefore a very clear shift from a symmetrical bowl is observed and instead suggests that the reaction is becoming easier at lower applied DC potentials. Another possibility for this would be if instead of the electron transfer the rate limiting step was ion migration into a layer at the electrode, indicating a possible inner sphere process. As the resistance decreases with a reduction in the applied potential this is likely to be linked with the insertion of a positively charged ion (likely $Li^+$) or the removal of a negatively charged ion ($Cl^-$). Pounds study discuss a high degree of structuring of the electrolyte at the electrode interface for molten salt simulations due to competition between the packing and coulombic interactions of the ions with the electrode and their co-ordination requirements with the

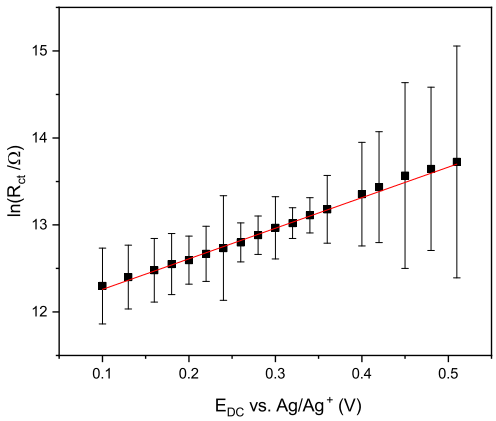


**Figure 7.24:** Logarithmic plot of the charge transfer resistance variation with applied DC potential for the 100 μm diameter Ta nanoring electrode in a solution containing 60 mM $EuCl_3$.

counterions in the melt. Their study indicated a clear difference between the number of chloride ions co-ordinated to the Eu(III) and Eu(II) species at a distance of about 8 Å and a slight difference of the density function. Very interestingly the computational model showed an increased potential mean force around this distance from the electrode for the Eu(III) species. It is therefore tempting to infer that the nanoelectrode response is because of this increased force felt by the Eu(III) species. Or the change in co-ordination number if this was required to happen before the redox species could undergo the electron transfer. If the reaction limiting factor was the migration of positive ions (or removal of negative ions) into a structured layer at the electrode surface this would be reflected by a decrease in the observed resistance with decreasing applied potentials, which would reflect the extracted values for the charge transfer resistance.

The charge transfer resistance increases monotonically with potential. It does appear to be exponential in shape and this was investigated further with a logarithmic plot of $R_{ct}$ against the applied DC potential which is shown in Figure 7.24. Modelling this with the equation $R_{ct} = \frac{R_{ct,min'}}{2}(\exp(\frac{\beta nF}{RT}(E - E_{min}))$, where all variables have the same meanings but the minimum value of $R_{ct}$ is taken at the start of the plot and $\beta$ is a combination of the Gaussian spread of potential already described as well as a kinetic factor. The gradient of the logarithmic plot was found to be 11.908 ± 0.017 $V^{-1}$, which gives a $\beta$ value of 0.196 ± 0.003. This corresponds to a kinetic factor $\alpha$ of 0.302 ± 0.005.

In order to provide an approximation of the rate constant for the Eu(II/III) couple a minimum value

was taken of the charge transfer resistance (which was extracted from the measured impedance). Combined with the area of the 50 nm thick 100 µm diameter nanoelectrode the rate constant for the reaction was calculated as $k^0 = 1.71 \pm 0.36$ cm $s^{-1}$. This represents the lower limit of the possible rate constant, as, if the surface layer theory is correct the true charge transfer resistance must be significantly lower than this. Otherwise a rising limb would be evident for the opposite side of the bowl plot. Despite only being a lower limit for the rate constant the calculated value is an order of magnitude higher than previous measurements which have reached values of 0.26 cm $s^{-1}$ in Corrigan's study which employed Pt microelectrodes.[87] Although in that measurement the fitted values of $R_{ct}$ showed discontinuity.

It is interesting that there is such a large difference in the rate of charge transfer and capacitance per unit area between the studies performed on micro- and nanoelectrodes within this work. The values extracted using nanoelectrodes would be expected to be more reliable. Firstly, the charge transfer region is more evident in nanoelectrode measurements as it would be expected to scale with critical length whereas the diffusional regime is proportional to the area. Moving from microelectrodes to nanoelectrodes the area/critical length decreases markedly. Therefore one would expect to be able to establish values more accurately using nanoelectrodes as has previously been performed for measurements in aqueous media.[99,119,124,125,140,231] Counteracting this, the deconvolution of parasitics with charge transfer was more challenging on the nanoelectrode measurements as they occurred on similar timescales. As the parasitic values were invariant with applied potential the data analysis appears reliable.

In the harsh environment damage to the electrode was always a concern. The nanoelectrode is expected to be more resilient to damage, as any fluctuation in the exposed band would not affect the critical dimension. This would be expected to cause less deviation in measured current and response, compared to any deviation in the microelectrode where any variation could contribute to the critical dimension. Although the band is non-ideal geometry, the recession depth is inconsequential compared to the cavity of the electrode. In the results presented there was a 500 nm depth of insulator and a 100 µm aperture. Previously this has been shown not to affect measurements,[140] and was confirmed within this work in aqueous media. Therefore the nanoelectrode response should be most reliable.

From the nanoelectrode measurements it seems likely that the main factor affecting the charge transfer is the ion transfer step at the surface of the electrode. There are several theories that

there is a high degree of local structure in the molten salt solution particularly at the electrode interface.[71, 145] This is the first experimental insight into this important feature. This data set was recorded at reasonably low temperature for the LiCl-KCl eutectic (around 40 °C above the literature value for the melting point of the eutectic). Therefore it would be important to study the reaction at higher temperatures using nanoelectrodes. This should elucidate whether ion transfer dominates the charge transfer resistance when there is more thermal energy within the system. It would also be fascinating to investigate if similar forms are seen for different redox species, particularly as they are likely to have different co-ordination numbers with the chloride ions.

## 7.3 Conclusions

Molten salt compatible nanoelectrodes were developed from the historic design of nanoelectrodes used for aqueous measurements. The same improvements were incorporated as for microelectrodes designed for molten salt measurements, with the incorporation of an additional underlying insulator layer and the replacement of the Ti adhesion layer with TiN as this was more resilient in the harsh environment of the molten salt, for the production of Pt nanoelectrodes. The fabrication procedure was modified to produce single nanoelectrodes to prevent the possible complications of array overlap in the measurements. The platinum nanoelectrodes were measured aqueously and a deviation was observed from the previously modelled equation for nanoring electrodes. Despite this a linear relationship was found as expected with the increasing diameter of the aperture. The higher measured currents could feasibly arise from the TiN layer being electroactive and contributing to the total thickness of the nanoband. This was consistent with the observation of multiple stripping peaks in the measurements performed with the optimised Pt nanoelectrodes in molten salt for silver plating and stripping, which indicated that the TiN was acting as another electroactive surface. For europium measurements it was harder to distinguish multiple features but a clear change in the measured current over time was observed in voltammetric measurements. Damage was also evident for the nanoelectrodes after measurements.

Both the electroactivity of the adhesion layer and the damage observed for the nanoelectrodes motivated a new design of nanoelectrodes using tantalum which did not require an adhesion layer. These were found to be highly resilient in the molten salt environment and despite the track resistance (which was discussed in Chapter 5) could be used for electroanalysis in the molten salt.

The impedance response was quite different to that observed for arrays but was found to show the expected variation with the applied potential around E'. A Warburg element was required to fit the impedance response within the modified Randles' circuit which was consistent with previous measurements on wide apertures. The non-linear resistance and the Warburg element were found to show the expected form across the applied $E_{DC}$ range. However, the thermodynamic fit had to be modified to find agreement between experimental data and theory, similar to that which had previously been performed for polymer films on electrode surfaces. This suggested that there was a spread in the redox potentials of the europium species. This was reflected in the Tafel plot for the voltammetric data.

The charge transfer resistance showed a very different form to previous aqueous measurements and instead seemed to decrease with a decreasing applied potential. An exponential function fitted this but required significant flattening from the typical thermodynamic or kinetic response with a transfer coefficient of 0.232. This is a clear deviation from the expected response, however, in the literature simulations have indicated that there is a defined local structure close to the electrode interface in molten salts. It could be that the increased local structure and interactions is becoming the rate limiting step at the nanoelectrode interface and ion interactions, particularly changes to the coordination structure of the europium species. For conclusive proof further measurements should be performed extending further away from the typical E' measured for the Eu(II/III) couple. From the fitted functions the shift in E' is very large and it seems unlikely that local destabilisation is the sole cause for the atypical form observed for the charge transfer resistance.

# Chapter 8

# Conclusions

Molten salts have found applications in a variety of industrial processes including pyrochemical reprocessing of spent nuclear fuel. Chloride melts are often used due to their reasonably low melting points, complexing ability and their reported reduced corrosion in comparison to fluoride melts. For pyrochemical reprocessing in the UK the LiCl-KCl eutectic is considered as a suitable solvent for the electrochemical dissolution of spent fuel and subsequent extraction in pyroprocessing. Particularly for the nuclear industry there is a desire to develop analytical techniques suitable for investigating molten salt systems. This necessitates overcoming challenge including elevated temperatures and the presence of reactive species in the melt, which can cause corrosion. The development of nanoelectrodes and the further development of microelectrodes to enhance their compatibility with the molten salt environment within this work addresses this need.

In Chapter 4 the exemplar reversible Eu(III)/Eu(II) redox reaction was benchmarked in the LiCl-KCl eutectic using tungsten macroelectrodes. This particularly focused on the reversibility (at typical experimental timescales) and proportions of both oxidation states within the melt. Differing proportions of the oxidation states of the europium species were found not to be fixed by thermodynamic reaction but instead by reduction of $EuCl_3$ with electrochemically (or chemically) generated reducing agents which were present within the salt. Therefore the drying method used to prepare the molten salt was found to have an impact on the proportion of species which would explain differences within literature reported values. Voltammetric and impedimetric techniques were used to probe the one electron transfer reaction and were found to give consistent results within this work. The reaction was found to be electrochemically reversible. The previously observed slow

kinetics at macroelectrodes,[167] are therefore likely to be other reactions or a surface layer on the carbon electrode used to study the reaction. There were still challenges for quantitation within these measurements, because the electroactive area of the macroelectrode was poorly defined due to the unknown wetting characteristics of the melt. It was also challenging to extract kinetic parameters from the impedance response as the linear diffusion was clearly the dominant process in the system. This demonstrates the requirement for developing well-defined minituarised electrodes, with enhanced diffusional mass transport, which are resilient in the harsh environment of the molten salt to enable quantitative analysis.

The focus of Chapter 5 was, therefore, the development of molten salt compatible micro- and nanoelectrodes which were resilient to the harsh environment. An issue identified which affected the yield of functioning microfabricated devices was connection between the electrode metal and the underlying silicon substrate, which is electrically conducting at the elevated temperatures. For aqueous measurements this had been of little concern, since even the doped silicon was not very conductive . As the perimeter of the immersed electrode chip was significantly larger than the exposed micro- or nanoelectrode at ambient temperatures if there was shorting through the bottom insulator this dominated the signal. In an ideal case a non-conductive substrate would be used. However, a trial of utilising a quartz substrate failed because the different thermal expansion of the layers caused the top insulator to crack and thereby result in a larger, undefined microelectrode area. This demonstrated that significant work would be required to find, and optimise, materials and processes in developing a completely new electrode architecture based on quartz. An alternative method was tested which aimed at improving the insulating layer between the substrate and electrode with the inclusion of a thin silicon nitride layer, which is known to be more dense and have fewer pinholes than the silicon oxide. This was found to be a suitable method to reduce the impact of the shorting failure mechanism. It should also be noted that the improvements discussed in Chapter 3 for the experimental set up also improved the yield of functioning electrodes. These improvements included ensuring a good electrical connection to the device. It also allowed the exchange of microfabricated electrode devices without removing the reference electrode, which often resulted in this breaking. This improved set-up would also help with compatibility in other larger scale systems (for instance within a flowing salt system which is under development at Edinburgh) where it would be impossible to take the system apart.

The results in Chapter 5 also showed that observed metal loss from the electrodes occurred

irrespective of the potential applied to the device, or whether redox species were present in the melt. Investigation into the cause focused on the adhesion layer, although this was found to be highly resilient in terms of both corrosion and adhesion to the dielectric layer in the melt. There was evidence of physical restructuring of the TiN adhesion material with immersion into the melt which caused a reduction in the sheet resistance of the samples and could result in additional stress. This physical change and stress could contribute to metal loss due to delamination. There was also evidence of multiple peaks in the measurement of silver plating and stripping from nanoelectrodes, highlighting a contribution from both the electrode metal and conductive adhesion layer in the molten salt, which would complicate quantitative measurements using nanoelectrodes.

Both of these factors showed that the use of an adhesion layer in the electrode structure was not ideal, and motivated the development of a new metal electrode system which did not require a seed layer for adhesion to the dielectrics. The resulting tantalum electrodes were found to be very resilient in the molten salt and showed very little evidence of physical damage. However, the tantalum electrodes were found to have a large impact from resistance (particularly evident in the impedance measurements in Chapters 6 and 7). This was thought to originate from the formation of a surface oxide when the wafers were loaded into the furnace at elevated temperature for the deposition of silicon nitride. The attempts to reduce the track resistance within the fabrication process was unsuccessful; likely due to the formation of surface films on the tantalum during reactive ion etching to expose the electrode and bond pad regions. Future work could investigate overcoming the surface film to produce functional tantalum electrodes with lower track resistance. The inherent resistance was successfully mitigated with increasing the track width. Despite this the tantalum electrodes developed were highly resilient in the melt and could be used for quantitative analysis.

In Chapter 6 the behaviour of the platinum microelectrodes were found to agree with theory in aqueous measurements with deviation from the limiting current equation observed for the largest diameter (100 μm) electrodes, which was expected as these were at the boundary of being true microelectrodes. In the molten salt measurements there was clear variation in the voltammetric measurements and impedimetric response in the measurement of Eu(III)/(II). The damage to the platinum microelectrode which was evident after removal from the melt precluded quantitative analysis of the system. In contrast, the tantalum electrodes were found to be far more resilient in molten salt and the cyclic voltammetry was consistent. Impedance measurements showed a

clear variation with the applied DC potential as theoretically expected. This occurred despite the influence of parasitic resistance and capacitance due to the track, as these were found to be invariant with potential and could be accounted for in the equivalent circuit fit. The modified Randles' circuit was found to provide a good fit to the other features in the impedance response. As opposed to previous measurements in literature with Pt microelectrodes which required the use of a constant phase element, a Warburg element fitted the data well suggesting a similar linear diffusion regime to aqueous measurements. From measurements around the standard potential, the expected bowl shape was observed for measurements of both the non-linear resistance and charge transfer resistance. Despite the improvement on the amount of error in these measurements it was unclear whether kinetic or thermodynamic fits better for both the charge transfer and non-linear resistances.

In Chapter 7 the measurements from the optimised nanoelectrodes were presented. In the historic design of nanoelectrodes a Ti adhesion layer was used to create an insulating layer due to the formation of an oxide. This method would not be successful for molten salt measurements due to previous examples of Ti removal in the melt and also possible oxide removal. The platinum nanorings with a titanium nitride adhesion layer showed deviation from limiting current expression but a clear linear trend with electrode aperture was observed, suggesting possible contribution to the signal from the adhesion layer. No deviation was observed (as with microelectrodes) with the large diameter aperture for the nanoelectrodes. These measurements also demonstrated the feasibility of measurement using a single nanoelectrode even at low concentrations of analyte in order to prevent the complication of diffusional overlap with the use of an array. The improved platinum nanoelectrodes were shown to change over time with silver plating and stripping measurements (in Chapter 5). In contrast, the tantalum nanorings were found to be more resilient in the melt and could overcome complications with signal from two different electroactive materials in the structure. This has enabled physical insight to be gained in the Eu(III)/Eu(II) redox process.

The impedance response on tantalum nanoelectrodes varied with applied potential in measurement of the Eu(III)/(II) reaction. As with the tantalum microelectrodes the influence of track parasitics were found to be reasonably potential invariant and could be compensated for in the equivalent circuit fit. A Warburg element was required to fit the impedance response, possibly due to the wide aperture of the nanoring electrode showing a larger influence of linear diffusion. Sub-Nernstian behaviour was observed for the Warburg impedance and the non-linear resistance. In comparison

these were found to be slightly offset from each other possibly due to the proximity to the surface of the electrode where the exchange was occurring. A modified thermodynamic fit, similar to that previously used for a film of material on the electrode, provided a very good fit to the extracted data. An interesting response was seen for the charge transfer resistance which monotonically increased with the applied potential. Although an increase could not be completely excluded at lower potentials it was found to be unlikely. Instead this was thought to be evidence of another step determining the rate of charge transfer such as changes in the co-ordination structure of the various Eu species close to the surface of the electrode. This corresponded with theoretical and simulated studies which have shown a high degree of structure occurring at the surface of an electrode within a molten salt.[172]

This work demonstrates the first use of a nanoelectrode to investigate physicochemical properties in a molten salt. The resilience of microfabricated devices has been improved to realise the first demonstration of nanoelectrode measurements in this harsh environment. The optimised nanoelectrodes were successfully used to study both diffusional and charge transfer processes occurring. Interesting features were noticed, which demonstrates the sensitivity and suitability of these devices for the study of electrochemical processes. The additional insight gained with these miniaturised electrodes into charge transfer steps has been highlighted. This work enhances the capability to study, and understand fundamental processes involved in nuclear pyroprocessing. Understanding the fundamentals of the reactions involved is essential to the industrial realisation of reprocessing spent fuel.

The measurements with nanoelectrodes has enabled the probing of localised structure of the molten salt and indicated the influence of local order on electrochemical reactions. This could be extended to other analytes within the melt. It would be particularly interesting to investigate if the dispersion of the standard potential, which was observed in the Eu(III)/(II) system, was present in redox reactions of other species. It would also be worth researching how the dispersion might vary with the temperature of the melt. These measurements were recorded at relatively low temperatures (around forty degrees above the melting point of the eutectic) so may be more pronounced than at higher temperatures where there is more thermal energy in the system. With the production of tantalum nanorings, which do not have an adhesion layer the electroanalysis of many reactions should be feasible. Tantalum was found to behave as an inert electrode material so could also be used for measurements of multiple analytes. Together this demonstrates tantalum nanoelectrodes

to be highly useful devices for fundamental study of the molten salt system. Molten salts are utilised in other industrial applications; such as the materials production (electrodeposition of metals, alloys and ceramics) and molten salt reactors. Molten salts are also under investigation for recycling batteries, which would also create complex mixtures of redox species similarly to pyroprocessing. The developed nanoelectrodes, which are resilient in this harsh environment, could be exploited for to probe kinetics and determine rate limiting steps for reactions relevant to these applications. Molten-salt compatible nanoelectrodes could offer similar benefits to the development of these processes.

For the future development of a practical micro- and/or nanoelectrode sensing system to monitor pyroprocessing there are still challenges that will need to be overcome. The lifetime of devices is likely to require further extension to limit the necessity of exchanging sensors. It would be imperative to have a target lifetime where the system must be known to function reliably before replacement. A system could be considered where there are protected electrochemical sensors, so that when the lower limit of the lifetime for the active device has been reached, a sensor could be deployed in-situ. The influence of radiation on the electrodes should be considered. Many of the materials utilised have been employed in space applications where they would be exposed to radiation.[252] Similar devices have also been employed to study radiotherapy efficacy.[253] The electrodes would therefore be expected to show some resilience but the impact on lifetime should be studied.

The other main area requiring development regards the signal. As previously outlined, there will be numerous analytes and high weight percentages present in a melt containing spent fuel. The overlap due to the similarity of redox potentials for the various species present in waste fuel should be explored. Techniques such as differential pulse voltammetry may be effective in the resolution of combined responses. In this work impedance spectroscopy was used to study all the processes involved with a single electrochemical reaction. For a monitoring system this would not be suitable due to length of measurement time and complications from different species. The impact on non-linearity at high weight percentages should also be explored. Simulated fuel, for the different varieties of melt that may be encountered pyroprocessing should be used to study the influence of these complicating factors. A large area of development would likely be the computational interpretation of the data collected. This has previously been shown to mitigate non-linearity and will be essential for approaching near real-time monitoring.

# References


[1] U.S. Energy Information Administration *Int. Energy Outlook* **2017**, *IEO2017*, 143.

[2] UK Parliament *HM Gov.* **2008**, *2050*, 1–103.

[3] World Nuclear Association; *Uranium, Electricity and Climate Change*; 2012.

[4] Department of Energy and Climate Change *Energy* **2011**, 218.

[5] Sovacool, B. K. *Energy Policy* **2008**, *36*, 2950–2963.

[6] Abdulaziz, R.; Ph.D. thesis; 2016.

[7] Stothard, M.; *Nuclear waste: keep out for 100,000 years*; 2016. https://www.ft.com/content/db87c16c-4947-11e6-b387-64ab0a67014c.

[8] Choi, S.-Y.; *Risk assessment of human intrusion into geological repository*; 2018.

[9] Mez, L. *Energy Policy* **2012**, *48*, 56–63.

[10] Kharecha, P. A.; Hansen, J. E. *Environ. Sci. Technol.* **2013**, *47*, 6715–6717.

[11] Murtanu, Y.; *Nuclear fission and fusion.* https://chem.libretexts.org/Bookshelves/Physical{_}and{_}Theoretical{_}Chemistry{_}Textbook{_}Maps/Supplemental{_}Modules{_}(Physical{_}and{_}Theoretical{_}Chemistry)/Nuclear{_}Chemistry/Fission{_}and{_}Fusion/Fission{_}and{_}Fusion.

[12] Wymer, R. G.; *An Overview of the Nuclear Separations Course Presentations*; 2008.

[13] Brandberg, S. G. *Nucl. Technol.* **1973**, *18*, 177–184.

[14] Hannum, W. H.; Marsh, G. E.; Stanford, G. S. *Sci. Am.* **2005**, *293*, 84–91.

[15] Delpech, S. *24 â Molten Salts for Nuclear Applications*; Elsevier Inc., 2013.

[16] Poinssot, C.; Bourg, S.; Ouvrier, N.; Combernoux, N.; Rostaing, C.; Vargas-Gonzalez, M.; Bruno, J. *Energy* **2014**, *69*, 199–211.

[17] Wymer, R. G.; *Spent Nuclear Reactor Fuel Reprocessing : Past , Present , and Future Why Should We Care About Reprocessing?*

[18] Nash, K.; Lumetta, G. *Advanced separation techniques for nuclear fuel reprocessing and radioactive waste treatment*; Woodhead Publishing, 2011.

[19] NNL *Natl. Nucl. Lab.* **2015**.

[20] CoRWM; *CoRWM Position Paper : Support for Disposal rather than Indefinite Storage*; Tech. Rep. 3649; 2018.

[21] NIRAB; *NIRAB Final Report*; Tech. Rep.; 2017. `http://www.nirab.org.uk/media/10139/nirab-117-3-nirab-final-report{_}web.pdf`.

[22] Till, C. E.; Chang, Y. I. *Plentiful Energy: The Story of the Integral Fast Reactor, the Complex History of a Simple Reactor Technology, with Emphasis on Its Scientific Basis for Non-specialists.*, 2011.

[23] Nawada, H. P.; Fukada, K. *J. Phys. Chem. Solids* **2004**, *66*, 647–651.

[24] Inoue, T.; Koyama, T.; Arai, Y. *Energy Procedia* **2011**, *7*, 405–413.

[25] Inoue, T.; Koch, L. *Nucl. Eng. Technol.* **2008**, *40*, 183–190.

[26] Yoo, J. H.; Seo, C. S.; Kim, E. H.; Lee, H. S. *Nucl. Eng. Technol.* **2008**, *40*, 581–592.

[27] Lee, H.; Park, G.-I.; Kang, K.-H.; Hur, J.-M.; Kim, J.-G.; Ahn, D.-H.; Cho, Y.-Z.; Kim, E.-H. *Nucl. Eng. Technol.* **2011**, *43*, 317–329.

[28] Selvaduray, G.; Goldstein, M. K.; Anderson, R. N. *Conserv. Recycl.* **1979**, *3*, 93–134.

[29] Choppin, G. R.; Morgenstern, A. *J. Radioanal. Nucl. Chem.* **1999**, *243*, 45–51.

[30] Sederburg, J. P.; Reddick, J. A.; *TBP and Diluent Mass Balances in the PUREX Plant at Hanford 1955-1991*; Tech. Rep.; 1994.

[31] Thompson, M. C.; Norato, M. A.; Kessinger, G. F.; Pierce, R. A.; Rudisill, T. S.; Johnson, J. D.; *Demonstration of the Urex Solvent Extraction Process With Dresden Reactor Fuel Solution*; Tech. Rep.; 2002. `https://sti.srs.gov/fulltext/tr2002444/tr2002444.pdf`.

[32] DePaoli, D.; *Role of Modeling g and Simulation in Used Fuel Recycling â¢ Introduction*; 2008.

[33] Christensen, D. C.; Bowersox, D. F.; McKerley, B. J.; Nance, R. L.; *Wastes from Plutonium Conversion and Scrap Recovery Operations*; Tech. Rep. 11069; 1988.

[34] Madic, C. *NEA/OECD 6th Inf. Exch. Meet. Actin. Fission Prod. Partitioning Transmutat.* **2000**, 53–64.

[35] Nakashima, K.; Kubota, F.; Maruyama, T.; Goto, M. *Ind. Eng. Chem. Res.* **2005**, *44*, 4368–4372.

[36] Burns, J. H. *Inorg. Chem.* **1983**, *22*, 1174–1178.

[37] May, I.; Volkovich, V. A.; Sharrad, C. A.; Bhatt, A. I.; Kinoshita, H.; Koster, A.; Charnock, J. M.; Griffiths, T. R.; Lewin, B. In *Proc. Electrochem. Soc.*; p 750.

[38] Brown, L. D.; Abdulaziz, R.; Simons, S. J. **2013**.

[39] Im, H.-j.; Yeon, J.-w. *J. Lumin.* **2018**, *196*, 302–305.

[40] Serrano, K.; Taxil, P. *J. Appl. Electrochem.* **1999**, *29*, 497–503.

[41] Serrano, K.; Taxil, P.; Dugne, O.; Bouvet, S.; Puech, E. *J. Nucl. Mater.* **2000**, *282*, 137–145.

[42] Bhatt, A. I.; Kinoshita, H.; Koster, A. L.; May, I.; Sharrad, C. A.; Volkovich, V. A.; Fox, O. D.; Jones, C. J.; Lewin, B. G.; Charnock, M.; Hennig, C. In *Atalante*; pp 1–7.

[43] Zhang, J. *J. Nucl. Mater.* **2014**, *447*, 271–284.

[44] Volkovich, V. A.; Bhatt, A. I.; May, I.; Griffiths, T. R.; Thied, R. C. *J. Nucl. Sci. Technol.* **2002**, *39*, 595–598.

[45] Parker, F. L.; *Introduction to Nuclear Chemistry and Fuel Cycle Separations*; 2008.

[46] Iizuka, M.; Koyama, T.; Kondo, N.; Fujita, R.; Tanaka, H. *J. Nucl. Mater.* **1997**, *247*, 183–190.

[47] Fusselman, S. P. *J. Electrochem. Soc.* **1999**, *146*, 2573.

[48] IAEA Technical Reports Series **2004**, STI/DOC/010/435.

[49] Cassayre, L.; Malmbeck, R.; Masset, P.; Rebizant, J.; Serp, J.; Soucek, P.; Glatz, J. P. *J. Nucl. Mater.* **2007**, *360*, 49–57.

[50] De Córdoba, G.; Laplace, A.; Conocar, O.; Lacquement, J. *J. Nucl. Mater.* **2009**, *393*, 459–464.

[51] Soucek, P.; Murakami, T.; Claux, B.; Meier, R.; Malmbeck, R.; Tsukada, T.; Glatz, J. P. *J. Nucl. Mater.* **2015**, *459*, 114–121.

[52] Laidler, J.; Battles, J.; Miller, W.; Ackerman, J.; Carls, E. *Prog. Nucl. Energy* **1997**, *31*, 131–140.

[53] Westphal, B.; Vaden, D.; Li, S.; Fredrickson, G.; Mariani, R. In *Glob. 2009*.

[54] Schulz, W. W.; Schiefelbein, G. F.; Bruns, L. E. *I EC Process Des. Dev.* **1969**, *8*, 508–515.

[55] Seiler, R. L.; Wiemels, J. L. *Environ. Health Perspect.* **2012**, *120*, 1230–1237.

[56] Sridharan, K.; Allen, T. R. *Corrosion in Molten Salts*; Elsevier Inc., 2013.

[57] Corrigan, D. K. D.; Blair, E. O.; Terry, J. J. G.; Walton, A. J.; Mount, A. R. *Anal. Chem.* **2014**, *86*, 11342–11348.

[58] Oh, S. Y.; Kim, J. Y.; Bae, S. E.; Cho, Y. H.; Yeon, J. W.; Song, K. *J. Lumin.* **2013**, *134*, 706–709.

[59] Masset, P.; Konings, R. J. M.; Malmbeck, R.; Serp, J.; Glatz, J. P. *J. Nucl. Mater.* **2005**, *344*, 173–179.

[60] Hofmeister, M.; Klein, L.; Miran, H.; Rettig, R.; Virtanen, S.; Singer, R. F. *Corros. Sci.* **2015**, *90*, 46–53.

[61] Rollet, A. L.; Bessada, C.; Rakhmatoulline, A.; Auger, Y.; Melin, P.; Gailhanou, M.; Thiaudière, D. *Comptes Rendus Chim.* **2004**, *7*, 1135–1140.

[62] Bessada, C.; Rollet, A. L. *In Situ Spectroscopy in Molten Fluoride Salts*; Elsevier Inc., 2013.

[63] Castrillejo, Y.; De La Fuente, C.; Vega, M.; De La Rosa, F.; Pardo, R.; Barrado, E. *Electrochim. Acta* **2013**, *97*, 120–131.

[64] LeBlanc, D. *Nucl. Eng. Des.* **2010**, *240*, 1644–1656.

[65] Uhlir, J. *J. Nucl. Mater.* **2007**, *360*, 6–11.

[66] Forsberg, C. W. In *Am. Nucl. Energy Symp. (ANES 2002)*; pp 1–10.

[67] Engel, J. R.; Grimes, W. R.; Rhoades, W. A.; Dearing, J. F. *Nucl. Technol.* **1979**, *46*, 30–43.

[68] Elsheikh, B. M. *J. Radiat. Res. Appl. Sci.* **2013**, *6*, 63–70.

[69] Abbasalizadeh, A.; Teng, L.; Seetharaman, S.; Sietsma, J.; Yang, Y. In *Rare Earths Ind. Technol. Econ. Environ. Implic.*; Elsevier Inc., 2015; pp 357–373.

[70] CRCT; *FactSage FT salt database.* `http://www.crct.polymtl.ca/fact/phase{_}diagram.php?xlabel={&}ylabel={&}maxx=1{&}minx=0{&}maxy=900{&}miny=0{&}calc=1{&}file=KCl-LiCl.jpg{&}y={&}cat=sa{&}dir=FTsalt{&}lang={&}type=b{&}coords=?229,239`.

[71] Cohen, Y. S.; Gabay, Y.; Cohen, Y. *J. Electrochem. Soc.* **2016**, *163*, 377–383.

[72] Salanne, M.; Madden, P. A. *Mol. Phys.* **2011**, *109*, 2299–2315.

[73] Calderoni, P.; Cabet, C. *Nucl. Corros. Sci. Eng.* **2012**, 842–865.

[74] Lambert, H.; Claux, B.; Sharrad, C.; Soucek, P.; Malmbeck, R. *Procedia Chem.* **2016**, *21*, 409–416.

[75] Nagai, T.; Fujii, T.; Shirai, O.; Yamana, H. *J. Nucl. Sci. Technol.* **2004**, *41*, 690–695.

[76] Martel, L.; Somers, J.; Berkmann, C.; Koepp, F.; Rothermel, A.; Pauvert, O.; Selfslag, C.; Farnan, I. *Rev. Sci. Instrum.* **2013**, *84*.

[77] Bessada, C.; Zanghi, D.; Pauvert, O.; Maksoud, L.; Gil-Martin, A.; Sarou-Kanian, V.; Melin, P.; Brassamin, S.; Nezu, A.; Matsuura, H. *J. Nucl. Mater.* **2017**, *494*, 192–199.

[78] Schroll, C. A.; Chatterjee, S.; Levitskaia, T. G.; Heineman, W. R.; Bryan, S. A. *Anal. Chem.* **2013**, *85*, 9924–9931.

[79] Schroll, C. A.; Chatterjee, S.; Levitskaia, T.; Heineman, W. R.; Bryan, S. A. *Electroanalysis* **2016**, *28*, 2158–2165.

[80] Castrillejo, Y.; Hernández, P.; Fernández, R.; Barrado, E. *Electrochim. Acta* **2014**, *147*, 743–751.

[81] Serp, J.; Chamelot, P.; Fourcaudot, S.; Konings, R. J. M.; Malmbeck, R.; Pernel, C.; Poignet, J. C.; Rebizant, J.; Glatz, J. P. *Electrochim. Acta* **2006**, *51*, 4024–4032.

[82] Zhang, J. *J. Nucl. Mater.* **2014**, *447*, 271–284.

[83] Iizuka, M.; Inoue, T.; Shirai, O.; Iwai, T.; Arai, Y. *J. Nucl. Mater.* **2001**, *297*, 43–51.

[84] Hoyt, N.; Pereira, C.; Willit, J.; Williamson, M.; *Voltammetry Method Evaluation*; Tech. Rep.; 2016.

[85] Pettine, W.; Jibson, M.; Chen, T.; Member, S.; Tobet, S.; Nikkel, P.; Henry, C. S. *IEEE Sensors* **2012**, *12*, 1187–1192.

[86] Bretag, A. H. *J. Gen. Physiol.* **2017**, *149*, 417–430.

[87] Corrigan, D. K.; Elliott, J. P.; Blair, E. O.; Reeves, S. J.; Schmüser, I.; Walton, A. J.; Mount, A. R. *Faraday Discuss.* **2016**, *190*, 351–366.

[88] Polk, B. J.; Stelzenmuller, A.; Mijares, G.; MacCrehan, W.; Gaitan, M. *Sensors Actuators, B Chem.* **2006**, *114*, 239–247.

[89] Barry, S.; Dawson, K.; Correa, E.; Goodacre, R.; O'Riordan, A. *Faraday Discuss.* **2013**, *164*, 283.

[90] Berduque, A.; Lanyon, Y. H.; Beni, V.; Herzog, G.; Watson, Y. E.; Rodgers, K.; Stam, F.; Alderman, J.; Arrigan, D. W. M. *Talanta* **2007**, *71*, 1022–1030.

[91] Huang, X.-J.; O'Mahony, A. M.; Compton, R. G. *Small* **2009**, *5*, 776–88.

[92] Metters, J. P.; Kadara, R. O.; Banks, C. E. *Analyst* **2011**, *136*, 1067–1076.

[93] Tan, F.; Metters, J. P.; Banks, C. E. *Sensors Actuators, B Chem.* **2013**, *181*, 454–462.

[94] Liébana, S.; Jones, L. J.; Drago, G. A.; Pittson, R. W.; Liu, D.; Perrie, W.; Hart, J. P. *Sensors Actuators, B Chem.* **2016**, *231*, 384–392.

[95] Arrigan, D. W. M. *Analyst* **2004**, *129*, 1157–1165.

[96] Morris, R. B.; Franta, D. J.; White, H. S. *J. Phys. Chem.* **1987**, *91*, 3559–3564.

[97] Seibold, J. D.; Scott, E. R.; White, H. S. *J. Electroanal. Chem.* **1989**, *264*, 281–289.

[98] MacFarlane, D. R.; Wong, D. K. Y. *J Electroanal Chem* **1985**, *185*, 197–202.

[99] Macpherson, J. V.; Jones, C. E.; Unwin, P. R. *J Phys Chem B* **1998**, *102*, 9891–9897.

[100] Lanyon, Y. H.; De Marzi, G.; Watson, Y. E.; Quinn, A. J.; Gleeson, J. P.; Redmond, G.; Arrigan, D. W. M. *Anal. Chem.* **2007**, *79*, 3048–3055.

[101] Nagale, M. P.; Fritsch, I. *Anal. Chem.* **1998**, *70*, 2902–2907.

[102] Nagale, M. P.; Fritsch, I. *Anal. Chem.* **1998**, *70*, 2902–2907.

[103] Nagale, M. P.; Ph.D. thesis; 1998.

[104] Penner, R. M.; Heben, M. J.; Longin, T. L.; Lewis, N. S. *Science (80-. ).* **1990**, *250*, 1118–1121.

[105] Mirkin, M. V.; Fan, F.-R. F.; Bard, A. J. *Science (80-. ).* **1992**, *257*, 364–366.

[106] Bach, C. E.; Nichols, R. J.; Beckmann, W.; Meyer, H.; Schulte, A.; Besenhard, J. O.; Jannakoudakis, P. D. *J. Electrochem. Soc.* **1993**, *140*, 1281.

[107] Katemann, B. B.; Schuhmann, W. *Electroanalysis* **2002**, *14*, 22–28.

[108] Penner, R. M.; Martin, C. R. *Anal. Chem.* **1987**, *59*, 2625–2630.

[109] Jeoung, E.; Galow, T. H.; Schotter, J.; Bal, M.; Ursache, A.; Tuominen, M. T.; Stafford, C. M.; Russell, T. P.; Rotello, V. M. *Langmuir* **2001**, *17*, 6396–6398.

[110] Heus, R. J.; Egan, J. J. *J. Electrochem. Soc.* **1960**, *107*, 824–828.

[111] Laitinen, H. A. *Pure Appl. Chem.* **1967**, *15*, 227–238.

[112] Senderoff, S. *J. Electrochem. Soc.* **1959**, 32–36.

[113] Stehle, G.; Duruz, J. J.; Landolt, D. *Electochmica Acta* **1981**, *27*, 783–789.

[114] Oxley, J. E.; Ph.D. thesis; 1961.

[115] Laitinen, H. A.; Tischer, R. P.; Roe, D. K. *J. Electrochem. Soc.* **1960**, *107*, 546–555.

[116] Carlin, R. T.; Osteryoung, R. A. *J. Electrochem. Soc.* **1989**, *136*, 1249.

[117] Pint, P.; Flengas, S. N. *J. Electrochem. Soc.* **1976**, *123*, 1042.

[118] Black, E. D.; DeVries, T. **1952**, *30*, 906–909.

[119] Woodvine, H. L.; Terry, J. G.; Walton, A. J.; Mount, A. R. *Analyst* **2010**, *135*, 1058–1065.

[120] Brady, C. L.; Ph.D. thesis; 2013.

[121] Relf, A.; Corrigan, D.; Brady, C. L. C.; Terry, J. G.; Walton, A. J.; Mount, A. R. *ECS Trans.* **2012**, *50*, 105–109.

[122] Blair, E. O.; Corrigan, D. K.; Terry, J. G.; Mount, A. R.; Walton, A. J. *J. Microelectomech. Syst* **2015**, *24*, 1346–1354.

[123] Blair, E. O. **2016**.

[124] Terry, J. G.; Schmüser, I.; Underwood, I.; Corrigan, D. K.; Freeman, N. J.; Bunting, A. S.; Mount, A. R.; Walton, A. J.; Terry, J. G.; Schmüser, I. *IET Nanobiotechnol.* **2013**, *7*, 125–34.

[125] Schmueser, I.; Walton, A. J.; Terry, J. G.; Woodvine, H. L.; Freeman, N. J.; Mount, A. R. *Faraday Discuss.* **2013**, *164*, 295.

[126] Bard, A. J.; Faulkner, L. R. *Electrochemical Methods, Fundamentals and Applications*, 2nd ed.; John Wiley & Sons Inc., 2001.

[127] Schmickler, W.; Santos, E. *Interfacial Electrochemistry*, 2nd ed.; Springer, 2010.

[128] Gileadi, E. *Physical Electrochemistry Fundamentals, Techniques and Applications*; Wiley VCH, 2011.

[129] Brett, C. M. A.; Brett, M. O. *Electrochemistry Principles, Methods and Applications*; Oxford University Press, 2003.

[130] Labrie, R. J.; Lamb, V. A. *J. Electrochem. Soc.* **1959**, *106*, 895–899.

[131] Pal, R.; Ananthasivan, K.; Anthonysamy, S.; Ganesan, V. *Electrochim. Acta* **2011**, *56*, 4276–4280.

[132] Wang, H.; Siambun, N. J.; Yu, L.; Chen, G. Z. *J. Electrochem. Soc.* **2012**, *159*, H740–H746.

[133] Forster, R. *Chem. Soc. Rev.* **1994**, 289–297.

[134] Stulík, K.; Amatore, C.; Holub, K.; Marecek, V.; Kutner, W. *Pure Appl. Chem.* **2000**, *72*, 1483–92.

[135] Amatore, C.; Pebay, C.; Thouin, L.; Wang, A. *Electrochem. commun.* **2009**, *11*, 1269–1272.

[136] Pons, S.; Fleischmann, M. *Anal. Chem.* **1987**, *59*, 1391–1399.

[137] Elliott, J. P.; Ph.D. thesis; 2017.

[138] Bond, A. M. A. *Analyst* **1994**, *119*, 1–21.

[139] Woodvine, H. L.; Ph.D. thesis; 2011.

[140] Schmüser, I.; Ph.D. thesis; 2015.

[141] Saito, Y. *Rev. Polarogr.* **1968**, *15*, 177–187.

[142] Brownson, D. A.; Banks, C. E. *The Handbook of Graphene Electrochemistry*, 2014.

[143] Randles, J. E. B. *Discuss. Faraday Soc.* **1947**, *1*, 11–19.

[144] Alden, J. A.; Compton, R. G. *Electroanalysis* **1996**, *8*, 30–33.

[145] Salanne, M.; Simon, C.; Turq, P.; Madden, P. A. *J. Phys. Condens. Matter* **2008**, *20*.

[146] Yu, T.; Howlader, M. M. R.; Zhang, F.; Bakr, M. *ECS Trans.* **2011**, *35*, 3–10.

[147] Pearson, G. L.; Bardeen, J. *Phys. Rev.* **1949**, *75*.

[148] Takahashi, M.; Katsuyama, Y.; Kanzaki, Y. *J. Electroanal. Chem.* **1975**, *62*, 363–371.

[149] Kanzaki, Y.; Takahashi, M. *J. Electroanal. Chem. Interfacial Electrochem.* **1978**, *90*, 305–312.

[150] Mayorshin, A. In *Fuel cycle Nucl. power Eng.*

[151] Subramanian, B.; Ashok, K.; Subramanian, K.; Sastikumar, D.; Selvan, G.; Jayachandran, M. *Surf. Eng.* **2009**, *25*, 490–495.

[152] EE Semi; *Properties of SiO2 and Si3N4 at 300K*; 2004. `http://eesemi.com/sio2si3n4.htm`.

[153] AZO Materials; *Properties: Silicon Nitride (Si3N4) Properties and Applications*; 2015. `http://www.azom.com/properties.aspx?ArticleID=53`.

[154] Semiconductor, V.; *The General Properties of Si, Ge, SiGe, SiO2 and Si3N4 June*; 2002.

[155] Zohni, O.; Buckner, G.; Kim, T.; Kingon, A.; Maranchi, J.; Siergiej, R. *J. Micromechanics Microengineering* **2007**, *17*, 1042–1051.

[156] Blair, E. O.; Ph.D. thesis.

[157] Deal, B. E.; Grove, A. S. *J. Appl. Phys.* **1965**, *36*, 3770.

[158] Wolf, S.; Tauber, R. N. *Silicon Processing for the VLSI Era, Vol 1: Process Technology*; Lattice Press, 1986.

[159] Yasuda, K.; Nohira, T.; Ogata, Y. H.; Ito, Y. *Electrochim. Acta* **2005**, *51*, 561–565.

[160] Schneider, H.; Schreuer, J.; Hildmann, B. *J. Eur. Ceram. Soc.* **2008**, *28*, 329–344.

[161] Gao, P.; Jin, X.; Wang, D.; Hu, X.; Chen, G. Z. *J. Electroanal. Chem.* **2005**, *579*, 321–328.

[162] Reeves, S. J.; Ph.D. thesis; 2018.

[163] Guo, S.; Zhang, J.; Wu, W.; Zhou, W. *Prog. Mater. Sci.* **2018**.

[164] Kim, B. Y.; Yun, J.-I. *ECS Electrochem. Lett.* **2013**, *2*, H54–H57.

[165] Kuznetsov, S. A.; Rycerz, L.; Gaune-Escard, M. *J. New Mater. Electrochem. Syst.* **2006**, *9*, 313–321.

[166] Bae, S. E.; Park, Y. J.; Min, S. K.; Cho, Y. H.; Song, K. *Electrochim. Acta* **2010**, *55*, 3022–3025.

[167] Bermejo, M. R.; de la Rosa, F.; Barrado, E.; Castrillejo, Y. *J. Electroanal. Chem.* **2007**, *603*, 81–95.

[168] Caravaca, C.; de Córdoba, G.; Tomás, M. J.; Rosado, M. *J. Nucl. Mater.* **2007**, *360*, 25–31.

[169] Kim, T. J.; Uehara, A.; Nagai, T.; Fujii, T.; Yamana, H. *J. Nucl. Mater.* **2011**, *409*, 188–193.

[170] Novoselova, A. V.; Khokhlov, V. A.; Shishkin, V. Y. *Russ. J. Appl. Chem.* **2001**, *74*, 1672–1677.

[171] Park, Y. J.; Kim, T. J.; Cho, Y. H.; Jung, Y.; Im, H. J.; Song, K.; Kwang, Y. J. *Bull. Korean Chem. Soc.* **2008**, *29*, 127–129.

[172] Pounds, M. A.; Salanne, M.; Madden, P. A. *Mol. Phys.* **2015**, *113*, 2451–2462.

[173] Pandian, S.; Naidu, S, V, N.; Rama Rao, P. *Bin. Alloy Phase Diagrams II Ed* **1990**, *2*, 1683–1685.

[174] Kuznetsov, S. a.; Gaune-Escard, M. *J. Nucl. Mater.* **2009**, *389*, 108–114.

[175] Merwin, A.; Phillips, W. C.; Williamson, M. A.; Willit, J. L.; Motsegood, P. N.; Chidambaram, D. *Sci. Rep.* **2016**, *6*, 1–6.

[176] Einstein, A. *Ann. Phys.* **1905**, *322*, 549–560.

[177] Castrillejo, Y.; Bermejo, M. R.; Díaz Arocas, P.; Martínez, A. M.; Barrado, E. *J. Electroanal. Chem.* **2005**, *575*, 61–74.

[178] Gese, N. J.; Ph.D. thesis; 2015.

[179] Gupta, P.; CRC Press, 2009; Vol. 37, pp 771–790.

[180] Mittal, S. *ACM Comput. Surv.* **2016**, *48*, 1–29.

[181] Xue, Y.; Wang, Q.; Yan, Y. D.; Chen, L.; Zhang, M. L.; Zhang, Z. J. *Energy Procedia* **2013**, *39*, 474–479.

[182] Blair, E. O.; Schmueser, I.; Corrigan, D. K.; Terry, J. G.; Smith, S.; Mount, A. R.; Walton, A. J. In *2016 Int. Conf. Microelectron. Test Struct.*; pp 28–31.

[183] Blair, E. O.; Basanta, L. P.; Schmueser, I.; Marland, J. R. K.; Buchoux, A.; Tsiamis, A. In *Int. Conf. Microelectron. test Struct.*; pp 179–184.

[184] Wang, H.; Ji, X.; Chen, C.; Xu, K.; Miao, L. *AIP Adv.* **2013**, *3*, 112102.

[185] Valencia-Jaime, I.; Sarmiento-Pérez, R.; Botti, S.; Marques, M. A.; Amsler, M.; Goedecker, S.; Romero, A. H. *J. Alloys Compd.* **2016**, *655*, 147–154.

[186] Liu, Z.; Yu, Q.; Zhao, Y.; He, R.; Xu, M.; Feng, S.; Li, S.; Zhou, L.; Mai, L. *Chem. Soc. Rev.* **2019**, *48*, 285–309.

[187] Ding, N.; Xu, J.; Yao, Y. X.; Wegner, G.; Fang, X.; Chen, C. H.; Lieberwirth, I. *Solid State Ionics* **2009**, *180*, 222–225.

[188] Luais, E.; GhamoussFouad; Wolfman, J.; Desplobain, S.; Gautier, G.; Tran-Van, F.; Sakai, J. *J. Power Sources* **2015**, *274*, 693–700.

[189] Huang, X. D.; Gan, X. F.; Huang, Q. A.; Yang, J. Z. *Front. Energy* **2018**, *12*, 225–232.

[190] Doi, T.; Marinescu, I. D.; Kurokawa, S. In *Adv. C. Polishing Technol.*, 1st ed.; Elselvier, 2011; Chapter 6, pp 297–304.

[191] Freund, L. B.; Suresh, S. *Thin Film Materials Stress , Defect Formation and Surface Evolution*; Cambridge University Press, 2008.

[192] Abadias, G.; Chason, E.; Keckes, J.; Sebastiani, M.; Thompson, G. B.; Barthel, E.; Gary, L.; Murray, C. E.; Stoessel, C. H.; Martinu, L. *J. Vac. Sci. Technol. A Vacuum, Surfaces, Film.* **2018**, *36*, 020801 1–48.

[193] Hutchinson, J. W. In *Tech. Univ. Denmark Notes a DCAMM Course.*

[194] Maurits, J. E. A. *IEEE Trans. Electron Devices* **1978**, *25*, 859–863.

[195] Goto, T.; Kado, Y.; Hagiwara, R. *Boron-Doped Diamond Electrodes in Molten Chloride Systems*; Elsevier Inc., 2013.

[196] Howe, J. Y.; Jones, L. E.; Cormack, A. N.; *The Oxidation of Diamond*; 2001.

[197] Li, Z. C.; Pei, Z. J.; Funkenbusch, P. D. *Proc. IMechE* **2010**, *225*, 975–989.

[198] Sirdeshmukh, D. B.; Sirdeshmukh, L.; Subhadra, K. G. In *Micro- macro-properties solids Therm. Mech. Dielectr. Prop.*, 2006; pp 37–75.

[199] DIEMAT; *Thermal properties of semiconductor and microelectronic packaging materials.* `http://diemat.com/docs/products/thermals/thermal{_}properties.php`.

[200] materials, A.; *Silica Â- Silicon Dioxide (SiO2)*; Tech. Rep.; 2001.

[201] Neyco; *Materials substrates.* `https://www.neyco.fr/en/our-products/materials/substrates-single-crystals/glass-quartz-ceramics`.

[202] Wang, H.; Liu, S.; Li, B.; Zhao, Z. *J. Fluor. Chem.* **2015**, *175*, 98–102.

[203] Castrillejo, Y.; Bermejo, M. R.; Barrado, A. I.; Pardo, R.; Barrado, E.; Martínez, A. M. *Electrochim. Acta* **2005**, *50*, 2047–2057.

[204] Xia, Z. C.; Hutchinson, J. W. *J. Mech. Phys. Solids* **2000**, *48*, 1107–1131.

[205] Klokholm, E. *IBM J. Res. Dev.* **1987**, *31*, 585–591.

[206] Nekkanty, S.; Ph.D. thesis; 2009.

[207] Microchem *Microchem. Prod. data* **2014**.

[208] Temple-Boyer, P.; Rossi, C.; Saint-Etienne, E.; Scheid, E. *J. Vac. Sci. Technol.* **1998**, *A 16*, 2003–2007.

[209] Zheng, B.; Zhou, C.; Wang, Q.; Chen, Y.; Xue, W. *Adv. Mater. Sci. Eng.* **2013**, *2013*.

[210] Musard, H.; Ph.D. thesis; 2016.

[211] Kobeda, E.; Irene, E. A. *J. Vac. Sci. Technol.* **1986**, 1–26.

[212] Uyemura, J. P. *CMOS Logic Circuit Design*; Springer Science & Business Media, 1999.

[213] Blair, E. O.; Corrigan, D. K.; Levene, H. J.; Schmueser, I.; Terry, J. G.; Smith, S.; Mount, A. R.; Walton, A. J. *IEEE Trans. Semicond. Manuf.* **2017**, *30*, 192–200.

[214] Asakura, S.; Mukaibo, T. *Electrochem. Acta* **1968**, *13*, 881–890.

[215] *ASM Alloy Phase Database*. `https://www.asminternational.org/materials-resources/online-databases/-/journal{_}content/56/10192/15469013/DATABASE`.

[216] Wolansky, D. In *IITC 2017 - 2017 IEEE Int. Interconnect Technol. Conf.*; pp 1–3.

[217] Leu, C.-C.; Lin, H.-T.; Hu, C.-T.; Chien, C.-H.; Yang, M.-J.; Yang, M.-C.; Huang, T.-Y. *J. Appl. Phys.* **2002**, *92*, 1511–1517.

[218] Indacochea, J. E.; Smith, J. L.; Litko, K. R.; Karell, E. J. *J. Mater. Res.* **1999**, *14*, 1990–1995.

[219] Fairey, B.; *High-Reliability Solid Tantalum Capacitors*.

[220] El-Sayed; Ph.D. thesis; 2006.

[221] Gill, J.; *Basic Tantalum Capacitor Technology*.

[222] Williams, K.; Muller, R. *J. Microelectromechanical Syst.* **1996**, *7157*.

[223] Williams, K. R.; Gupta, K.; Wasilik, M. *J. Microelectromechanical Syst.* **2003**, *12*, 761–778.

[224] Kuo, Y. *Japanese J. Appl. Phys. Part 1 Regul. Pap. Short Notes Rev. Pap.* **1993**, *32*, 179.

[225] Martz, J. C.; Hess, D. W.; Anderson, W. E. *J. Appl. Phys.* **1990**, *67*, 3609–3617.

[226] Solla-Gullón, J.; Rodríguez, P.; Herrero, E.; Aldaz, A.; Feliu, J. M. *Phys. Chem. Chem. Phys.* **2008**, *10*, 1359–1373.

[227] Vogt, S.; Su, Q.; Gutierrez-Sanchez, C.; Nöll, G. *Anal. Chem.* **2016**, acs.analchem.5b04814.

[228] Henihan, G.; Schulze, H.; Corrigan, D. K.; Giraud, G.; Terry, J. G.; Hardie, A.; Campbell, C. J.; Walton, A. J.; Crain, J.; Pethig, R.; Templeton, K. E.; Mount, A. R.; Bachmann, T. T. *Biosens. Bioelectron.* **2016**, *81*, 487–494.

[229] Sun, T.; Blanchard, P. Y.; Mirkin, M. V. *Anal. Chem.* **2015**, *87*, 4092–4095.

[230] Jouihan, H.; *Iron - Prussian Blue Reaction - Mallory's Method*; 2012. `http://www.bio-protocol.org/e222`.

[231] Piper, A.; Ph.D. thesis; 2017.

[232] Konopka, S. J.; McDuffie, B. *Anal. Chem.* **1970**, *42*, 1741–1746.

[233] Ngamchuea, K.; Eloul, S.; Tschulik, K.; Compton, R. G. *J. Solid State Electrochem.* **2014**, *18*, 3251–3257.

[234] Heinze, J. *Angew. Chemie Int. Ed. English* **1993**, *32*, 1268–1288.

[235] Gonzalez, J.; Molina, A.; Martinez-Ortiz, F.; Lopez-Tenes, M.; Compton, R. G. *Electrochim. Acta* **2016**, *213*, 911–926.

[236] Royea, W. J.; Krüger, O.; Lewis, N. S.; *Frumkin corrections for heterogeneous rate constants at semiconducting electrodes*; 1997.

[237] Gavaghan, D. J.; Feldberg, S. W. *J. Electroanal. Chem.* **2000**, *491*, 103–110.

[238] Kisza, A. *J. Electroanal. Chem.* **2002**, *534*, 99–106.

[239] Frishknecht, A. L.; Halligan, D. O.; Parks, M. L.; *Electrical Double Layers and Differential Capacitance in Molten Salts from Density Functional Theory*; Tech. Rep.; 2014.

[240] Kłos, J.; Lamperski, S. *Electrochem. Acta* **2016**, *213*, 574–577.

[241] Kłos, J.; Lamperski, S. *J. Chem. Phys.* **2019**, *150*, 064704–01–08.

[242] Fellner, P.; Matiašovsky, K. *Chem. zvesti* **1972**, *26*, 36–40.

[243] Sandison, M. E.; Cooper, J. M. *Lab Chip* **2006**, *6*, 1020–1025.

[244] Piper, A.; Alston, B. M.; Adams, D. J.; Mount, A. R. *Faraday Discuss.* **2018**, *00*, 1–3.

[245] Baker, W. S.; Crooks, R. M. *J. Phys. Chem. B* **1998**, *102*, 10041–10046.

[246] Freeman, N. J.; Sultana, R.; Reza, N.; Woodvine, H.; Terry, J. G.; Walton, A. J.; Brady, C. L.; Schmueser, I.; Mount, A. R. *Phys. Chem. Chem. Phys.* **2013**, *15*, 8112–8118.

[247] Moreno, J. J. G.; Nolan, M. *Appl. Mater. Interfaces* **2017**, *9*, 38089–38100.

[248] Brown, A. P.; Anson, F. C. **1977**, *49*, 1589–1595.

[249] Posadas, D.; Fonticelli, M.; Presa, M. J. R.; Florit, M. I. *J. Phys. Chem. B* **2001**, *105*, 2291–2296.

[250] Albery, J. W.; Boutelle, M. G.; Colby, P. J.; Hillman, A. R. *J Electroanal. Chem.* **1982**, *133*, 135–145.

[251] Albery, W. J.; Bartlett, P. N.; Wilde, P.; Darwent, J. R. *J. Am. Chem. Soc.* **1985**, *107*, 1854–1858.

[252] Miller, L. M. In *Proc. SPIE*; pp 1–13.

[253] University of Edinburgh; *Tumour study could help improve radiotherapy*; 2016. `https://www.ed.ac.uk/news/2016/tumour-study-could-help-improve-radiotherapy`.